The role of the zinc finger transcription factor Gli3 in murine hindbrain development

Dissertation

zur

Erlangung des Doktorgrades (Dr. rer. nat.)

der

Mathematisch-Naturwissenschaftlichen Fakultät

der

Rheinischen Friedrich-Wilhelms-Universität Bonn

vorgelegt von

Erick Ariel Martínez Chávez

aus Mexiko Stadt, Mexiko

Bonn, Februar 2019

Angefertigt mit Genehmigung der Mathematisch-Naturwissenschaftlichen Fakultät
der Rheinischen Friedrich-Wilhelms-Universitäts Bonn

1. Gutachter: Prof. Dr. Sandra Blaess

2. Gutachter: Prof. Dr. Walter Witke

Tag der Promotion: 18.06.19

Erscheinungsjahr: 2019

TABLE OF CONTENTS

ABBREVIATIONS

5Gn	Trigeminal ganglion
5n	Trigeminal nerve
5N	Trigeminal nucleus
7n	Facial nerve
7N	Facial nucleus
8n	Vestibulocochlear nerve
9n	Glossopharyngeal nerve
10n	Vagus nerve
12N	Hypoglossal nucleus
AP	Anteroposterior
AES	Anterior extramural stream
ASCL1	Achaete-scute homolog 1
ATOH1	Atonal homolog 1
BARHL	BARH Like homeobox transcription factor (e.g. BARHL1, BARHL2)
BCO	Brother of CDO
BMP	Bone morphogenetic protein (e.g. BMP4, etc.)
BRN3.2	Brain-specific homeobox/POU domain protein 3B
BrdU	Bromodesoxyuridin
CAMs	Cell adhesion molecules
CES	Cochlear extramural stream
CF	Climbing fiber
CFN	Climbing fiber neuron
CNS	Central nervous system
clRL	Caudal lower rhombic lip
CXCL12	C-X-C motif chemokine 12
CXCR4	C-X-C motif chemokine receptor 4
DAO	Dorsal accessory olive
DCC	Deleted in colorectal cancer receptor
DCN	Deep cerebellar nuclei
DiI	1, 1´ - Dioctadecyl-3, 3, 3´, 3´- tetramethylindocarbocyanine
DM	dorsomedial group subnucleus
DV	Dorsoventral
ECN	External cuneate nucleus
ECM	Extracelullar matrix
eMFNs	Ectopic mossy fiber neurons

Er81	ETS-related 81 transcription factor
En1	Engrailed 1
FBMNs	Facial branchiomotor neurons
FGF	Fibroblast growth factor (e.g. FGF8, FGF17, etc.)
FOXP2	Forkhead-Box-Protein P2
GAD	Glutamate decarboxylase (e.g. GAD1, GAD2)
GAS1	Growth arrestin-specific 1
GDF7	Growth differentiation factor 7
GBX2	Gastrulation brain homeobox 2
GCN	Granular cell neuron (cerebellar)
GLI	Gli receptor protein (e.g. GLI1 – GLI3)
GLIA	Gli receptor protein activator form
GLIR	Gli receptor protein repressor form
GFP	Green fluorescent protein
HoxPG	Hox paralog group (e.g. HoxPG3 – HoxPG5).
ICP	Inferior cerebellar peduncle
ION	Inferior olivary nucleus
IMS	Intramural stream
ISH	*In situ* hybridizaiton
ISL1	Insulin gene enhancer protein Islet 1
LBX1	Ladybird homeobox 1
LHX	LIM homeobox domain protein (e.g. LHX2 and LHX9)
LMX1A	LIM homeodomain transcription factor 1 α
LRN	Lateral reticular nucleus
MAFB	V-maf avian musculoaponeurotic fibrosarcoma oncogene homolog B
MAO	Medial accessory olive (var. rMAO; rostral medial accessory olive)
MF	Mossy fiber
MFN	Mossy fiber neuron
NCC	Neural crest cell
Nes	Nestin
NGN1	Neurogenin 1
NTN1	Netrin 1
NPC	Neural progenitor cells
NTN1	Netrin1
NKX6.1	Transcription factor NK6 homeobox 1 (var. NKX2.2)
OLIG	Oligodendrocyte transcription factor (e. g. OLIG2, OLIG3)
PAX	Paired box protein (e.g. PAX2, PAX3, PAX6)

PES	Posterior extramural stream
PN	Pontine nucleus
PNS	Peripheral nervous system
PO	Principal olive
Pr5	Principal trigeminal nucleus
PRC	Polycomb repressor complex
PRPH	Peripherin
PTCH	Patched receptor (e.g. PTCH1, PTCH2)
PTF1A	Pancreas transcription factor 1a
r	Rhombomere (e.g. r1-r8)
RA	Retinoic acid
RL	Rhombic lip
RN	Red nucleus
RTN	Reticulotegmental nucleus
ROBO	Roundabout receptor (e.g. ROBO1-ROBO3)
RP	Roof plate
Sc	Spinal cord
SHH	sonic hedgehog
Smo	Smoothened
SOL	Solitary nucleus
SOC	Superior olivary complex
sp5	Spinal trigeminal tract
Sp5	Spinal trigeminal nucleus
Sp5c	Spinal trigeminal nucleus *pars caudalis*
Sp5ic	Spinal trigeminal nucleus *pars interpolaris* and *caudalis*
Sp5o	Spinal trigeminal nucleus *pars oralis*
SUFU	Suppressor of Fu
TAG-1	Transient axonal glycoprotein 1
TGF-ß	Transforming Growth Factor-ß
uRL	Upper rhombic lip
VCN	Ventral cochlear nucleus
vGLUT	vesicular glutamate transporter (e.g. vGLUT2)
VLL	Ventral lateral lemniscus
WNT	Wingless/integrated (e. g. WNT1, WNT3A, WNT8, etc.)

SUMMARY

The zinc finger transcription factor GLI3 is a downstream component of the Sonic Hedgehog signaling pathway and functions mostly as a transcriptional repressor. GLI3 is required for the proper development of dorsal forebrain, dorsal midbrain and cerebellum. In contrast, the function of GLI3 in the development of the posterior dorsal hindbrain is not well understood. Precerebellar mossy fiber and climbing fiber neurons (MFNs and CFNs) provide afferent input into the cerebellum and arise from progenitor pools at the dorsal edge of the posterior embryonic hindbrain, the caudal part of the lower rhombic lip (clRL). These neurons follow well defined migratory routes before settling at different axial levels in the hindbrain. Previous studies demonstrated that precerebellar migratory streams are disrupted and precerebellar nuclei are disorganized in *Gli3* null mutant mice (*Gli3 extra toe*; *Gli3*$^{xt/xt}$). This thesis dissects how GLI3 influences the development of the murine precerebellar system and investigates the function of GLI3 in non-precerebellar structures in the developing posterior hindbrain. The analysis of *Gli3*$^{xt/xt}$ embryos at different embryonic stages shows that precerebellar progenitors are properly established in the clRL of *Gli3*$^{xt/xt}$ embryos, but the generation of a subpopulation of CFNs is compromised. Moreover, the migration of MFNs is severely altered: the onset of migration in MFNs that remain in the posterior hindbrain (posterior extramural stream) is delayed and the MFNs migrating anteriorly (anterior extramural stream; AES) fail to assemble into a compact migratory stream. Moreover, the subset of AES neurons arising from the most posterior part of the clRL fails to migrate anteriorly and settles at ectopic posterior positions. Aside from the defects in precerebellar system development, the only other alteration in the hindbrain of *Gli3*$^{xt/xt}$ mutants uncovered in this study was a change in neurotransmitter phenotype in neurons of the spinal trigeminal nucleus. To investigate whether GLI3 plays a cell- or non cell-autonomous role in precerebellar neurons, *Gli3* was conditionally inactivated either in all MFN progenitors or in the central nervous system (CNS) after embryonic day 10.5. In these conditional gene inactivation models, the precerebellar system developed normally, suggesting that the function of GLI3 in precerebellar development is not cell-autonomous and may even be outside of the CNS. Analysis of cranial ganglia and their projections in *Gli3*$^{xt/xt}$ embryos revealed an increased size of the trigeminal ganglion and a severe disorganization of its central descending projections, the spinal trigeminal tract (sp5). Neurons of the AES were in close contact with the sp5 during their anteriorly-directed migration in control embryos, while the AES-sp5 interactions were disrupted in *Gli3*$^{xt/xt}$ mutants. Thus, the normal development of the sp5 requires GLI3 function and might be a prerequisite for correct AES migration. These results point to a novel mechanism in precerebellar migration, but further studies will be necessary to investigate whether and how the sp5 acts as a guiding structure for precerebellar migration, and which other hindbrain nuclei and projections influence precerebellar migration.

ZUSAMMENFASSUNG

Der Zinkfinger-Transkriptionsfaktor GLI3 ist eine der nachgeschalteten Komponenten des Sonic Hedgehog Signalwegs, und fungiert hauptsächlich als transkriptioneller Repressor. GLI3 ist für die normale Entwicklung des dorsalen Vorderhirns, des dorsalen Mittelhirns und des Cerebellums erforderlich. Im Gegensatz dazu ist die Funktion von GLI3 während der Entwicklung des posterioren dorsalen Hinterhirns nicht gut verstanden. Präcerebelläre Moos- und Kletterfaserneurone (MFN und KFN) senden afferente Projektionen zum Cerebellum und entstehen aus Vorläuferzellen am dorsalen Rand des posterioren embryonalen Hinterhirns, der kaudalen unteren Rautenlippe (kuRL). Diese Neuronen folgen klar definierten Migrationswegen, bevor sie sich auf verschiedenen axialen Ebenen im Hinterhirn ansiedeln. Bisher ist bekannt, dass in Mäusen, die homozygot für ein *Gli3* Nullallel (*Gli3 extra toe*; *Gli3*$^{xt/xt}$) sind, die präcerebellären Migrationsströme gestört und die präcerebellären Kerne desorganisiert sind. Diese Promotionsarbeit untersucht sowohl die Funktion von GLI3 in nicht-präcerebellären Strukturen im sich entwickelnden posterioren Hinterhirn als auch wie GLI3 die Entwicklung des murinen präcerebellären Systems beeinflusst. Die Analyse von *Gli3*$^{xt/xt}$-Embryonen zeigt, dass präcebelläre Vorläuferzellen in der kuRL von *Gli3*$^{xt/xt}$-Embryonen richtig etabliert sind, aber die Bildung einer Subpopulation von KFN beeinträchtigt ist. Darüber hinaus ist die Migration von MFN stark verändert: Der Migrationsbeginn der MFN, die im posterioren Hinterhirn verbleiben (posteriorer extramuraler Strom; PES), ist verzögert und die MFN, die ins anteriore Hinterhirn wandern (anteriorer extramuraler Strom; AES) bilden im Unterschied zu MFN in Kontrollembryonen keinen kompakten Migrationsstrom aus. Darüber hinaus wandert die Teilpopulation der AES-Neurone, die aus dem am weitestens posterior liegenden Teil der kuRL stammt, nicht nach anterior und siedelt sich anstatt in ektopischen posterioren Positionen an. Abgesehen von diesen Defekten in der Entwicklung des präcerebellären Systems, ist die einzige andere Veränderung im Hinterhirn von *Gli3*$^{xt/xt}$-Mutanten, die in dieser Studie gezeigt werden konnten, eine Änderung im Neurotransmitter-Phänotyp in den Neuronen des *Nucleus spinalis nervi trigemini*. Um zu untersuchen, ob GLI3 eine zellautonome oder nicht zellautonome Rolle in präcerebellären Neuronen spielt, wurde *Gli3* entweder in MFN Vorläuferzellen oder im Zentralnervensystem (ZNS) konditionell inaktiviert. In diesen konditionellen Geninaktivierungmodellen entwickelte sich das präcerebelläre System normal, was darauf hindeutet, dass die Funktion von GLI3 in der präcerebellären Entwicklung nicht zellautonom ist und möglicherweise sogar außerhalb des ZNS liegt. Die Analyse der Hirnnerven-Ganglien und ihrer zentralen Projektionen in *Gli3*$^{xt/xt}$ -Embryonen zeigt, dass das Ganglion trigeminalis in *Gli3*$^{xt/xt}$ -Embryonen vegrößert ist und dass seine zentralen absteigenden Projektionen zum *Nucleus spinalis nervi trigemini* (sp5) disorganisiert sind. Neuronen des AES stehen während ihrer nach anterior gerichteten Migration in

Kontrollembryonen in engem Kontakt mit dem sp5, während die AES-sp5-Interaktion in *Gli3*$^{xt/xt}$-Mutanten gestört ist. Die abnormale Entwicklung des sp5 in *Gli3*$^{xt/xt}$ Maus-mutanten könnte daher einen indirekten Effekt auf die AES-Migration haben. Diese Ergebnisse deuten auf einen bisher nicht beschriebenen Mechanismus in der präcerebellären Migration hin. Weitere Studien werden notwendig sein, um zu untersuchen, ob und wie der sp5 als Migrationshilfe für die präcerebellären MFN dient und welche anderen Hinterhirnkerne und Projektionen die präcerebelläre Migration beeinflussen.

1. INTRODUCTION

1.1. Early patterning of the neural tube

The neural tube represents a cylindrical structure in the embryo that can be subdivided into four regions: the forebrain, the midbrain, the hindbrain, and the spinal chord. The lateral margins of the neural plate fuse at the roof area in the forebrain and midbrain, but remain open at the level of the hindbrain and anterior spinal cord. In the anterior and medial hindbrain, the dorsal edges of the neural tube are widely separated and form a rhombic groove, known as the fourth ventricle. At posterior levels, the edges of the neural tube approach to each other towards the spinal cord. Neural tube closure or neurulation occurs with a characteristic sequence of events along the embryonic axis (Greene and Copp, 2014). Neural tube closure starts around embryonic day (E)8.5 at three defined regions of the neural tube: At the future cervical-hindbrain boundary (defined as closure I), at the forebrain/midbrain boundary (termed Closure 2) and at the most anterior extremity of the forebrain (termed Closure 3). Closure spreads to the rest of the neural tube in a zipper-like manner and finishes around E10. Parallel to neurulation, an array of inductive signals start to define the progenitor populations distributed along the anteroposterior (AP) axis of the neural tube. Signals arising from the notochord, floorplate, and roof plate pattern the neural tube in a dorsoventral (DV) manner, while signals from local organizers nested at different anteroposterior levels dictate a AP position (Kiecker and Lumsden, 2012). The signaling pathways patterning the neural tube are introduced in the following sections.

1.2. Sonic hedgehog specifies ventral progenitor domains

1.2.1. Signaling pathway

Sonic hedgehog (Shh) is a ligand belonging to a family of three evolutionary conserved proteins regulating several developmental processes in bilateria. Shh is synthesized as a 45 kDa hydrophobic protein with a distinct N-terminal signal sequence that undergoes an autocatalytic processing during its trafficking to the plasma membrane, to yield an insoluble ~20kDa N-terminal signaling domain and a ~20kDa C-terminal domain with no known signaling role (Robbins et al, 2012). Once at the membrane, Shh binds to the high affinity patched receptors (PTCH1 and/or PTCH2), which form a multimolecular complex with the co-receptors CAM-related/downregulated by oncogenes (CDO), brother of CDO (BCO) and growth arrestin-specific 1 (GAS1), that modulate different Shh functions and affinity (Figure 1) (Briscoe and Thérond 2013).

Ptch1 is widely expressed throughout the embryo, while *Ptch2* is most predominant in the skin and in the testis. The PTCH receptors are coupled to Smoothened (SMO), a Frizzled-class G-protein coupled receptor (GPCR). Upon PTCH activation, SMO translocates and accumulates at the primary cilium, a microtubule non-motile organelle present in almost all

vertebrate cells, an antenna-like structure that allows cells to detect extracellular stimuli and modulate an appropriate intracellular response (Pazour and Witman, 2003). In the absence of SHH, the PTCH receptors localize at the base and within the primary cilia, and inhibit SMO accumulation in the primary cilia (Figure 1) (Rohatgi et al 2007). At the primary cilia, SMO modulates the activity of the GLI-Krüppel family of zinc finger transcription factors, a family of three proteins (GLI1, GLI2 and GLI3) homologous to the *Drosophila* cubitus interruptus (Lee et al., 2016). All GLI forms have similar DNA-binding specificities imparted by five tandem C2H2 zinc-fingers that comprise the DNA-binding domain. In addition, they all contain a C-terminal activation domain, whereas only GLI2 and GLI3 contain an N-terminal repressor domain (Briscoe and Thérond, 2013). SMO translocation to the primary cilium inhibits the activity of the cytoplasmatic protein Suppressor of Fu (SUFU), which otherwise binds and sequesters GLI in a complex that promotes its phosphorylation (via several protein kinases: PKA, CKI and GSK3ß) and subsequent ubiquitylation at specific residues to remove the C-terminal transactivation domain by partial degradation (Figure 1). Both repressor (GLIR) and activator (GLIA) forms translocate to the nucleus and bind genomic target sites to regulate transcription. The full-length form of the GLI transcription factors enhances transcription of target genes, while the C-terminal truncated form represses them (Figure 1) (Briscoe and Thérond, 2013; Lee et al., 2016).

1.2.2. Role of Shh in brain development

Shh expression is initiated around E7.5 in the axial mesoderm, including the notochord and prechordal plate, which underlie the neural plate. Shortly afterward, SHH induces the floor plate cells of the forming neural tube to express *Shh* themselves. This results in a concentration gradient of ventral SHH signals that diffuses dorsally. As the active state of the GLI transcription factors depends on the presence or absence of SMO, the distribution of GLIA and GLIR follows a gradient similar to that of SHH; meaning that GliA is mainly present in ventral regions, while GLIR is mainly present in dorsal regions of the neural tube (Figure 1). Different ratios of GLIA/GLIR and a specific signal duration activate different genes at a given position. In the ventral neural tube, for example, genes encoding the transcription factor NK6 homeobox 1 (NKX6.1), oligodendrocyte transcription factor 2 (OLIG2) and NKX2.2 are induced at progressively higher concentrations of SHH (Briscoe and Thérond, 2013). Binding of GLIA or the removal of GLIR proteins from the enhancer elements induces a positive regulation. In addition to these patterning functions, SHH also regulates the survival and proliferation of several progenitor and stem cell populations. An example of this is the proliferation of the granule cell precursors and oligodendrocytes in the cerebellum, which in response to SHH secreted from the Purkinje Cells, express proliferative factors, including the transcription factor *Myc*, cyclin D1, and insulin-like growth factor 2 (*Igf2*) (NG J

and Curran T. 2011). This function also expands to the adult brain, where SHH is crucial for maintaining the neural stem cells niches that continuously supply new neurons to different parts of the forebrain (Ahn and Joyner, 2005; Lai et al, 2003).

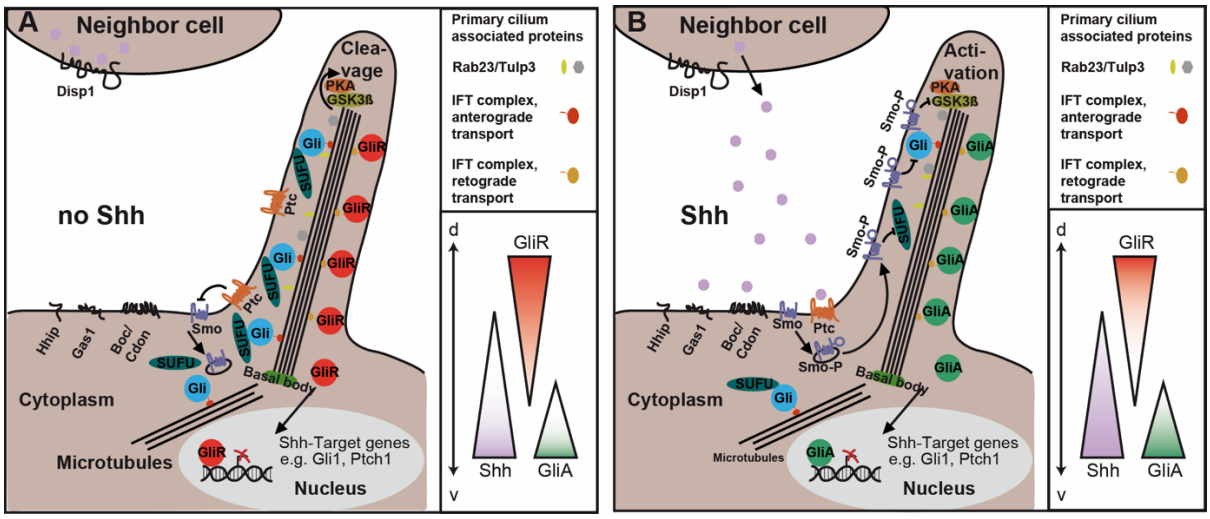

Figure 1. SHH signaling pathway. (A) In the absence of SHH, the receptor PTCH1, enriched in and around the primary cilium, keeps SMO outside of the primary cilium. GLI2 and GLI3 localize and move within the cilium with the help of intraflagellar transport proteins (IFT complexes). In the cillium GLI2 and GLI3 associate with SUFU and become phosphorylated via kinases like PKA and GSK3ß results in their proteolytical cleavage into repressors (GLI2R and GLI3R) (Hui and Angers, 2011; Murdoch and Copp 2010; Goetz and Anderson, 2010). (B) In the presence of SHH, SMO is phosphorylated and gated into the primary cilium (Lee et al., 2016), where it antagonizes the SUFU-GLI association and the kinases promoting GLI proteolytical cleavage, hence resulting in the production of nuclear translocation of GLI activators and transcription induction. Note that additional SHH receptors and regulators exist. These include Shh receptors that promote (CDON, BOC, and GAS1) or attenuate (Hhip) Shh signaling, as well as negative Shh regulators acting between SMO and GLI proteins (e.g. RAB23, TULP3). Also, note that a different gradient of GLIA and GLIR exists depending on the presence or absence of Shh.

1.2.3. GLI3R regulates the development of the dorsal neural tube

Although both, GLI2 and GLI3, have an activator and repressor form, mouse mutant studies indicate that GLI2 is mainly responsible for the activator function in response to SHH and that GLI3 is the main repressor in its absence (Bai et al, 2004; Litingtung and Chiang 2000). In *Shh* null mutants for example, in which ventral cell types (interneurons and motoneurons) of the spinal cord are missing, the alterations are rescued by additionally removing GLIR (Litingtung and Chiang 2000), while inactivation of Gli2 results in loss of ventral cell types in the spinal cord (Matise et al, 1998) and strong reduction (but not acomplete loss) in the expression of the SHH singaling readout Gli1 (Bai et al. 2004). This might reflect a difference in their post-translational processing or a relative strength of the transcriptional activator/inhibitor domains of the two proteins (Briscoe and Thérond, 2013). In contrast, GLI1 lacks a transcriptional repressor domain and, in mammals, even its activator function seems

to have only a minor role in amplifying the transcriptional response. Null mutants for *Gli1* are viable and appear normal, while the double *Gli1/Gli2* mutants are severely altered and die soon after birth (Park et al, 2000). GLI2 is required to induce most ventral cell types in the neural tube, while GLI3 the dorsal cell types (Hui and Angers, 2011). Upon *Shh* inactivation, a severe loss of ventral and dorsal-midline structures is observed in the cerebellum, midbrain, thalamus, and cortex. In contrast, the simultaneous inactivation of *Shh* and *Gli3* partially rescues these defects (Grove et al, 1998; Theil et al, 1998, Aoto et al, 2002, Blaess et al, 2006), showing that SHH inhibition on GLI3R is required for the normal development of the ventral neural tube.

Strategies to study the function of *Gli3* in development include the use of mice carrying mutations in the *Gli3* regulatory units or in the gene *per se*, which is localized on chromosome 7p13 in human (Vortkamp et al, 1992). In mice, there are three known mutants for *Gli3* that arose as spontaneous mutations: Two *Gli3* extra-toe null mutants (*Xt*) and the hypomorph *Polydactyly nagoya* (*Pdn*) with a milder phenotype than the $Gli3^{Xt/Xt}$ mutants (Hayaska et al, 1980; Thien and Ruther, 1999). The mutant $Gli3^{XtH/XtH}$ has a deletion of the *Gli3* promoter region and a deletion in the 5´ region (Schimmang et al, 1992), the $Gli3^{XtJ/XtJ}$ has a deletion of 51.5 Kb including most of the zinc finger coding domain and the complete 3´region of the *Gli3* gene (Maynard et al, 2002). The $Gli3^{Pdn/Pdn}$ mutant has a retrotransposon integration of 5542 bp in the third intron of the *Gli3* gene that results in the formation of two different transcripts (Thien and Ruther, 1999; Ueta et al, 2002). The $Gli3^{XtJ/XtJ}$ mutants have alterations in the dorsal brain that correlate with changes in other signaling pathways. In the forebrain, for example, a reduction of dorsally derived structures and an expansion of ventrally derived areas occurs. These alterations include exencephaly due to neural tube closure defects (Copp, 1994), an expansion of the subpallium at the expense of the pallium (Aoto et al, 2002, Kuschel et al, 2003), the absence of specific medial cortical tissues (i.e. hippocampus, cortical choroid plexus and cortical hem) (Johnson, 1967; Theil et al, 1999), and alterations in cortical lamination (failure to develop a distinct marginal zone, subplate or cortical plate, while having an aggregation of cells types like the Cajal-Retizus) (Theil, 2005, Friedrichs et al, 2008). The cortical alterations are caused by initial patterning defects and a delayed neurogenesis that affects the formation of the preplate, which later splits into the subplate and marginal zone, therefore causing a severe dysmorphogenesis of the cortex. This phenotype correlates with the loss of expression of several members of the bone morphogenetic protein (BMP) and wingless/integrated (WNT) signaling families in the anteroposterior midline and cortical hem, respectively (Grove et al, 1998, Tole et al, 2000, Kuschel et al., 2003; Friedrichs et al., 2008; Magnani et al., 2014). At the same time, the expression of members of the fibroblast growth factor family (FGF; specifically *Fgf8*) is expanded beyond the commissural plate (Thiel et al, 1999, Magnani et al, 2013), influencing

the production of pallial cells. Consistently, if beads expressing *Fgf8* are ectopically added to dorsal telencephalic tissue, an induction of subpallial and repression of pallial specific genes takes place (Kuschel et al, 2003), suggesting that GLI3 is required to confine *Fgf8* to the commissural plate to ensure proper patterning of the cortex.

Additional alterations in *Gli3*$^{XtJ/XtJ}$ mutants include the expansion and improper specification of dorsal midbrain structures, and the small and unfoliated cerebellum with ectopic clusters of Purkinje cells forms in the hindbrain (Blaess et al, 2008). Both alterations also correlate with the expansion of *Fgf8* expression in the isthmic organizer (Aoto et al, 2002) and removal of one copy of *Fgf8* partially rescues the phenotype in the cerebellum (although not in the midbrain) (Blaess et al, 2008), suggesting that GLI3 mediates patterning in this region, at least partially, through regulation of *Fgf8* expression.

Taken together, GLI3 is required for the proper development of the dorsal structures in the brain, as it patterns the tissue and interacts with other morphogenes. As the proper establishment of early structures in development provides an environment influencing other late-occurring developmental processes, GLI3 can also play indirect roles in other brain development events, including axonal guidance of callosal, corticothalamic/thalamocortical, and lateral olfactory axons (Amaniti et al., 2013; Amaniti et al., 2015; Magnani et al, 2010; Magnani et al, 2013). Aside from the cerebellum, the role of GLI3 in the development of the hindbrain has not been explored in detail.

1.3. Interactions of GLI3 with the BMP and WNT signaling pathways

How GLI3 regulates signaling pathways like WNT and BMP is not well understood, but it has been shown that GLI3 interacts with downstream elements of these pathways (Ulloa et al., 2007; Liu et al., 1998). Importantly, these interactions are biderectional, since *Gli3* expression is also regulated by BMP and WNT (Meyer and Roelink, 2003; Ulloa and Marti, 2010). Moreover, during DV patterning, the ventrally secreted SHH signals counteract the BMP and WNT signals from the roof plate and vice-versa, producing a complex network of interactions that pattern the neural tube (Liem et al., 2000; Patten and Placzek, 2002; Watanabe et al., 1998). Some of these interactions are now introduced in more detail.

1.3.1. WNT signaling pathway

The Wnt signaling pathway influences cell patterning, cell fate determination, cell migration and cell polarity depending on the combination of a specific Wnt molecule, receptors, co-receptors and developmental context (Ciani and Salinas, 2005; Bielen and Houart, 2014). There are 19 different WNT molecules found in mammals (mice and humans) that signal through 10 different G-protein coupled receptors of the Frizzled family. Depending on the co-receptors activated, WNTs can signal in two ways. WNTs including WNT1, WNT3A and

WNT8 signal preferentially via co-receptors activating the downstream factor ß-catenin (canonical signaling), while WNT5A and WNT11 use co-receptors that signal in a ß-catenin independent manner (non-canonical signaling; Ciani and Salinas, 2005; Bielen and Houart, 2014). Depending on the context and ligands, the ß-catenin pathway regulates cell growth and balance between progenitor cell expansion and differentiation in the nervous system (Zechner et al, 2003). ß-catenin overexpression or removal at early stages of development results in hyperproliferation and reduced proliferation, respectively (E10.5-E12.5 in mouse; before 18 hours post fertilization in zebrafish), whereas removal at later stages only affects DV patterning (after 18 hours post fertilization in zebrafish, unknown in mice) (Zechner et al, 2003; Bonner et al, 2008). The proliferative function seems to be regulated via WNT1 and WNT3A, but not other WNT ligands. (Megason and McMahon, 2002). In mice, double mutants for *Wnt1/Wnt3a* show a reduced number of the most dorsal progenitors and an expansion of intermediate progenitors in the spinal cord (Muroyama et al, 2002). In contrast the overexpression of ß-catenin results in the inhibition of genes defining ventral populations (Ulloa and Martí, 2010). The expansion of *Wnt1/Wnt3a* expression and concomitant negative regulation of ventral markers are at least partially dependent on the interaction of transcription factors downstream of ß-catenin, like the T cell factor (TCF) and lymphoid enhancer-binding factor (LEF), with GLI3 via highly conserved non-coding DNA regions. TCF/LEF bind and positively modulate *Gli3* expression resulting in antagonization of Shh signaling (Alvarez-Medina et al, 2009; Yu et al., 2008), hence negatively influencing the expression of ventral progenitor factors. In the presence of a TCF dominant-negative form, a dorsal expansion of ventral identity markers and the suppression of dorsal markers occurs (Ulloa and Martí, 2010). Consistently, in mutants with stabilized ß-catenin, *Gli3* expands towards the floor plate and a reduction of several progenitor domains occurs, whereas the disruption of WNT signaling results in the expansion of ventrally located progenitors (Yu et al., 2008). Interestingly, GLI3 can also interact with ß-catenin and regulate it negatively when GLI3 is present at high levels, probably working as a break for positive feedback (Ulloa et al., 2007).

The ß-catenin independent pathway (non-canonical pathway) controls the transcription of genes involved in actin polymerization and microtubule stabilization to regulate planar cell polarity. Planar cell polarity influences morphogenetic movements during gastrulation, neural tube closure, and cell migration, and can also influence cell fate, axonal growth and guidance (van Amerongen et al, 2008; Niehrs, 2012). In the case of axonal growth and guidance, SHH (via GLIA) induces the expression of the WNT antagonists *Sfrp1* and *Sfrp2* along the spinal cord to attract commissural axons to more anterior axial levels after crossing the floorplate (Lyukysyutova et al, 2003; Domanitskaya et al, 2010). Studies in the retina indicate that GLI3 and SFRP1 modulate the antagonistic interplay between WNT and SHH signals suggesting

that this might be a conserved regulatory system between both pathways (Borday et al., 2012).

1.3.2. BMP signaling pathway

BMPs are part of the Transforming Growth Factor-ß (TGF-ß) superfamily of proteins involved in the control of cell fate decisions, tissue patterning, cell proliferation, death, and differentiation. BMPs signal through a canonical pathway (SMAD-dependent) or a non-canonical pathway (SMAD-independent). The SMADs represent a family of proteins that are phosphorylated upon activation of type I and type II serine/threonine kinase receptors for BMP and form a protein complex that translocates to the nucleus to activate or repress gene expression (Liu and Niswander, 2005). The BMP non-canonical signaling pathway acts via Ras-MAPK kinases, Rho-like GTPases, and phosphatidylinositol-3-kinases (PI3K)/Akt, that actively interact with elements of the SMAD-dependent pathway to determine the final outcome of the cellular response (Zhang, 2009). During early brain development, a BMP dorsoventral gradient arising from the roof plate and dorsal ectoderm dorsalizes and patterns the neural tube. If constitutive active forms of the BMP receptors are ectopically expressed in cells of the ventral neural tube, a transformation to dorsal fates occurs, whereas the loss of BMP signaling induces a substitution of the most dorsal cell types of interneurons and a dorsal expansion of the adjacent populations in the spinal cord (Zhang, 2009).

Gain and loss of function studies suggest that the BMPs regulate different WNT ligands and receptors positively (dorsal expressed elements) or negatively (medial and ventral elements) (Chesnutt et al., 2004; Chizhikov and Millen, 2004; Ille et al., 2007). In addition, activation of the WNT pathway rescues the cell proliferation defects caused by overexpressing *Noggin* (a BMP pathway inhibitor), and a double mutation of BMP receptors (BMPR1A and BMPR1B) reduces the expression of *Wnt* in the dorsal spinal cord (Liu and Niswander, 2005). Consistently, the addition of BMP4 in the chick neural tube produces the induction of WNT1 and WNT3A, whereas the addition of Noggin inhibits them (Marcelle et al 1997). Moreover, it has been shown that GLI3 interacts with several SMAD proteins (Liu et al., 1998) and BMP antagonists (Lopez-Rios et al., 2012), linking GLI3 and the BMP pathway.

1.4. Development of the hindbrain

The mammalian hindbrain is the most posterior brain region composed of the cerebellum, pons and medulla oblongata. The pons and medulla contain the nuclei and central targets of the cranial nerves that innervate the muscles of the head and neck; nuclei controlling information related to hearing and taste; centers controlling arousal, sleep, blood pressure, breathing, gastrointestinal functions and nuclei containing most of the brain´s noradrenergic (locus coeruleus) and serotonergic (raphe nuclei) neurons. Moreover, the hindbrain contains

an array of nuclei that form the main cerebellar input, defined as the precerebellar system, which controls information regarding movement and balance (Bloch-Gallego et al., 2005; Di Meglio and Rijli, 2013; Sotelo and Chedotal 2013). The mouse hindbrain is segmented along the anterior-posterior axis into eight transient linage-restricted compartments or rhombomeres (Kiecker and Lumsden, 2005). Each rhombomere (r) has a spatially segregated group of progenitors that generate clonally related neurons with little intermixing between neighboring segments. The nuclei within the hindbrain are normally generated by neuronal subpopulations of multi-rhombomeric origin that maintain the same anterioposterior order from their time of origin to the end of their migration. Yet, certain non-conventional hindbrain populations undergo a phase of long-distance tangential migration across several rhombomeres before settling at their final destination (Wingate and Lumsden, 1996). Examples of this are the branchiomotor neurons of the facial nucleus (7N) controlling the muscles responsible for facial expression and some groups of neurons in the precerebellar system.

1.4.1. The Hox genes specify the anteroposterior axis in the hindbrain

Cell specification and segmentation of the hindbrain in individual rhombomeres follows a strict anteroposterior sequence that is dependent on a gradient of retinoic acid (RA) secreted from the somitic mesoderm located at posterior territories that diffuses anteriorly. RA acts through the receptors RARα, RARß and RARγ and retinoid X receptors (RXRα, RXRß and RXRγ). RA receptors act as ligand-dependent transcriptional regulators of the Homeobox family of transcription factors (*Hox* genes) and other genes patterning the hindbrain, by binding to retinoic acid response elements (RAREs) at the promoter regions of *Hox* genes (Marshall et al, 1996; Gould et. al 1998; Zhag et al 2000).

The Hox genes are critical regulators of the cell type specification and positional identity in the AP axis of the hindbrain and are responsible for the generation of the different rhombomere compartments. In most vertebrates, the Hox genes comprise 39 genes distributed across four clusters (*HoxA*, *HoxB*, *HoxC,* and *HoxD*), all of which share a 60 amino acid region encoding the homeodomain that mediates DNA binding (Philippidou and Dasen 2013). Hox genes within a cluster belong to one of 13 paralog groups (PG, *Hox1-Hox13*), and a single cluster contains a single subset of the 13 groups (Philippidou and Dasen 2013). A hallmark of clustered Hox genes is the direct correlation between their linear arrangement along the chromosome and their place and time of expression during early development (Dubole and Dollé 1989, Grahal et al, 1989, Lewis 1978), a property referred to as colinearity (Kmita and Duboule, 2003). The Hox1-5 paralog groups (HoxPG) are generally expressed in the hindbrain, while the Hox4-Hox11 PG are expressed in the spinal cord. Hox gene expression starts with that of the HoxPG1 (*Hox1a* and *Hox1b*) at E7.5 and is followed

by the HoxPG2 and HoxPG3 at E8.5 (Tümpet et al 2009), and later by the HoxPG5 (*Hoxa5*) at E10.5 (Joksimovic et al, 2005). Hox gene expression is regulated by the Polycomb repressor complex (PRC) and Trithorax complex that introduce specific histone marks modulating the chromatin compaction state. The PRC deposits the repressive histone mark H3K27me3 (trimethyl-lysine-27 on histone H3) (Dicroce and Helin, 2013) and the Thritorax complex deposits the active H3K4me3 chromatin mark (Schuettengruber et al, 2011). RA binding to their receptors in the domains results in the activation and fast removal of the repressive marks in the chromatin as well as the acquisition of neuronal identity (Marshall H. et al, 1996; Mazzoni et al, 2013). Afterwards, a complex network of auto and cross-regulation among the Hox genes restricts or reinforce their own expression in the specific rhombomeres in a process mediated through autoregulatory elements (AREs) (Gould et al 2000, Alexander et al 2009). Different combinations of Hox genes determine the identity of the different rhombomeres and ablation of their expression leads to changes in progenitor distribution, neuronal fate, and connectivity. This can be exemplified by the motor neurons, where Hox gene misexpression results in ectopic MNs populations along the anteroposterior axis (Philippidou and Dasen, 2013). If for example, *Hoxa3/b3* expression is ablated in r1-r4, a reduction of the Olig2 precursor population generating somatic motor neurons (MNs) and an expansion of the V2 interneuron progenitors occurs, whereas overexpression of *Hoxa3* increases the somatic MNs at the expense of V2 interneurons (Guidato et al, 2003).

The Hox genes also influence the neuronal migration and final position identity. An example is the intrinsic topographic organization of the migrating pontine neurons, which is conserved from their point of origin through migration and until its final position by the restricted expression of particular Hox genes (Di Meglio et al., 2013) (Figure 4C). In mutants for *Ezh2*, the enzymatic component of PRC2 maintaining the Hox expression in the hindbrain (although not in the spinal cord) (Golden and Dasen, 2012; Di Meglio et al., 2013), results in the misexpression of Hox genes and in the misposition of pontine neurons (Di Meglio et al 2013). This suggests that the ordered clearance of epigenetic repressive modifications in response to transient patterning signals of RA encodes an anteroposterior neural identity and that the maintenance of these chromatin domains have implications in the final position of the neurons.

1.4.2. Transcription factors defining the progenitor pools of the dorsal hindbrain - the rhombic lip

The cells in the hindbrain arise from a layer of progenitor cells located in the ventricular zone of the fourth ventricle. During the course of development, this progenitor layer subdivides into different subpopulations by a hierarchy of transcription factors, whose expression is induced by the morphogenes defining the DV axis. The ventricular zone at the edges of the alar plate

are referred to as rhombic lip (*Rautenlippe;* RL) and the transcription factors defining it include , the homeodomain transcription factor PAX6, and proneural factors of the basic helix-loop-helix (bHLH) family, like oligodendrocyte transcription factor 3 (OLIG3), atonal homolog 1 (ATOH1), neurogenin 1 (NGN1), achaete-scute homolog1 (ASCL1) and pancreas transcription factor 1a (PTF1A), which function downstream of the Notch pathway to define neuronal progenitors and promote their differentiation (Machold et al, 2007, Ray and Dymecki, 2009, Imayoshi and Kageyama 2014). The combinatorial code of these transcription factors regulates the expression of an additional group of genes that induce the differentiation of the dorsal neural types categorized in two classes (A and B) with four members each (dA1 – dA4; dB1 – dB4) (Storm et al, 2009) (Fig 2). The regulation of these transcription factors follows complex interactions involving the BMP, WNT, and Notch signaling pathways. A description of these interactions is provided below.

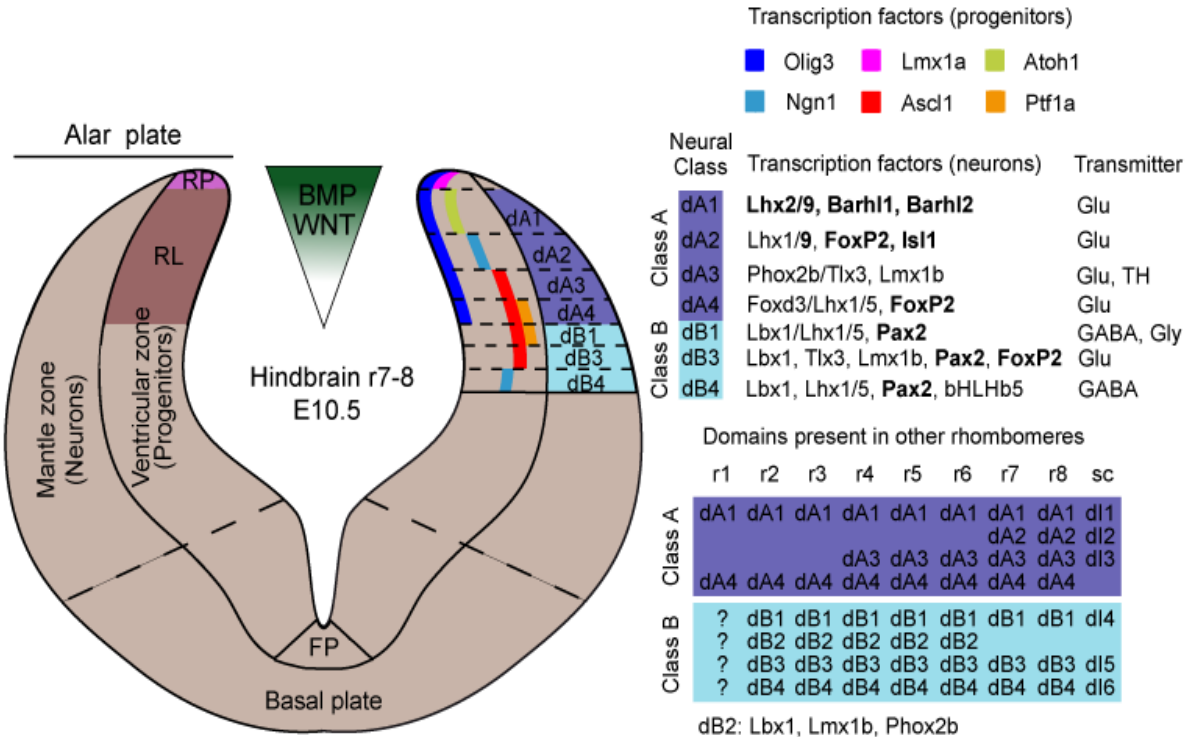

Figure 2. Transcription factors defining the rhombic lip. Schematic of an E10.5 coronal section depicting the general organization of the hindbrain at r7-r8. The morphogenes BMP and WNT induce the expression of transcription factors defining the progenitor populations in the the alar plate. These transcription factors parcellate the progenitor layer at the ventricular zone and induce the expression of additional transcription factors necessary to induce neuronal differentiation at the mantle layer. Neurons are divided into two main classes (dA and dB). The transcription factors analyzed in this thesis are in bold letters. The morphogene expression, and hence, the transcription factors defining progenitor and neuronal population, changes depending on the axial level. The progenitor domains present at different axial levels are shown in the lower right corner. FP: floor plate; RL; rhombic lip; RP: roof plate

1.5. Rhombic lip induction and progenitor cell specification

1.5.1. The BMP dorsoventral gradient regulates *Lmx1a* to establish the roof plate

The induction of the different transcription factors delineating the RL follows a sequential activation regulated by a transient wave of BMP molecules secreted by the epidermal ectoderm flanking the neural plate. The BMP signals induce the expression of the LIM-homeodomain transcription factor 1 alfa (*Lmx1a*) shortly after neural tube closure, which is necessary to delineate the roof plate and ependymal cells of the choroid plexus. In addition, *Lmx1a* also plays a role in the generation of a small number of r1 derived hindbrain neurons like the unipolar brush cells and deep cerebellar nuclei neurons between E12.5 and E16.5 (Chizhikov and Millen, 2004; Chizhikov et al 2010). *Lmx1a* is dispensable for the induction of the roof plate, but it is required for its normal growth and to maintain the fate of the cells, as mutations that inactivate its function (*dreher* mouse phenotype) produce an increased number of *Atoh1* fated neurons at the expense of *Lmx1a*-expressing cells. Consequently, the roof plate becomes smaller between E9.25 and E10.5 in the dreher mutant (Chizhikov et al 2010). Once the roof plate is established, it produces BMP6, BMP7, and growth differentiation factor 7 (GDF7). This second wave of BMPs promotes the induction of the different neurons arising from the RL.

1.5.2. WNT1 defines and controls the progenitor domains of the dorsal rhombic lip by regulating *Olig3* expression

In the mouse, a WNT1 DV gradient present at E8.0 induces the expression of *Olig3* at E9.25 via the canonical signaling pathway (Zechner et al, 2007). OLIG3 regulates the generation of *Atoh1*, *Ngn1* and *Ptf1a* progenitors, and the relative proportion between class A and class B neurons by suppressing the transcription factor *Lbx1* (ladybird homeobox 1) defining the class B neurons (Storm et al., 2009). *Olig3* deficient mice show a downregulation of *Atoh1*/*Ngn1* and a dorsal expansion of *Ptf1a* towards these subdomains, which results in a reduction of the dA1, dA2, and dA3 neurons. In these mutant mice, the class B neurons expand dorsally towards the A domains in r4-r7 (although not from r1-3), resulting in the change of fate and complete loss of the dA4 neurons (Müller et al 2005, Liu et al 2008, Storm et al, 2009). Gain of function experiments suggest that in addition to these functions, *Olig3* also cooperates with *Ptf1a* to determine the expression of the forkhead transcription factor *Foxd3* (Forkhead box D3), which is necessary for the fate determination of dA4 neurons present in r7, but not for those originating in r4-6 (Yamada et al., 2007, Storm et al., 2009).

1.5.3. PAX6 patterns the dorsoventral axis by regulating Shh and BMP

Similar to OLIG3, the transcription factor PAX6 regulates the generation of RL neurons, but at later time points (~ E11.5, when its expression starts in the RL) (Landsberg et al., 2005).

PAX6 promotes expression of the BMP transcriptional targets *Msx1, Msx2,* and *Msx3*, which initiate and maintain *Atoh1* expression (Engelkamp et al 1999, Landsberg et al, 2005). Mice deficient for *Pax6* show a reduction of the *Atoh1* domain and an expansion of the *Ngn1* domain (Landsberg et al, 2005). As a consequence, the proportion of *Atoh1* and *Ngn1*/*Ptf1a*-expressing neurons changes (Landsberg et al, 2005, Benzing et al, 2011). In addition, PAX6 seems to play a role in initiating the migration of RL neurons (e.g. precerebellar neurons, see below), as its inhibition delays the onset of their migration and midline crossing by half a day, resulting in ectopic clustering of the cells (Benzing et al, 2011).

1.5.4. Cross-regulation between progenitor populations in the rhombic lip

The bHLH proneural factors are transcriptional activators that bind to target DNA sequences as heterodimeric complexes using a conserved sequence known as E-box (Imayoshi and Kageyama 2014). Depending on the expression dynamics, the proneural genes promote the proliferation or the cell-cycle exit and differentiation of neural progenitor cells (NPC) (Imayoshi and Kageyama, 2014). An oscillatory expression correlates with the multipotent and proliferative state, whereas sustained expression regulates fate determination (Imayoshi and Kageyama, 2014). Proneural gene activation results in the upregulation of Notch ligands (e.g. Delta and Serrate) that interact with Notch receptors present at the surface of the neighboring cells. Notch receptor activation induces the expression of bHLH repressive factors, such as *Hes*, *Hey* and *Id* family members, which inhibit cell differentiation (a process referred to as lateral inhibition) (Kawaguchi et al., 2008; Pierfelice et al., 2011). Thus, proneural genes sort out single cells within the germinal zone to become neurons and keep the remaining in an undifferentiated state for subsequent waves of neurogenesis.

In addition, the proneural genes negatively cross-regulate each other, restricting the extent of their expression domains. In the RL, *Ngn1* inhibition produces a ventral expansion of *Atoh1*, whereas a dorsal expansion of the *Ngn1* domain occurs in the absence of *Atoh1* (Gowan et al 2001). NGN1 is also able to inhibit the ventrally located *Ascl1* expression, which otherwise expands dorsally (Bertrand et al, 2002). Similarly, PTF1A negatively regulates *Atoh1* and *Ascl1*, as *Ptf1a* inhibition induces a small fraction of the cells composing the lineage to transform into Atoh1-derived neurons (Pascual et al, 2007; Yamada et al, 2007), whereas most of them change to a dB3 *Ptf1a*-/*Mash1*+ phenotype or die (Yamada 2007; Yamada 2014; Iskusnylch et al 2016). As a result of these regulatory loops, the proneural genes have a transient expression and a well-delimited expression area. Once differentiation starts and the progenitor cells exit the cell cycle, the neurons leave the ventricular zone and accumulate laterally in the mantle layer where they fully differentiate to mature neurons using positive feedback mechanisms (Bertrand et al, 2002) that induce the appearance of pan-neuronal markers and neuronal specific markers (Figure 2). An example of this is represented by

ATOH1, which induces the appearance of pan-neuronal markers like ß-tubulin (Kawauchi and Saito, 2008) and of neuronal specific markers, including the homeobox transcription factors of the BarH class, BARHL1, and BARHL2, and of the LIM homeobox proteins LHX2 and LHX9 (Saba et al., 2003, 2005; Kawauchi and Saito, 2008; Klisch et al., 2011; Lai et al., 2011). BARHL1 and BARHL2 play important roles in neuron specification, survival, and/or cell migration and regulate *Lhx2* and *Lhx9* expression in spinal cord dI1 interneurons (Reig et al., 2007; Chellappa, 2008, Kawauchi et al., 2010). LHX2 and LHX9 play a role in neuron subtype specification and migration (Li et al., 2004; Saba et al., 2003, 2005; Chellapa et al., 2008; Ding et al., 2012, Wilson et al., 2008). BARHL1 and BARHL2 have functional redundancy and can work either as activators or as repressors depending on the tissue, developmental context and the target genes (Reig et al., 2007; Chellappa, 2008). In the spinal cord, *Barhl1* absence does not generate any obvious developmental phenotype (Chellappa et al., 2008), whereas *Barhl2* ectopic expression leads to an increase of commissural neurons (Saba et al., 2003, 2005) and changes in their subtype specification (Ding et al., 2012). In contrast, in the RL, *Barhl1* knockout mice exhibit aberrant neuronal migration and elevated apoptosis of several *Atoh1*-derived populations that lead to strong morphological alterations (Li et al., 2004), whereas *Barhl2* knock out seems to produce only slight alterations in the cerebellum (Ding, 2009).

1.5.5. Neuronal populations of the rhombic lip

In mammals, the RL can be divided based on the three important neuronal systems arising from it: the cerebellar-RL, the auditory-RL and the precerebellar-RL (Table1; Farago et al., 2006; Wulliman et al., 2011). The cerebellar-RL is devoid of Hox gene expression, arises from r1 and gives rise to some cell types of the cerebellar cortex. The auditory-RL expresses Hox genes of the PG 1-3, arises from r2-r5 and gives rise to the cochlear nuclei. Finally, the precerebellar-RL (a.k.a. posterior or caudal rhombic lip; clRL) expresses Hox genes of the PG 3-5, arises from r6-r8 and gives rise to the precerebellar system (Farago et al., 2006; Wulliman et al., 2011). The cellular components of all three systems are influenced by the proneural genes previously described (Table 1), which keep a similar dorsoventral distribution along the AP axis, although with small differences (Figure 2). These include changes in the size of the domains (Hoshino et al., 2012), the presence or absence of specific proneural genes/transcription factors (i.e *Ngn1* is only expressed in r7-8; *Ascl1* is present as a continuous progenitor domain in r7-8, but as two separated domains at r2-6) (Sieber et al., 2007; Storm et al, 2009), and changes in the neurotransmitter phenotype of the neurons generated from a particular progenitor domain (i.e. *Ptf1a*-expressing progenitors give rise to GABAergic neurons from the cerebellar-RL, GABAergic and glycinergic neurons from the auditory-RL, and glutamatergic neurons from the precerebellar-RL; Hoshino, 2012).

As this thesis mainly focuses on the development of the precerebellar system, a description of its components, development and neuron migratory strategies is provided in the next sections.

1.6. The precerebellar system

About 39 hindbrain cell groups distributed along the hindbrain and spinal cord are known to provide some sort of projection to the cerebellum and hence, are referred to as precerebellar nuclei (Fu et al., 2011). Of these, five nuclei have been often referred to as the major precerebellar nuclei because their efferents project almost entirely to the cerebellum (Landsberg et al., 2005; Machold et al., 2005; Wang et al., 2005). The others have been referred to as minor precerebellar nuclei due to their less prominent projections to the cerebellum (Fu et al., 2011). The major precerebellar nuclei (from now on, simply referred to as precerebellar nuclei) derive from the RL in r6-r8, as described above (Farago et al., 2006). These include the pontine nucleus (PN), the reticulotegmental nucleus (RTN), the lateral reticular nucleus (LRN), the external cuneate nucleus (ECN) and the inferior olivary nucleus (ION) (Figure 3) (Fu et al, 2011). Depending on their projections to the cerebellum, the precerebellar nuclei can be divided into two main groups: Mossy fibers neurons (MFN; derived from *Atoh1*-expressing progenitors) and present in the PN, RTN, LRN, ECN, and the climbing fiber neurons (CFN; derived from *Ptf1a*-expressing progenitors), which form the ION.

The MFN fibers or mossy fibers (MF) reach the cerebellum at different time points and locations depending on their origin. They make contact with the deep cerebellar nuclei, or with the dendrites of cerebellar granule cells and axons of Golgi cells, with which they form a unique synaptic structure called glomerulus. Depending on the origin of these projections, their function varies. The PN MFs modulate functions related to vision, planning, initiation, and execution of movement, those of the RTN relate to visual-motor integration, the LRN MFs contribute to the coordination of movement and MFs of the ECN are involved in regulating proprioception and cutaneous signals (Sillitoe et al., 2012). The CFN projections or climbing fibers (CF) reach the cerebellum starting around E14-E15 in the mouse and make synaptic contact with Purkinje cells dendrites (Figure 3; Reeber et al., 2012; Sillitoe et al., 2012). The CF arising in the posterior ION primarily synapse with Purkinje cell dendrites in the vermis of the cerebellum, whereas those arising from anterior parts terminate mainly in the cerebellar hemispheres (Altman and Bayer, 1997; Sotelo, 2004). The function of the CFs relates to the timing and learning of movements (Sillitoe et al., 2012). The precerebellar neurons project to the contralateral side of the cerebellum (ION, PN and RTN neurons) or to the ipsilateral side of the cerebellum (ECN and LRN) (Kawauchi et al., 2006). The projections

from the ION, ECN, and LRN form part of an axonal bundle known as the inferior peduncle, whereas those of the PN/RTN form the middle peduncle (Watson, 2012).

Transcription factor	Earliest day of expression	Examples of nuclei/neurons generated	References
Lmx1a	E8.5	Non-neuronal RL cells (choroid plexus) Cerebellar-RL (small number of unipolar brush cells and deep cerebellar neurons)	Falli et al. 2002, Chizhikov et al., 2010
Atoh1	E9.5	Cerebellar-RL (granule cells , deep cerebellar nuclei) Auditory-RL (lateral lemniscus, cochlear neurons) Precerebellar-RL (All mossy fiber nuclei) Miscellaneous: Proprioceptive/vestibular system (parabrachial neurons and mesopontine tegmental system). Some spinal trigeminal nuclei neurons.	Akazawa et al.,1995; Machold and Fishell, 2005; Wang et al.,2005; Farago et al., 2006; Okada et al., 2007; Rose et al., 2009
Ngn1	E10.5	Cerebellar-RL (some Golgi, Lugaro, Purkinje and granule cells) Auditory-RL (Discrete populations of the cochlear nuclei, lateral lemniscus, vestibular nuclei) Precerebellar-RL (some cells in the pontine nucleus and it might contribute with some neurons of the inferior olivary nucleus) Miscellaneous: Reticular formation (intermediate, lateral and gigantocellular reticular nuclei)	Landsberg et al., 2005; Ray and Dymecki, 2009; Kim et al., 2010, Obana et al., 2010, 2015
Ptf1a	E9.5	Cerebellar-RL (Purkinje cells and molecular layer interneurons) Auditory-RL (inhibitory cochlear and vestibular nuclei) Precerebellar-RL (Inferior olivary nucleus	Hoshino et al., 2005; Yamadaet al., 2007; Storm et al., 2009; Fujiyama et al., 2009; Lugani 2013; Iskusnylch et al., 2016
Ascl1	E9.5	Cerebellar-RL (deep cerebellar nuclei interneurons, Purkinje cells) Miscellaneous: Trigeminal sensory system (Spinal trigeminal nucleus), reticular formation (parvicellular, gigantocellular, pontine reticular nuclei)	Oshawa et al., 2005; Dauger et al., 2003; Pattyn et al., 2006; Kim et al., 2008

Table 1. Earliest time point of proneural gene expression and neuronal cells generated from the mouse rhombic lip.

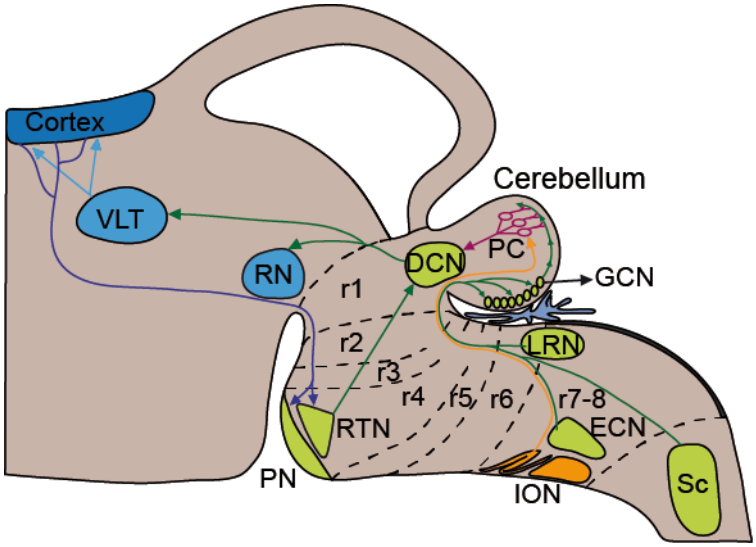

Figure 3. The precerebellar system. The precerebellar neurons receive information from several motor systems and redirect it to the cerebellum for processing. The cerebellum integrates and modulates the sensory information and redirects it to additional areas in the brain for further processing. These include include the red nucleus (RN) in the anterior midbrain, the ventrolateral thalamus (VLT), and motor cortex in the forebrain. These areas project back to the precebellar nuclei, closing the circuit. The precerebellar neurons are distributed along the AP axis of the hindbrain and spinal cord, and can be subdivided into two groups based on their lineage and projections: The MFN arise from *Atoh1*+ progenitors (green) and send mossy fibers that connect with the deep cerebellar neurons (DCN), or with the granule cell neurons (GCN) and Golgi cells. The CFN (orange) arise from *Ptf1a*+ progenitors and send climbing fibers that contact Purkinje cells (PC). **DCN:** deep cerebellar nuclei; **ECN:** external cuneate nucleus; **PN:** pontine nucleus; **RTN:** reticular tegmental nucleus; **RN:** Red nucleus; **Sc:** spinal cord; **VLT:** ventrolateral thalamus.

The ION neurons are the first precerebellar neurons generated (E9-E11; Pierce, 1973), followed by the LRN (E11.5-E12.5), the ECN (E11.5-E12.5), the RTN (E12.5-E13.5) and the the PN (E13.5-E17) (Pierce, 1966, 1973; Altman and Bayer 1987; Machold and Fishell, 2005; Wang et al., 2005; Okada et al., 2007). Shortly after their generation and in the same chronological order, the neurons start migrating tangentially towards the ventral midline through different semicircular streams (Figure 4A). The ION neurons migrate through the mantle zone, just above and parallel to the marginal layer, in the so-called internal migratory stream (IMS; E10.5-E15) and remain in the rhombomeres from which they originate (r7-r8) (Bourrat and Sotelo, 1990, Reeber et. al., 2012). The MFN move along the marginal layer (extramurally), just beneath the pia, and divide into two streams: the so-called posterior extramural stream (PES; E12.5-E15.5), which remains posteriorly (r7-8) and gives rise to the ECN and LRN (Okada et al., 2007; Hatanaka et al., 2016), and the anterior extramural stream (AES; E13.5-E18.5), which transgresses the rhombomeric boundaries until reaching the base of r3-r4 to give rise to the PN and RTN. The AES represents the longest and most complex migratory path in the hindbrain. The AES neurons arising from r7-r8 direct anteriorly and meet with the neurons arising from r6 to then altogether make a short ventral turn. Next,

the AES neurons migrate anteriorly through r4-r5, passing just between the root of vestibulocochlear nerve (8n) (dorsally located), and the roots of glossopharyngeal nerve (9n) and facial nerve (7n) (both ventrally located). Once the AES neurons reach the root of the trigeminal nerve (5n) at the posterior part of r2, they make a ventral turn, cross the lemniscal nuclei and settle down at the basal plate between r3-r5 (Figure 4C) (Nichols and Bruce, 2006, Geisen et al., 2008). Precerebellar neurons traveling in the IMS and AES finish their migration once they reach the midline, whereas neurons in the PES cross the midline to reach their final position on the contralateral side. Once precerebellar tangential migration is completed, the neurons redistribute and aggregate into organized nuclei. The ION develops a laminated structure composed of different lamellae or subnuclei, the main being the dorsal accessory olive (DAO), the principal olive (PO), and the medial accessory olive (MAO). In the case of the MFN (both PES and AES), the neurons leave the pial surface and migrate radially into the mantle layer using the fibers of the radial glia originating at the ventricular zone. If a similar switch to radial migration occurs in the ION neurons during the formation of the complex layered ION structures remains unknown (Hatanaka et al., 2016).

The final distribution of the precerebellar neurons correlates with the time and place of their generation. The precerebellar neurons start their migration in a chronological order after their generation and follow each other in what has been described as chain migration (Bourrat and Sotelo, 1991; Ono et al., 2004; Kawauchi et al., 2006). In the posterior ION, the cells generated earlier locate medially whereas those generated later locate laterally. A correlation between cell generation and final position is not clear in the anterior ION, mainly due to cell rearrangement during nucleogenesis (Bourrat and Sotelo, 1991). In the case of the MFNs, the early-born neurons start their tangential and radial migration at earlier stages and locate deeper within the mantle layer. The early-born cells are followed by later-born cells that settle marginally (closer to the pia) and do not change to a radial migration, but instead migrate only laterally (Kawauchi et al., 2006; Watanabe and Murakami, 2009; Shinohara et al., 2013).

A correlation with the place of birth (rhombomeric origin) is also observed by the conservation of specific Hox genes during migration and nucleogenesis. In the LRN for example, the posterior part of the nucleus expresses members of the HoxPG5 and HoxPG4, whereas the anterior neurons only members of the HoxPG4. Similarly, in the PN, the most posterior part of the nucleus express HoxPG3/PG4/PG5, those in the middle HoxPG3/PG4 and the most anterior part only the HoxPG3 (Figure 4C; Di Meglio et al., 2013).

1.7. Mechanisms controlling precerebellar tangential migration and axon guidance

1.7.1. The Netrin and Slit guidance system

Several mechanisms are thought to control precerebellar migration, including attractive and repulsive signals that act either in a contact-dependent (i.e. molecules present in the substrates through which the neurons move, e.g. radial glia, other neurons, axons, and

extracellular matrix) or contact-independent manner (i.e. long-range diffusable molecules). Among these guidance cues, the secreted extracellular matrix (ECM) molecule Netrin1 (NTN1) and the membrane-bound Slit molecules play a central role in directing the tangential migration and/or axonal guidance of precerebellar neurons. A central aspect in precerebellar tangential migration is that all neurons are initially directed towards the ventral midline. Thus, it was long believed that the ventral midline (in particular the floor plate) had a strong influence on the final position of precerebellar neurons and their projections and that this was mediated by a combination of NTN1 and Slit gradients that emerged from it (reviewed in Sotelo and Chedotal, 2013). This idea has changed recently thanks to new genetic approaches. The current view is described in the following section.

Ntn1 expression in the hindbrain is induced by SHH signaling, but its expression is epigenetically confined to the neural progenitor cells (NPCs) of the ventral ventricular layer and to the floor plate cells of the hindbrain by the EZH2, a member of the Polycomb repressive complex 2 (Di Meglio et al., 2013). The NPCs end-feet release NTN1 locally at the pial surface, where it associates with laminin deposited along the basal membrane to serve as a substrate that promotes cell and growth cone movement. NTN1 works as a chemoattractant and as a chemorepulsive cue depending on the receptors sensing it. Chemoattraction occurs when NTN1 interacts with homodimers of the deleted in colorectal cancer receptor (DCC) (Moore et al., 2007; Dominici et al., 2017; Varadarajan et, 2017; Yamauchi et al., 2017), or heterodimers of DCC and the Roundabout receptor 3 (ROBO3) (Zelina et al., 2014), while chemorepulsion when NTN1 interacts with heterodimers of DCC and UNC5 receptors (UNC5A-UNC5C) (Hong et al., 1999; Moore et al., 2007; Lai et al., 2011). If *Ntn1* expression is expanded by conditionally knocking out *Ezh2*, the precerebellar AES migrates ventrally at posterior levels (Di Meglio et al., 2013). In contrast, if *Ntn1*, *Dcc* or *Robo3* are ablated, the precerebellar neurons leave the RL but their migration toward the floor plate is stalled when the neurons reach the r2/r3 border to turn ventrally or is strongly compromised (affected trajectory with several neurons remaining at dorsal parts of the stream and/or exiting the CNS), and midline crossing of their axons is almost completely abolished (Marillat et al., 2004; Sotelo and Chédotal, 2013; Di Meglio and Rijli, 2013; Dominici et al., 2017; Moreno-Bravo et al., 2018; Yung et al., 2018). A final function of NTN1 in precerebellar development is as a survival factor, as in its absence more than half of the ION neurons die (Bloch-Gallego et al., 1999; Llambi et al., 2001, Marcos et al., 2009).

Regarding the chemorepulsive effect of NTN1, which is mediated by the UNC5 receptors, studies in *Unc5b* and *Unc5c* null mutants suggest that it has an indirect influence on precerebellar neuronal migration, while it has a direct influence on precerebellar axonal projections (Di Meglio et al., 2013; Kim and Ackerman, 2011). *Unc5b* is exclusively expressed during AES migration and is downregulated when the neurons reach the midline.

During migration, *Unc5b* is expressed in a dorsoventral gradient that correlates to the Hox genes expressed within the AES and therefore, to the rhombomeric origin of these precerebellar cells. It is highly expressed in r6 derived-neurons (HoxPG2/HoxPG3+ neurons), lower in neurons with an r7 origin (HoxPG4+ neurons), and absent from r8 derived-neurons (HoxPG5+ neurons). The *Unc5b* gradient is generated because *Unc5b* is positively regulated by the HoxPG2 (present in all the AES) and negatively by the HoxPG5 (present in the ventral AES). Because the populations with more *Unc5b* expression (dorsal cells) are more sensitive to NTN1 repulsion than those with less expression (ventral cells), an influence on the particular neuronal position within the AES and PN/RTN is thought to exist. If *Unc5b* is knocked out, the integrity of the AES is compromised and the dorsal populations spread into ventral levels of the AES. This effect is likely indirect, as no phenotype exists if *Unc5b* is overexpressed in the AES via conditional ablation of *Ezh2* (EZH2 restricts HoxPG5 expression and thus, expression of *Unc5b*), but only if *Ezh2* is also ablated in the environment (thus also increasing *Ntn1* expression) (Di Meglio et al., 2013). In the case of *Unc5c*, it is expressed by the ION and the PES at E14.5 (in the ION expression decreases at E16.5) and in the AES when the neurons reach the midline (Kim and Ackerman, 2011), where it may play a role in ending migration (Schmid et al., 2007). In *Unc5c* null mutants, the IMS and PES migrate normally, but a Hoxb5+/Unc5b- subpopulation of AES neurons settle ectopically at posterior levels (Kim and Ackerman, 2011; Di Meglio et al., 2013). This alteration is likely indirect, because *Unc5c* is not expressed during the active phase of migration, and as its overexpression in E13.5 mice does not generate any obvious alteration (Di Meglio et al., 2013). In axonal migration, UNC5C plays an important role in steering the ION, ECN and PN/RTN axons away from the midline and keep them in their proper position (Kim and Ackerman, 2011). In the absence of *Unc5c*, the ION and ECN (but not LRN) projections fail to navigate as part of the inferior cerebellar peduncle (ICP), an axonal bundle that they normally form in conjunction with the spinocerebellar tract (Altman and Bayer, 1997). In the case of the PN/RTN, the axons turn anteriorly after crossing the midline and project parallel to it, instead of crossing it and then project dorsally to the cerebellum(Kim and Ackerman, 2011).

Regarding the Slit molecules, three members exist (Slit1-Slit3). They are synthesized by the floor plate and some nuclei within the hindbrain, like the 7N and hypoglossal nucleus (12N). The Slit molecules interact with the ROBO1 and ROBO2 receptors, which induce a repulsive signal that is thought to occur via formation of DCC/ROBO1 and DCC/ROBO2 heterodimers that silence NTN1 signal (Stein and Tessier-Lavigne, 2001). This effect is crucial for midline crossing of axonal projections (Marillat et al., 2004). Here, ROBO3 is thought to repress ROBO1/ROBO2 before the leading processes reache the midline. Afterwards, *Robo3* is downregulated, hence a repulsive Slit response towards the midline is activated (Marillat et

al.,2004). Studies using knockout mice for *Slit1*-*Slit3* and for *Robo1*/*Robo2* indicated that the SLIT repressive effect could also influence precerebellar migration (Di Meglio et al., 2008; Geisen et al., 2008), yet the conditional inactivation of *Robo1*/*Robo2* in precerebellar neurons now indicate that they only play a minor direct role (Dominici et al., 2018). In conclusion, the cellular and axonal migration of precerebellar neurons is strongly influenced by NTN1 and SLIT molecules to which the neurons react at different time points by controlling the expression or activity of different receptors in a cell-type-dependent manner.

1.7.2. Additional mechanisms controlling precerebellar tangential migration

Several additional molecules are known to interact with the precerebellar neurons and further influence their behavior during migration. An example of this is the interaction of the MFN with multiple elements found in the substrate of their superficial route. The MFN are thought to move in a type of chain migration using each others leading processes (Ono and Kawamura, 1989, 1990; Yee et al., 1999; Kyriakopoulou et al., 2002, Taniguchi et al., 2002, Kawauchi et al., 2006) and use tangentially oriented neuronal fibers as scaffold to reach the midline and the contralateral side (Kyriakopoulou et al., 2002; Denaxa et al., 2005). In addition, the neurons are known to interact with several elements of the basal membrane (as previously introduced with NTN1), which are required for migration. Cell-cell and cell-fiber interactions occur via several cell-adhesion molecules (CAMs) like the transient axonal glycoprotein 1 (TAG-1; aka.: contactin-2) and cadherins (e.g. N-cadherin), which are a family of calcium-dependent homophilic cell adhesion proteins. Knock out and knock down of these molecules produces slower and aberrant PES migration that results in a reduced number of PES neurons reaching the contralateral side (Denaxa et al., 2001, 2005; Kyriakopoulou et al., 2002; Taniguchi et al., 2006) and the formation of ectopic aggregates in the ipsilateral ECN and LRN (Kawauchi et al., 2006). This suggests that the MFN are reactive to environmental cues controlling their radial migration into the medulla at defined locations along the circumferential axis and that their competence to respond to these cues is time-dependent (Kawauchi et al., 2006). A similar effect is observed in mutants of the Nuclear Factor 1b (NFIB) (Kumbasar et al., 2009). NFIB is a member of a family of transcription factors regulating axon formation, dendritogenesis, and migratory behavior, that regulates the expression of EphrinB1, N-cadherin and TAG1 (Wang et al., 2007, 2010). *Nfib* null mutants show a delay in PES migration accompanied by an ectopic group of cells at the midline (Kumbasar et al., 2009). *Nfib* null mutants also show a delay in AES migration, but this seems to be related to a reduction in progenitor neurogenesis and not to errors in migration, as the neurons follow a proper trajectory, although in a reduced number (Kumbasar et al., 2009).

An additional molecule influencing MFN migration is the C-X-C motif chemokine 12 (CXCL12; aka. SDF-1), which is secreted by the meninges and function as a chemoattractant important for maintaining the superficial MFN migration. In knock out mutants for *Cxcl12* or of its receptor *Cxcr4* (C-X-C motif chemokine receptor 4), a derailing of MFN into the medulla occurs (Vilz et al., 2005; Zhu et al., 2009). In consequence, the neurons fail to migrate anteriorly and form multiple ectopic clusters of cells at random posterior positions. In the case of the PES, only small derailments occur and the LRN/ECN still form normally (Zhu et al., 2009).

1.7.3. Mechanisms controlling precerebellar nucleogenesis

ION cell rearrangements occur between E15 - E18 (Backer et al., 2007) and are influenced by SLITS (Di Meglio et al., 2008) and cadherins (e.g. Cadherin-7, Cadherin-11, Cadherin-20, etc.). Cadherins have a wide and dynamical expression in the ION (Suzuki et al., 1997; Backer et al., 2002, 2007; Takahashi and Osumi, 2008). In double mutants for *Slit1/Slit2* or *Robo1/Robo2* (Di Meglio et al., 2008) all lamella of the ION are abnormal, yet the strongest defects occur in the DAO, which strongly expresses *Robo2* and the non-soluble cadherin 11 (Backer et al., 2007; Di Meglio et al., 2008). As the ROBO receptors are able to inhibit cadherin-mediated adhesion (Rhee et al., 2002, 2007; Blockus and Chédotal, 2016) and the absence of the Rho-guanine exchange factor Trio (necessary for the cadherin-mediated downstream signaling activation) produces similar lamellation defects than those in *Robo1/Robo2* and *Slit1/Slit2* mutants (Backer et al., 2007), it was proposed that ION nucleogenesis might be influenced by ROBO homophilic and heterophilic interactions and/or by modulating cadherin-mediated cell adhesion (Backer et al., 2007; Di Meglio et al., 2008). Consistent with the role of cadherins in ION nucleogenesis, mutants for the *cyclin-dependent kinase 5* (*Cdk5*), a factor involved in regulating cadherin-mediated adhesion (Kwon et al., 2000; Kawauchi, 2014), have similar alterations in cell rearrangement after tangential migration (Oshima et al., 2002). Additional molecules involved in ION nucleogenesis include Reelin, an extracellular matrix glycoprotein known to mediate radial migration in the brain (Goffinet, 1992). In *Reeler* mutants, the postmitotic ION neurons are able to complete their tangential migration, but they are unable to reorganize in the lamellated cytoarchitecture of the mature ION (Goffinet, 1984, 1992; Tissir and Goffinet, 2003).

Nucleogenesis in the ECN and LRN is also influenced by SLIT/ROBO interactions, since in mutants for *Slit/Robo*, the LRN is thinner and smaller than in wild-type brains and the ECN is less compact and disorganized (Di Meglio et al., 2008). If this mechanism of cell rearrangement also occurs through cadherins or if it also plays role in PN/RTN rearrangement is unknown. PN/RTN cell rearrangement is known to be influenced by the immunoglobulin adhesion molecule kin of irregular chiasm-like protein (KIRREL3; aka.:

NEPH2), which is specifically active in neurons that have entered the presumptive nuclear region. In knock-down mice for *Kirrel3* most of the neurons remain stuck along the ventral midline, where tangential migration finishes, therefore disrupting the nuclear organization (Nishida et al., 2011). Finally, Reelin appears to play a subtle role in redistributing the cells within all precerebellar nuclei, as *Reeler* mice have smaller nuclei with ventrally shifted neurons (Tanaka et al., 2007).

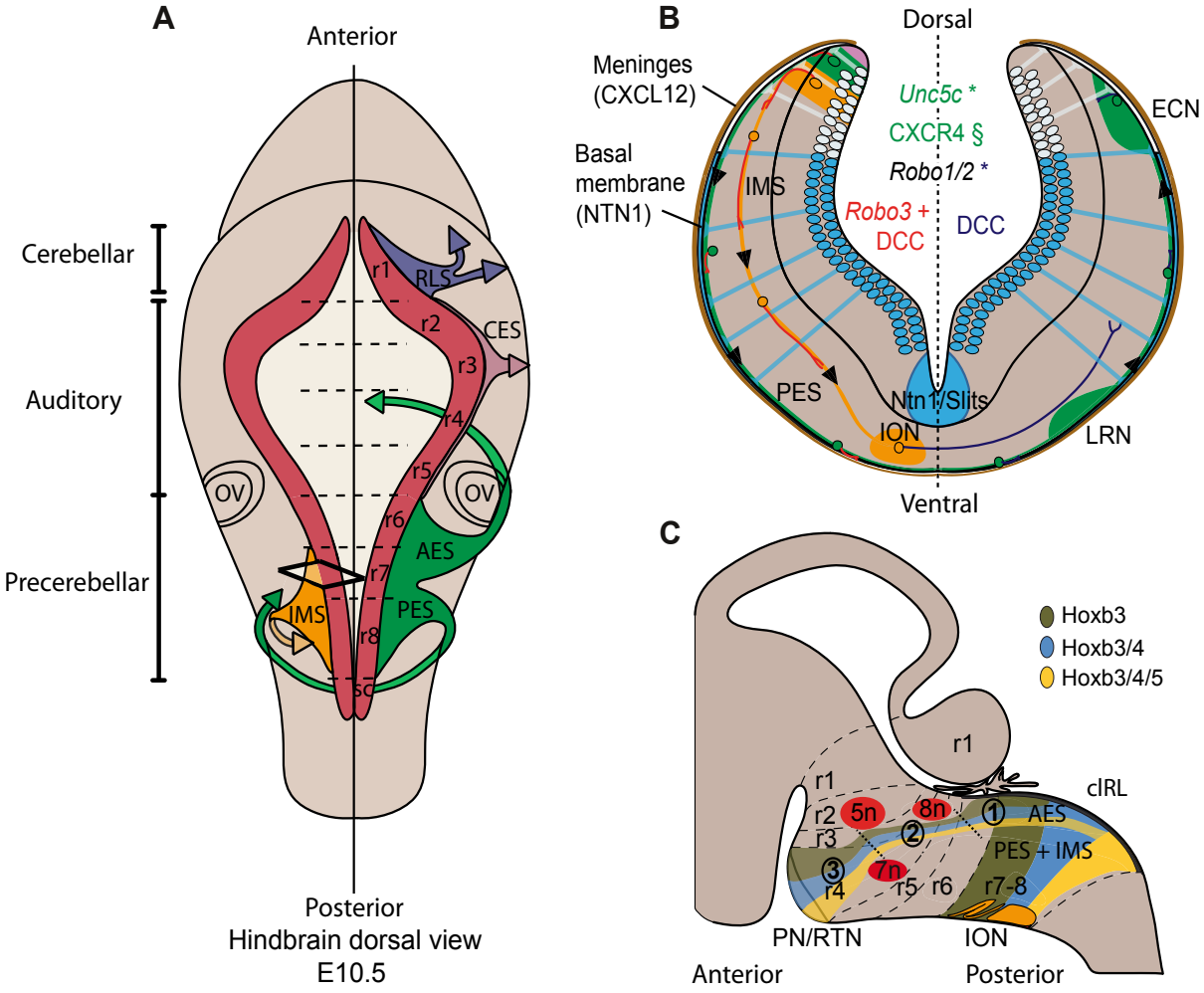

Figure 4. Rhombic lip migration. (A) Dorsal view of the E10.5 hindbrain. The schematic depicts the migratory streams originating at different anteroposterior levels of the RL and the nuclei or cell types that the migratory streams give rise to (cerebellar, auditory and precerebellar). Note that all precerebellar streams reach the midline and that the PES is the only stream reaching the contralateral side. **Figure legend continues on the following page.**

Figure 4. (B) Schematic of a coronal section through the E14.5 hindbrain at the level of r7. The precerebellar neurons arise from progenitor domains in the RL and use progenitor processes to migrate radially towards the pia (Kawauchi et al., 2006). Once at the pia, the neurons incorporate into their respective migratory streams (intramural or extramural) and migrate towards the ventral midline. Migratory guidance is provided by haptotactic molecules at the basement membrane like NTN1 (blue), and by chemotactic molecules like the meningeal CXCL12 (brown). Both, MFN and CFN express DCC, ROBO3 and ROBO1/2 before reaching the midline (dashed line), and switch off ROBO3 upon reaching it. In addition, the MFN specifically express *Cxcr4* and *Unc5c* (shown in green). *Cxcr4* is only detected before midline crossing but the protein product is detected after midline crossing. ROBO1/2 do not play a direct role in precerebellar migration. **(C)** Schematic of a sagittal section of an E14.5 hindbrain showing the precerebellar migratory streams and Hox gene expression in the streams. The posterior extramural stream (PES) and intramural stream (IMS) follow a direct ventral migration, while the anterior extramural stream (AES) follows three phases of migration (encircled numbers). (1) The neurons make a short ventrally-oriented turn. (2) The neurons move anteriorly towards and between the trigeminal (5n), facial (7n), and vestibulocochlear (8n) nerve roots, which are devoid of NTN1. (3) The neurons turn ventrally towards the ventral midline. A Hox code is established depending on the rhombomeric origin of a particular neuron and is conserved throughout migration and nucleogenesis. **CES:** cochlear extramural stream; **RLS:** rostral or anterior rhombic lip stream; **OV:** otic vesicle.

2. OBJECTIVES AND RESEARCH DESIGN OF THE STUDY

GLI3 is required for the proper development of dorsally-derived structures in the dorsal forebrain, dorsal midbrain and anterior hindrain (cerebellum). *Gli3* loss of function leads to region-specific alterations (i. e. dorsal forebrain reduction, dorsal midbrain expansion, reduced and unfoliated cerebellum). The role of GLI3 in the development of the posterior hindbrain remains poorly studied (Persson et al., 2002; Lebel et al., 2007), but previous work from the Dr. Blaess' research group indicates an important role of GLI3 in the development of the precerebellar system, including alterations in MFN distribution and a reduction of the CFN population (Arellano, 2011). Whether GLI3 has a direct role in these changes or in patterning the clRL from which these neurons arise remains unknown.

The aim of this thesis was to uncover the role that GLI3 plays in the development of the hindbrain, and in particular in the formation of the precerebellar system. As a first step, *Gli3* expression in the hindbrain was characterized at different stages of embryonic development to uncover the cell populations in which GLI3 may play a direct role. Subsequently, the hindbrain of *Gli3* null mice (*Gli3*$^{XtJ/XtJ}$ mice; in the following simply referred to as *Gli3*$^{Xt/Xt}$ mice) were analyzed. Markers were used to identify specific hindbrain neuronal populations and to obtain insight into the overall hindbrain phenotype in absence of *Gli3* function. This analysis showed that the major alterations in absence of *Gli3* are restricted to the precerebellar system. Thus, this study focused on understanding the mechanisms behind the precerebellar phenotype. To investigate the underlying mechanisms of the precerebellar phenotype in *Gli3*$^{Xt/Xt}$ embryos four approaches were taken: (1) The establishment and proliferative state of the progenitor domains generating MFN and CFN were analyzed. (2) The main guidance cues (and their receptors) previously described as influencing precerebellar migration as well as hindbrain structures (e.g. other nuclei, the ventral midline) thought to facilitate precerebellar migration were studied in *Gli3*$^{Xt/Xt}$ mice. (3) To clarify whether GLI3 plays a cell-autonomous or non-cell autonomous role in the development of the precerebellar system *Gli3* was inactivated in specific cell populations (e.g. in a subset of precerebellar progenitors) or at specific time points (in the CNS after E10.5) using the Cre-loxP system. (4) To study whether alterations in the cerebellum (target area of precerebellar neurons) generated in *Gli3*$^{Xt/Xt}$ mice influence the development of the precerebellar system, *Gli3* was inactivated in the cerebellum using the Cre-loxP system. This analysis showed that GLI3 might influence CFN differentiation, but that it does not play a cell-autonomous role in migrating MFNs. Moreover, it demonstrated that GLI3 influences the development of the precerebellar system before E10.5 and that it may do it by regulating structures originating outside of the CNS. To clarify this last point, an analysis of cranial ganglia and their projections was performed in *Gli3*$^{xt/xt}$ embryos. This revealed an increased size of the trigeminal ganglion and a severe disorganization of its central descending projections, the spinal trigeminal tract (sp5).

3. Materials and Methods

3.1. Materials

3.1.1 Technical equipment

Appliance	Model/Cat. No.	Manufacturer	Registered Office
5x objective	EC PlnN 5x/0.16 M27	Carl Zeiss	Jena, DE
10x objective	EC PlnN 10x/0.3 DICI 1.11µm	Carl Zeiss	Jena, DE
20x objective	EC PlnN 20x/0.5 DIC II 0.67 µm	Carl Zeiss	Jena, DE
40x objective	Pln Apo 40x/1.3 Oil DIC III 0.26 µm	Carl Zeiss	Jena, DE
63x objective	Pln Apo 63x/1.4 Oil DIC II 0.24µm	Carl Zeiss	Jena, DE
Autoclave	DX-150 benchtop	Systec	Wettenberg, DE
Balance	AC211S	Sartorius	Göttingen, DE
Balance	ATL-822-1	Sartorius	Göttingen, DE
Centrifuge	Pico 17	Thermo Fisher Scientific	Schwerte, DE
Centrifuge	Labofuge 400R 75008-162	Thermo Fisher Scientific	Schwerte, DE
Fluorescence Lamp	Illuminator HXP120C	Carl Zeiss	Jena, DE
Gel chambers	Model 41-1525 Model 40-1515	Peqlab	Erlangen, DE
Heating Block	Dry bath Typ15103	Thermo Fisher Scientific	Schwerte, DE
Heating Plate	flattening table OTS 40 01 - 4002 - 00	Medite	Burgdorf, DE
Hot plate	Hi1220	Leica	Wetzlar, DE
Hybridization oven	InSlide Out 241000	Boekel Scientific	Feasterville, USA
Incubator (bacteria)	AL01-07	Advantage-Lab	Schilde, BE
Magnetic stirrer	AGE 1200 rpm	VELP Scientifica	Usmate, IT
Micro-centrifuge	Corning LSE Mini Microcentrigure, 120 V	Thermo Fisher Scientific	Schwerte, DE
Microscope Camera (stereomicroscope)	DFC290	Leica Microsystems	Wetzlar, DE
Microscope Camera (ApoTome)	AxioCam MRm	Carl Zeiss	Jena, DE
Microscope Color Camera (ApoTome)	AxioCam MRc	Carl Zeiss	Jena, DE
Microscope (ApoTome)	AxioObserver Z1 SIP66732	Carl Zeiss	Jena, DE
Microwave	MW7809	Severin	Sundern, DE
Mini-centrifuge	3722L	Thermo Fisher Scientific	Schwerte, DE
pH Meter	FE20 FiveEasy	Mettler Toledo	Giessen, DE
Pipette-boy Accu-jet pro	26300	Brand	Wertheim, DE
Power supply electrophoresis	EV231	Peqlab	Erlangen, DE
Power supply	Power Supply 231	Carl Zeiss	Jena, DE
Refrigerators and	G 2013 Comfort	Liebherr Kendro	Lindau Hanau, DE

Freezers 4°C, -20°C, -80°C	HERAfreeze		
Rocking Platform	4440148	VWR	Darmstadt, DE
Shaker	Nutation mixer	VWR	Darmstadt, DE
Spectrophotometer	Nanodrop 1000	Peqlab	Erlangen, DE
Stereomicroscope with fluorescence	Model MZ10F 10446377	Leica Microsystems	Wetzlar, DE
Thermoblock	230-1.00AT	Peqlab	Erlangen, DE
Thermocycler	DANN engine PTC-200	BioRAD	München, DE
Vacuum pump	Vacuubrand	Brand	Wertheim, DE
Vibratome	HM650V	Microm	Dresden, DE
Vortex	Vortex genius	IKA	Staufen, DE
Water bath	10679808	GFL	Burgwedel, DE

3.1.2 Data acquisiton and analysis

Computing process	Software	Producer	Registered Office
DNA sequence analysis	DNA strider 1.4f18	CEA	Saclay, FR
Gel documentation	Quantity One	Bio-Rad	München, DE
Image acquisition	ZEN 2 (blue edition) V 2.0	Carl Zeiss	Jena, DE
Image acquisition	Leica Application Suite 3.3.0	Leica	Wetzlar, DE
Image editing	Adobe Illustrator CS3	Adobe Systems	München, DE
Image processing	Adobe Photoshop CS3	Adobe Systems	München, DE
Image processing	ImageJ 1.47b	Wayne Rasband, National Institutes of Health	Bethesda, USA
Image processing	ImageJ 1.47n (Fiji)	Wayne Rasband, National Institutes of Health	Bethesda, USA
Statistical analysis	OriginPro 8 SR0 V8.0724(B724)	OriginLab Corporation	Northhampton, USA

3.1.3 Consumables

Item	Model/Cat. No.	Manufacturer	Registered Office
12-well culture plate	353043	BD Biosciences	Heidelberg, DE
24-well culture plate	353047	BD Biosciences	Heidelberg, DE
Autoclave tape	SteriClin sticky tape	VP group	Feuchtwangen, DE
Blades	Apollo	Apollo Herkenrath GmbH & Co KG	Solingen, DE
Culture dishes 100x20mm	831802003	Sarstedt	Sarstedt, USA
DermaClean gloves	PFC 4303971	Ansell	München, DE
Dissecting tools	Forceps, scissors etc.	Fine Science Tools	Heidelberg, DE
Embedding cassettes	Histosette	VWR	Darmstadt, DE
Embedding molds	Peel-A-Way	Polysciences Inc.	Eppelheim, DE

Eppendorf tubes 1.5mL	72690	Sarstedt	Nümbrecht, DE
Filter tips	ART 100/200/1000 barrier tips	Thermo Fisher Scientific	Schwerte, DE
Glass capillaries	GB150F-8P	Science Products	Hofheim, Germany
Hydrophobic pen (Dako Pen)	S2002	Agilent	California, USA
Hybridization cover slips	HybriSlip HS 60	Sigma Aldrich	St. Louis, USA
Microscope cover glasses	LAME110071	Labomedic	Bonn, DE
Microscope slides	Superfrost	Menzel-Gläser	Braunschweig, Germany
Microscope slides	Superfrost ultra plus	Menzel-Gläser	Braunschweig, Germany
Parafilm	Laboraty film `M	Pechiney Plastic Packaging	Chicago, USA
Pasteur plastic pippets 1 ml	2655181	VWR	Darmstadt, DE
PCR tubes	PCR strip tubes 0,2 mL	VWR	Darmstadt, Germany
Petri dishes	Falcon petri dishes (15 mm)	BD Biosciences	Heidelberg, Germany
Pipettes (10, 20, 200,1000µL)	FA10002M FA10003M FA10005M FA10006M	Gilson	Middleton, USA
Pipette tips	Gilson pipette Tipps (0,5-20 µL, 20-200 µL, 200-1000 µL)	Greiner Bio-One	Frickenhausen, Germany
Razor Blade	121-6	Plano GmbH	Wetzlar, DE
Rein Rotmarder Brush	149-2120	VWR	Darmstadt, DE
Reagent tubes	Eppendorf tubes (0,5 mL; 1,5 mL; 2 mL)	Eppendorf	Hamburg, Germany
Serological pipettes	4487 (5ml) 4488 (10 ml) 4489 (25 ml)	Corning Life Sciences	Kaiserslautern, DE
Slide boxes	Micro slide box (plastic)	VWR	Darmstadt, DE
Syringes	Plastipak 1 ml	BD Bioscience	San Jose, USA

3.1.4 Chemicals and reagents

Chemicals	**Catalog no.**	**Manufacturer**	**Registered Office**
Acetic anhydride (Ac_2O)	1.00639.1000	VWR	Darmstadt, DE
Ampicilin	A5354	Sigma-Aldrich	Steinheim, DE
Agarose	16500-500	Life Technologies	Darmstadt, DE
Ampuwa water	40676.00.00	Ampuwa, Fresenius	Bad Homburg, DE
Aqua-PolyMount	18606	Polysciences Inc.	Eppelheim, DE
Ascorbic acid	A4403	Sigma-Aldrich	Steinheim, DE
Benzyl alcohol	402834	Sigma-Aldrich	Steinheim, DE
Benzyl bezoate	B6630	Sigma-Aldrich	Steinheim, DE
Bisbenzimide H33258	B2883	Sigma-Aldrich	Steinheim, DE

(Hoechst 33258) 10mg/mL			
BM purple AP substrate	11442074	Roche	Penzberg, DE
Bromophenol blue	A1120.005	AppliChem	Darmstadt, DE
Calcium chloride dihydrate ($CaCl_2 \cdot 2H_2O$)	22322.295	VWR	Darmstadt, DE
Chlorophorm ($CHCl_3$)	22711.260	VWR	Darmstadt, DE
Bromodeoxyuridine (BrdU)	B5002	Sigma-Aldrich	St. Louis, DE
Bromophenol blue	A1120.005	AppliChem	Darmstadt, DE
Chlorophorm ($CHCl_3$)	22711.260	VWR	Darmstadt, DE
Denhardt´s Solution 50x concentrate	D2532	Sigma-Aldrich	Steinheim, DE
Dextran sulfate	A4970.0250	AppliChem	Darmstadt, De
Digoxigenin-labeled NTPs	112777073910	Roche	Penzberg, DE
DMSO	D8418	Sigma-Aldrich	Steinheim, DE
DNA ladder (1kb)	10787-018	Life Technologies	Darmstadt, DE
DNA loading buffer	R0611	Life Technologies	Darmstadt, DE
dNTPs (100mM)	28-4065-52	GE Healthcare	Dornstadt, DE
Eosin solution	318906	Sigma-Aldrich	Steinheim, DE
Dulbecco´s Phosphate Buffered Saline (DPBS)	14190-094	Thermo Fisher Scientific	Schwerte, DE
Ethylenediaminetetraacetic acid (EDTA)	E6511	Sigma-Aldrich	Steinheim, DE
Ethanol	20821.321	VWR	Darmstadt, DE
Ethidium bromide	2218.2	Carl Roth	Karlsruhe, DE
Ferricyanide	131503	AppliChem	Damstadt, DE
Formamide	155-15026	Life Technologies	Darmstadt, DE
Glucose	G7528-250g	Sigma-Aldrich	Deisenhofen, DE
Goat serum	G9023519	Sigma-Aldrich	Steinheim, DE
Hematoxylin	H3136	Sigma-Aldrich	Deisenhofen, DE
Hydrochloric acid (HCl)	470301-256	VWR	Darmstadt, DE
Igepal	I8896	Sigma-Aldrich	Deisenhofen, DE
Isoflurane	Forane 2594.00.00	Abbott	Wiesbaden, DE
Isopropanol	P/7500/15	Thermo Fisher Scientific	Schwerte, DE
Lithium chloride (LiCl)	203637	Sigma-Aldrich	St. Louis, USA
Phosphate buffered saline	10010023	Fisher Scientific	Schwerte, DE
Postassium chloride (KCl)	26764.260	VWR	Darmstadt, DE
Magnesium chloride ($MgCl_2$)	25108.260	VWR	Darmstadt, DE
Normal donkey serum (NDS)	017-000-121	Jackson ImmunoResearch	Suffolk, UK
Normal goat serum (NGS)	NSO2L	Sigma-Aldrich	St. Louis, USA
Paraffin	Paraplast Plus 125387-89-5	McCormick Scientific	Richmond, USA
Paraffin remover	41-5600-00	Medite	Burgdorf, DE
Paraformaldehyde (PFA)	0335.2	Carl Roth	Karlsruhe, DE
PCR purification kit	28104	Qiagen	Hilden, DE
PCR run buffer (10x)	18067017	Life Technologies	Carlsbad, USA
Penicillin Streptomycin 100x	P4333	Sigma-Aldrich	Steinheim, DE
Polyethinelglycol	P5413	Sigma-Aldrich	Steinheim, DE
Plasmidial DNA isolation kit	K210017	Life Technologies	Darmstadt, DE
Ribonucleic acid, transfer,	R5636	Sigma-Aldrich	Steinheim, DE

from Bakers Yeast			
RNase away	10328011	Thermo Fischer Scientific	Schwerte, DE
RNAse inhibitor	13398800	Roche	Penzberg, DE
Sarcosyl	L9150	Sigma-Aldrich	Steinheim, DE
Sodium acetate (NaOAc)	106268	Merck	Darmstadt, DE
Sodium azide (NaN_3)	S2002	Sigma-Aldrich	Deisenhofen, DE
Sodium chloride (NaCl)	470302-522	VWR	Darmstadt, DE
Sodium dihydrogen phosphate ($NaH_2PO_4 \cdot 2H_2O$)	28013.264	VWR	Darmstadt, DE
Sodium bicarbonate ($NaHCO_3$)	27775.293	VWR	Darmstadt, DE
Sodium citrate ($Na_3C_6H_5O_7$)	470302-530	VWR	Darmstadt, DE
Sodium hydroxide (NaOH)	31627.290	VWR	Darmstadt, DE
Sucrose	27480.360	Sigma-Aldrich	Deisenhofen, DE
Tetramisole hydrochloride	L9756	Sigma-Aldrich	Steinheim, DE
ThermoClean	25220100	Bioanalytic	Freiburg, DE
Tissue Tek O. C. T.	4583	Sakura	Alphen aan den Rijn, NL
Triethanolamine	28746290	VWR	Darmstadt, DE
Tris-HCl	108219.1000	Merck Millipore	Darmstadt, DE
Triton X-100	1.08219.1000	Merck Millipore	Darmstadt, DE
Tween20	28829.183	VWR	Darmstadt, DE
UltraPure LMP Agarose	15517-022	Life Technologies	Darmstadt, DE
X-gal	730-1498	VWR	Darmstadt, DE
Xylene	CN80.2	Carl Roth	Karlsruhe, DE

3.1.5. Buffers and solutions

Buffer/Solution	Content
Agar LB-medium	40 g of LB medium according to Miler in 1 L H_2O Autoclave, let cool to ~ 50°C, add 1mg/ml ampicilin, plate and store at 4°C
Acetylation solution	125 µl actiy anhydride (Ac_2O) 650 µl HCl 130 µl Triethanolamine (TEA) 49 ml Ampuwa water prepare freshly
Blocking solution	For immunohistochemistry: 10% NDS, 0.1% Triton X-100 in PBS 1X For *in situ* hybridization: 10% NGS, 0.1% Tween20 in PBS 1X
Borate buffer 0.1 M, pH 8.5 (for BrdU staining)	3.1 g boric acid 4.8 g Sodium tetraborate decahydrate Take to 1 liter
Citrate buffer, 10 mM, pH (6.0) (for antigen retrieval in paraffin sections)	1.92 g Citric acid (anhydrous) adjust pH to 6.0 Take to 1 liter
Hybridization buffer	50 mlFormamide (deionized) 50% 20 ml 50% Dextran sulfate (25g DexSulfate Sodium Salt/ 50ml (in H2O) 10%

	1 ml 100x Denhardt's (Rnase free) 1% 2.5 ml yeast tRNA (10mg/ml) 250µg/ml 6 ml 5M NaCl 0.3M 2 ml 1M Tris-HCl, pH8 20mM 1 ml 0.5M EDTA 5mM 1 ml 1M NaPO4 (pH8) 10mM 5 ml 20% Sarcosyl (can't autoclave) 1% 11.5 ml DEPC-H_2O (1ml DEPC in 1L of dH_2O; alternatively use Ampuwater) Total: 100 ml
LB-medium	25 g of LB medium powder according to Miller in 1L dH_2O Autoclave and cool to room temperature Add ampicillin (1mg/ml)
Loading buffer (electrophoresis)	For a 10X solution: 50% glycerol 0.4% Bromophenol blue 0.4% Xylene cyanol
Lysis buffer	333 µl 1.5M Tris pH 8.8 (final is 50 mM) 20 µl 0.5 M EDTA (final is 1 mM) 500 µl 10% Tween (final is 0.5%) 9.1 ml H_2O
NTMT	2ml 5M NaCl (100mM) 10ml 1M Tris-HCl pH9.5 (100mM) 5ml 1M MgCl2 (50mM) 0.1ml Tween-20 (0.1%) 82.9ml dH_2O before use, add 0.5mg/ml levamisole (add 50mg or 1 ml of 50mg/ml stock solution).
Paraformaldehyde (PFA)	For a 20% solution: 500g PFA 2.0L ultrapure H_2O Adjust pH to 7.0 Total: 2.5 L
PBS	For a 5x stock solution: 40 g NaCl (137mM) 1 g KCl (2,7mM) 7.1 g Na_2HPO_4 (10mM) 1.36 g KH_2P_4 (2mM) in 1 L dH_2O For a 1x working solution: 100 ml of 5x PBS 400 ml of MilliQ water
PBT	499.5 ml 1x PBS + 500 µl Triton X-100
PBTw	499.5 ml 1x PBS + 500 µl Tween20
RNAse buffer	100ml of 5M NaCl (0.5M) 10ml of 1M Tris-HCl, pH7.5 (10mM) 10ml of 0.5M EDTA, pH8 (5mM) 880ml of dH_2O
Saline sodium citrate buffer (SSC)	For a 20X stock solution: 88.2g NaCitrate 174g NaCl Adjust pH to 7.0 Total: 1000 ml
TE buffer pH 8.0	1mL 1M Tris-HCl pH 8.9, 200 µl 0.5 EDTA in 100 ml dH_2O
Triethanolamine (TEA)-HCl 0.1M	130 ul HCL 12M and 650 ul TEA (Fluka90279) in 50ml Ampuwa water
Tris-acetate-buffer (TAE) 50x	242 g Tris-base 57.1 mL Glacial acetic acid

Electrophoresis)	100 mL 0,5M EDTA, pH8.0
X-gal run Buffer	1.25 ml of 200mM potassium ferrocyanide (5mM) 45.5 ml X-gal washing buffer 2 ml X-gal substrate (25 mg X-gal/1 ml DMF)
X-gal washing Buffer	1 ml of 1M $MgCl_2$ (2mM) 500 ml of Igepal Ca-30 (0.1%) 0.25 ml 10% deoxycholate solution (0.05%) 500 ml PBS

3.1.6. Enzymes

General enymes	**Cat. No.**	**Manufacturer**	**Registered Office**
Deoxyribonuclease (DNAse, 1000U)	M610A	Promega Corp	Mannheim, DE
Proteinase K (for *in situ* hybridization)	03115879001	Roche	Penzberg, DE
Ribonuclease (RNAse A)	PureLink 12091-021	Life Technologies	Darmstadt, DE
Restriction enymes	**Cat. No.**	**Manufacturer**	**Registered Office**
BamHI	RO189S	New England Biolabs	Frankfurt am Main, DE
EcoRV	RO195S	New England Biolabs	Frankfurt am Main, DE
NotI	RO189S	New England Biolabs	Frankfurt am Main, DE
SphI	RO182S	New England Biolabs	Frankfurt am Main, DE
DNA/RNA polymerases	**Cat. No.**	**Manufacturer**	**Registered Office**
Taq DNA Polymerase Recombinant (500U)	10342-020	Roche	Penzberg, DE
Taq RNA SP6 Polymerase (1000U)	10810274001	Roche	Penzberg, DE
Taq RNA T3 Polymerase (1000U)	11031163001	Roche	Penzberg, DE
Taq RNA T7 Polymerase (1000U)	10881767001	Roche	Penzberg, DE

3.1.7 RNA *in situ* probes

RNA probe	**Plasmid description**	**Restriction enyme (antisense probe)**	**RNA polymerase (antisense probe)**	**Reference**
Ascl1	pGEM7; insert 1.1 kb	XbaI	SP6	Sudarov et al., 2011
Atoh1	insert; 4kb	Knp1	T7	Corrales et al., 2004
Barhl1	pT7T3D-pacI 2.897 kb; insert 0.9 kb	EcoR1	T3	Bulfone et al., 2000
Barhl2	pBluescriptSK- 3.569 kb; insert 0.7 kb	HindIII	T3	Saba et al., 2003
Brn3.2	pBS ; insert 524 bp fragment	XhoI	T7	De Diego et al., 1999
Cxcr4	pCRII-TOPO, Insert	EcoRV	SP6	Tissir et al., 2004

	1 kb			
Cxcl12	pCRII-TOPO, Insert 1 kb	EcoRV	SP6	Tissir et al., 2004
En1	pBluescriptKS	ClaI	T7	Joyner Lab, Sloan Kettering Instiutute, NY
Er81	pbluescript SK; Insert 0.6 kb	SpeI	T7	Joyner Lab, Sloan Kettering Instiutute, NY
Gad1		NotI	T7	James Li, University of Connecticut
Gad2	pluescriptKS	HindIII	T3	James Li. University of Connecticut
Gbx2		HindIII	T7	Joyner Lab, Sloan Kettering Instiutute, NY
Gli3	pBluescriptII KS-; Insert 1.2 kb	EcoRV	T3	Corrales et a., 2004
Hoxb3	pBluescript KS; insert 0.7 kb	BamH1	T3	Rob Crumlauf
Hoxb4	pBluescript KS; insert 1,9 kb	Bgl2	T7	Rob Crumlauf
Hoxb5	pT7T3D 2.497 kb; Insert 1.3 kb	EcoRI	T3	Rob Crumlauf
Isl1	PGEM3; insert 1.5 kb	HindIII	T7	Blaess et al., 2008
Lhx2	pBluescript; Insert 1.3 kb	EcoR1	T3	Rétaux et al., 1999
Lhx9	pGEM-T-easy; insert 1.2 kb	NdeI	T7	Rétaux et al., 1999
Lmx1a	pBluescript; insert 1.6 kb	AgeI	T7	Blaess et al., 2011
MafB		EcoRV	T7	Farago et al., 2006
Netrin1				Hammond et al., 2009
Ngn1	Insert 0.5 kb	SacI	SP6	Liu et al., 2008
Olig3	Insert 1.3 kb	XhoI	T7	Liu et al., 2008
Pax2	pBluescriptKS	EcoRI	T7	Asano and Gruss, 1992
Pax6		XbaI	T7	Joyner Lab, Sloan Kettering Instiutute, NY
Ptf1a	pYX-Asc; Insert 1.6 kb	EcoRI	T3	not described previously
Robo1	pbluescript SK+ 2.9 Kb; insert 1 kb	XhoI	T3	Bagri et al., 2002
Robo2	pbluescript SK+ 2.9 kb; insert 1.7 kb	XhoI	T3	Bagri et al., 2002
Robo3	pbluescript SK-; insert 470 bp	XbaI	T7	Marillat et al., 2004
Slit1	pbluescript 3.7 kp; insert 0.8 kb.	BamH1	T7	Bagri et al., 2002
Slit2	pbluescript 3.9 kb; 1.6 kb	XbaI	T7	Bagri et al., 2002
Slit3	pCR2.1 3.0 kb; insert 0.7 kb	HindIII	T7	Geisen et al., 2008
Unc5b	pBluescript LION 2.93 kb; insert	Not1	T7	Lu et al., 2004
Unc5c	Gibco BRL; insert 0.580 kb	Not1	Sp6	Przyborski et al., 1998

Vglut2	pbluescript SKII-	EcoR1	T3	Annas Thesis
Wnt1	pGEM4; insert 1.29 kb	ClaI	Sp6	Joyner

3.1.8. Antibodies

Ms = mouse, rb = rabbit, gt = goat, gp = guinea pig, rt = rat, sh = sheep

All primary antibodies were of the IgG class unless stated otherwise.

All secondary antibodies were raised in donkey unless stated otherwise.

Primary antibody	**Dilution**	**Cat. No.**	**Manufacturer**	**Registered Office**
α-DIG-AP Fab fragments (sh)	1:5000	11093274910	Roche	Penzberg, DE
α-BARHL1	1:500	HPA004809	Sigma-Aldrich	Deisenhofen, DE
α-BrdU (ms)	1:50	555627	BD Biosciences	Heidelberg, DE
α-cleaved Caspase-3 (rb)	1:200	9664S	Cell Signaling	Leiden, NL
α-DCC (gt)	1:500	SC-6535 (A-20)	Santa Cruz	Texas, USA
α-FOXP2 (gt)	1:200	EB05226	Everest Biotech	Oxfordshire, UK
α-GFP (rb)	1:400	A11122	Life Technologies	Darmstadt, DE
α-GFP (rt)	1:1000	04404-26	Nacalai Tesque	Kyoto, JP
α-ISL1 (ms)	1:200	39.3F7	DSHB	Iowa, USA
α-NGN1 (gt)	1:200	A-20	Santa Cruz	Texas, USA
α-PRPH (rb)	1:200	AB1530	Merck Millipore	Massachusetts, USA
α-TUJ1	1:500		Santa Cruz	Texas, USA
Secondary and Tertiary antibodies	**Dilution**	**Cat. No.**	**Manufacturer**	**Registered Office**
Alexa 488 α-rb	1:500	A21206	Life Technologies	Darmstadt, DE
Alexa 488 α-rt	1:500	AB150149	Life Technologies	Darmstadt, DE
Alexa 488 α-ms	1:500	A21202	Life Technologies	Darmstadt, DE
Alexa 647 α-rb	1:500	A31573	Life Technologies	Darmstadt, DE
Biotynilated α-gp	1:200	706-065-148	Jackson ImmunoResearch	Suffolk, UK
Biotynilated α-rb	1:200	711-065-152	Jackson ImmunoResearch	Suffolk, UK
Biotynilated α-rt	1:200	712-065-150	Jackson ImmunoResearch	Suffolk, UK
Biotynilated α-ms	1:200	715-065-150	Jackson ImmunoResearch	Suffolk, UK
Cy3 α-gt	1:200	05-165-147	Jackson ImmunoResearch	Suffolk, UK
Cy3 α-ms	1:200	715-165-150	Jackson ImmunoResearch	Suffolk, UK
Cy3 α-rb	1:200	11-165-152	Jackson ImmunoResearch	Suffolk, UK
Cy3 α-Streptavidin	1:1000	016-160-084	Jackson ImmunoResearch	Suffolk, UK

3.1.9. Mouse lines

Name	Allele symbol	Mutation	Reference
CD1	Wild-type	Wild-type	
C57BL6J	Wild-type	Wild-type	
Atoh1-Cre	*Tg(Atoh1-cre)1Bfri*	Transgenic	Mataei et al., 2005
En1-Cre	$En1^{tm2(cre)Wrst}$	Targeted knock-in	Kimmel et al., 2000
$Gli3^{flox}$	$Gli3^{tm1AljJ}$	Targeted knock-out	Blaess et al., 2008
$Gli3^{Xt}$	$Gli3^{Xt\text{-}J}$	Spontaneous	Hui and Joyner, 1993
$R26^{lacZ}$	$Gt(ROSA)26Sor^{tm1Sor}$	Targeted knock-out	Soriano, 1999
$R26^{EYFP}$	$Gt(ROSA)26Sor^{tm1(EYFP)Cos}$	Targeted knock-out	(Srinivas et al., 2001)
Nestin-Cre	*Tg(Nes-cre)1Kln*	Transgenic	Tronche et al., 1999
Pax3-Cre	$Pax3^{tm1(cre)Joe}$	Targeted knock-in	Lang et al., 2005

3.2. Methods

3.2.1. Mouse breeding

The Gli3xt mice were kept in a C56Bl6/J background. All other strains were kept in a CD1 background. Genetic drift was reduced by intercrossing the mice every second or third generation with outbred wild type mice. The mice were housed in IVC cages under the approval of the University of Bonn animal care and use committee. A maximum of 5 adult mice or two adult mice with their pups were kept together before weaning (the 3rd week after being born). Mice were kept under controlled light (12 hrs light/darkness) environment and were supplied with food and water *ad libitum*.

Matings were set-up with males of at least 8 weeks of age and females of at least 6 weeks old. A maximum of two females was put together with one male. A vaginal plug was taken as a sign of a successful mating (embryonic day 0.5; E0.5). Genotyping to maintain a mouse line was done by obtaining a small piece of the ear and running the correspondent PCR protocol. The marks generated also functioned to discern the mice from each other. Pregnant mice were dissected before 12:00 Hrs and a small piece of the tail or yolk sac of the embryos was used for PCR-based genotyping (Kimmel et al., 2000; Soriano 1999).

3.2.2. BrdU treatment and embryo dissection

Pregnant mothers carrying embryos at different embryonic stages (E9.5 – E18.5) were sacrificed by cervical dislocation. The skin from the stomach was removed and a midline incision on the peritoneum was done to expose the abdominal cavity. The uterine horn was removed and placed in ice-cold PBS (1X). The embryos were extracted from the uterus/visceral yolk sac and placed in ice-cold PBS. Embryos between E9.5 – E10.5 were immediately transferred to 4% PFA, embryos from E12.5-E18.5 were decapitated

immediately. A small tissue sample was obtained (either tail or yolk sac) for genotyping using PCR. For further processing, the brain was kept within the skull for embryos between E13.5 – E15.5, while the brain was extracted from the skull for those between E16.5 – E18.5. Brain extraction was achieved by peeling the skin from the head, followed by the removal of the skull cap and the careful detachment of the brain from the peripheral nerves. In all cases, the samples were fixed 4hrs - overnight in 4% PFA at 4 °C. Afterwards, the tissue was processed to be embedded.

100 μg of bromodeoxyuridine (BrdU) per gram of mouse weight body were injected intraperitoneally (i.p.) 1 hr before dissection of the embryos to label proliferating cells (cells in S-Phase). Pregnant mothers were sacrificed and embryos were dissected as described above.

Animal experiments were performed in strict accordance with the regulations for the welfare of animals issued by the Federal Government of Germany, European Union legislation and the regulations of the University of Bonn. The protocols were approved by the Landesamt für Natur, Umwelt und Verbraucherschutz Nordrhein-Westfalen (Permit Number: 84-02.04.2015.A341).

3.2.3. Methods in histology

3.2.3.1. Tissue embedding

The tissue was embedded in either paraffin or in an optimal cutting temperature compound (O.C.T. compound) depending on the experiments planned. The first option was used to obtain better morphological preservation of the $Gli3^{xt/xt}$ null mutant brain, which has the tendency of being morphologically abnormal. This procedure was used mainly if *in situ* hybridization experiments were planned, as several antibodies do not work under these conditions. Embedding in O.C.T. compound was used for most of the approaches were immunostainings were required, yet the hybridization of several *in situ* probes was also done in these sections.

For paraffin embedding, the tissues were washed three times in 1x PBS for 5 min each wash. Afterwards, the tissue was dehydrated in ascending concentrations of Ethanol (room temperature) as follows: two times in 70% EtOH, one time in 80% EtOH, two times in 95% EtOH, two times in 100% EtOH. The times for these washes depended on the stage of the tissue (embryo, head or brain) in question and were done 10 min for E9.5 embryos, 15 min for E10.5 – E11.5 embryos, 20 min for E12.5 embryos – E14.5 heads, and 30 min for E15.5 – E18.5 brains. Next, the tissues were transferred once into a 50% EtOH/50% xylol solution using the same times for the dehydration and afterwards three times into xylol (E9.5: 5 min, E10.5 – E11.5: 10 min, E12.5 – E14.5: 15 min, E15.5 – E18.5: 20 min). After this procedure, the tissues were washed three times into melted paraffin (60 °C) using the same times as the

deyhdration. Finally, the tissues were quickly transferred into embedding molds filled with melted paraffin. Once the tissue was given the desired orientation, the tissues/molds were removed from the heating plate and were let to cool down. The samples were stored at room temperature.

For O.C.T. embedding, the tissue was washed three times in 1x PBS for 5 minutes each. The tissues were then transferred to 1xPBS with 15% sucrose and then to 1xPBS with 30% sucrose. In both cases, the tissue was left at 4 °C overnight, or until the tissue submerged. Finally, the tissues were transferred into cryo-molds filled with O. C. T. compound, were oriented in the desired position and were placed on dry ice to freeze. The blocks were stored at – 80 °C.

3.2.3.2. Tissue sectioning

Sectioning of the paraffin blocks was done using a microtome. The blocks were removed from the mold, were positioned on microtome chuck in the orientation desired for sectioning and were attached to it using melted paraffin. Once the paraffin had solidified, the blocks were put on the microtome and were sectioned with a 7 μm thickness. The sections were unfolded in water and transferred onto superfrost ultra plus adhesion slides. Two adjacent sections were collected on a series of ten slides and until the slides were full. This provided a good representation of the whole brain per slide and a way to obtain comparable sections on different slides for the experiments. The slides were left to dry overnight on a heat plate at 37 °C to bind the tissue to the glass and were stored on slide boxes at room temperature.

Sectioning of O.C.T. blocks was done using a cryostat with an overall temperature of – 20 °C. The blocks were removed from storage at -80 °C and were placed on dry ice to handle them. The blocks were stuck on cryostat sample holders in the desired orientation using liquid O.C.T. and were directly transferred into the cryostat for 30 min to allow them to warm up to the temperature of the cryostat chamber. Sections of 14 μm were collected on a series of ten superfrost ultra plus adhesion slides and until the slides were full. One single section was collected in those samples between E9.5 - E14.5 and two in those between E16.5 - E18.5. Next, the sections were dried at room temperature for two hours or in a warm chamber at 37 °C for 1 hr. The sections were either directly processed for immunohistochemistry/RNA *in situ* hybridization or were stored in slide boxes at – 30 °C until being used.

3.2.3.3. Hematoxylin and Eosin staining

The histological properties of some sections were analyzed by staining the nuclei and cytoplasm with this method. The stainings were done in paraffin sections dewaxed in three consecutive washes of 100% Xylol for 3 min and were gradually rehydrated by putting the

slides two times in 100% EtOH for 2 min, 2 times in 95% EtOH for 2 min, one time in 80% EtOH for 2 min, one time in 70% EtOH for 2 min. The slides were washed for 2 min in MilliQ water, stained in Hematoxylin for 3 min and rinsed under tap water for 2-5 min. Next, the slides were washed with Eosin for 3 min. This was followed by dehydration in ethanol (one time 70%, two times 95% and two times 100%; 3 min each) and xylol (three times, 3 min each). The slides were mounted in PolyMount and stored at room temperature.

3.2.4. Methods in molecular biology

3.2.4.1. PCR genotyping

The tissue obtained was digested in 100 μl lysis buffer with 1 μl proteinase K at 60 °C for 4 hrs (embryo) – 8 hrs (born mice), followed by proteinase heat inactivation at 95°C for 10 min. The samples centrifuged for 5 – 10 seconds at 2000 x G in a microcentrifuge. 1μl of the supernatant containing the genomic DNA was used for PCR amplification. The primers and protocols used for genotyping are now listed:

Primer	**Sequence 5´- 3´**	**Tm °C**
Cre	F: TAAAFATATCTCACGTACTGACGGTG R: TCTCTGACCAGAGTCATCCTTAGC	F:58.4 R: 61.6
Gli3 flox	Gli3 antisense (G3-AS3): CTGCTCAGTGCTCTGGGCTCC Gli3 sense (G3-S1): CTGGATGAACCAAGCTTTCCATC	G3-AS3: 63.4 G3-S1: 58.1
Gli3^{xt}	Gli3 primer 1 WT: GGCCCAAACATCTACCAACACATAG Gli3 primer 2 WT: GTTGGCTGCTGCATGAAGACTGAC Gli3 primer 3 XT: TACCCCAGCAGGAGACTCAGATTAG Gli3 primer 4 XT: AAACCCGTGGCTCAGGACAAG	Gli3 primer 1 WT: 60.6 Gli3 primer 2 WT: 62.0 Gli3 primer 3 XT: 62.2 Gli3 primer 4 XT: 59.7
Rosa26	RR1: AAAGTCGCTCTGAGTTGTTAT RR2: GCGAAGAGTTTGTCCTCAACC RR3: GGAGCGGGAGAAATGGATATG	RR1: 51.9 RR2: 57.6 RR3: 57.6

F= forward primer, R= reverse primer, WT= wild type, MT= mutant

3.2.4.2. PCR protocols

PCR reaction mix and thermocycler protocol:

***Cre* PCR**

Solution	**Volume**	**Program**	**Temp (°C)**	**Time (min)**
Sample (supernatant)	1 μl	1) 1st denaturation	95	2:00
Run buffer (1x)	2 μl	2) Denaturation	95	0:40
dNTPs (25nM)	0.16 μl	3) Annealing	59	1:00
F primer (5 μM)	1 μl	4) Elongation	72	0:50

R primer (5 μM)	1 μl	5) Incubation	8	∞
$MgCl_2$ (1.5 mM)	0.60 μl	35 Cycles (step 2-4)		
Taq Polymerase (1 U)	0.2 μl			
dH_2O	14.04 μl			
Total volume	20 μl			

Results after electrophoresis: WT: No band, MT: 300 bp

***Gli3-flox* PCR**

Solution	**Volume**	**Program**	**Temp (°C)**	**Time (min)**
Sample (supernatant)	1 μl	1) 1st denaturation	94	5:00
Run buffer (1x)	2 μl	2) Denaturation	94	0:30
dNTPs (25nM)	0.16 μl	3) Annealing	60	1:00
G3-S1 primer (5 μM)	1 μl	4) Elongation	72	1:00
G3-AS3 primer (5 μM)	1 μl	5) Incubation	8	∞
$MgCl_2$ (1.5 μM)	0.60 μl	30 Cycles (step 2-4)		
Taq Polymerase (1 U)	0.2 μl			
dH_2O	14.04 μl			
Total volume	20 μl			

Results after electrophoresis: WT: 200 bp, MT: 500 bp

***Gli3-XT* PCR**

Solution	**Volume**	**Program**	**Temp (°C)**	**Time (min)**
Sample (supernatant)	1 μl	1) 1st denaturation	94	5:00
Run buffer (1x)	2 μl	2) Denaturation	94	0:30
dNTPs (25nM)	0.16 μl	3) Annealing	60	1:00
Gli3 primer 1 WT (5 μM)	1 μl	4) Elongation	72	1:00
Gli3 primer 2 WT (5 μM)	1 μl	5) Incubation	8	∞
Gli3 primer 3 MT (5 μM)	1 μl	30 Cycles (step 2-4)		
Gli3 primer 4 MT (5 μM)	1 μl			
$MgCl_2$ (1.5 μM)	0.60 μl			
Taq Polymerase (1 U)	0.2 μl			
dH_2O	12.04 μl			
Total volume	20 μl			

Results after electrophoresis: WT: 193 bp, MT: 580 bp

***Rosa26* PCR**

Solution	Volume	Program	Temp (°C)	Time (min)
Sample (supernatant)	1 μl	1) 1st denaturation	94	5:00
Run buffer (1x)	2 μl	2) Denaturation	94	0:30
dNTPs (25nM)	0.16 μl	3) Annealing	60	1:00
RR1 primer (5 μM)	1 μl	4) Elongation	72	1:00
RR2 primer (5 μM)	1 μl	5) Incubation	8	∞
RR3 primer (5 μM)	1 μl	30 Cycles (step 2-4)		
$MgCl_2$ (1.5 μM)	0.60 μl			
Taq Polymerase (1 U)	0.2 μl			
dH_2O	13.04 μl			
Total volume	20 μl			

Results after electrophoresis: WT: 500 bp, MT: 220 bp

3.2.4.3. Electrophoresis

Samples of ~ 100 ng DNA or RNA were separated using a 1.5% - 3% agarose gels depending on the size of the sample. 13 μl of the samples were loaded by mixing them with 2 μl of a loading buffer and the gel was run in 1x TAE buffer for 40 min at 110V. In the specific case of RNA, the samples were heated at 70 °C for 10 min and let cool down for 2 min. before being loaded into the gel. The size of the samples was determined using a 1 kb DNA ladder that ran in parallel to the sample and the nucleic acids were visualized by staining them using ethidium bromide (10 μg/ml) or gel red (1:10000). Visualization was achieved using gel documentation (Gel Doc) system with an ultraviolet (UV) light transilluminator.

3.2.4.4. Generation of RNA *in situ* probes

3.2.4.4.1. Bacteria transformation and DNA isolation

Plasmids containing the DNA inserts were used to generate the RNA *in situ* probes used in this study. In short, small plasmid aliquotes kindly provided by different laboratories (listed below) were amplified by heat shock transformation of *Escherichia coli* DH5α competent cells. The cells were thawed on ice for 5 minutes and 1 μl of the desired plasmid was added. Incubation on ice continued for 30 minutes, was followed by 45 seconds of warm incubation at 42 °C using a thermo-block and was finalized by a 2 min ice incubation. 900 μl of LB medium free of antibiotic was added and the cells were grown for 1 hour at 37 °C in a thermo-block with agitation (225 rpm). A small volume (50 – 200 μl) of the bacteria were plated on Petry dishes with LB-agar supplemented with the appropriate antibiotic. The

bacteria were incubated at 37 °C overnight. One of the resulting colonies were picked with a sterile pipette tip and used to inoculate 3 ml LB medium supplemented with 20 μl/ml ampicillin. The bacteria were let to grow under agitation (225 rpm) at 37 °C for 6 hrs. 200 μl of these bacteria were used to inoculate 200 ml LB medium with antibiotic. The cells were let to grow under agitation (225 rpm) at 37 °C for 12 - 14 hrs. The bacteria were then centrifugated at 4000 x *g* for 10 min., the pellet was resuspended and lysed to obtain the DNA, which afterwards was purified using the Pure Link Hi Pure Plasmid Maxiprep kit of Invitrogen according to the manufacturer´s protocol. The DNA purity level and concentration were measured using a NanoDrop system (Peqlab). A sample with a ratio of ~ 1.8 A260/280 and ~ 2.0 A260/230 was considered pure and was used to be linearized.

3.2.4.4.2. DNA linearization and transcription

A pure DNA sample was linearized using specific restriction enzymes (New England Biolabs or Roche) following the conditions provided by the manufacturer. As a base protocol, 20 μg DNA were digested at 37 °C using 50U restriction enzyme diluted in 100 μl of 1X restriction buffer (specific for each enzyme) for 3 hrs 20 min. The enzyme was subsequently heat inactivated by 20 min. incubation at 65 °C or 80° C. Linearization was confirmed by agarose gel electrophoresis. The DNA was subsequently purified using a QiAquick PCR Purification Kit (Qiagen), the DNA was collected in AmpuWater, and its purity was verified using the NanoDrop. A sample with a ratio of ~ 1.8 A260/280 and ~ 2.0 A260/230 was considered as pure and was used for DNA transcription to generate RNA *in situ* probes.

In vitro transcription was used to synthesize Digoxigenin (DIG) - labeled RNA antisense *in situ* probes. Labeling was achieved by using a DIG-labeled NTP mix (containing UTP-labeled bases). A solution with a final volume of 20 µl containing 1 µg DNA, 2 µl 10x transcription buffer (Roche), 2 µl DIG-labeling mix (Roche), 0.5 µl RNase inhibitor (Roche) and 1.5 µl of RNA polymerase (1000 U, Roche), was incubated for 3 hrs at 37 °C. The DNA template was removed by incubating with 1 µl DNAse (1000 U, Promega) for 15 min. at 37 °C and the RNA was precipitated at – 80°C for 15 minutes by adding 2 µl 0.2 M EDTA, 1.25 µl 8M LiCl and 75 µl 100% Ethanol. The RNA was recovered by centrifugation at 16000 x *g* at 4 °C, washed with 200 µl 70% ethanol and centrifuged again at 16000 x *g* at 4 °C. The RNA was resuspended in 50 µl ApuWater and its concentration was measured using a NanoDrop. An RNA sample with a ratio of ~ 2.0 A260/280 and ~ 2.2 A260/230 was considered as pure and was used for *in situ* hybridization. For longer preservation of the RNA, 0.5 µl RNase inhibitor were added and storage was done at – 80 °C.

3.2.4.5. RNA *in situ* hybridization

This approach was used to analyze the expression of different markers within the hindbrain and was done in both, paraffin and frozen sections. Previous to *in situ* hybridization, the paraffin sections were de-waxed in three consecutive washes of 100% Xylol for 3 min and were gradually rehydrated by putting the slides two times in 100% EtOH for 2 min, 2 times in 95% EtOH for 2 min, one time in 80% EtOH for 2 min, one time in 70% EtOH for 2 min and one time in AmpuWater for 1 min. In the case of the frozen sections, they were just removed from the freezer at – 30 °C and thawed for 30 min at room temperature.

Several prehybridization washes were done to reduce background staining and improve access of the RNA probe. The slides were treated as follows. In the case of paraffin sections, the sections were post-fixed in 4% PFA in Dulbecco´s Phosphate buffered saline (DPBS) for 10 min, washed 3 times with DPBS for 5 min each. The sections were then incubated for 8 min in DPBS with proteinase K (4 μg/ml for tissue between E9.5 – E16.5, 10 μg/ml for tissue between E17.5 – E18.5). Next, the sections were washed two times in DPBS for 5 minutes to get rid of the proteinase K, were refixed in 4% PFA in DPBS for 5 min, and were again washed 3 times in DPBS. Afterwards, the sections were immersed in freshly prepared acetylation solution for 10 min. The sections were washed three times in DPBS (5 min each) and then dehydrated 5 min in 70% EtOH and in 1 min in 95% EtOH. In the case of the frozen sections, the sections were as well post-fixed in 4% PFA in Dulbecco´s Phosphate buffered saline (DPBS) for 10 min, washed 3 times with DPBS for 5 min each but no treatment with proteinase K or refixation with PFA was done. Instead, the sections were directly treated immersed in acetylation solution for 10 min, then washed in ApuWater for 5 min and dehydrated in an increased concentration of EtOH (70%, 80%, 95% and 100%, 1 min each). Next, they were washed in chloroform for 5 min, in 100% EtOH for 1 min, in 95% EtOH for 1 min and were let to dry to next be hybridized.

Once the paraffin or frozen sections were completely dried, they were positioned horizontally in a humid box filled with 50 ml of a 50% formamide/50% MilliQ water solution and were hybridized with the desired probe diluted in hybridization buffer. For this, 1 μg probe/ml hybridization buffer was heated for 2 min at 80°C, then cooled down for 1 min and then distributed on the sections. The slides were covered with RNase-free coverslips to avoid drying of the solution and were incubated for 12-15 hrs at 55 °C. After this time, several high stringency post-hybridization washes were done to remove unspecific probe hybridization. These washes were equal for both, paraffin and frozen section. The coverslips on the sldies were removed by submerging the slides in 5x SSC at 65 °C and the slides were directly put in 2x SSC with 50% formamide at 65 °C for 30 min. The slides were next washed three times in RNase buffer (10 min each) at 37 °C. Afterwards, the slides were incubated for 30 min in 20 μg RNase A/ml RNase buffer at 37 °C to remove the not hybridized RNA. The RNase was

removed by washing the slides for 15 min in RNAse buffer at 37 °C. Afterwards, two washes (20 min each) of 50% formamide in 2x SSC at 65 °C were done, followed by single washes of 2x SCC and 0.1x SSC for 15 min each at 37 °C. Next, the slides were washed in 1x PBS + 0.1% Tween-20 (PBTw) for 15 min at room temperature and then blocked for 1 hr at room temperature with 10% goat serum in PBTw. After this, the sections were incubated overnight and at room temperature with an alkaline phosphatase-coupled anti-digoxigenin antibody diluted 1:5000 in 1% goat serum PBTw. The unbound antibody was removed by washing the sections four times (15 min each) in PBTw. Next two washes (10 min each) were done in NTMT buffer and once in 0.5 mg levamisole/ml NTMT to block the endogenous alkaline phosphatase. After all this procedure, the slides were incubated in 25 mg levamisol/50 ml BM purple in the darkness. The BM purple served as a chromogenic substrate to generate a blue-purple precipitate that revealed the pattern of RNA hybridization. The time of incubation was dependant on the RNA-probe in question and in the strength of its signal and it ranged between ~ 2 - 6 days. The enzymatic reaction was stopped by washing three times in 1x PBS 5 min each and the slides were mounted using AquaPolymount and glass coverslips. If the sections were meant to be further treated for immunohistochemistry, they were fixed again in 4% PFA in 1x PBS and treated as described in the next section (3.2.5.1). Storage was done in slide boxes at room temperature if the slides were only hybridized, and at 4 °C if they had been combined with immunohistochemistry.

3.2.5. Methods in cell biology

3.2.5.1. Immunohistochemistry on frozen sections

The sections were removed from the freezer at – 30 °C and were left to dry at room temperature for 30 min. A perimeter surrounding the tissue was delineated using a hydrophobic pen (Dako Pen). The slides were put in Coplin jars filled with 1x PBS for 5 min to remove the O.C.T. and were re-fixed for 5 min with 4% PFA at room temperature. The PFA was removed and two consecutive washes were done in 1x PBS (5 min each) to completely get rid of it. Next, the slides were washed 5 min in PBT (1x PBS with 0.1 % Triton X-100) and then blocked in 10% normal donkey serum (NDS) in PBT for 1 hr at room temperature. Aftwerwards, the sections were incubated with the primary antibody of election diluted in 3%NDS in PBT for 4 hrs at room temperature or overnight at 4°C. Three washes in PBT for 5 minutes followed and the sections were next incubated in the secondary antibody of election diluted in 3% NDS in PBT for 2 hrs at room temperature. These last two steps were repeated if a tertiary antibody was used (e.g. streptavidin antibody). To visualize the cell nuclei, a Hoechst fluorescent counterstaining (Hoechst 33258, 1:10000) was added to the secondary or tertiary antibody solution. The unbound antibody was removed by washing the slides two times in PBT for 5 minutes followed by two washes in 1x PBS for 5 minutes.

Finally, the sections were mounted with an AquaPolymount medium, were let to dry in the darkness overnight and were imaged with a fluorescent microscope or stored at 4 °C

3.2.5.2. Immunohistochemistry on paraffin sections

The sections were de-waxed and rehydrated as specified in the ISH protocol (section 3.2.4.5.). A heat-induced antigen retrieval was used to improve antibody binding by microwaving the tissue in 0.1M Citrate Buffer, pH 6.0. The tissue was boiled for 3 min and was cooled down by rinsing the cooker with cold tap water. The slides were transferred 1 min to AmpuWater and then to 1x PBS for 5 min. From here on, the slides were treated as for immunohistochemistry for frozen section, meaning that they were washed in PBT, blocked, incubated in the antibodies, washed again and mounted as described in the previous section (3.2.5.2.).

3.2.5.3. BrdU treatment and immunohistochemistry

Sections obtained from embryos that were treated with BrdU were fixed for 10 min with 4% PFA at room temperature, washed 3 times in 1x PBS (5 min each) and then incubated in 2 N HCl for 30 min at 37 °C. The acid was neutralized by treating the sections in 0.1 M boric acid buffer (pH 8.5) for 10 min. The sections were then washed 3 times in 1x PBS and 1 time in PBT for 5 minutes each time. Afterwards, the sections were treated as for regular immunohistochemistry in frozen sections starting with the blocking step as described in section 3.2.5.2.

3.2.5.4. Whole mount immunohistochemistry

After dissection and overnight fixation in 4% PFA in 0.1 M PBS, the brains of E13.5 and E16.5 animals were rinsed three times in 0.1 M PBS. Next, the tissue was pretreated with Methanol and immunolabeled as described by Renier et al., 2014, with adaptations to the protocol (https://idisco.info/idisco-protocol/update-history/). In short, the tissue was dehydrated in ascending series of Methanol, bleached in 5% H_2O_2 in Methanol, and rehydrated again in descending concentrations of Methanol. The brains were then permeabilized in 0.1 M PBS with 0.2% Triton X-100, 20% DMSO, 0.3 M glycine at 37°C for 24 hrs. The brains were next blocked in 0.1 M PBS, 0.2% Triton X-100, 10% DMSO, 6% Donkey Serum at 37°C for 24 hrs, rinsed three times in 0.1 M PBS, 0.2% Tween-20 with 10 ug/ml heparin (PTwH) at RT 1 hr each, and incubated with rabbit anti-Barhl1 (1:500, HPA004809, Sigma Aldrich) in PTwH, 5% DMSO, 3% Donkey Serum at 37°C for 24hrs. The tissue was next rinsed in PTwH for 10 min, 15 min, 30 min, 1 hr and then 2 hrs. These washes were followed by incubation of the tissue with secondary antibody in PTwH/3% Donkey Serum at 37°C for 1 day. Colorimetric detection was achieved using the HRP

Vectastain Elite ABC Kit /PK-6100; Vector Laboratories) and the DAB Peroxidase Substrate (SK-4100; Vector Laboratories) as follows. The tissue was washed three times in TBS 2 hrs each, followed by a 1 hr wash in freshly prepared ABC Kit reagent. The slides were rinsed three times in Tris-HCL 30 min each and covered in the DAB Peroxidase Substrate. The reaction was stopped by washing the tissue three times in TBS 3 minutes each, followed by a wash in TBS with 0.04% sodium azide.

3.2.5.5. Whole mount X-Gal staining

This method was used to analyze the expression of *Gli3* (E10.5 and E14.5 $Gli3^{lacZ/+}$ embryos), and to validate the recombination pattern of the *Atoh1* (E12.5 and E18.5 $Atoh1^{Cre/+}$, $R26^{lacZ/+}$ embryos) and *En1* (E18.5 $En1^{Cre/+}$, $R26^{lacZ/+}$ embryos) mouse lines. To do this, dissected embryos/brains were fixed for 10 min in 4% PFA and the tissues were washed with X-gal washing buffer for 2x 10 min. Subsequently, the samples were incubated in X-gal reaction buffer at 37°C for 4 hrs overnight. Afterwards, the tissue was washed three times with X-gal washing buffer for 10 min and mounted in AquaPolymount, a glycerol-based mounting medium.

3.2.5.6. Neurotracer labeling

After mouse dissection, the brains of wild type and $Gli3^{xt/xt}$ mice were removed with the trigeminal nerves attached to them and were fixed overnight with 4% PFA at 4°C. The brains were rinsed 3 times in PBS previous to labeling. Several small crystals of 1, 1´ - Dioctadecyl-3, 3, 3´, 3´- tetramethylindocarbocyanine (carbocyanine, D282; Molecular Probes) were attached to the tip of a glass needle generated with a micropipette puller. Working under a dissecting microscope, the crystals were either placed medially and laterally on the exposed area of a single cerebellar hemisphere to label the precerebellar neurons or on the 5n root to label the sp5 tract. In some embryos, the 3, 3´- Dioctadecyloxacarbocyanine (DiO, D275; Molecular Probes) was used instead of the DiI to label the 5n). The brains were stored in 1% PFA at 37°C for 4 days and for 1 month at room temperature in the dark. The brains were washed in PBS, were embedded in 3% Ultra Pure LMP Agarose (15517-022, Life Technologies), and were cut at a thickness of 80 μm with a vibratome. The sections were counterstained with Hoechst dye, were mounted on Fluoromount (F4680, Sigma Aldrich), and were imaged on the few next days. To visualize the distribution of the different precerebellar neurons, several adjacent sections were immunostained for Barhl1 (1:500, HPA004809, Sigma Aldrich) and FoxP2 (1:200, EB05226; Everest Biotech).

3.2.6. Data acquisition and analysis

3.2.6.1. Imaging

Bright field pictures of the sections treated for *in situ* hybridization were taken using two different microscopes. Small tissue areas (e.g. half of a hemisphere or low zoom magnifications) were obtained using either a 5x or a 10x air objectives in a Leica DM1000LED upright microscope coupled to a Leica DFC290 camera. The software used to acquire images was the Leica Application Suite 3.3.0. Larger tissue areas were obtained using a Zeiss AxioObserver Z1 inverted microscope coupled to an AxioCam MRc camera. Several individual pictures were taken using 5x, 10x, 20x and 40x air objectives and were automatically stitched together with the Mosaicx function in the Zen 2 blue edition software (Zeiss) to create a single image.

The immunofluorescent signal was captured using the Zeiss AxioObserver Z1 inverted microscope coupled to an AxioCam MRm camera. Several pictures were taken using 10x, 20x air objectives and 40x, 63x immersion objectives and stitched together using the Mosaicx function. An ApoTome system was used in the particular case of the images taken with the immersion objectives to remove the out-of-focus light and generate sharper images. In several cases (e.g. to study the axonal projections), Z-stacks of a particular region of interest were generated using the 40x and 63x immersion objectives and full image frames were reconstructed from a maximum intensity projection of all frames with the same sample plane illuminated with different light sheet focus positions (ZEN 2, Carl Zeiss).

3.2.6.2. Axial orientation and tissue comparison

Different approaches were combined to gain insight into the axial position in the hindbrain to be able to align, compare and quantify the different brain sections. These included specific morphological features, like the location of the otic vesicle, of the different motor nuclei and cranial nerves (Bruce et al., 1987; Guthrie, 2007; Nichols and Bruce, 2006; Geisen et al., 2008), and of other reference nuclei (only for stages E14.5 – E18.5), like the precerebellar nuclei *per se*, the cochlear nuclei (Farago et al., 2006), or nuclei surrounding them. For this purpose, several reference book chapters or brain atlases were used (Paxinos et al., 2007; Paxinos et al, 2012; Schambra and Connelly, 2008; Sillitoe et al, 2012; Watson C, 2012). Additional orientation was obtained by the general expression of *Hox3* - *Hox5* genes in the hindbrain (Philipidou and Dasen, 2013). As the rhombomeric boundaries in the hindbrain take a flexed geometry during development, standard coronal sections contain different rhombomeric levels distributed as oblique mediolateral stripes (Farago et al., 2006). Therefore, to indicate the rhombomeric level for coronal sections between E14.5 – E18.5, the most ventral structures of the hindbrain were used.

3.2.6.3. Data quantification

3.2.6.3.1. Assessment of the expression area and proliferative state of the progenitor domains

The size of the different progenitor domains of the caudal rhombic lip was obtained by measuring the expression area of a particular RNA probe (*Wnt1, Lmx1a, Olig3, Atoh1, Ptf1a, Ascl1*) or antibody (NGN1) in adjacent sections that covered the whole clRL (r6 - r8; approximately of 720 μm; 14 μm x 10 slides x 5 levels). To do this, the ventricular area positive to each probe was delineated manually in each section using the freehand tool of Image J and normalized to that of the whole ventricular area, measured in the same way. The statistical analysis consisted of a Kruskal-Wallis test with a statistical significance set at $p<0.05$ (Origin 8, Origin Lab; Prism7, GraphPad). At least 3 animals per marker and condition were analyzed and the values were represented as mean ± SD. Several of these animals were injected with BrdU to assess the proliferative status of the progenitor domains. Their RNA expression pattern was overlapped with the BrdU immunostaining signal on adjacent sections using Image J. Next, the BrdU positive cells were counted using the cell counter plugin and were divided by all DAPI cells in the region. An n=3 was only possible to do in the *Atoh1* and NGN1 domains at r7. The statistical significance between control and mutants was assessed using a Student´s t-test with a $P<0.5$, and the values were represented as mean ± SD (Origin 8, Origin Lab; Prism7, GraphPad).

3.2.6.3.2. IMS/ION area assessment

The area occupied by the IMS/ION was assessed by quantifying the expression area of the *Brn3.2* and *Er81* RNA signal in E13.5 – E15.5 coronal adjacent sections along the whole rostrocaudal extent of the ION. To do this, the area positive to each probe was delineated manually in each section using the freehand tool of Image J and was normalized to the whole area of its respective hemisphere, measured in the same way. The different sections were aligned as described in section 3.2.6.2. and their areas were compared between controls and mutants using either a Kruskal-Wallis test (E13.5), or a one-way ANOVA with a post-hoc Tukey test (E14.5 and E15.5). In the last case, a Levene´s test was used to confirm equality of variances. The statistical significance was set at a $P<0.5$ (Origin 8, Origin Lab). As the sectioning of the tissue was always the same (14 μm of difference between each section x 10 slides), a whole picture of the neuron distribution during migration and cell establishment, as well as changes in the size of the ION, were possible to obtain, therefore giving a better idea of how the IMS differs from one condition to the other. To know how the total size of the ION hanged once it has finished its migration, the values obtained from the E15.5 mice were added and compared using a Student´s t-test with a $P<0.5$. In all cases, the values were represented as mean ± SD. (Origin 8, Origin Lab).

3.2.6.3.3. Trigeminal ganglion area and caspase-3 activation

The area and caspase-3 activation in the 5Gn were measured on coronal adjacent sections of E14.5 control and *Gli3*$^{xt/xt}$ hindbrains immunostained for ISL1 and active caspase-3. The sections were aligned as described in section 3.2.6.2. and the ISL1 positive cells were quantified using the Image J cell counter plugin. The anteroposterior extension of the 5Gn was shorter in the control (~ 140 μm; 14 μm x 10 slides x 1 level) as in the *Gli3*$^{xt/xt}$ mutant (~ 280 μm; 14 μm x 10 slides x 2 levels). Using the same methodology, the caspase-3 positive cells were quantified and next, they were divided by the number of ISL1 positive cells. As no level 2 existed in the controls, the measurements were obtained using only level 1. In all cases, the measurements of 3 controls and 4 mutants were tested for statistical significance using a Student´s t-test with a $P<0.5$ and the values were represented as the mean ± SD (Origin 8, Origin Lab; Prism7, GraphPad).

4. RESULTS

4.1 *Gli3* expression in the embryonic hindbrain

Gli3 is expressed in the dorsal neural tube during development and plays a role in the establishment of several dorsal brain structures (Blaess et al., 2006; Blaess et al., 2008; Haddad-Tóvolli et al., 2012; Hui et al., 1994; Theil et al., 1999; Willaredt et al., 2008). A detailed expression pattern map of *Gli3* was necessary to get insight into where and when GLI3 could play a role in precerebellar neuron and general hindbrain development. To this end, ribonucleic acid (RNA) *in situ* hybridization (ISH) for *Gli3* and ß-gal expression in *Gli3-lacZ* knock-in mice ($Gli3^{lacZ/+}$, Garcia et al., 2010) was examined at different developmental stages. *Gli3* was expressed in the entire dorsal area (alar plate), including the clRL, and in the developing trigeminal ganglia (5Gn) (Figure 5A-C, Ray and Dymecki, 2009). By E10.5, *Gli3* was no longer expressed in the most dorsal part of the alar plate (MF progenitor population, *Wnt1*- and *Atoh1*-positive), but continued to be expressed in the adjacent *Atoh1*-negative CF domain and all class dB progenitors, as well as in the 5Gn (Figure 5D-H). These data suggested that GLI3 had the potential of playing a direct role in MFN development at early time points of development, but a more sustained role in CFN and other alar plate neurons. Consistent with this idea, the *Barhl1*-positive MF migratory streams and nuclei were negative for *Gli3* at E14.5 and E18.5, while *Gli3* was expressed in the ION (Figure 5I-Q). In the ION, *Gli3* expression was restricted to a particular ETS-related 81 (*Er81*)-positive subset that corresponds to the principal olivary nucleus (PO) at E18.5 (Figure 5R-Z; Xiang et al., 1996; Hashimoto et al., 2012). Moreover, a few non-precerebellar hindbrain structures including the ventral lateral lemniscus (VLL, basal plate-derived) and superior olivary complex (SOC, dA1 and basal plate-derived) (both part of the auditory circuit; di Bonito et al, 2013b), the nucleus of the solitary tract (SOL, dA3-derived) (involved in processing viscerosensory information from the body; Sieber et al, 2007; Hernandez-Miranda, 2017), expressed *Gli3* at E18.5 (Figure 5BB-EE). In addition, even though mRNA expression was not found in the spinal trigeminal nucleus (Sp5) and vestibular nuclei (Ve) at these stages (dA/dB derived nuclei) analysis of ß-gal expression in the $Gli3^{lacZ/+}$ knock-in mice at E14.5 showed ß-gal expression. This is likely due to the relatively high stability of the ß-gal protein so that ß-gal expression can be detected even after *Gli3* mRNA is no longer expressed (Figure 5M-N). These results indicate that the Sp5 and Ve are derived from *Gli3*-expressing progenitors.

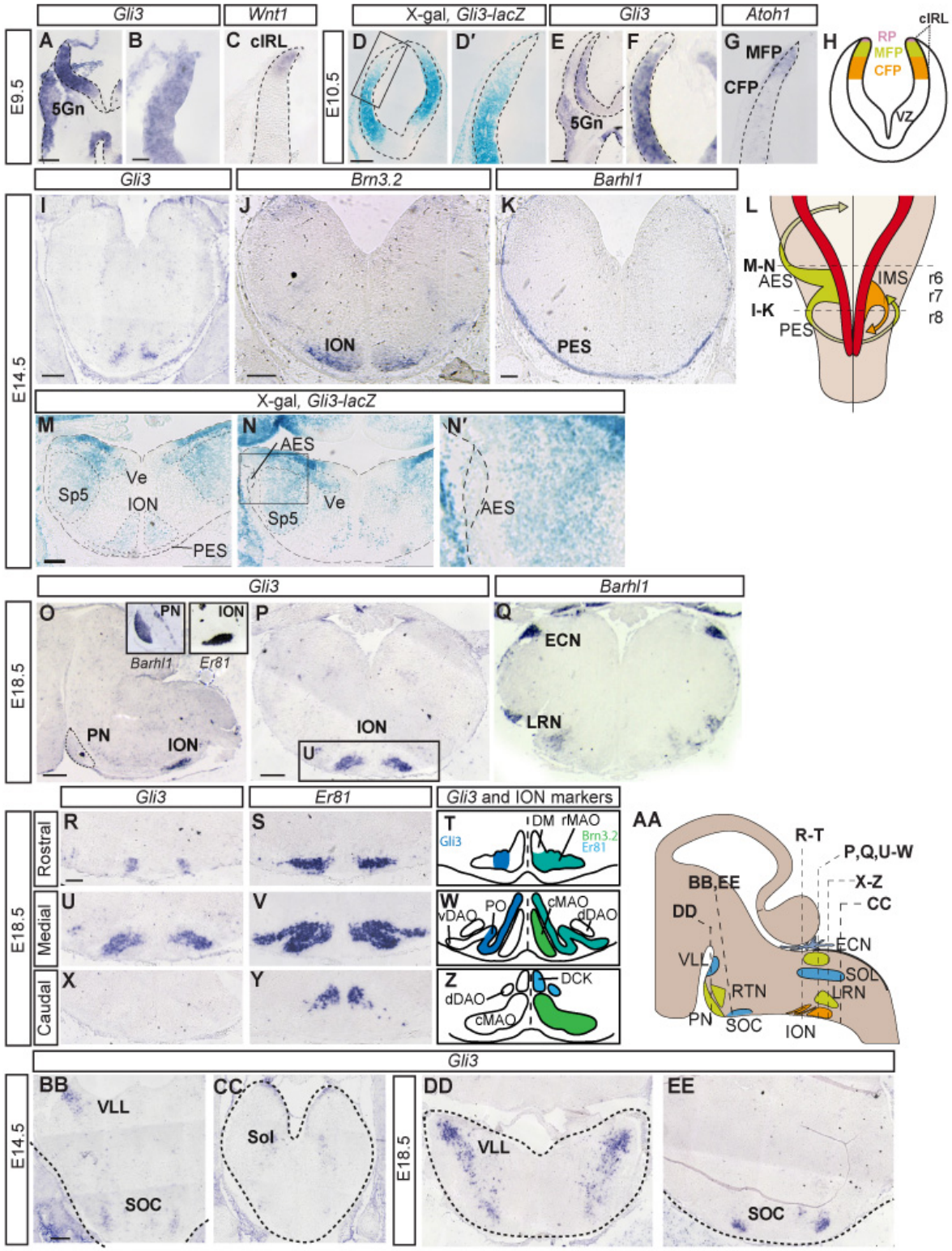

Figure 5. ***Gli3* expression pattern in the hindbrain. (A-C)** RNA *in situ* hybridization for *Gli3* and *Wnt1* in E9.5 horizontal sections. *Gli3* is expressed throughout the dorsal hindbrain including the *Wnt1*-expressing caudal rhombic lib (clRL). *Gli3* is also expressed in the forming trigeminal ganglia (5Gn). n=2 embryos. **(D-H)** X-gal staining in sections from *Gli3*$^{lacZ/+}$ embryos and *in situ* hybridization for *Gli3* and *Atoh1* at E10.5. *Gli3* is no longer expressed in the roof plate (RP) or MF progenitor domain (MFP) but is maintained in the CF progenitor domain (CFP), and 5Gn. (D′) Higher magnification of the boxed area in D. (H) Schematic of the anterior hindbrain at E10.5. VZ: ventricular zone. n=3 embryos for *in situ* analysis, n=2 embryos for X-gal analysis. (Figure legend continues on the following page).

Figure 5. (I-K) *In situ* hybridization for *Gli3, Brn3.2* and *Barhl1* at E14.5; n=3 embryos. *Gli3* is expressed in a subdomain of the forming ION, but it is not expressed in the PES at E14.5. Anteroposterior level of sections is indicated in (L). **(L)** Schematic depicting the precerebellar migratory streams. **(M,N)** X-gal staining in sections from E14.5 *Gli3*$^{lacZ/+}$ embryos showing expression of the reporter in the spinal trigeminal nucleus (Sp5) and ION. The AES is lacZ negative. (N′) Higher magnification of the boxed area in N. Anteroposterior level of sections is indicated in (L). n=1 embryo. **(O-Z)** *In situ* hybridization for *Gli3, Er81* and *Barhl1* at E18.5. At E18.5, *Gli3* is expressed in an *Er81*-positive ION subdomain in that corresponds to the principal olivary nucleus (PO) and part of the rostral medial accessory olive (rMAO). The MF nuclei (ECN, LRN, PN) are *Gli3*-negative. (U) Higher magnification of the boxed area in P. Schematics for each AP level and with the expression pattern of markers delineating the ION (*Er81* and *Brn3.2*) are provided for better visualization (T, W, Z). Anteroposterior level of sections is indicated in (AA). (BB-EE) *In situ* hybridization for *Gli3* on coronal sections at E14.5 and E18.5 show expression of *Gli3* in non-precerebellar nuclei including the ventral lateral lemniscus (VLL), superior olivary complex (SOC), and solitary nucleus (SOL). n=3 embryos. (AA) Schematic depicting the precerebellar nuclei and *Gli3*-expressing nuclei (blue). DCK: dorsal cap of Kooy; cMAO: caudal medial accessory olive; vDAO ventral accessory olive; dDAO: dorsal accessory olive. Scale bars: 50 µm (A,E); 100 µm (B, C, D´, F, G); 200 µm (I-EE).

4.2. Phenotype of the precerebellar system in absence of *Gli3*

To study the role of GLI3 in the hindbrain, *Gli3*$^{xt/xt}$ mutants were analyzed. As described in the introduction, *Gli3*$^{xt/xt}$ mutants have a deletion of 51.5 Kb including most of the zinc finger coding domain and the complete 3´region of the *Gli3* gene that generates a nonfunctional protein (Maynard et al, 2002). These mutants die at birth and thus, the latest time point that could be analyzed was E18.5. Previous studies from Arellano in E14.5 and E18.5 *Gli3*$^{xt/xt}$ hindbrains suggested that GLI3 plays a major role in the development of the precerebellar system (Arellano, 2011). Arellano described that the PN/RTN is not properly formed and that several MFNs settle ectopically at the ventral midline along the anterior-posterior axis of the hindbrain. In addition, she described a broader PES with neurons located at the midline, a not well defined LRN and ECN, and an overall size reduction and cell disorganization of the ION (Arellano, 2011). Based on these initial findings, the developmental mechanisms that underlie the phenotype in *Gli3*$^{xt/xt}$ mutants were investigated to dissect the role of GLI3 in hindbrain development. In the current study, an initial overview of the phenotype was generated at E18.5, a stage when the migration of all precerebellar neurons is completed (Bloch-Gallego et al, 2005; Ray and Dymecki, 2009; Sotelo and Chedotal, 2013). The distribution of the precerebellar MFNs was analyzed by means of a genetic fate mapping approach in an *Atoh1-Cre* reporter mouse line that allowed the visualization of the entire *Atoh1*-derived lineage. An additional marker was the transcription factor BARHL1, which is downstream of ATOH1 (Saba et al., 2003, 2005; Kawauchi and Saito, 2008; Klisch et al., 2011; Lai et al., 2011) and is present in a subset of *Atoh1*-derived neurons, including the precerebellar MFNs (Figure 6 and 7). The analysis confirmed the distribution of ectopically positioned MFN (eMFN) along the AP axis of the hindbrain (Figure 6B and P). Most of these ectopic neurons were positioned at the ventral midline of the hindbrain and formed ectopic

nuclei (Figure 6B, F, N, and P), while others were still present in the migratory stream (Figure 6F, J, N, and P). An analysis of the neurons remaining in the migratory streams at this time point showed that MFNs were positioned at all axial levels in continuous and undefined streams (Figure 6F, J, N, and arrowheads in P). At posterior levels, the ectopic *Barhl1*-expressing cells appeared to be partially located in an extramural position, suggesting that these were remnants of the PES (Figure 6J and N, compare Figure 15C). Most of the cells accumulated at the basal plate and formed a protuberant ectopic nucleus that spanned the midline and localized ventral to the ION (Figure 6B and N). A small group of these cells delaminated into the tissue between the two bilateral halves of the ION (Figure 6N arrowhead). At the alar plate, a superficial layer of cells localized at the pia, while others tended to delaminate towards the mantle zone at the level of the ECN and LRN, and also between these nuclei (Figure 6H, J, and N). The cells delaminating between the ECN and LRN may be part of a minor group of precerebellar neurons that derive from the clRL and travel as part of the PES to the contralateral side and delaminate into the superficial mantle of the Sp5i and Sp5c around E15.5 (Okada, et al, 2007).

To dissect the LRN and ECN nuclei in these posterior cell populations in the mutant brains, expression of *Er81,* which is present in the ECN (as determined in this thesis), was analyzed. Thus, it was possible to discern the ECN from LRN and Sp5 neurons (Figure 6G, I, K, M). The results indicated that part of the ECN cells did not reach their final position at E18.5, but instead either delaminated at ectopic positions or stayed in extramural positions (Figure 6I and M). No *Er81*+ neurons were found at the midline, suggesting that the ECN neurons reached at least the alar plate. At anterior levels (r4-r6), remnants of the *Barhl1*-expressing AES were observed in some controls (Figure 6C and E). In the $Gli3^{xt/xt}$ mutant, the putative AES persisted either as continuous or non-continuous clusters of extramurally distributed cells (Figure 6F). *Barhl1*-expressing cells did not appear to cross the ventral midline, forming two clusters on the contralateral side of the ventral midbrain (Figure 6F). Interestingly, the cells composing these nuclei remained separated from those in the contralateral hemisphere and had a morphology that strongly resembled that of the PN/RTN (Fig 6C-F). The localization of these cells on both sides of the ventral midline was distinct from ectopic MFNs (eMFNs) located at posterior levels, which formed protuberant cell clusters spanning the midline.

The ION was identified by means of Forkhead-Box-Protein P2 (FOXP2) immunostaining and *Er81* RNA *in situ* hybridization (Figure 6Q, S, U, and W; Hashimoto et al, 2012; Gray, 2013). The ION was reduced in size, and completely absent in r7 (Figure 6R and V). As a consequence, the general morphology of the ION was lost and several subnuclear compartments were abnormally distributed (Figure 6T and X).

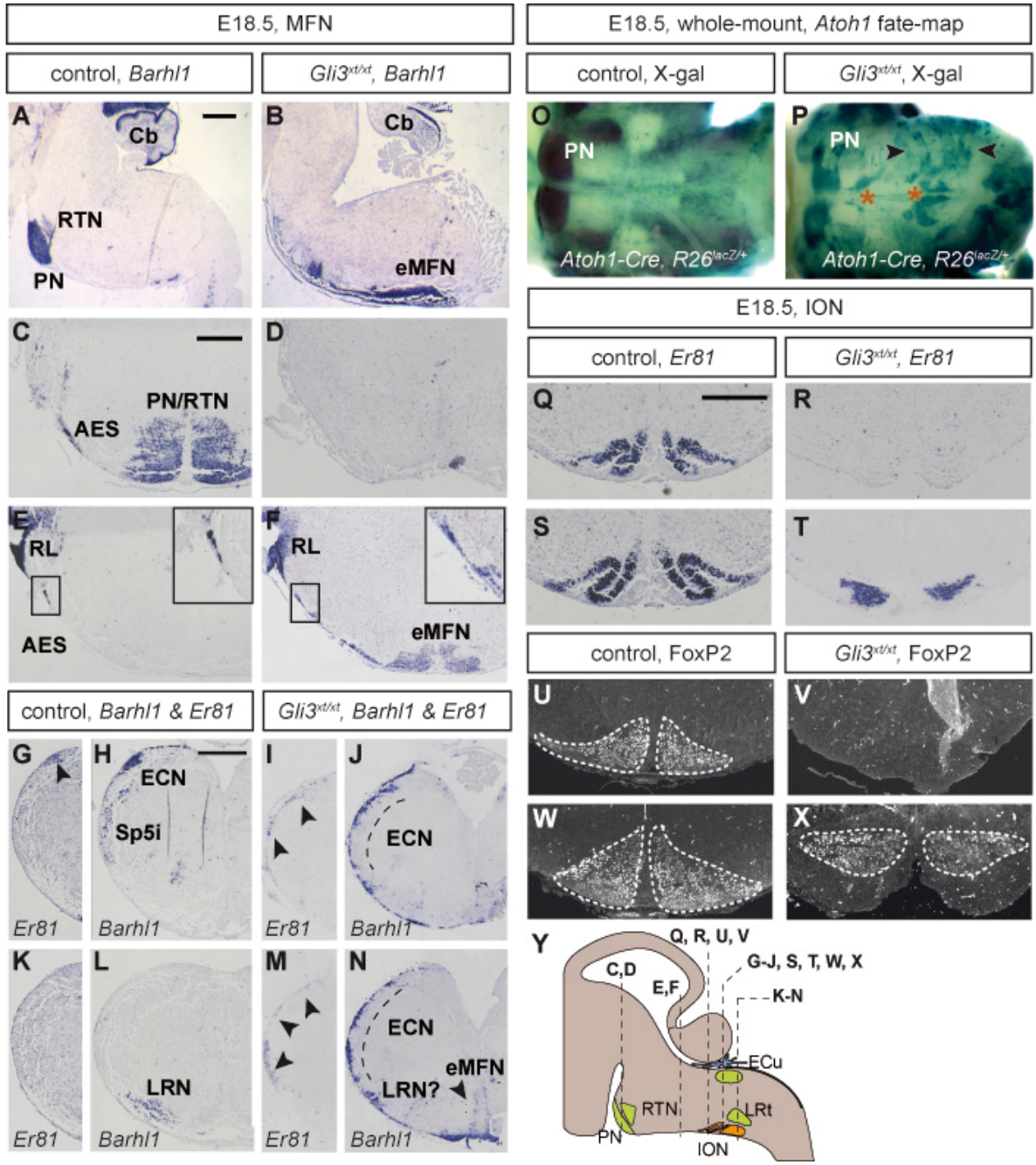

Figure 6. Precerebellar phenotype of the *Gli3*$^{xt/xt}$ mice at E18.5. (A-F) *In situ* hybridization for the MFN marker *Barhl1*. In *Gli3*$^{Xt/Xt}$ brains, the PN/RTN do not form a nucleus at r4 and instead are dispersed along the ventral midline of r3-r8 (A-B, midline sagittal sections). These ectopic MFNs (eMFNs) tend to form clusters that resemble the normal morphology of the PN/RTN (C and F). **(G-N)** *In situ* hybridization for *Barhl1* and *Er81*. *Barhl1*- and *Er81*-double-positive cells constitute the ECN in controls but are spread out extramurally in the *Gli3*$^{Xt/Xt}$ mutant (arrowheads in I and M, and dotted line in J and N). In additon, the Sp5i and LRN are not identifiable and clusters of eMFNs locate at the midline. Number of embryos analyzed: 9 controls, 5 mutants (A. B); 20 controls, 15 mutants for *Barhl1*, 5 controls, 3 mutants for *Er81* (C-N). **(O-P)** Ventral view of *Atoh1-Cre, R26-reporter* whole mounted brains stained for X-Gal showing the distribution of the *Atoh1*-lineage in control and *Gli3*$^{xt/xt}$ mutants. The PN is partially formed in the *Gli3*$^{xt/xt}$ mutant. Notice the massive migrations towards the midline (arrowheads) and the cluster of eMFNs at the midline (red asterisks) (P). Figure legend contineus on the following page.

Figure 6. (Q-X) Coronal sections of the ION at r7 (Q, R, U, V) and r8 (S, T, W, X) hybridized for *Er81* or stained for FOXP2. The ION is absent from r7 and has a size reduction and altered morphology at r8 in the *Gli3*$^{xt/xt}$. **(GG)** Diagram showing the axial level of the different coronal sections. N≥3 for each marker and genotype analyzed. Scale bar: 400 μm.

4.3. The precerebellar MF nuclei, but not the CF nuclei, have a variable phenotype in *Gli3*$^{xt/xt}$ mutants at E18.5

An interesting point of the *Gli3*$^{xt/xt}$ phenotype at E18.5 was that although the alterations observed in the ION were consistent between mutants, the MFN phenotype showed variations regarding the distribution and the size of the nuclei they formed. In most of the cases (n=11/20), the eMFNs generated a continuous nucleus that started either at r4 or at r5 and extended until the most posterior rhombomeres (r7-r8; Figure 6B). In these cases, the size of the nucleus varied from anterior to posterior, being smaller at anterior levels and bigger posteriorly. More than a quarter of the brains (n=7/20) had eMFN clusters of variable size at both the PN/RTN and/or ION level, with sporadic isolated cell clusters distributed along the AP axis (Figure 7B-D). Finally, in a small number of animals (n=2/20), all eMFNs concentrated at the most posterior rhombomeres (r6 - r8; Figure 7N). Importantly, even though a big level of variation existed between the size and position of the eMFN clusters, they remained in all cases separated at the midline, vaguely resembling the PN/RTN in control animals (Figure 6C, Figure 7F-H, J-L). In addition to these variations, isolated eMFN cell clusters were frequently detected further away from the midline, lateral to the AES at r4-r6 (n=17/20) (Figure 7F-H, arrowheads), or cells that had delaminated into the tissue on both sides of the ventral midline at r7-r8 (n=18/20) (Figure 7J-L, arrowheads).

4.4. Identity of ectopic MFN clusters in *Gli3*$^{xt/xt}$ mutants

To investigate whether the *Barhl1*-positive cells located along the ventral midline of r4-r8 were PN/RTN neurons or a mixture of all MFNs, the expression of *Barhl1*, *Barhl2*, *Brn3.2* (Brain-specific homeobox/POU domain protein 3B) and *Lhx2 (LIM Homeobox Protein 2)* was analyzed (Figure 8). *Barhl2*, *Brn3.2,* and *Lhx2* are expressed in PN/RTN neurons but not in ECN/LRN neurons at E18.5. *Barhl2* is mainly expressed by the anterior two thirds of the PN and is absent from the RTN (Figure 8A3), *Lhx2* is expressed by the anterior third of the PN and RTN (Figure 8A4), and *Brn3.2* is expressed in the PN and RTN (although weakly) (Figure 8A5), In E18.5 *Gli3*$^{xt/xt}$ mutant embryos, the eMFNs expressed a mixture of these three transcription factors in a disorganized fashion. Neurons anterior to r6 were mainly positive for *Barhl1* and *Lhx2*+ with weak *Barhl2* and *Brn3.2* expression and thus, may represent neurons with RTN characteristics (Figure 8B1-B5). eMFNs located at r6-r8 were *Barhl1, Barhl2, Lhx2, and Brn3.2* positive (Figure 8D1-D5). Interestingly, the neurons that delaminated into the mantle zone on both sides of the midline at r7-r8 (arrowheads in figure

8D1-D5) were *Barhl2* and *Lhx2* negative, suggesting that they are not PN/RTN but rather PES-derived cells. In conclusion, these experiments show that the PN/RTN neurons colonize ectopic positions in *Gli3*$^{xt/xt}$ mutants, partially settling in regions where PES-derived neurons are localized. PES-derived neurons accumulate at ectopic positions at the ventral midline or in extramural locations but stay restricted to r6-8.

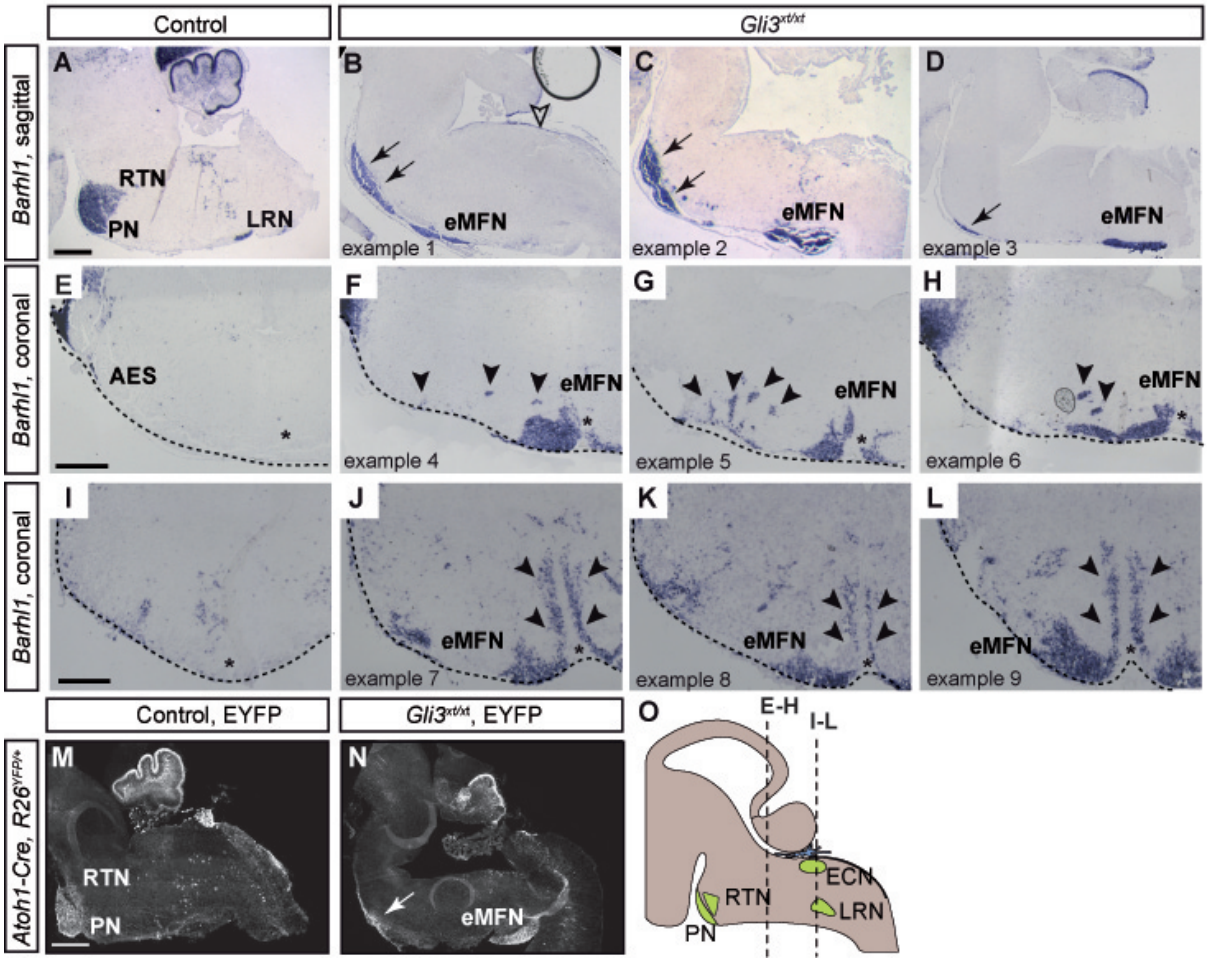

Figure 7. MFN phenotype variability in *Gli3*$^{xt/xt}$ mutants at E18.5. (A-H) Midline sagittal (A-D) and coronal (E-H) sections of control and *Gli3*$^{xt/xt}$ mutant hindbrains hybridized for *Barhl1.* In some *Gli3*$^{xt/xt}$ mutants, the PN and RTN are partially formed at their normal position in r4 (B-D, arrows). Several MFNs are in ectopic positions (eMFNs) along the ventral midline (asterisks) of the hindbrain (r5-6; E-F and r7-8; I-L). These clusters remain separated at ventral midline and resemble the morphology of the PN/RTN. Note the presence of small, more laterally located *Barhl1*-positive cell clusters at r5-6 (arrowheads in E-F) that suggest ectopic cell delamination from the AES in *Gli3* $^{xt/xt}$ hindbrains. Also, note the presence of cell delamination at the ventral midline of r7-8 (arrowheads in I-L). **(M-N)** Immunostaining for GFP in sagittal sections of E18.5 *Atoh1-Cre; R26*$^{EYFP/+}$ brains. Neurons derived from *Atoh1*-expressing rhombic lip cells settle ectopically in *Gli3*$^{xt/xt}$ mutants. Arrow indicates remnants of the PN/RTN. (O) Schematic of the embryonic hindbrain. Level of sections in E-L are indicated. Scale bar: 400 μm.

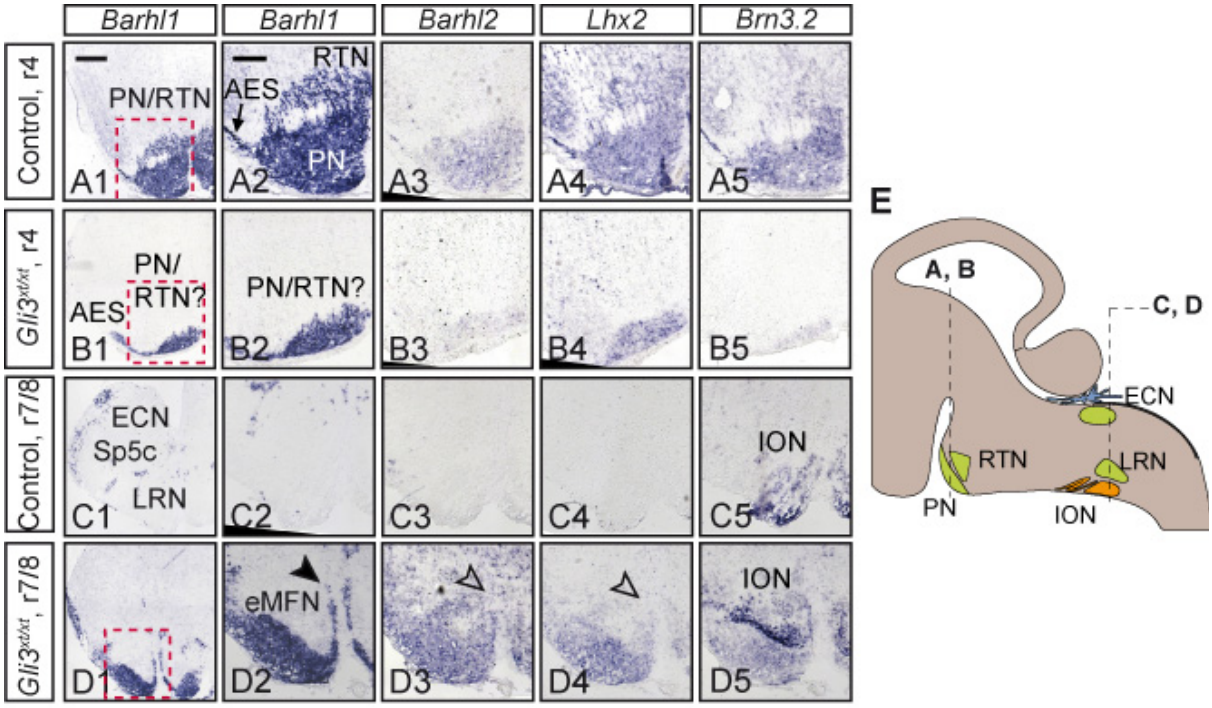

Figure 8. Cell populations composing the eMFNs in *Gli3* $^{xt/xt}$ mutants at E18.5. Adjacent coronal sections of control and *Gli3*$^{xt/xt}$ hindbrains at E18.5 hybridized for *Barhl1*, *Barhl2*, *Lhx2*, and *Brn3.2*. **(A-B)** r4 sections show that in the control, the PN expresses *Barhl2*, *Lhx2* and *Brn3.2*, and the RTN only *Lhx2* and parts of it *Brn3.2* (A1-A5). In the *Gli3* $^{xt/xt}$ mutant, the MFNs reaching this axial level express *Lhx2*, but have only a residual *Barhl2* and *Brn3.2* expression that suggests an RTN phenotype. **(C-D)** r7-r8 sections show that compared that most of the ectopic MFN (eMFNs) located at the midline of the *Gli* $^{xt/xt}$ mutant are *Barhl2*+/*Lhx2*+/*Brn3.2*+ (PN cells), but that some of them located between the two bilateral halves of the ION are *Barhl2*- and *Lhx2*- (PES neurons) (arrowheads in D2-D4). Filled arrowheads represent the presence of signal and empty arrowheads lack of signal. N≥3 for each marker, stage, and condition analyzed. Scale bars: 400 μm (A1, B1, C1, and D1); 200 μm (A2-D8).

4.5. Connections of precerebellar neurons to the cerebellum in *Gli3*$^{xt/xt}$ mutants

As described in the introduction, MFNs project to the deep cerebellar nuclei, granule cells, and Golgi cells, whereas CFNs project to Purkinje cells. The abnormal distribution of MFNs and CFNs observed in *Gli3*$^{xt/xt}$ mutant may have a direct impact on their ability to establish projections to the cerebellum. To investigate whether the neurons in the altered precerebellar system of *Gli3*$^{xt/xt}$ mutant were still able to establish connections with the cerebellum, retrograde axonal tracing using the lipophilic dye DiI (1, 1´ - Dioctadecyl-3, 3, 3´, 3´-tetramethylindocarbocyanine) was performed. In controls, DiI crystal placement on one cerebellar hemisphere resulted in the expected labeling of the contralateral PN and ION, and only weak labeling of the ipsilateral nuclei (Figure 9A and D, ipsilateral left, contralateral right). In *Gli3*$^{xt/xt}$ mutants, only a small cluster of eMFNs at r6-r8 and a few cells of CFNs were labeled (Figure 9B and F). These results suggest that the ectopic location of precerebellar neurons in *Gli3*$^{xt/xt}$ mutants might interfere with their ability to project to their appropriate target areas in the cerebellum. Alternatively or in addition, the aberrant development of the

cerebellum in *Gli3*$^{xt/xt}$ mutants (see introduction, Blaess et al. 2008) might hamper the formation of precerebellar-cerebellar connections.

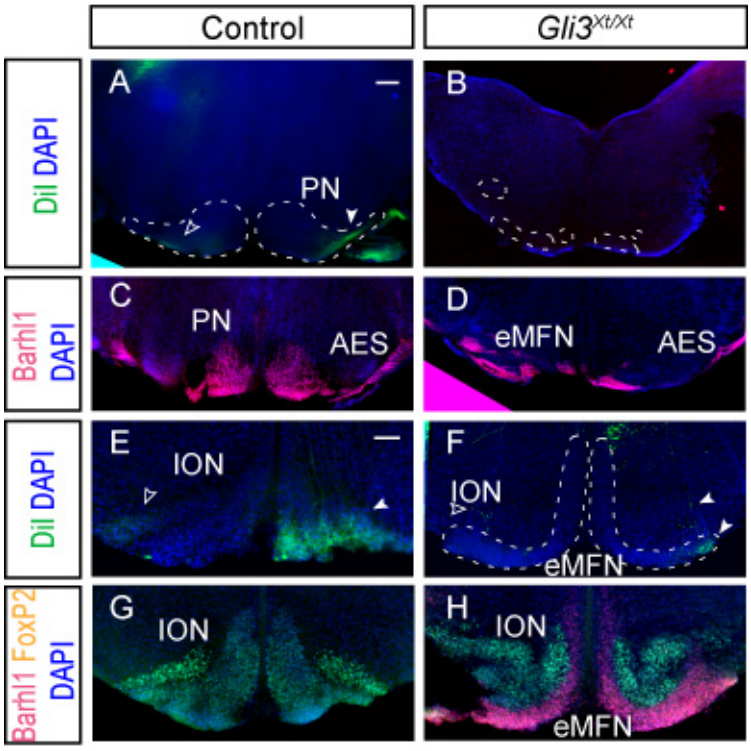

Figure 9. Hemicerebellar DiI injection and retrograde labeling of precerebellar nuclei on E18.5 control and *Gli3*$^{xt/xt}$ hindbrains. In the DiI crystal placement in the cerebellum results on strong labeling of the contralateral pontine nucleus (PN) (A) and inferior olivary nucleus (ION) (E) (filled arrowheads) in control animals. Weak labeling, corresponding to some labeled neurons and projections from the contralateral nuclei, is also seen ipsilaterally (empty arrowheads). The left side of each image corresponds to the side of DiI injection. Scale bar: 200 μm (A-D), 100 μm (E-H).

4.6. GLI3 does not play a role in patterning the clRL progenitor domains

The phenotype found in the precerebellar system of the *Gli3*$^{xt/xt}$ mutant could be explained by alterations in cell patterning, cell-fate miss-specification and/or migration. All these possibilities were examined in this doctoral thesis and the results are described below. To evaluate if the precerebellar phenotype can be explained by the established function of GLI3 as a regulator of early patterning events in the dorsal neural tube, transcription factors defining the progenitor domains in the clRL were analyzed in control and *Gli3*$^{xt/xt}$ mutants at E10.5; a time point when the progenitor domains are already established (Figure 10). Different AP levels of the clRL were analyzed and the area spanned by the transcription factors defining specific progenitor domains of the class A progenitors was quantified (Figure 10A-W). This analysis indicated that the progenitor domains changed in size along the AP axis in both control and *Gli3*$^{xt/xt}$ mutants: *Wnt1*, *Olig3*, *Lmx1a*, *Atoh1,* and NGN1 were, in general, bigger at more anterior levels, *Ptf1a* and *Ascl1* were bigger at more posterior levels. However, no alteration in the size of the progenitor domains existed between controls and

Gli3$^{xt/xt}$ mutants. The only difference occurred in the most posterior areas in the progenitor domain positive for *Ptf1a*, where a decrease in the size of the domain was observed in *Gli3*$^{xt/xt}$ mutants compared to controls (Figure 10V). To examine whether the proliferative state of the progenitor domains (*Atoh1* and NGN1) might be affected in the absence of *Gli3*, proliferating cells were labeled using Bromodesoxyuridin (BrdU) injections given 1 hour before dissection of E10.5 embryos (Figure 10X). No difference in the number of BrdU positive cells per area between control and mutant was detected. In conclusion, the establishment of the progenitor domains composing the clRL does not seem to be strongly affected in the *Gli3*$^{xt/xt}$ mutant.

4.7. GLI3 in neuronal differentiation and cell migration

Based on the analysis of progenitor domains, GLI3 does not play an obvious role in the establishment of the precerebellar progenitor domains. Some studies indicate a role of GLI3 in neuronal differentiation (Nguyen et al., 2005; Wang et al., 2011, 2014). To address this issue in the development of the precerebellar system, several transcription factors necessary for the differentiation of the different precerebellar neurons were studied at different stages of development in control and *Gli3*$^{xt/xt}$ mutants. This analysis allowed two things: 1) To monitor changes in cell fate specification of the different precerebellar populations, 2) to track down their migratory pathway over time. The results are now presented starting with the CFN followed by the MFN.

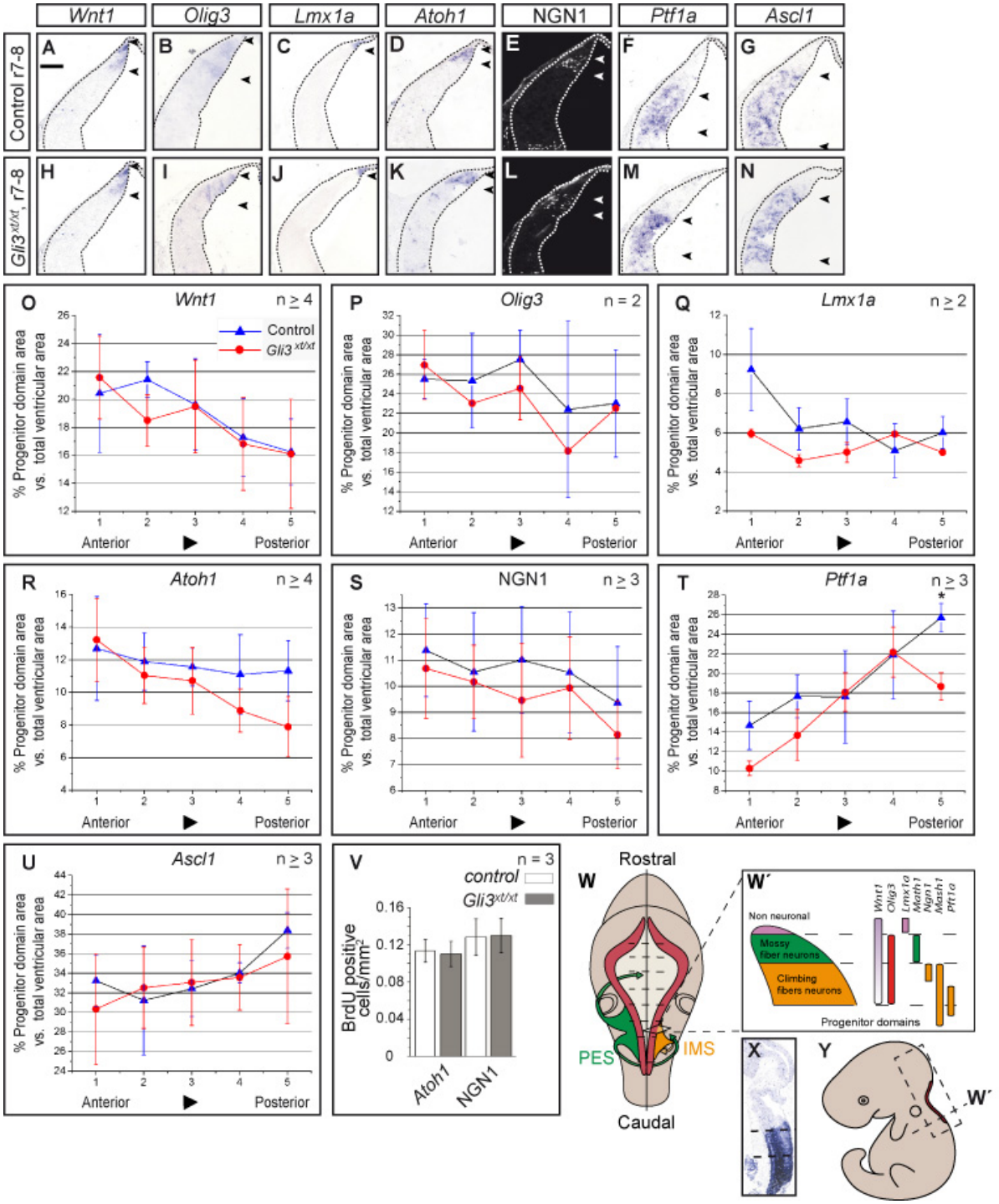

Figure 10. MF and CF progenitor domains are not altered in *Gli3*$^{xt/xt}$ mutants. (A-N) *In situ* hybridization or immunostaining in clRL representative horizontal sections at r7 (level 4 in quantification) for diverse markers influencing the establishment of the clRL progenitor domains. *Wnt1* (A, H) and its downstream target *Olig3* (B, I) are normally expressed. An unchanged expression of *Lmx1a* suggests a normal establishment of the roof plate (C, J) whereas that of *Atoh1*, NGN1 (protein), *Ptf1a* and *Ascl1* suggest a normal establishment of the precerebellar progenitor domains (D-G, K-N). **(O-U)** Area quantification of all the clRL markers relative to the whole ventricular area at r6 (level 1 and 2), r7 (level 3 and 4) and r8 (level 5) showing that the progenitor domains change relative to their AP axial level. No significative changes were observed in any of them, except in r8 for *Ptf1a* (T). Significance was assessed using a Kruskal-Wallis test in samples with an n ≥ 3. Note that statistical significance was not assessed in case of *Olig3* and *Lmx1a* because of low sample size. Values are represented as mean ± SD. Figure legend continues on the following page.

Figure 10. (V) Quantification of BrdU-positive cells (1-hour BrdU pulse) within the *Atoh1* and NGN1 domain at r7 shows no significant difference between the control and mutant conditions (Student´s t-test). Values are represented as mean ± SD. **(W)** Schematic of a dorsal hindbrain showing the precerebellar populations arising from the clRL and the markers analyzed (W´). **(X)** *In situ* hybridization for *Hoxb4* on an E10.5 sagittal section showing the area analyzed. **(Y)** Schematic of a whole embryo sagittal section showing the area analyzed. Scale bar = 50 μm.

4.7.1. GLI3 plays a role in the generation of CFNs

The CFNs are characterized by the expression of transcription factors like *Foxp2*, present in all ION neurons (Gray, 2013), and *Brn3.2* and *Er81*, which define ION populations that are partially complementary and partially overlapping (Xiang et al, 1996; Hashimoto et al, 2011). Using these transcription factors, different CFN populations were identified and monitored throughout their migration in the IMS and up to the establishment of the ION (Figure 11). The approach allowed several novel observations in control animals and the identification of alterations in specific cell populations and neuronal migration in *Gli3*$^{xt/xt}$ mutants. As described in the introduction, the CFNs are generated between E9-E11 and migrate between E10.5 and E15. An analysis of the *Brn3.2* and *Er81* cell populations at E12.5 confirmed the presence of the IMS in all controls (Figure 11A1 and B1), but indicated that the IMS was just starting to form in *Gli3*$^{xt/xt}$ mutants (Figure 11C1 and D1). In controls, the IMS consisted of three populations. The first one consisted of *Er81+/Brn3.2-* cells that were at the ventral tip of the stream at E12.5 and that were at the midline at E13.5 (compare Figure 11A1 and B1 with Figure 11A2 and B2). Just dorsal to these cells, a second population consisting of *Er81+/Brn3.2+* neurons was present in the stream at E12.5 (Figure 11A1 and B1) and E13.5 (Figure 11A2 and B2) and were found at the midline at E14.5 (Figure 11A3 and B3). Finally, a third population of *Er81-/Brn3.2+* cells was observed close to the rhombic lip at E12.5 and E13.5 (Figure 11A1 and A2). These cells reached the midline at E14.5 (Figure 11A3). The data suggests that the three populations identified in the IMS maintained their organization during migration. Once the cells reached the midline, their distribution rearranged to form the different subnuclei composing the ION at E15.5 and E16.5 (Figure 11A4-A5 and B4-B5; Xiang et al, 1996; Hashimoto et al, 2011).

In *Gli3*$^{xt/xt}$ mutants, only two distinct populations could be identified in the IMS based on their gene expression. These were an *Er81+/Brn3.2+* at the tip of the IMS (Figure 11C2 and D2) that reached the midline at E14.5 (Figure 11C3 and D3) and *Er81-/Brn3.2+* neurons that reached the midline only between E15.5 or E16.5 (Figure 11C2-C5). Although the start and end point of IMS cell migration was different in *Gli3*$^{xt/xt}$ mutants, the cells started to rearrange to form a mature ION at E15.5 (Figure 11C4 and D4). To quantify the differences in ION populations between controls and *Gli3*$^{xt/xt}$ mutants, the area of each marker was measured at different time points and AP levels, and was normalized with the area of the overall neural tissue on the respective side of the hindbrain (Figure 11E-G). The neurons in the control

IMS/ION covered an AP area of ~ 700 μm at E13.5 (5 sections, Figure 11E) that expanded up to ~ 980 μm at E15.5 (7 sections, Figure 11G). In the mutant, the neurons occupied an area of ~ 560 μm at E13.5 (4 sections) that reached ~ 700 μm (5 sections) at E15.5 (a reduction of 28.57%). In the E13.5 control hindbrain, *Brn3.2*+ cells were mainly found at posterior levels and *Er81*+ cells were mainly at anterior levels at E13.5 (Figure 11E). By E14.5 and E15.5, the cells rearranged. Most of the *Brn3.2*+ and *Er81*+ cells concentrated medially and fewer at the lateral edges of the ION (Figure 11F and G). In *Gli3*$^{xt/xt}$ mutants, the *Brn3.2*+ and *Er81*+ cell populations were located mainly at the most posterior sections and a strong overlap existed between them at all times (both anteroposteriorly and lateromedially) (Figure 11E-G). By the end of migration (E15.5), a clear loss of the anterior ION was observed. At this stage, quantification of the total area covered by *Er81* and *Brn3.2* indicated that the area covered by *Er81*+ cells was reduced by 54% +/- standard error of the mean (SEM) and the area covered by Brn3.2+ cells by 55% +/- SEM (Figure 11H).

The strong ION size reduction could be caused by the absence of a particular CFN population (as described above), by an increase in apoptotic cell death or by a change in neuronal fate. To address the second possibility, immunostaining using an antibody for cleaved caspase-3 was performed on coronal sections of E14.5 control and *Gli3*$^{xt/xt}$ mutant embryos. In both cases, no signal was found in the ION (Figure 12B and E). This was in contrast with the strong signal of the trigeminal ganglion (5Gn) at this developmental stage, which served as positive control (Agerman et al, 2000; Figure 12C and F). To test a potential change in neuronal fate, it was analyzed whether the ION neurons, which are mostly glutamatergic, adopted this neurotransmitter phenotype. To this end, *in situ* hybridization for *vGlut2* was performed in control and *Gli3*$^{xt/xt}$ mutant embryos at E14.5 by (Figure 13; Yamada et al, 2007; Gray, 2013). The results showed no change in the proportion of *vGlut2*+ cells relative to the total size of the ION, even though a qualitative reduction in the number of *vGlut2*+ cells appeared to exist compared to the control (Figure 13H1-H5; use F1-G5 as a reference). Previous studies in the adult demonstrated a small dispersed number of GABAergic neurons in the ION (Fredette et al, 1992; Yamada et al, 2007). To test if this population was present in the *Gli3*$^{xt/xt}$ mutants, the expression of the GABAergic marker *Glutamate decarboxylase 1* (*Gad1*) was examined at E14.5. In the control, but no *Gad1* mRNA could be detected in the ION (Figure 13D1-D5), whereas in the *Gli3*$^{xt/xt}$ mutants, ectopic *Gad1*+ populations were found at levels were the ION forms in controls (Figure 13I1-I5). These results suggest that the ectopic *Gad1*+ populations were either ION neurons that had changed their fate, or that they corresponded to non-ION populations invading the area normally occupied by the ION.

Finally, an analysis of Hox gene expression in the ION, which reflects the place of cell origin and positional identity during migration and nucleogenesis (Di Meglio et al, 2013, Philippidou

and Dasen, 2013), was performed at E14.5 and E18.5 (Figure 16C5-C7, D5-D7 and 18E-J, T-AA). The analysis indicated a similar Hox gene expression in the ION of control and *Gli3*$^{xt/xt}$ embryos. Three populations existed with the AP order and relative proportion within the ION. These were 1) a *Hoxb3+/Hoxb4+/Hoxb5+* population located at the most posterior area, 2) a *Hoxb3+/Hoxb4+/Hoxb5-* population located at an intermediate AP level and 3) a *Hoxb3+/Hoxb4-/Hoxb5-* located anteriorly (Figure 16A4-A6 and B4-B6; E5-E7 and F5-F7 and not shown). The results suggest that the strong size reduction observed in the anterior levels of the ION of *Gli3*$^{xt/xt}$ mutants does not result from the loss of a specific cell population (i.e. the most anteriorly located *Hoxb3+/Hoxb4-/Hoxb5-* cells), but that it is the result of general cell loss that does not relate to a cell death event at E14.5. Moreover, they suggest that the IMS cell migration maintains its AP organization in *Gli3*$^{xt/xt}$ mutants, even in the absence of the *Er81+/Brn3.2-* population.

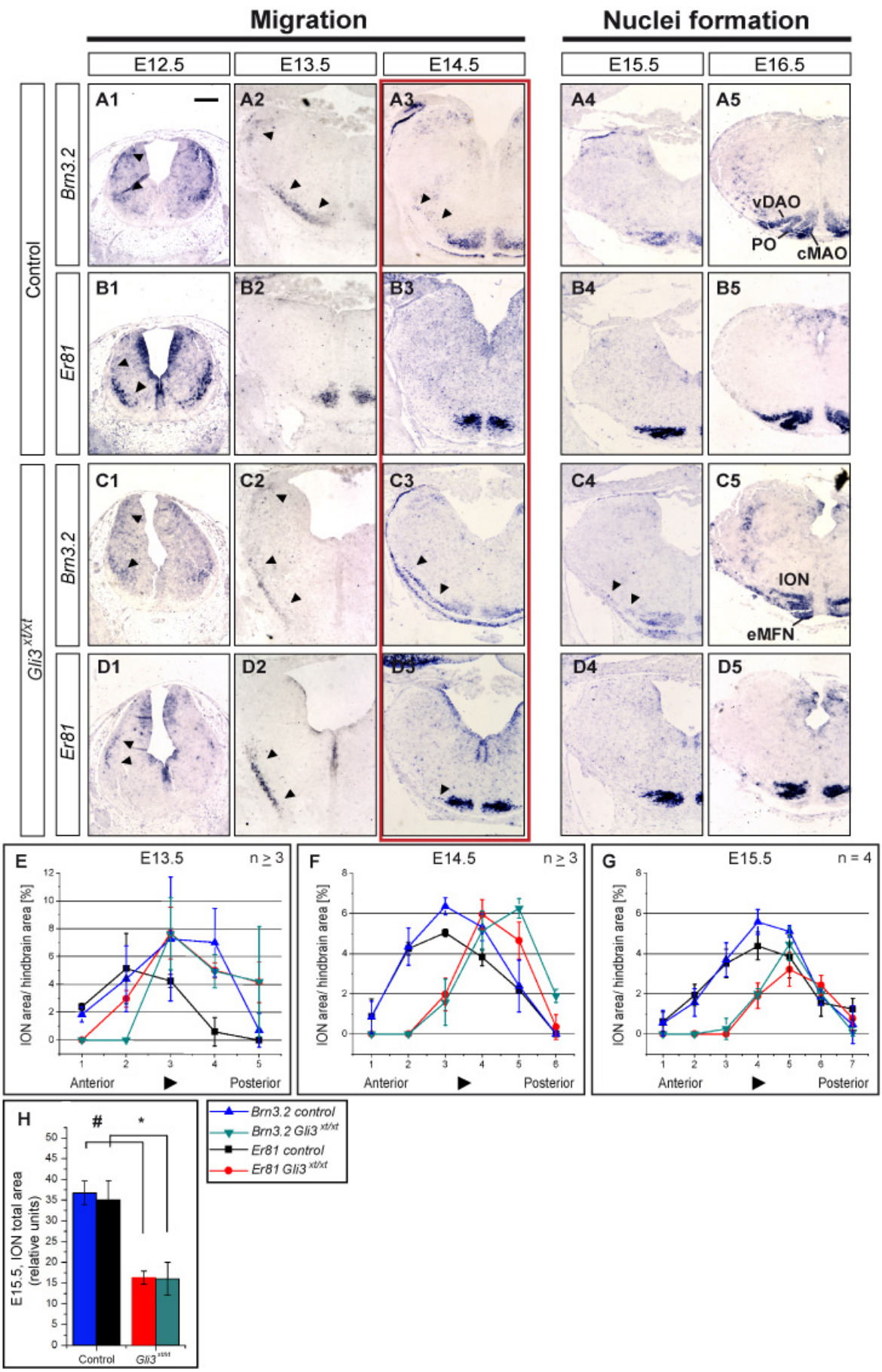

Figure 11. Figure legend continues on the following page

Figure 11. ION cell migration and nuclei formation. (A1-D5) Coronal sections of control (A1-B5) and *Gli3*$^{xt/xt}$ (C1-D5) hindbrains hybridized with *Brn3.2* andfd *Er81 in situ* probes at different time points. The arrowheads point to the cells within the IMS. Note the small number of cells within the stream at E12.5 (C1 and D1) and the persistence of the IMS until E15.5 in *Gli3*$^{xt/xt}$ mutants (C4). The images within the red rectangle relate to ION magnifications found within the red rectangle in Figure 13. **(E-G)** Quantification of the *Brn3.2* and *Er81* positive area in E13.5-E15.5 coronal sections along the AP extent of the ION. The areas were normalized to the size of the hindbrain (right or left half) for each quantified section and expressed as a percentage. Level 5 at E13.5, level 6 at E14.5 and level 7 at E15.5 represent the most posterior section analyzed. In the mutant, the ION cells are located posteriorly. **(H)** Total area quantification of the ION at E15.5. n≥3 for each marker, stage, and genotype analyzed. Scale bar: 200 μm.

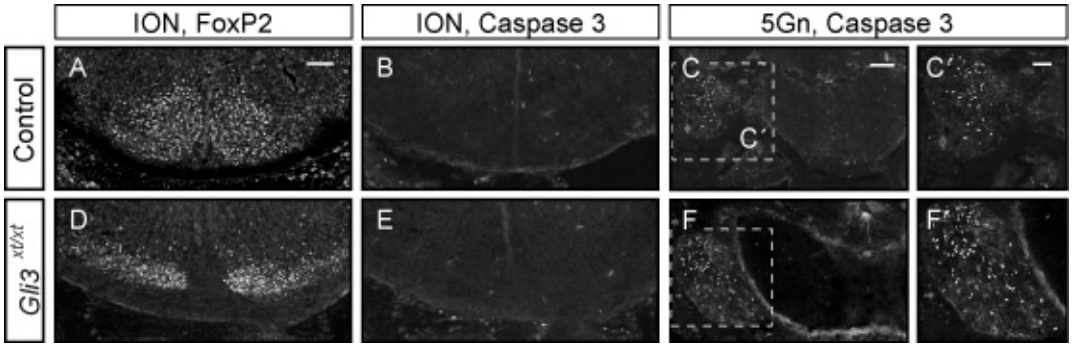

Figure 12. Analysis of apoptotic cell death in the ION at E14.5. Immunostaining for FOXP2 to visualize the ION in controls (A) and *Gli3*$^{xt/xt}$ mutants (D) and for cleaved caspase-3 to visualize apoptotic cell death in the ION (B and E) or in adjacent sections at the level of the trigeminal ganglion (5Gn; positive control) (C and F). N≥3 for each genotype analyzed. Scale bars: 100 μm (A, B, C´, D, E and F´), 200 μm (C and F).

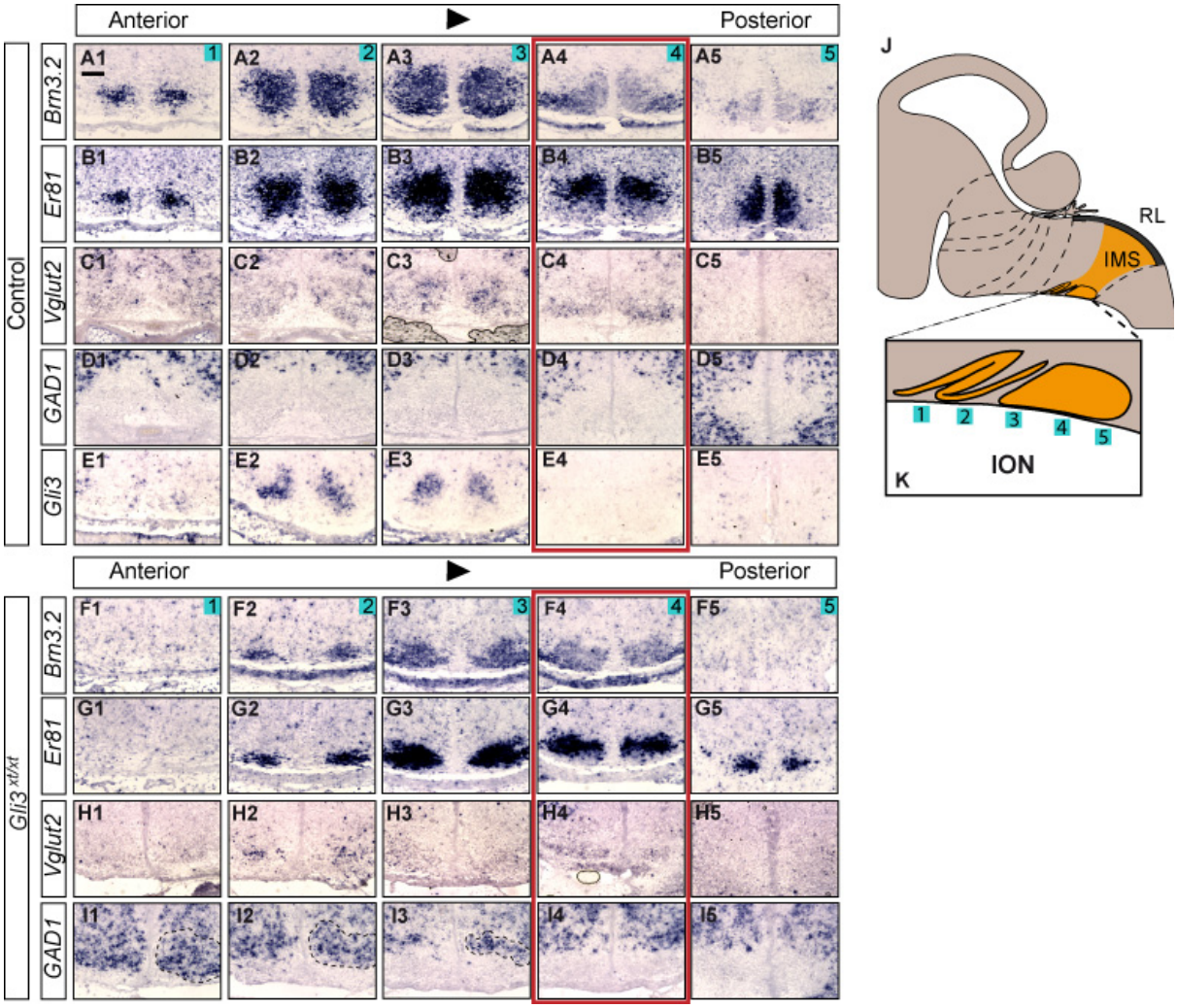

Figure 13. ION cell fate at E14.5. (A-I) Control and *Gli3*$^{xt/xt}$ coronal sections at the level of the ION hybridized with *Brn3.2, Er81, vGlut2, Gad1* and *Gli3* (only control) *in situ* probes in mutants. In the control, *Vglut2* is found in most of the ION (C1-C4), *Gad1* is absent (D4-D5), and *Gli3* is expressed in a subgroup of anterior ION cells (E1-E5). In the *Gli3*$^{xt/xt}$ mutant, *Vglut2* expression is reduced (H1-H4) and *Gad1* is expressed more anteriorly than in controls (I1-I3). Note that *Gli3* expression in the control correlates with the anterior area where the ION did not form in *Gli3*$^{xt/xt}$ mutants. **(J)** Schematic of the axial levels studied in the ION. N≥3 for each marker and condition analyzed. Notice that the images within the red rectangle are magnifications of the figures within the red rectangle in Figure 11. Scale bar: 100 μm.

4.7.2. GLI3 in the generation of early *Atoh1*-derived neuronal populations

Precerebellar MFNs are generated between E11.5 and E17, a time point when *Gli3* is no longer expressed in the *Atoh1*-expressing progenitor domain. This suggests that GLI3 does not play a cell-autonomous role in MFN differentiation or migration. Thus, the MFN alterations observed in the E18.5 *Gli3*$^{xt/xt}$ mutants are likely caused an indirect role of GLI3 in migration. Previous studies indicate that MFN migration occurs in close contact with projections of other neuronal populations (Rakic 1985; Ono and Kawamura 1990) and/or in contact with the leading processes of other migrating precerebellar neurons (Ono and Kawamura 1990; Kawauchi et al., 2006). This suggests that early-generated neurons could

serve as migrating scaffolds for MFN migration (Laumonnerie et al., 2015). Before the birth of precerebellar MFNs, a group of *Atoh1*-derived neurons arises between E9.5 and E10.5 and migrates extramurally through the „caudal rhombic lip stream“ to form part of the medial Sp5ic, the gracilis, the cuneate, the medullary reticular-dorsal, the pre-Bötzinger complex and the rostroventral respiratory group (Rose et al., 2009). All these neurons are reported to be *Barhl1* negative, but *Lhx2* and *Lhx9* positive. In addition, all these cell groups, except for the pre-Bötzinger complex and the rostroventral respiratory group are reported to be positive for *Barhl2* (Rose et al., 2009). To study if GLI3 could influence the differentiation or migration of these cell populations, *in situ* hybridizations for *Barhl1, Barhl2, Lhx2,* and *Lhx9* were done in controls and *Gli3*$^{xt/xt}$ mutants at E10.5 (Figure 14). In controls, all transcription factors were expressed at E10.5, although with different distributions. *Barhl1* was expressed by the progenitor area and by a group of differentiated neurons (Figure 14B), whereas *Barhl2*, *Lhx2,* and *Lhx9* were restricted to differentiated neurons that could also express *Barhl1* or not (Figure 14C-E). The pattern of transcription factor expression in *Gli3*$^{xt/xt}$ mutants was comparable to controls (Figure 14F-J). Moreover, fate-mapping of *Atoh1*-derived neurons in *Atoh1-Cre, R26*$^{flox\text{-}stop\text{-}flox\ EYFP}$ mice (Matei et al., 2005) showed a similar distribution of enhanced yellow fluorescent protein (EYFP)-positive cells between controls and *Gli3*$^{xt/xt}$ mutants (Figure 14A, F). Overall, these results suggest that loss of GLI3 function does not affect lineage specification or migration of early *Atoh1*-derived neurons.

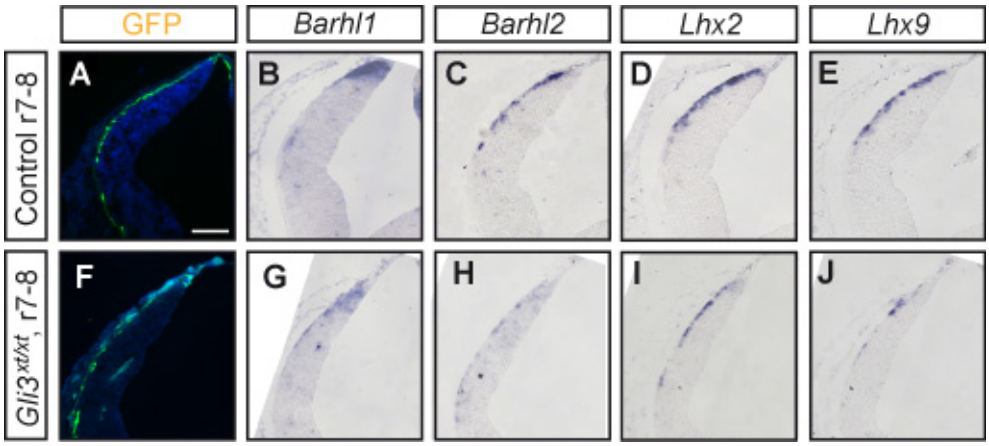

Figure 14. Early *Atoh1*-derived neuronal populations at E10.5. GFP immunolabeling of *Atoh1*-derived cells and *in situ* hybridization for *Barhl1, Barhl2, Lhx2* and *Lhx9* on horizontal sections of E10.5 *Atoh1-Cre, R26*$^{EYFP/+}$, *Gli3*$^{xt/+}$ controls and *Atoh1-Cre, R26*$^{EYFP/+}$, *Gli3*$^{xt/xt}$ mutants at r7. **(A-E)** Control sections showing *Atoh1*-derived cells (GFP-positive) with short projections that migrate extramurally (A). The progenitor domain and some of the neurons at the ventricle and pia layer are *Barhl1*-positive (B), while the neurons at the pia are mainly *Barhl2*-, *Lhx2*-, and *Lhx9*-positive (C-E). **(F-J)** Mutant sections showing a comparable cell distribution and marker expression as in controls. Number of experiments analyzed: GFP: 3 controls and 3 mutants, *Barhl1*: 8 controls and 6 mutants, *Barhl2*, *Lhx2,* and *Lhx9*: 4 controls and 4 mutants. Scale bar: 50 μm.

4.7.3. GLI3 in the generation and migration of precerebellar MFNs

In contrast to the early *Atoh1*-derived neurons, all MFNs express *Barhl1* (Li et al., 2004; Rose et al., 2009). Therefore, this transcription factor was used to study MFN differentiation and migration over time. To this end, different developmental stages were analyzed from E12.5, when the PES neurons have just been generated and begin their migration, to E18.5, when AES neuronal migration ends and most of the MFNs are arranged in nuclei. In the control, the PES started to form at E12.5 (Figure 15A). At E13.5 the neurons were already at the midline and the LRN started to form (Figure 15B). The PES ceased to exist around E14.5 - E15.5, when the ECN formed (Figure 15C and D). The AES was identified as a defined stream located at r6 in E13.5 sections. The AES persisted at the subsequent stages and up to E18.5 (Figure 15-N; Figure 7; Nichols and Bruce, 2006). In *Gli3*$^{xt/xt}$ mutants, several MFNs were first seen forming a stream at E13.5 (one day after the control) at the level where the PES would normally form (Figure 15G). At around E14.5, the cells reached the midline and started to form an ectopic nucleus below the ION and to populate the area of the presumptive LRN (Figure 15H). By E15.5, some cells were found delaminating on both sides of the ventral midline, while others started accumulating between the presumptive LRN and the area where the ECN would normally form (Figure 15I). These last cell populations showed no rearrangement at E16.5 (Figure 15J) or E18.5 (see Figure 6 and 7), suggesting that cell migration ceased between E15.5 and E16.5. The potential AES was first identified at E14.5 as small dispersed *Barhl1*+ cell clusters at r6 (Figure 10P). These cells started to reach the midline of r5-r6 at E15.5 (Figure 15Q) and to settle as nuclei at E16.5 (Figure 15R). *Barhl2*+ *in situ* hybridization at E14.5 to specifically label AES neurons confirmed that these cells were part of the AES, but also several neurons that had already started to migrate ventrally at r7-r8 (arrowheads in Figure 15 H´ and P´). These results were consistent with the eMFN distribution found at E18.5 along the whole AP axis (see Figure 8). Confirmation of the delayed onset and disorganization of the MFN migratory streams in *Gli3*$^{xt/xt}$ hindbrains was obtained by performing whole-mount immunostaining for BARHL1 at E13.5 and E16.5 (Figure 15Q-T). In controls, most of the PES neurons located at the midline at E13.5, while only a few *Barhl1*-positive neurons were seen migrating at this time point.

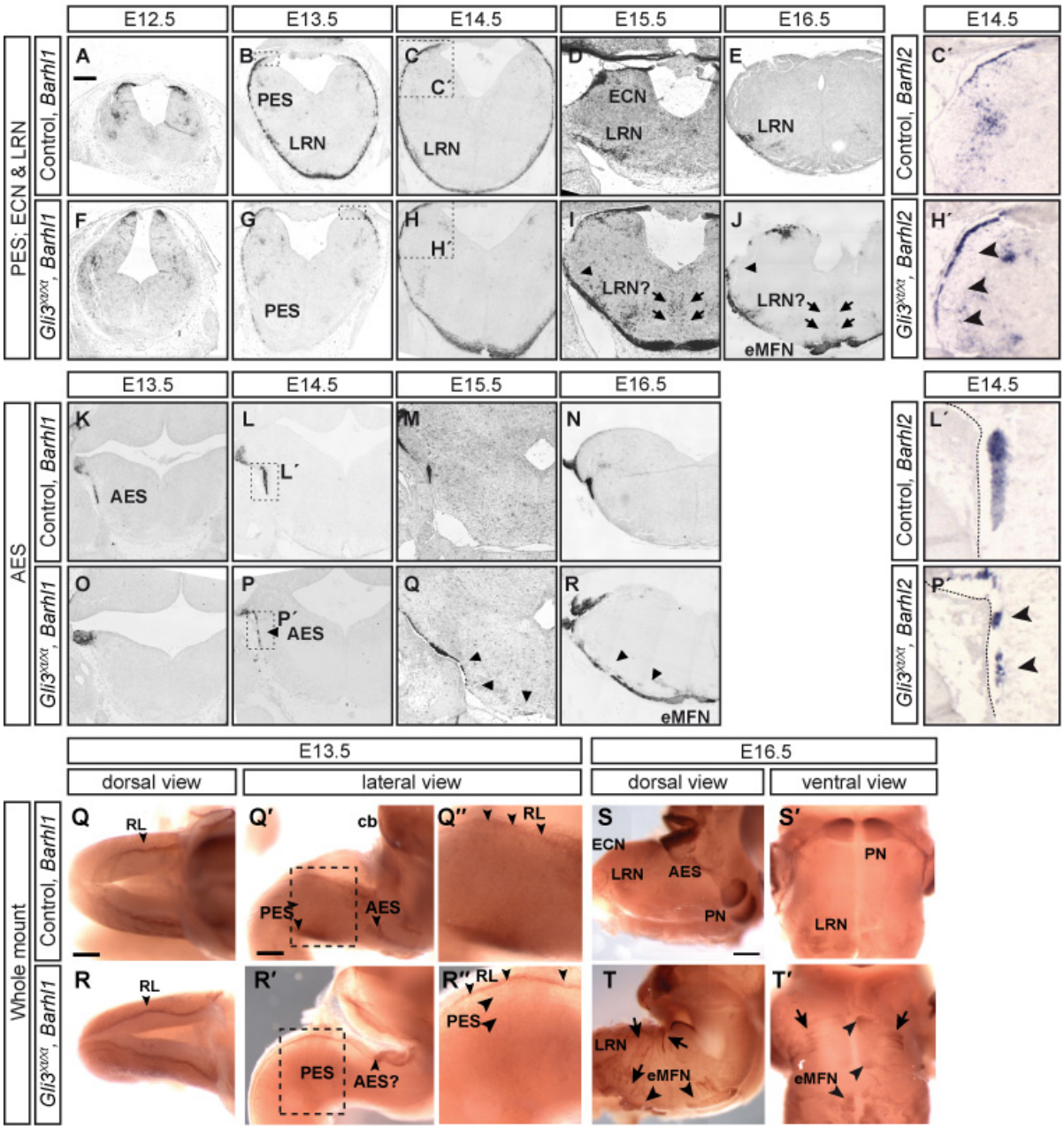

Figure 15. MFN migration and nuclei formation in the *Gli3*$^{xt/xt}$ mutant. (A-N) Coronal sections of control and *Gli3*$^{xt/xt}$ hindbrains hybridized for *Barhl1* at different time points of migration and nuclei formation. The *Gli3*$^{xt/xt}$ PES reaches the midline with a delay of one day relative to controls (A-C, F-H) and delaminate at the midline (I and J, arrows) or continue to the contralateral site (I and J, arrowheads). The AES is a compact stream that is first seen at E13.5 in controls (K). In the *Gli3*$^{xt/xt}$ mutant, the cells are dispersed and direct towards the ventral midline at r7-r8 (C´and H´, arrowheads) and r5-r6 (P-R; L´ and Q´) until establishing ectopic nuclei (eMFN) (J and R). N≥3 for each stage and condition analyzed. **(Q-T)** Whole-mount immunostaining for BARHL1 at E13.5 (Q-R) and E16.5 (S-T) showing the delayed onset and disorganization of the MFN migratory streams (arrows) and the formation of ectopic MF nuclei (arrowheads) along the anteroposterior axis in the *Gli3*$^{xt/xt}$ mutant hindbrain. Q´´and R´´ are higher magnifications of the boxed area in U´and V´. In the E13.5 the Bahrl1 immunostained cells remain concentrated at the rhombic lip (RL) and only weak staining is seen in the PES cells, consistent with the analysis in sections, in which the PES is thinner or barely present in E13.5 mutants (in G). Note that the whole mount pictures are composed of several stitched images to have the entire hindbrain in focus. Number of embryos analyzed: E13.5: 8 controls and 2 mutants, E16.5: 4 controls and 3 mutants. Scale bars: 200 μm.

4.7.4. The r7-r8 derived-AES cells fail to turn anteriorly in *Gli3$^{xt/xt}$* mutants

To investigate whether a specific subset of AES cells fail to turn anteriorly in *Gli3$^{xt/xt}$* embryos, the AES was topographically subdivided into three different subsets based on the particular *Barhl2, Lhx2, Brn3.2* (this thesis) and Hox gene expression (Figure 16; Di Meglio et al, 2013). In controls, *Barhl1* and *Hoxb3* were present in all the AES, *Barhl2* mainly in the upper two thirds, *Lhx2* only in the upper third, *Brn3.2* mainly in the lower two thirds, *Hoxb4* only in the lower two thirds and *Hoxb5* only in the lower third (Figure 16). Importantly, *Barhl2* and *Lhx2* were absent from the PES (Figure 17A1-A4, C1-C3), thus their expression pattern was also used to distinguish the AES from the PES. Moreover, as all these transcription factors were expressed during migration (Figure 17) and until nucleogenesis (Figure 19 and see Figure 8), their combined expression served to obtain precise information regarding MFN rhombomeric origin (r6-r8) and cell-type (PES or AES). Based on this approach, the different MFNs populations were delineated in *Gli3$^{xt/xt}$* mutants.

In *Gli3$^{xt/xt}$* mutants, most of the AES cells reaching r4-r6 at E14.5 were *Lhx2*+ (Figure 17B4 and Figure 18E2, F2), although some of them were also *Barhl2*+ and/or *Brn3.2*+ (Figure 16B3, B5). Consistent with this, most of these cells were *Hoxb3+/Hoxb4-/Hoxb5-* (Figure 17-B6-B8; Figure 18E3-E5 and F3-F5). In r7-r8, several *Barhl2+/Lhx2+/Brn3.2*+ (AES cells) were seen in the dorsal and medial alar plate as part of the extramural stream directing to the ventral midline, where already several *Barhl2-/Lhx2-/Brn3.2*+ cells (PES neurons) had settled (Figure 17D1-D3). Interestingly, the AES cells were *Hoxb3+/Hoxb4*+ and/or *Hoxb5*+ (Figure 17D5-D7; Figure 18G3-G5, H3-H5). The distribution of the *Barhl2*+, *Lhx2*+ and *Brn3.2*+ populations in the AES of the *Gli3$^{xt/xt}$* mutant was consistent with the final positioning of PN/RTN neurons at E18.5, as the neurons anterior to r6 were mainly *Barhl1+/Lhx2*+ and those eMFN at r6-r8 mainly *Barhl1+/Barhl2+/Lhx2+/Brn3.2*+ (see section 3.4 and Figure 19D). Moreover, Hox gene expression analysis at E18.5 indicated that the neurons in r4-6 were mainly *Hoxb3+/Hoxb4-/Hoxb5-* (Figure 19F-J, Q-S), while those in r7-r8 mainly *Hoxb3+/Hoxb4+/Hoxb5-* and *Hoxb3+/Hoxb4+/Hoxb5*+ (Figure 19F-J, Y-AA). In summary, these results suggest that the AES is split in *Gli3$^{xt/xt}$* mutants: the r6-derived part (*Hoxb3+/Lhx2*+) partially retains its ability to migrate anteriorly, while the r7-r8-derived part (*Hoxb3+/Hoxb4*+ or *Hoxb3+/Hoxb4+/Hoxb5*+) follows a direct route towards the ventral midline (Figure 19K and BB).

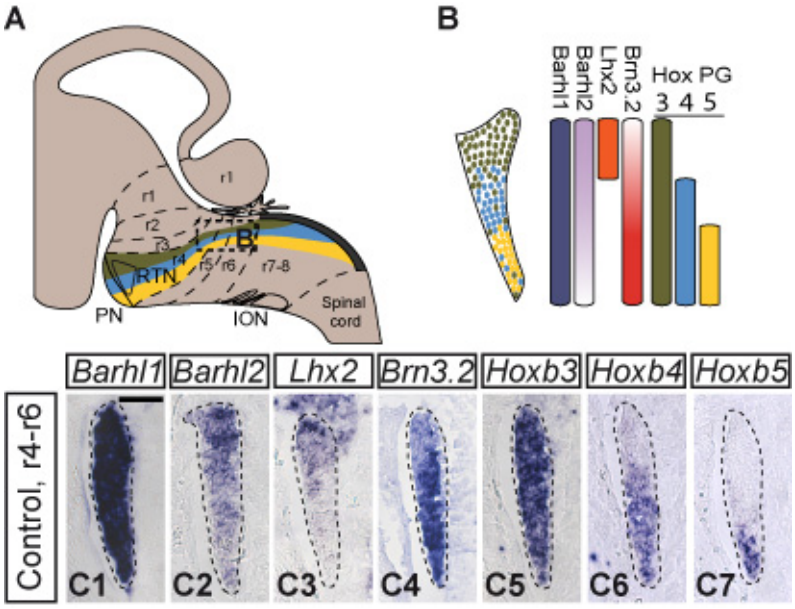

Figure 16. Cell subpopulations in the AES. A) Schematic of an E14.5 hindbrain sagittal section showing the three subpopulations of MFNs that form the anterior extramural stream AES. Each subpopulation expresses a particular HoxPG depending on their rhombomeric. (B) Magnification of the area delineated in A illustrating the expression of *Barhl1*, *Barhl2, Lhx2, Brn3.2,* and the HoxPG3 – HoxPG5 in the AES. Note that *Barhl2* is mainly expressed by the *Hoxb3+/Hoxb4+/Hoxb5-* population, *Lhx2* only in the *Hoxb3+/Hoxb4-/Hoxb5-* population and *Brn3.2* mainly in the *Hoxb3-/Hoxb4+/Hoxb5+*. **(C1-C7)** Magnifications of the AES at r4-r6 showing the expression pattern illustrated in B. Number of embryos analyzed: 5 for *Lhx2, Brn3.2,* and *Barhl2*; 8 for Hoxb3 – Hoxb5. Scale bar: 50 μm.

4.8. Guidance molecules and receptors directing precerebellar migration in the *Gli3*$^{xt/xt}$ mutant

Interfering with the function of guidance factors such as Netrin1 (NTN1), SLITs (SLIT1-3), and the chemokine CXCL12 or their respective receptors results in aberrant precerebellar neuronal migration and in phenotypes that partially resemble the ones observed in *Gli3*$^{xt/xt}$ mutants (Di Meglio et al., 2008; Dominici et al., 2018; Geisen et al., 2008; Gilthorpe et al., 2002; Kim and Ackerman, 2011; Kuwako et al., 2010; Marillat et al., 2004; Moreno-Bravo et al., 2018; Zhu et al., 2009). To test if any of these guidance systems were altered in the *Gli3*$^{xt/xt}$ mutants, an analysis of the various guidance factors and receptors was performed between E13.5 and E15.5 by ISH or immunohistochemistry (IHC) (Figure 20 - Figure 23 and Figure 31; Di Meglio et al., 2008; Dominici et al., 2018; Geisen et al., 2008; Gilthorpe et al., 2002; Kim and Ackerman, 2011; Kuwako et al., 2010; Marillat et al., 2004; Moreno-Bravo et al., 2018; Zhu et al., 2009).

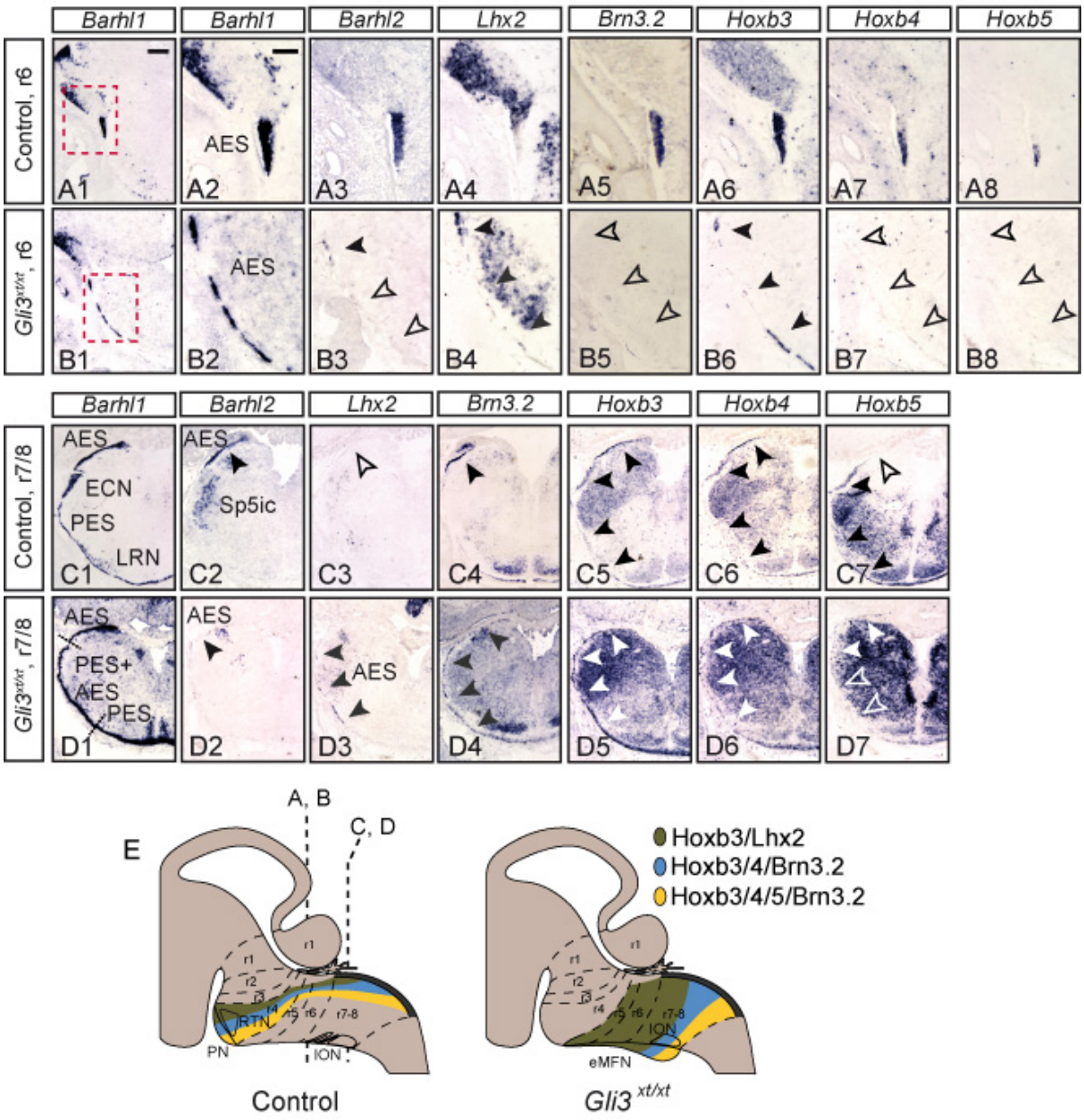

Figure 17. The r7-r8-derived portion of the AES fails to turn anteriorly in *Gli3*$^{xt/xt}$ mutants. Adjacent coronal sections of E14.5 control and *Gli3*$^{xt/xt}$ hindbrains hybridized for *Barhl1*, *Barhl2*, *Lhx2*, *Brn3.2*, *Hoxb3, Hoxb4,* and *Hoxb5*. **(A1-A8)** In r6 control hindbrains, the AES is organized in subpopulations according to the expression pattern defined in Figure 17. **(B1-B8)** In *Gli3*$^{xt/xt}$ mutants, the AES in r5/6 contains cells that are *Hoxb3/Lhx2* positive and *Hoxb4/Hoxb5* negative (see arrowheads). A few *Barhl2 and Brn3.2* positive cells are seen at this axial level. **(C1-C7)** In r7/r8 of controls, the emerging AES is a compact, dorsally-restricted cluster positive for *Brn3.2* and *Hoxb3/Hoxb4* or *Hoxb3/Hoxb4/Hoxb5*. **(D1-D7)** In *Gli3*$^{xt/xt}$ mutants, the Hox gene expression pattern is conserved in the AES at the level of r7/r8, but the AES expands ventrally (arrowheads). Note that most of the PES cells localize at the ventral midline (*Barhl2-/Lhx2-*). Also, note that the PES and ION are *Hoxb3/4/5* positive. Filled arrowheads indicate positive signal and open arrowheads indicate lack of signal for a particular *in situ* probe. **(E)** Schematic of the gene expression patterns in the AES. Number of embryos analyzed: 5 controls, 4 mutants for *Lhx2, Brn3.2* and *Barhl2*; 8 controls, 7 mutants for *Hoxb3/4/5.* Scale bars: 200 μm (A1, B1, C1, D1); 100 μm (A2-A8, B2-B8).

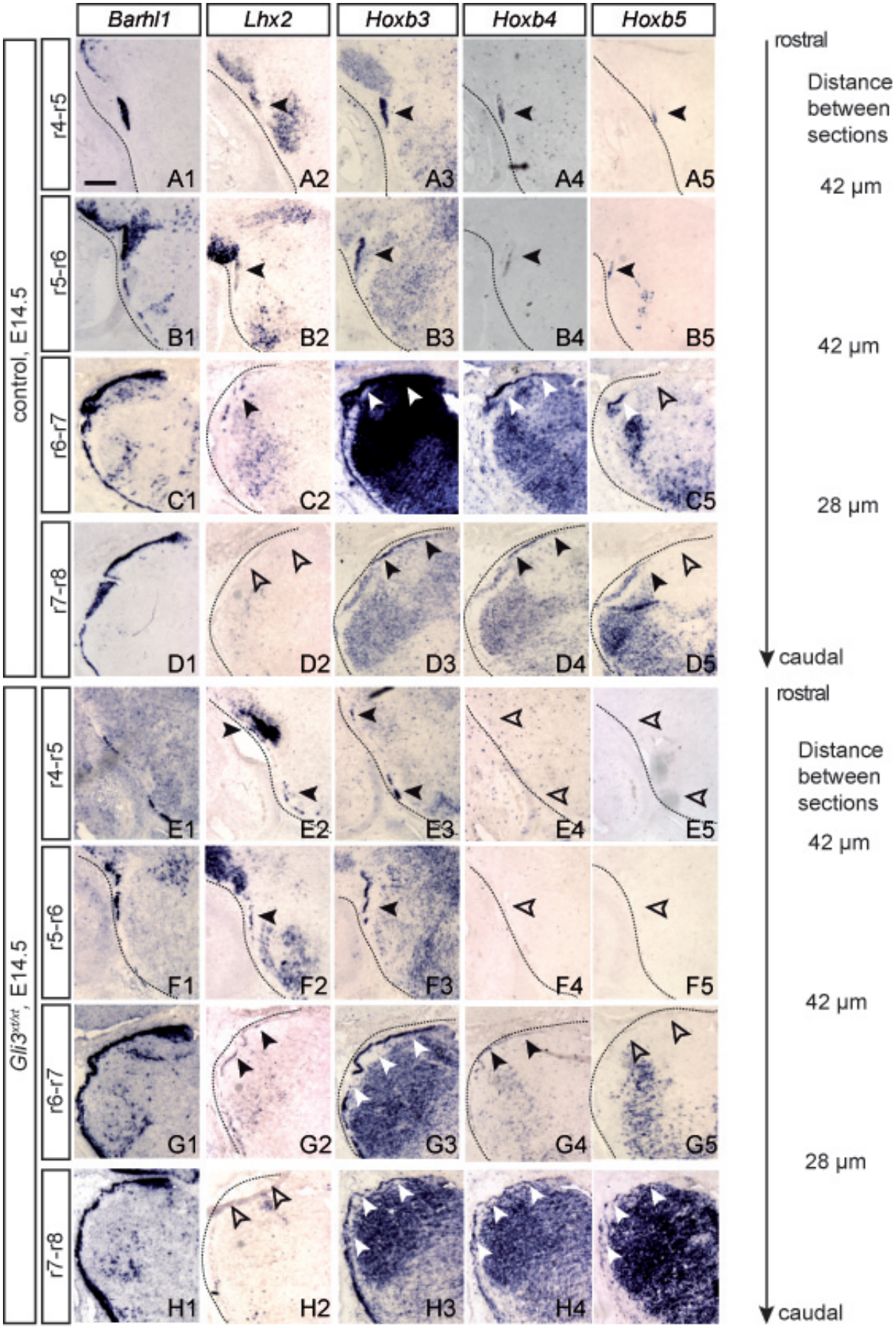

Figure 18. The r7-r8-derived portion of the AES fails to turn anteriorly in *Gli3*$^{xt/xt}$ mutants (Figure legend continues on page 79).

Figure 18. This figure complements figure 16 and shows all AP axial levels analyzed. *In situ* hybridization for *Barhl1, Lhx2, Hoxb3, Hoxb4* and *Hoxb5* on control and *Gli3*$^{xt/xt}$ coronal sections at E14.5. Scale bars: 200 µm.

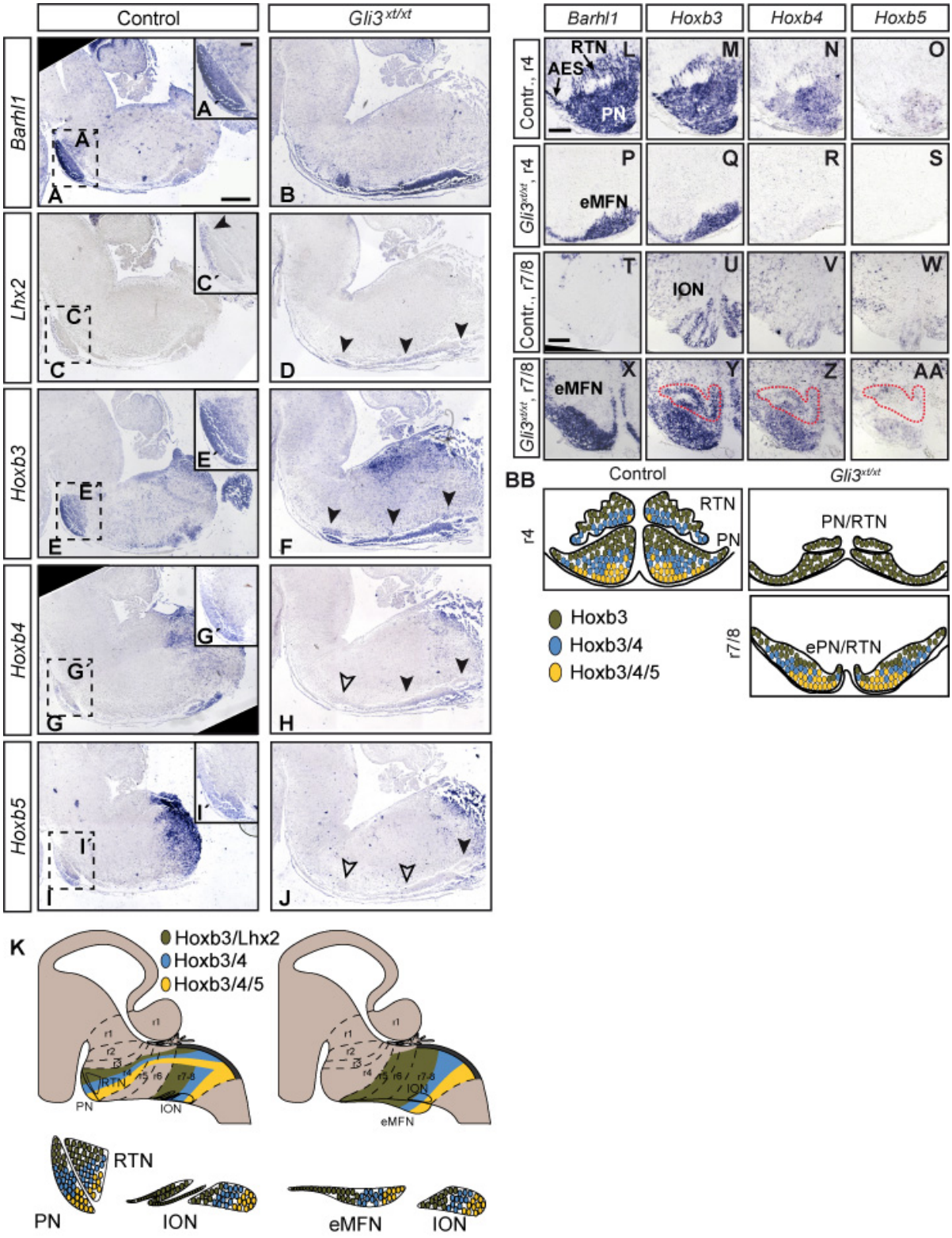

Figure 19. Cell populations composing the MFN and ION in the *Gli3*$^{xt/xt}$ mutant at E18.5 (Figure legend continues on the following page).

Figure 19. (A-J) Adjacent sagittal sections of control and *Gli3*$^{xt/xt}$ hindbrains hybridized for *Barhl1*, *Lhx2, Hoxb3, Hoxb4,* and *Hoxb5.* The boxed areas delineate the area of higher magnification images in A´, C´, E´, G´, I´. In control hindbrains, the PN/RTN are organized from dorsal-to-ventral according to the rhombomeric-origin of the cells and by specific combinations of Hox gene expression: All PN/RTN express *Hoxb3* (r6-derived), the intermediate part *Hoxb3* and *Hoxb4* (r7-derived) and the caudoventral part *Hoxb3, Hoxb4* and *Hoxb5* (r8-derived). In addition, the r6-derived PN/RTN are *Lhx2* positive. In *Gli3*$^{xt/xt}$ mutants, the PN/RTN cells are distributed along r4-r8, but keep an order relative to their rhombomeric origin, as defined by specific combinations of Hox-gene expression: *Hoxb3*-positive cells locate in r4-r6, *Hoxb4*-positive cells in r7-r8 and *Hoxb5*-positive cells in r8 (F, H, J). *Lhx2* expression is observed throughout the ectopic cell clusters (D). **(K)** Schematic summarizing the gene expression patterns in the PN/RTN neurons in controls and *Gli3*$^{xt/xt}$ mutants. **(L-AA)** Adjacent coronal sections of control and *Gli3*$^{xt/xt}$ hindbrains in r4 and r7/r8 hybridized for *Barhl1*, and *Hoxb3-Hoxb5* confirming the Hox gene expression described in sagittal sections. Note that all three Hox genes are expressed in the ION in controls and *Gli3*$^{xt/xt}$ mutants (Y-AA, ION outlined in dotted red line). **(BB)** Schematic summarizing the *Hoxb* expression pattern in the PN/RTN. Number of embryos analyzed: sagittal sections (3 controls, 3 mutants), coronal sections (3 controls, 4 mutants). Scale bars: 400 µm (A-J), 200 µm (L-AA), 100 µm (A´, C´, E´, G´, I´).

4.8.1. Netrin 1 and DCC/UNC5 receptors

Ntn1 was expressed in the floor plate and in the ventricular neuroepithelium in controls (Dominici et al., 2017; Varadarajan et, 2017; Yamauchi et al., 2017). A similar expression pattern was found in *Gli3*$^{xt/xt}$ mutants at E13.5 (Figure 20A-D) or E14.5 (not shown). The Netrin receptor DCC, which mediates an attractive response to NTN1, was analyzed at E14.5 (Figure 31) and E15.5 (Figure 21). At E14.5, DCC was present in the already established LRN (Figure 30O1, and Q1), and ECN (Figure 31M1). The formation of these nuclei is delayed and/or compromised in *Gli3*$^{xt/xt}$ mutants, thus no DCC signal was found in these areas at this time point (Figure 32P1, and R1). At E15.5, DCC was no longer present in the LRN (Figure 21A1-A7, C1-C7), while the cells in the LRN area at E15.5 were positive (Figure 21B1-B7, D1-D7). Regarding the AES, all neurons appeared to be positive for DCC at both stages and conditions, even when present as single cells in *Gli3*$^{xt/xt}$ mutants (Figure 21F2-F3; Figure 32L1-L3 and N1-N3). These results indicate that DCC is not affected in *Gli3*$^{xt/xt}$ mutants. The Netrin receptors UNC5B and UNC5C, which mediate repulsive effects, were analyzed at E14.5. In controls*, Unc5c* was present in all the ION and PES neurons but was not detectable in the AES at this time point (Figure 22A6, A7, and C6; Kim and Ackerman, 2011; Di Meglio et al., 2013). In *Gli3*$^{xt/xt}$ mutants, *Unc5c* was expressed in the ION and PES neurons (including the ectopic PES cells at the midline separating the two bilateral halves of the ION (Figure 22A6, B6, B7, and D6), and was also absent from the AES. Thus, *Unc5c* expression is not affected in *Gli3*$^{xt/xt}$ mutants. *Unc5b* is expressed in the upper one-third of the AES (*Hoxb3+/Hoxb4-/Hoxb5-*) in control embryos (Di Meglio et al., 2013). In the experiments performed here, the *in situ* hybridization signal for *Unc5b* was very weak in controls, thus it was impossible to draw a conclusion about potential changes in *Unc5b* expression in the scattered migratory streams in *Gli3*$^{xt/xt}$ mutants (Figure 22B5, D5).

4.8.2. Slit molecules and ROBO receptors

Previous analysis of triple *Slit1/Slit2/Slit3* and double *Robo1*/*Robo2* knockout mice suggested an important role of this pathway in CFN and MFN migration (Di Meglio et al., 2008, Geisen et al., 2008). This prompted an analysis of *Slit* and *Robo* expression in the hindbrain of *Gli3*$^{xt/xt}$ mutants and controls at E13.5 and E15.5. In controls, *Slit1* was expressed in the floor plate, in part of the ventricular neuroepithelium and in the RL at both time points (Figure 20E, G, and not shown; Causeret et al., 2002). Starting at E15.5, *Slit1* was also expressed in the VCN (Figure 20S). *Slit2* was expressed in the floor plate, the RL, the facial motor nucleus (7N) and the hypoglossal nucleus (12N) (Figure 20I, K and not shown; Causeret et al., 2002; Geisen et al., 2008). Starting at E15.5, it was also expressed in part of the ventricular area, and in a neuronal population lateral to the ventricle (not shown). *Slit3* was only studied at E13.5. It was expressed in the floor plate, the RL, the 7N and 12N (Figure 20 M and O). The expression pattern of Slit1-3 was maintained in *Gli3*$^{xt/xt}$ mutants (Figure 20F, H, J, L, N, P, T, V).

Robo1/*Robo2* were expressed in the ION of control embryos at E13.5 and E15.5. They showed particularly high levels of expression in the *Brn3.2*+ population and a weak to non-existent expression in the *Er81*+ population at these stages (Figure 23A6-A9, E6-E9, see arrowheads). A similar expression pattern (higher levels in *Brn3.2*+ ION neurons) was found in the *Gli3*$^{xt/xt}$ mutant at these stages (Figure 23B6-B9, F6-F9, see arrowheads). In the control PES, *Robo1/Robo2* were expressed at E13.5 (Figure 21A3-A4) and the expression was similar in *Gli3*$^{xt/xt}$ mutants (Figure 21B3-B4). In the AES of controls, *Robo1*/*2* expression showed a dorsoventral gradient: the upper one-third of the AES (*Hoxb3+/Hoxb4-/Hoxb5-*) was only weakly positive, while the lower two thirds (*Hoxb4*+ and *Hoxb5*+ populations) were strongly positive. This expression pattern appeared to be conserved in *Gli3*$^{xt/xt}$ mutants when considering the altered distribution of these AES subsets. The AES in r7-r8 was *Robo1+/Robo2*+ (Figure 21F3-F4), and the AES in r4-r6 mainly *Robo1-/Robo2*- (Figure 21H3-H4). The results indicate that the expression of the Robo receptors is not altered in CFN or MFN in *Gli3*$^{xt/xt}$ mutants since the altered distribution of *Robo1/Robo2* expression seems to be simply related to changes in the distribution of the neurons. After completing the analysis for this thesis, a recent study, in which *Robo1* and *Robo2* were conditionally inactivated in precerebellar progenitors, indicated that these receptors do not play a cell-autonomous role in precerebellar migration (Dominci et al., 2018). Thus, even if *Robo1/Robo2* expression were chaged in *Gli3*$^{xt/xt}$ mutants, these changes would not be causative for the observed phenotype.

The expression of the *Robo3* receptor, which in mammals has a higher affinity for DCC than for SLITs (Zelina et al., 2014), and which is required for the ventral migration of all precerebellar neurons before their axons have crossed the midline (Di Meglio et al., 2008;

Marillat et al., 2004; Zelina et al., 2014), was analyzed in E13 and E15 controls and *Gli3*$^{xt/xt}$ mutants. *Robo3* expression was comparable in controls and mutants. The PES and AES neurons expressed *Robo3* at E13.5 (Figure 23A5, B5, C5, D5) and E15.5 (Figure 23E5, F5, G5, H5). ION neurons did not express *Robo3* at these time points, likely since ION axons cross the midline starting at E12.5 (Figure 21 A10, B10, E10, F10; Marillat et al., 2004).

4.8.3. CXCL12 and CXCR4

The chemokine CXCL12 interacts with the CXCR4 receptor in AES neurons to keep their compact and extramural migration (Vilz et al., 2005; Zhu et al., 2009). *In situ* hybridizations for *Cxcl12* at E15.5 and of *Cxcr4* at E14.5 were performed to analyze potential alterations in their expression in *Gli3*$^{xt/xt}$ mutants. *Cxcl12* was expressed in the meninges and VCN of both, controls and *Gli3*$^{xt/xt}$ mutants (Figure 20Q, Q´, R and R´). In controls, *Cxcr4* was expressed in AES neurons but not in PES (Figure 22A4, C4, Zhu et al., 2009). In *Gli3*$^{xt/xt}$ mutants, *Cxcr4* was expressed in the AES in r7-r8 but was downregulated in the AES in r4-r6 (Figure 22B4, D4, see arrowheads), suggesting that the anterior migration of the AES is independent of *Cxcr4* in absence of *Gli3*. Since inactivation of *Cxcr4* results in striking AES delamination from the extramural path (Zhu et al., 2009), the reduced *Cxcr4* expression in the AES may explain the partial delamination of AES neurons into the intramural space observed at E16.5 and E18.5 (Figure 9F-H and Figure 15R).

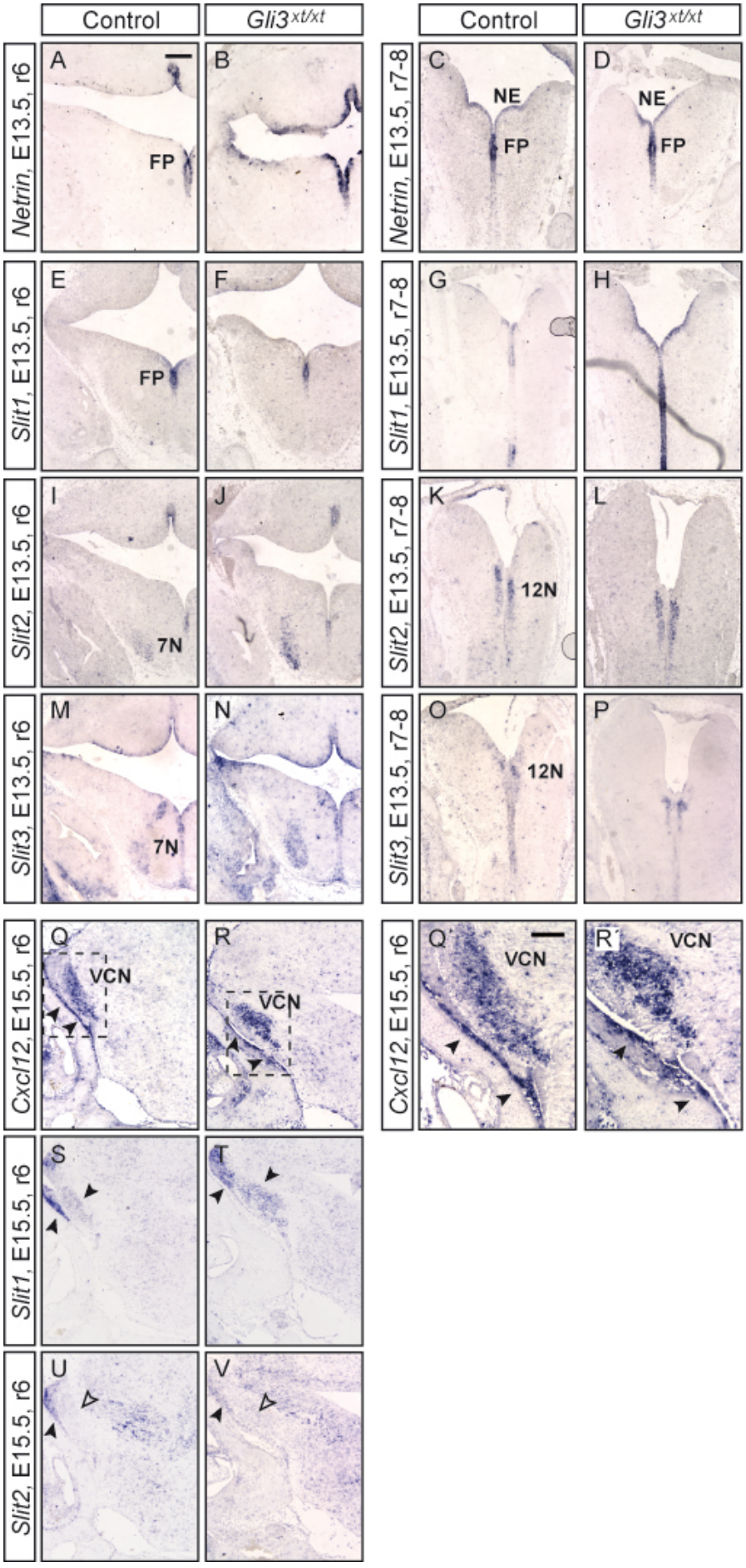

Figure 20. Guidance cues in the *Gli3*$^{xt/xt}$ mutant (Figure legend continues on the following page).

Figure 20. Coronal sections of E13.5 and E15.5 control and *Gli3*$^{xt/xt}$ hindbrains at r6 and r7-r8 hybridized for different guidance molecules. A comparable expression pattern exists between E13.5 controls and *Gli3*$^{xt/xt}$ mutants for *Ntn1* in the floor plate (FP) and ventricular zone (A-D), for *Slit1* in the FP (E-H), for *Slit2* in the FP, facial motor nucleus (7N) and hypoglossal nucleus (12N) (I-L), and for *Sli3* in the FP, 7N and 12N (M-P). A comparable expression pattern also exists between E15.5 controls and *Gli3*$^{xt/xt}$ mutants for *Slit1* in the ventral cochlear nucleus (VCN) and for *Slit1/Slit2* in the RL (S-V). *Cxcl12* has a similar expression in the meninges and VCN of E15.5 controls and *Gli3*$^{xt/xt}$ mutants (Q-R´, arrowheads point to the meninges). N≥3 for each marker and genotype. Scale bar: 200 μm (A-V), 100 μm (Q´and R´).

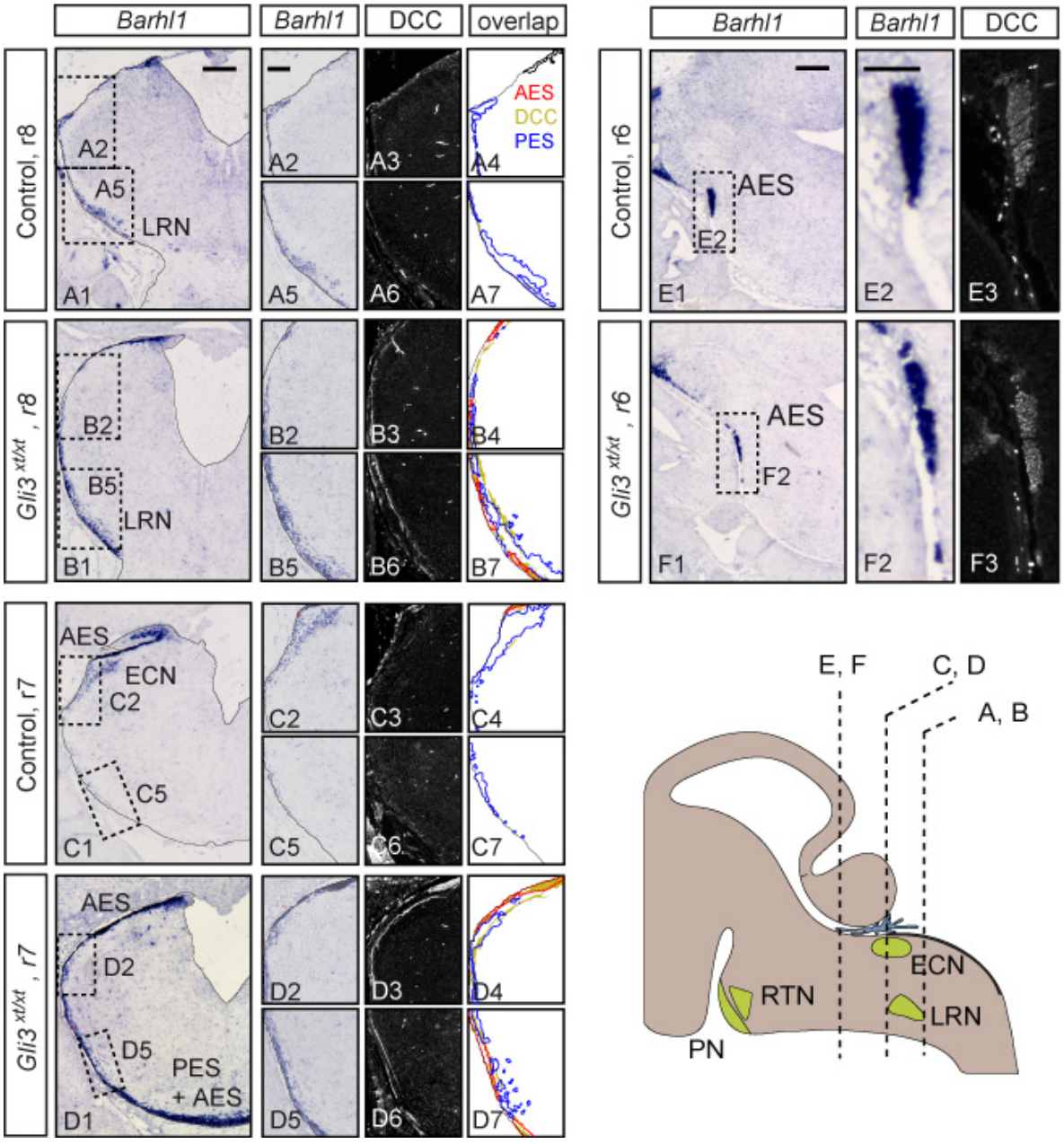

Figure 21. DCC distribution in the *Gli3*$^{xt/xt}$ mutant (Figure legend continues on the following page.

Figure 21. Coronal sections of E15.5 control and *Gli3*$^{xt/xt}$ hindbrains at r8, r7 and r6 stained for DCC and adjacent sections hybridized for *Barhl1.* In the control, the LRN and ECN are already positioned (A1, C1) and some DCC+ projections are seen between these two nuclei, adjacent to the pia (A2-A7 and C2-C7). In the *Gli3*$^{xt/xt}$ mutant, some cells have settled at the LRN (B1, B5), but no ECN is formed (D1, D2). Several DCC+ fibers exist between the LRN and prospective ECN area (B2-B7 and D2-D7), but not elsewhere. These same projections are present in E14.5 controls but not *Gli3*$^{xt/xt}$ mutants (relate to figure 23), suggesting that they potentially belong to PES neurons. The AES neurons of E15.5 controls and *Gli3*$^{xt/xt}$ mutants are DCC+ (F1-F3). N≥3 for each marker and genotype analyzed. Scale bars: 200 μm (A1-D7, E1, and F1); 100 μm (E2, E3, F2 and F3).

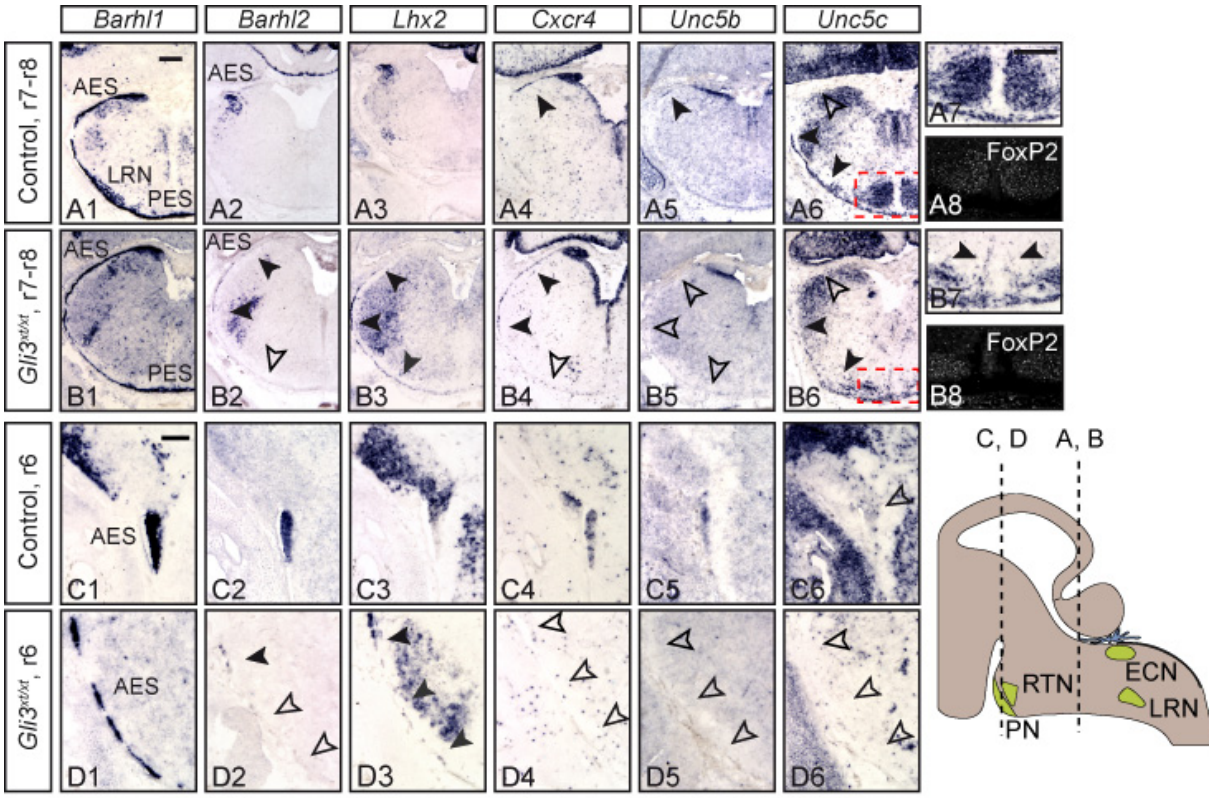

Figure 22. Expression of Cxcr4 and Unc5 receptors in the *Gli3*$^{xt/xt}$ mutant. Coronal sections of E14.5 control and *Gli3*$^{xt/xt}$ hindbrains at r6 and r7-r8 hybridized for *Cxcr4*, *Unc5b*, *Unc5c.* Adjacent sections hybridized for *Barhl1*, *Barhl2* and *Lhx2* are provided to distinguish AES from PES neurons. *Cxcr4* is expressed in the AES in controls (A4, C4). In *Gli3*$^{xt/xt}$ mutants, Cxcr4 expression is excluded from the AES in r4-r6, but present in the AES migrating ectopically in r7-r8 (B4, D4). *Unc5b* and *Unc5c* have a complementary expression in the MFN in controls: *Unc5b* is expressed in the AES (A5, C5) in a gradient (high expression in r6-derived neurons and low in those derived from r7-r8), while *Unc5c* in the PES (A6, C6) and ION (A6, A7). In *Gli3*$^{xt/xt}$ mutants, *Unc5b* is not detected in the AES at any time point and *Unc5c* remains restricted to the PES and ION (B6 and D6), including the ectopic PES cells delaminating at the ventral midline between the two bilateral halves of the ION (B7 and B8). The black arrowheads point to mRNA signal, the empty arrowheads mean no signal. N≥3 for all markers and genotypes analyzed, but *Unc5b* (n=2). Scale bars: 200 μm (A1-B8); 100 μm (C1-D6).

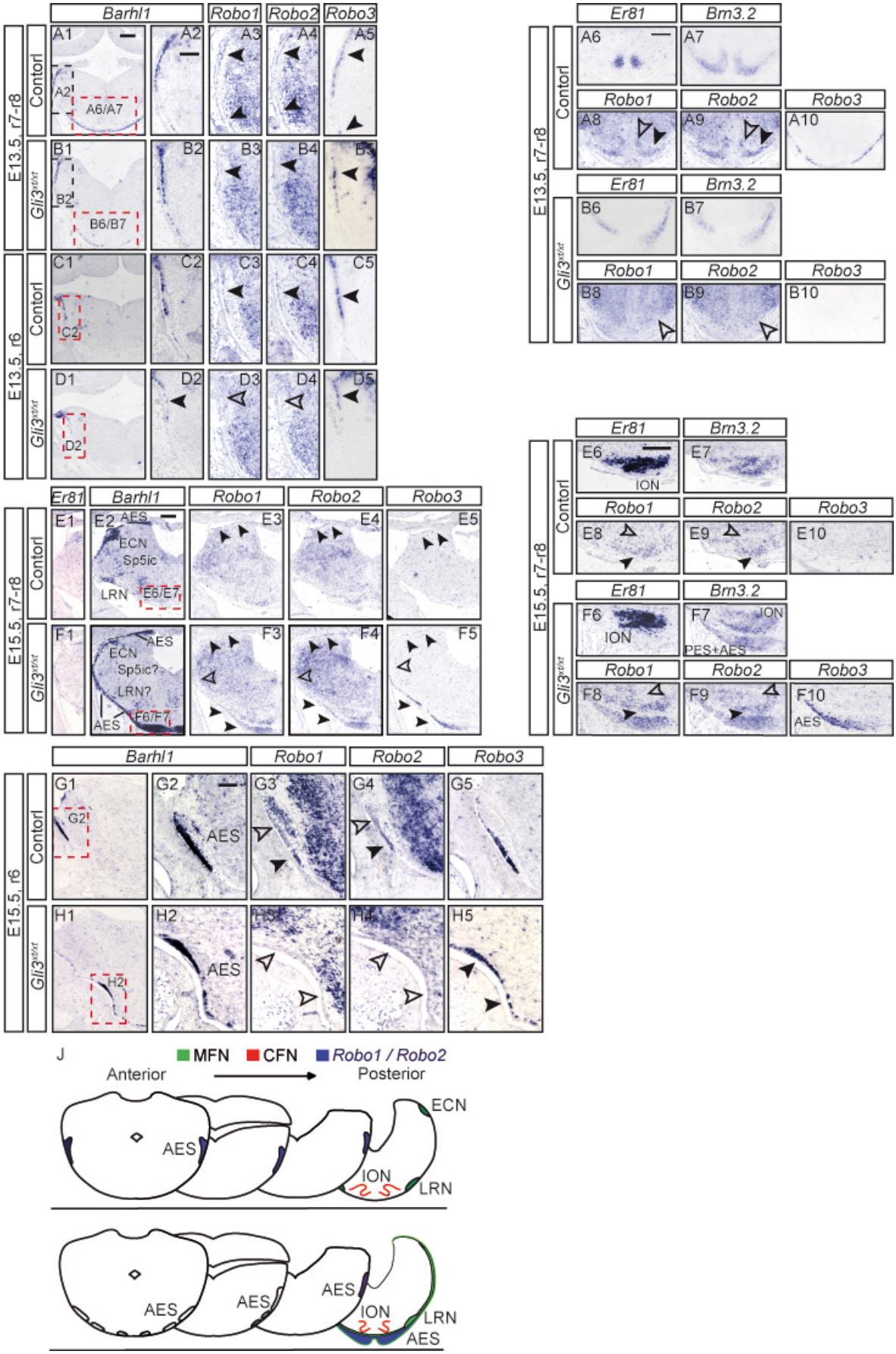

Figure 23. *Robo* receptor expression in the *Gli3*$^{xt/xt}$ mutant (Figure legend continues on the following page).

Figure 23. Coronal sections of E13.5 and E15.5 control and *Gli3*$^{xt/xt}$ hindbrains at r6 and r7-r8 hybridized for *Robo1*, *Robo2,* and *Robo3*. Adjacent sections hybridized for *Barhl1*, *Er81* and *Brn3.2* are provided to visualize the CFN and MFN. **(A-D)** ISH in E13.5 brains. *Robo1-Robo3* are expressed in the PES of controls and *Gli3*$^{xt/xt}$ mutants (A3-A5, B3-B5). In the IMS, *Robo1/Robo2* are only expressed in *Er81-/Brn3.2+* of controls and *Gli3*$^{xt/xt}$ mutants (A6-A9, B6-B9). Note that the cell distribution is different in the *Gli3*$^{xt/xt}$ mutants at this developmental stage and that all neurons are *Er81+/Brn3.2+*, and thus *Robo1-/Robo2-* (see arrowheads). *Robo3* is no longer expressed in the IMS of controls and *Gli3*$^{xt/xt}$ mutants (A10, B10), indicating that their axons have already crossed the midline. *Robo1-Robo3* are expressed in the AES arising from r6 in controls (C3-C5), while only *Robo3* is expressed in *Gli3*$^{xt/xt}$ mutants (D3-D5). **(E-H)** ISH in E15.5 brains. At E15.5, the IMS migration is over in controls and *Gli3*$^{xt/xt}$ mutants. The *Er81-/Brn3.2+* ION cells remain *Robo1+/Robo2+* (E8-E9, F8-F9). *Robo1* and *Robo2* are mainly expressed in the lower 2/3 of the AES in controls, while Robo3 is expressed in all the stream (E3-E5, G3-G5). In *Gli3*$^{xt/xt}$ mutants, the AES in r7-r8 is *Robo1+/Robo2+/Robo3+* (F3-F5), but only *Robo3+* in r4-r6 (H3H5). The black arrowheads point to mRNA signal, the empty arrowheads mean no signal. **(J)** Diagram explaining the *Robo1/Robo2* expression in MFNs. N≥3 for each marker and genotype analyzed. Scale bars: 200 μm (A1, A6-A10; B1, B6-B10; E1-F10, G1, and H1); 100 μm (A2-A5; B2-B5; C2-C5; D2-D5; G2-G5 and H2-H5).

4.9. GLI3 does not play a cell-autonomous role in the migration of mossy fiber neurons

Gli3 was only expressed in the MF progenitors before E10.5 and was absent from the differentiated neurons in the AES and PES (Figure 5), suggesting that *Gli3* regulates MFNs migration non-cell-autonomously. As just described in section 3.8, the expression of *Cxcr4, Robo1, and Robo2* was altered in the AES of *Gli3*$^{xt/xt}$ mutants. These defects appear to be the consequence of the cell reorganization in the AES of *Gli3*$^{xt/xt}$ mutants, rather than the primary cause for the altered migratory streams in *Gli3*$^{xt/xt}$ mutants. To explore further whether GLI3 has a cell-autonomous function in the development of MFNs, *Gli3* was specifically inactivated in the *Atoh1*-lineage (Figure 24 and Figure25; Matei et al., 2005, Blaess et al., 2008). In this mouse model (referred to as *Atoh1-Gli3* cko, genotype *Atoh1-Cre, Gli3*$^{xt/flox}$), Cre-mediated recombination and thus inactivation of *Gli3* occurs specifically in MF and other RL progenitors around E9.5 (Figure 24A-D; see table 1). Recombination was visualized by the presence of EYFP (*R26* $^{flox\text{-}stop\text{-}flox\ EYFP}$; Matei et al., 2005) (Figure 24B, J, N) or ß-gal expression (*R26* $^{flox\text{-}stop\text{-}flox\ lacZ}$*; Soriano et al., 1999*). In E18.5 *Atoh1-Gli3 cko* brains, the location and size of MFN were comparable to controls (Figure 25E-F). Detailed analysis of all precerebellar nuclei indicated identical cell distribution in the PN/RTN (Figure 24G-N), ECN and LRN (Figure 25O-V). The ION was analyzed to examine potential indirect effects of the inactivation of *Gli3* in MFNs, but no alterations could be detected in the *Atoh1-Gli3* cko mice (Figure 25W-Z). The localization and organization of the AES and PES in the E14.5 *Atoh1-Gli3* cko was also comparable between controls and *Atoh1-Gli3* cko (Figure 25A1-A3, B1-B3, C1-C4, D1-D4). Moreover, the analysis of Hox genes, *Barhl2* and *Lhx2* indicated that both streams maintained their topographical organization (Figure 25A4-A6, B4-B6, C5-C7,

D5-D7). In summary, these data confirmed that GLI3 does not play a cell-autonomous role in MFN migration.

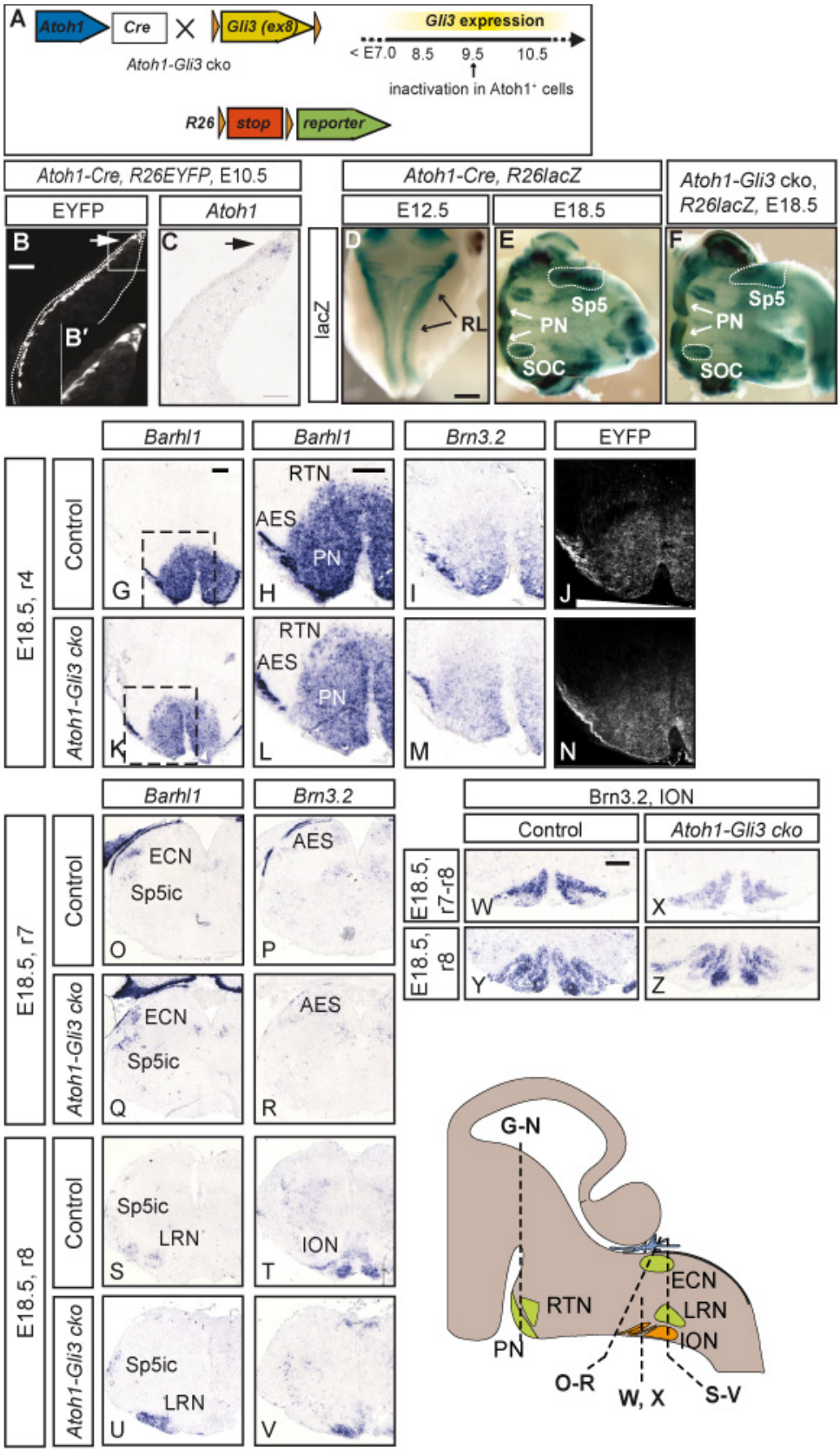

Figure 24. Conditional inactivation of *Gli3* in the *Atoh1*-lineage does not affect the morphology and final distribution of MFN (Figure legend continues on the following page).

Figure 24. (A) Conditional inactivation of *Gli3* in *Atoh1*-expressing progenitors (Atoh1-Gli3 cko) combined with an *R26* reporter allele. **(B, C)** Coronal sections of *Atoh1-Cre* mice crossed with an $R26^{lacZ/+}$ reporter were immunostained for EYFP and hybridized for *Atoh1* showing that the EYFP product allows cell lineage tracing of *Atoh1*-derived neurons, while *Atoh1* mRNA expression the visualization of progenitors cells. **(D-F)** Whole-mount staining for X-gal in *Atoh1-Cre* mice crossed with an $R26^{lacZ/+}$ shows recombination in the RL at E12.5 (D) and in RL-derived neurons at E18.5 (E). The staining in the *Atoh1-Gli3 cko* indicates no changes in cell distribution (F). **(G-Z)** *In situ* hybridization (*Barhl1* and *Brn3.2*) and immunostaining for GFP in *Atoh1-Cre,* $R26^{EYFP/+}$, $Gli3^{xt/+}$ control and *Atoh1-Cre,* $R26^{EYFP/+}$, $Gli3^{xt/flox}$ mutant mice. E18.5 coronal sections at different anteroposterior levels showing that the distribution and morphology of MF and CF nuclei do not differ between controls and *Atoh1-Gli3 cko*. The PN/RTN form in r4 (G-N) and the ECN, LRN, and ION in r7-r8 (O-Z). **PN**: pontine nucleus; **SOC**: superior olivary complex; **Sp5**: spinal trigeminal nucleus. At least 3 controls and 3 mutants were analyzed for marker, stage, and condition. Scale bars: 50 μm (B, C), 200 μm (G-Z), 500 μm (D-F).

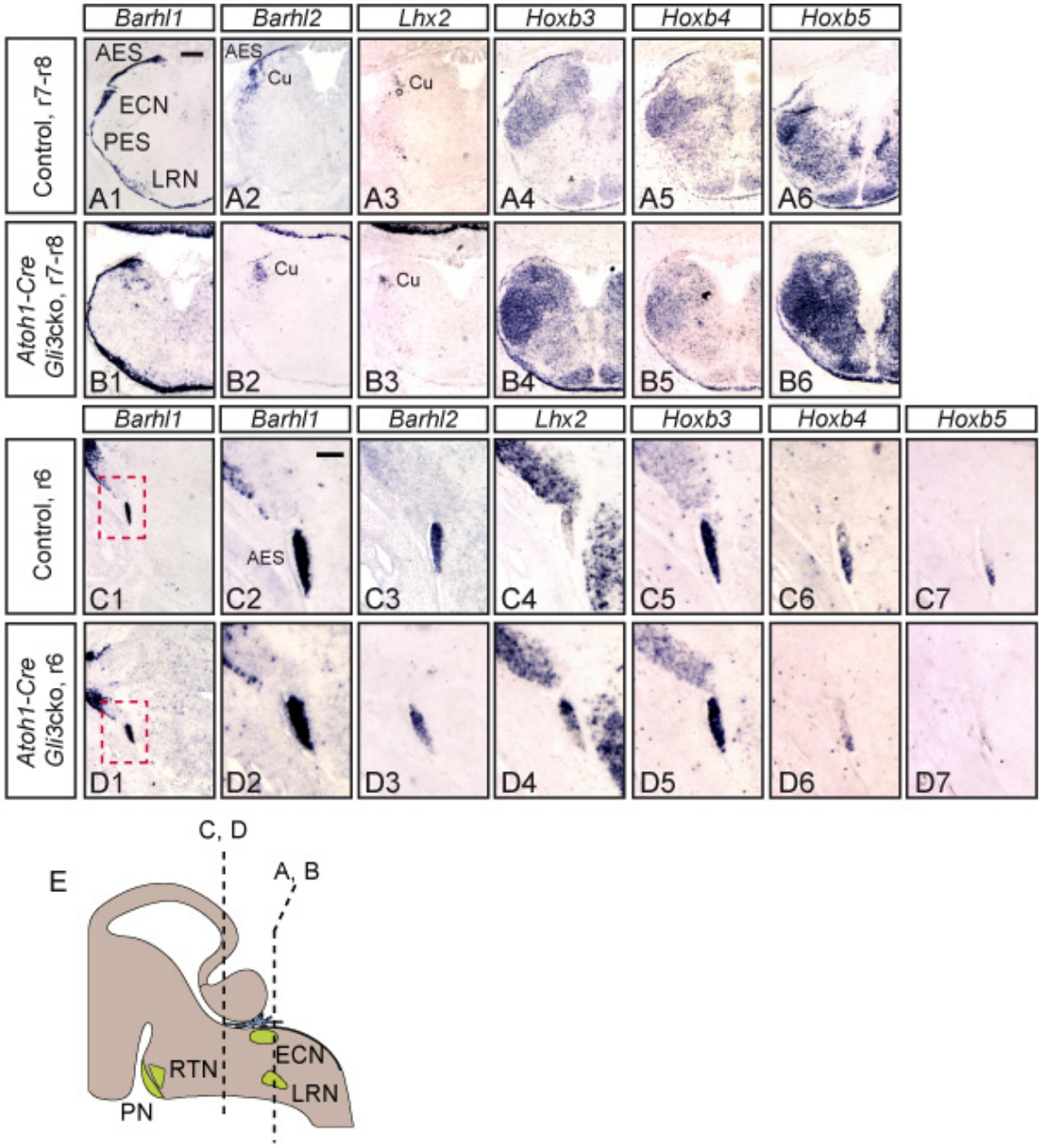

Figure 25. Figure legend continues on the following page.

Figure 25. The MFN extramural streams remain unchanged in the *Atoh1-Gli3 cko*. Coronal sections of E14.5 control and *Atoh1-Gli3 cko* hindbrains hybridized for *Barhl1*, *Barhl2, Lhx2, Hoxb3, Hoxb4* and *Hoxb5* to separate the different populations within the streams. The PES is not delayed and the AES does not invade the ventral regions at r7-r8 in mutants (A-B). The internal *Barhl2*/*Lhx2* gradients and Hox gene expression are conserved in the AES in mutants (C-D). 8 controls and 4 mutants were analyzed for each marker and condition. Scale bars: 200 μm (A1-B6, C1, and D1), 100 μm (C2-C7 and D2-C7).

4.10. The organization of non-precerebellar hindbrain nuclei is not obviously altered in the *Gli3$^{xt/xt}$* hindbrain

The previous results indicate that alterations in the precerebellar system of *Gli3$^{xt/xt}$* mutants are non-cell autonomous. To identify potential alterations in the rest of the hindbrain, the whole hindbrain was analyzed at E14.5 in controls and *Gli3$^{xt/xt}$* mutants using the expression of markers defining diverse nuclei distributed along the whole AP axis (Figure 2, bold letters). Analysis of *Isl1* (*Islet 1*, ventral hindbrain progenitors) expression showed that the trigeminal (5N), 7N and 12N hindbrain motor nuclei were properly formed in *Gli3$^{xt/xt}$* mutants (Figure 26A1-A6). The principal trigeminal nucleus (Pr5) and spinal trigeminal nucleus (Sp5) are located along the migratory pathway of the AES or the AES and PES respectively and could play a role in MFN migration. The Pr5 and Sp5 were analyzed using the expression *Lhx2*, *Lhx9*, *Pax2*, *vGlut2*, and *Gad1* (Rose et al., 2009; Gray 2013; Iskusnylch et al 2016; Hernandez-Miranda et al., 2017). The Pr5 was composed of a major v*Glut2*+/*Lhx2*+ cell population, a discrete number of *Lhx9*+ cells, and a *Pax2*+ cell population in controls (Figure 26B1-D1 and F1). In *Gli3$^{xt/xt}$* mutants, the *vGlut2* signal was qualitatively reduced as compared to controls (Figure 26D2) and ectopic *Pax2+/Gad1+* cell populations were observed (Figure 26F2-G2). The *pars oralis* of the Sp5 (Sp5o) was composed of *Lhx2+/vGlut2*+ cells and was comparable between controls and *Gli3$^{xt/xt}$* mutants (Figure 26B3,D3,B4,D4). The *pars interpolaris* and *pars caudalis* of the Sp5 (SP5ic) were identified as the most lateral part of the alar plate at an AP level located between the 7N and the most posterior hindbrain (Watson 2012). This nucleus was composed of by a population of *Lhx9*+ cells and a population of *Gad1*+/*Gad2*+/*Pax2*+/*Gbx2*+ cells (Figure 26F5, G5, I5; Sieber et al, 2007; Rose et al, 2009; Gray, 2013; Iskusnykh et al, 2016). Compared to controls, the *Gli3$^{xt/xt}$* mutants had a qualitative decrease in *Gad1* signal (Figure 26G6). The *Gli3*-expressing VLL (*Lhx2*+/*Lhx9*+/*En1*+, Figure 26B1,C1,E1), SOC (*En1*+/*Gad1*+, Figure 26E1, G1) and SOL (*Pax2*+/*Gad1*+/*Gbx2*+, Figure 26F5,G5,I5) (Sieber et al, 2007, Storm et al, 2009, Gray, 2013, Iskusnykh et al, 2016, di Bonito and Studer, 2017), were comparable between controls and *Gli3$^{xt/xt}$* mutants (VLL: Figure 26B2,C2,E2; SOC Figure 26E2,G2; SOL Figure 26F6,G6,I6). The median raphe nucleus (MnR) (*Pax2*+/*Gad1*+/*Gad2*+, Figure 26F1,G1,H1) and the gigantocellular reticular nucleus (Gi) (*Pax2*+/*Gad1*+/*Gbx2*+, Figure 26F5,G5,I5) were analyzed as examples of ventrally derived nuclei and they were also

formed in *Gli3*$^{xt/xt}$ mutants (MnR, Figure 26F2,G2,H2; Gi Figure Figure 26F6,G6,I6). To assess whether GLI3 might play a general role in the development of auditory-RL (r2-r5 derived-neurons), the cochlear extramural stream (CES) and ventral cochlear nucleus (VCN) were examined (Farago et al, 2006; Wang et al, 2005). The VCN was delineated using the expression of *Lhx2* and *Vglut2* at E14.5 (Figure 26B3,D3; Rose et al, 2009), and of *MafB* (v-maf avian musculoaponeurotic fibrosarcoma oncogene homolog B) at E18.5 (Figure 27F; Farago et al, 2006). The CES was identified as a stream surrounding the VCN that was positive for *Barhl1*, *Lhx2*, *Lmx1a*, and *Robo3*, but negative for *Barhl2* (Figure 27A-E; Renier et al, 2010, this thesis). The expression pattern and structure of the VCN (Figure 28B4,D4; Figure 27L) and CES (Figure 27G-K) were comparable between controls and *Gli3*$^{xt/xt}$ mutants. This indicates that not all the *Atoh1*-derived neurons in the RL are altered in *Gli3*$^{xt/xt}$ mutants. Moreover, it indicates that the CES and the AES do not intermix at any time in *Gli3*$^{xt/xt}$ mutants, which might have been possible, as the AES and CES neurons are in close contact during their migratory phase in r6 (Nichols and Bruce, 2006; Farago et al, 2006), and the AES neurons reaching r4-r6 in *Gli3*$^{xt/xt}$ mutants have a similar gene expression profile as the CES (*Barhl1+/Barhl2-/Lhx2+/Hoxb3+/Hoxb4-/Hoxb5-*). While subtle changes in other non-precerebellar hindbrain nuclei and their projections might exist, the results obtained here suggest that the cerebellum (Blaess et al., 2008), and the precerebellar system, are the only severely altered structures in the hindbrain of *Gli3*$^{xt/xt}$ mutants. In addition, cells in the trigeminal nuclei (Pr5 and Sp5) appear to have a changed neurotransmitter phenotype, an observation that needs to be explored in further detail in the future.

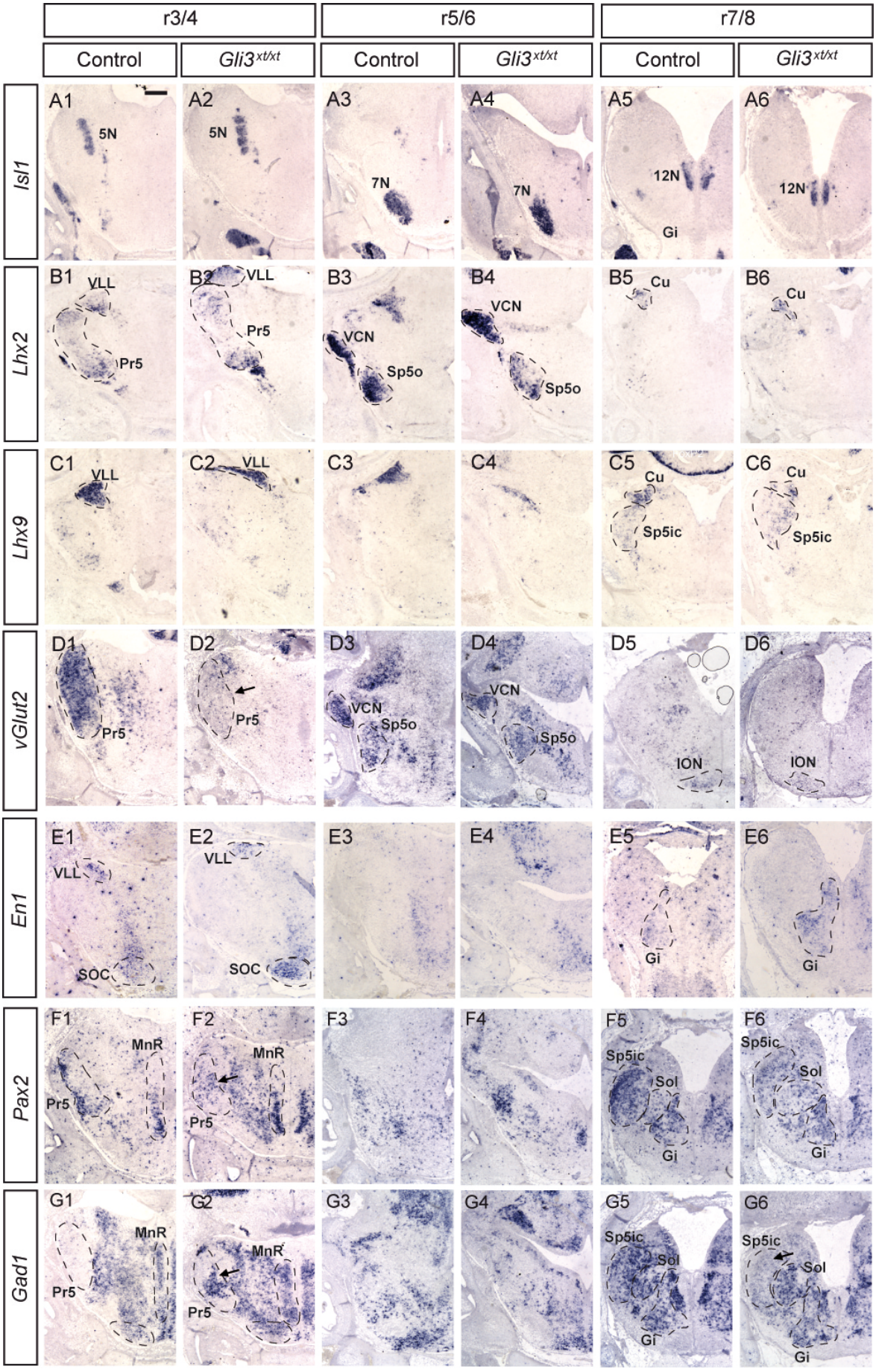

Figure 26. Figure and figure legend continue on the following page

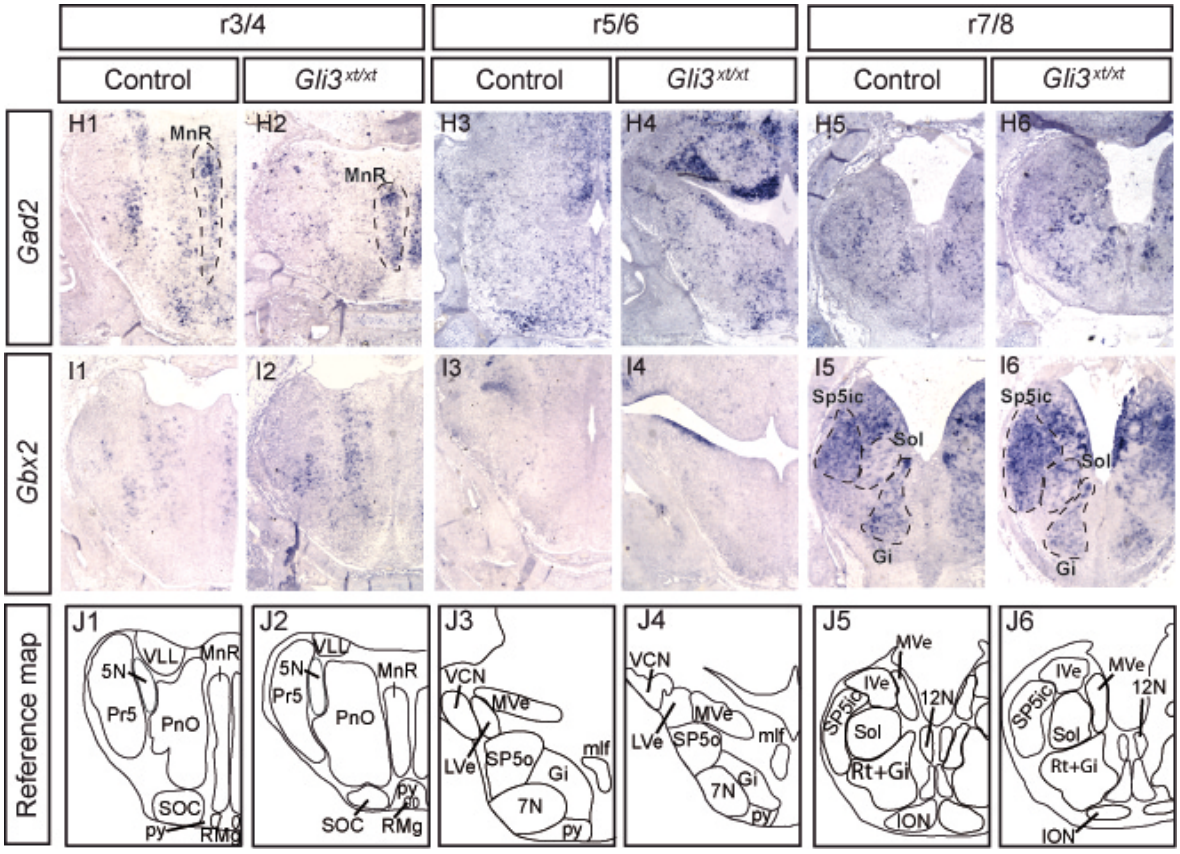

Figure 26. Analysis of non-precerebellar hindbrain nuclei in *Gli3*$^{xt/xt}$ mutants. Coronal sections of controls and *Gli3*$^{xt/xt}$ mutants at r2-3 (A1-I1 and A2-I2), r5-6 (A3-I3 and A4-I4), and r7-8 (A5-I5 and A6-I6) hybridized for various RNA *in situ* probes, as indicated. A reference map for the various nuclei is provided (J1-J6). **(A)** *In situ* hybridization for *Isl1* shows that the motor nuclei of the cranial nerves form properly in *Gli3*$^{xt/xt}$ mutants. 8 controls and 8 mutants were analyzed **(B)** *Lhx2* expression in the ventral lateral lemniscus (VLL), the principal sensory trigeminal nucleus (Pr5), the ventral cochlear nucleus (VCN), the oral division of the spinal trigeminal nucleus (Sp5o), and the cuneate nucleus (Cu) is comparable between controls and *Gli3*$^{xt/xt}$ mutants. 5 controls and 5 mutants were analyzed. **(C)** *Lhx9* expression in the VLL, the interpolar/caudal division of the spinal trigeminal nucleus (Sp5ic), and the Cu of controls and *Gli3*$^{xt/xt}$ mutants is comparable. 2 controls and 2 mutants were analyzed **(D)** *Vglut2* is expressed in the Pr5, VCN, Sp5o, and ION of controls and *Gli3*$^{xt/xt}$ mutants. The expression is reduced in the Pr5 of *Gli3*$^{xt/xt}$ mutants (see arrowhead), compared to controls. 3 controls and 3 mutants were analyzed **(E)** *En1* is expressed in the VLL, the superior olivary complex (SOC), and the gigantocellular reticular nucleus (Gi). The expression pattern is comparable between controls and *Gli3*$^{xt/xt}$ mutants. 3 controls and 2 mutants were analyzed. **(F)** *Pax2* is expressed in cells of the Pr5, median raphe nucleus (MnR), Sp5ic, solitary nucleus (Sol) and Gi in controls and *Gli3*$^{xt/xt}$ mutants. In *Gli3*$^{xt/xt}$ mutants, *Pax2* is ectopically expressed in the Pr5. 3 controls and 3 mutants were analyzed. **(G)** *Gad1* is expressed in the MnR, Sp5ic, Sol, and Gi of controls and *Gli3*$^{xt/xt}$ mutants. In *Gli3*$^{xt/xt}$ mutants, the expression appears to be reduced in the Sp5ic and *Gad1* is ectopically expressed in the Pr5. 3 controls and 3 mutants were analyzed **(H)** *Gad2* is expressed in the MnR of controls and *Gli3*$^{xt/xt}$ mutants. 3 controls and 3 mutants were analyzed. **(I)** The expression of *Gbx2* is comparable in the Sp5ic, Sol, and Gi of controls and *Gli3*$^{xt/xt}$ mutants. 2 controls and 2 mutants were analyzed. **5N:** trigeminal nucleus; **7N:** Facial nucleus; **12N:** Hypoglossal nucleus; **IVe:** inferior vestibular nucleus; **LVe:** lateral vestibular nucleus; **MVe:** medial vestibular nucleus; **mlf:** medial longitudinal fasciculus; **PnO:** pontine reticular nucleus, oral part; **py:** pyramidal tract; **RMg:** raphe magnus nucleus; **Rt:** reticular formation. Scale bar: 200 μm

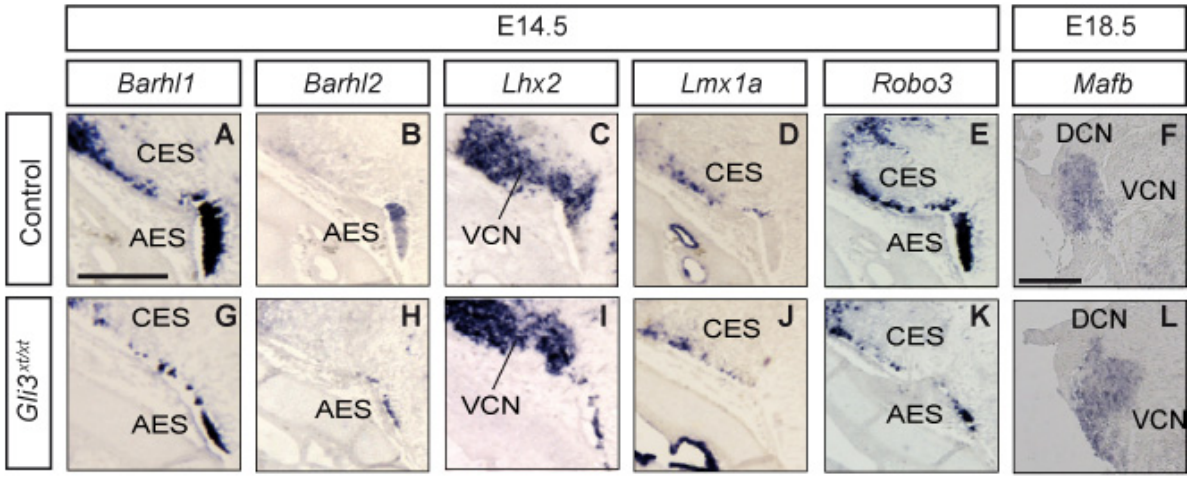

Figure 27. The cochlear nuclei develop normally in *Gli3*$^{xt/xt}$ mutants. Coronal sections of E14.5 (A-E, G-K) and E18.5 (F,L) controls and *Gli3*$^{xt/xt}$ hindbrains at the level of the cochlear nuclei (r6). The cochlear extramural stream (CES, Barhl1-, Lmx1a-, and *Robo3*-positive in G, I, J, respectively) and VCN (*Lhx2* and *Mafb* positive in I and L, respectively) in the *Gli3*$^{Xt/Xt}$ hindbrain are comparable to the CES and VCN in controls (A-F). The *Barhl2* positive AES (B,H) is clearly separated from the CES (D,J) in both control and mutant hindbrain. 5 control and 4 mutant embryos were analyzed for *Lhx2* and *Barhl2*; 3 controls and 3 mutants for *Robo3*; 4 controls and 4 mutants for *Lmx1a*; 3 controls and 3 mutants for *Mafb*. Scale bar: 200 μm (A-E, G-K), 400 μm (F, L).

4.11. The inactivation of *Gli3* in the cerebellum does not alter precerebellar neuron development

PN/RTN axonal extension and targeting events respond to cues encountered in the environment, including contact with the synaptic target, and are accompanied by the initiation of a specific gene expression program (Diaz et al., 2002). In heterozygous *Lurcher* mice, a dominant-active mutation that causes Purkinje cell death and a subsequent loss of granule cells (Caddy and Biscoe, 1979), mossy fibers are impaired in their ability to switch from an axon extension state to one of synapse formation. In addition, these mice have an ectopic distribution of PN/RTN neurons along the AP axis that partially resembles the alterations found in *Gli3*$^{xt/xt}$ mutants (Resibois et al., 1997). Precerebellar projections reach the cerebellum between E14 - E16 (Reeber et al, 2012, Rahimi-Balei et al., 2015), thus, precerebellar AES migration could potentially be influenced by the alterations in cerebellar growth and foliation found in *Gli3*$^{xt/xt}$ mutants (Blaess et al., 2008). To investigate if this was the case, *Gli3* was condionally inactivated in the midbrain and r1 of the hindbrain starting at E8.5 using an *Engrailed 1* (*En1*)-Cre line (Kimmel et al., 2000; Blaess et al., 2008). This mouse model is referred to as *En1-Gli3* cko (genotype *En1*$^{Cre/+}$, *Gli3*$^{xt/flox}$; Figure 28A). The cerebella of *En1-Gli3* cko embryos were reduced in size and their foliation was altered, but the phenotype was less severe than in the *Gli3*$^{xt/xt}$ mutants likely because of the later onset of *Gli3* inactivation in the conditional mouse model (Figure 28F-I; Blaess et al., 2008). In contrast, the morphology, position, and Hox gene expression in the ECN, LRN, and ION in r7-r8 was comparable between controls and *En1-Gli3* ckos at E15.5 (Figure 28D1-E5).

Similarly, the AES maintained its compact morphology and cell topography (as indicated by Hox gene expression) in *En1-Gli3* cko embryos (Figure 28F1-G6). As expected from these results, an analysis at E18.5 indicated a comparable precerebellar nuclei formation in control and *En1-Gli3* cko embryos (Figure 28H-K). These results indicate that alterations in the cerebellum are not the primary cause for the phenotype in the precerebellar system. However, a possible influence of an even more severe cerebellar phenotype cannot be fully excluded, since the *Gli3* null cerebellar phenotype could not be fully recapitulated in *En1-Gli3* cko embryos.

4.12. Precerebellar neurons develop normally when *Gli3* is inactivated in the CNS after E10.5

Sections 4.9 and 4.11 indicate that GLI3 does not play a cell-autonomous role in MFN migration. Based on the continuous expression of *Gli3* in a subdomain of the ION throughout embryonic development, GLI3 might play a cell-autonomous role in the assembly of the ION. The defects observed in the ION could in turn influence MFN development. To examine this possibility, a CNS specific *Gli3* conditional knock-out was generated using $Nestin^{Cre/+}$ mice (termed *Nes-Gli3* cko, genotype $Nes^{Cre/+}$, $Gli3^{xt/flox}$) (Figure 29 and 30; Tronche et al., 1999; Blaess et al., 2008, Yamaguchi et al., 2000). In this mouse model, recombination in the entire CNS occurs around E10.5 (Figure 29A, B; Graus-Porta et al., 2001; Blaess et al., 2006). The analysis of the precerebellar nuclei in *Nes-Gli3* cko at E18.5 indicated an identical MFN (Figure 29C1, D1) and CFN (Figure 29C2, D2) distribution as in controls. Moreover, Hox gene expression in the whole hindbrain was comparable between controls and *Nes-Gli3* cko (Figure 29C3-D5). The localization, morphology, and Hox gene expression in the AES and PES were also comparable between E15.5 controls and *Nes-Gli3* cko mutants (Figure 30). Overall, these results demonstrated that the normal development of the precerebellar system does not depend on *Gli3* expression in the ION or other CNS elements after E10.5, suggesting that the alterations found in the precerebellar system of the $Gli3^{xt/xt}$ mutant have to occur before E10.5 and/or be the result of alterations that originate outside of the CNS.

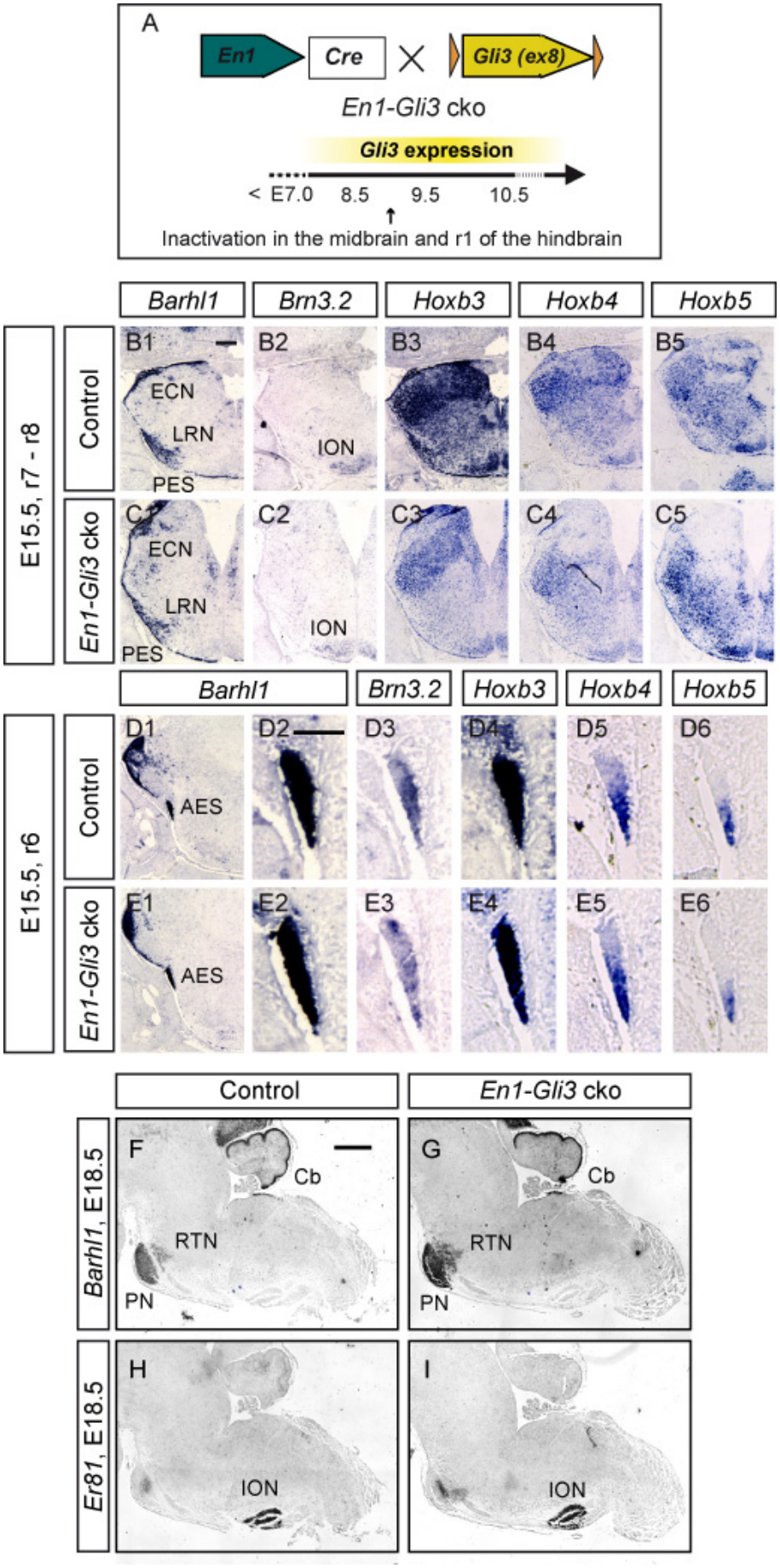

Figure 28. Figure legend continues on the following page.

Figure 28. Inactivation of *Gli3* in the cerebellum and *Gli3*-expressing hindbrain nuclei adjacent to the PN/RTN does not alter precerebellar neuron development. (A) Conditional knock-out of *Gli3* in the Cerebellum (Cb), ventral lateral lemniscus (VLL) and superior olivary complex (SOC) using $En1^{Cre/+}$ mice (*En1-Gli3 cko*). **(B-E)** Coronal sections of E15.5 control and *En1-Gli3 cko* animals at r7-r8 (B-C) and r6 (D-E) hybridized for *Barhl1, Brn3.2, Hoxb3, Hoxb4,* and *Hoxb5*. All precerebellar nuclei and streams are comparable between the control and the *En1-Gli3 cko*. **(F-I)** Sagittal sections of E18.5 control and *En1-Gli3 cko* showing that the general morphology and position of the PN, RTN, and ION remain unchanged in the *En1-Gli3 cko*. N≥3 for each marker and genotype analyzed. Scale bars: 400 μm (B; F-J), 200 μm (B-E).

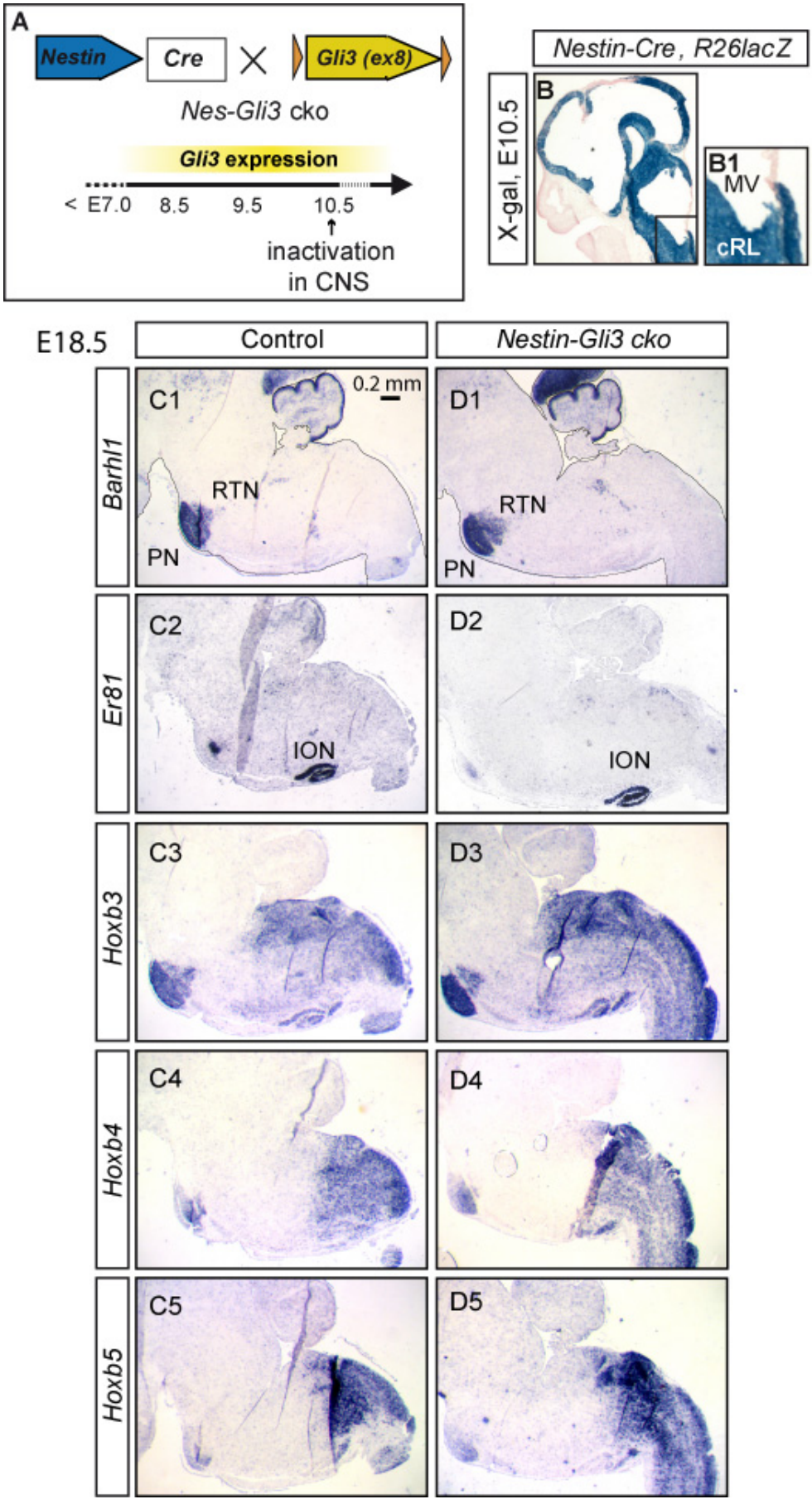

Figure 29. Figure legend continues on the following page.

Figure 29. Inactivation of *Gli3* in neural progenitors after E10.5 does not result in defects in the precerebellar system. (A) Conditional knock-out of *Gli3* in the CNS using *Nestin*$^{Cre/+}$ mice (*Nes-Gli3 cko*). **(B)** Sagittal section of an E10.5 embryo (*Nestin*$^{Cre/+}$, *R26*$^{lacZ/+}$ reporter mouse) stained for X-gal showing recombination in the caudal rhombic lip (clRL), but not in the medullary velum (MV). Inset in B: higher magnification of the boxed area. N=2 embryos. **(C-D)** Sagittal sections of E18.5 control and *Nes-Gli3 cko* animals hybridized for *Barhl1, Er81, Hoxb3, Hoxb4,* and *Hoxb5 in situ* probes The MFN and ION are established in their correct position and the whole hindbrain has a comparable Hox gene expression. N=4 for each marker, stage, and genotype. Scale bars: 200 μm.

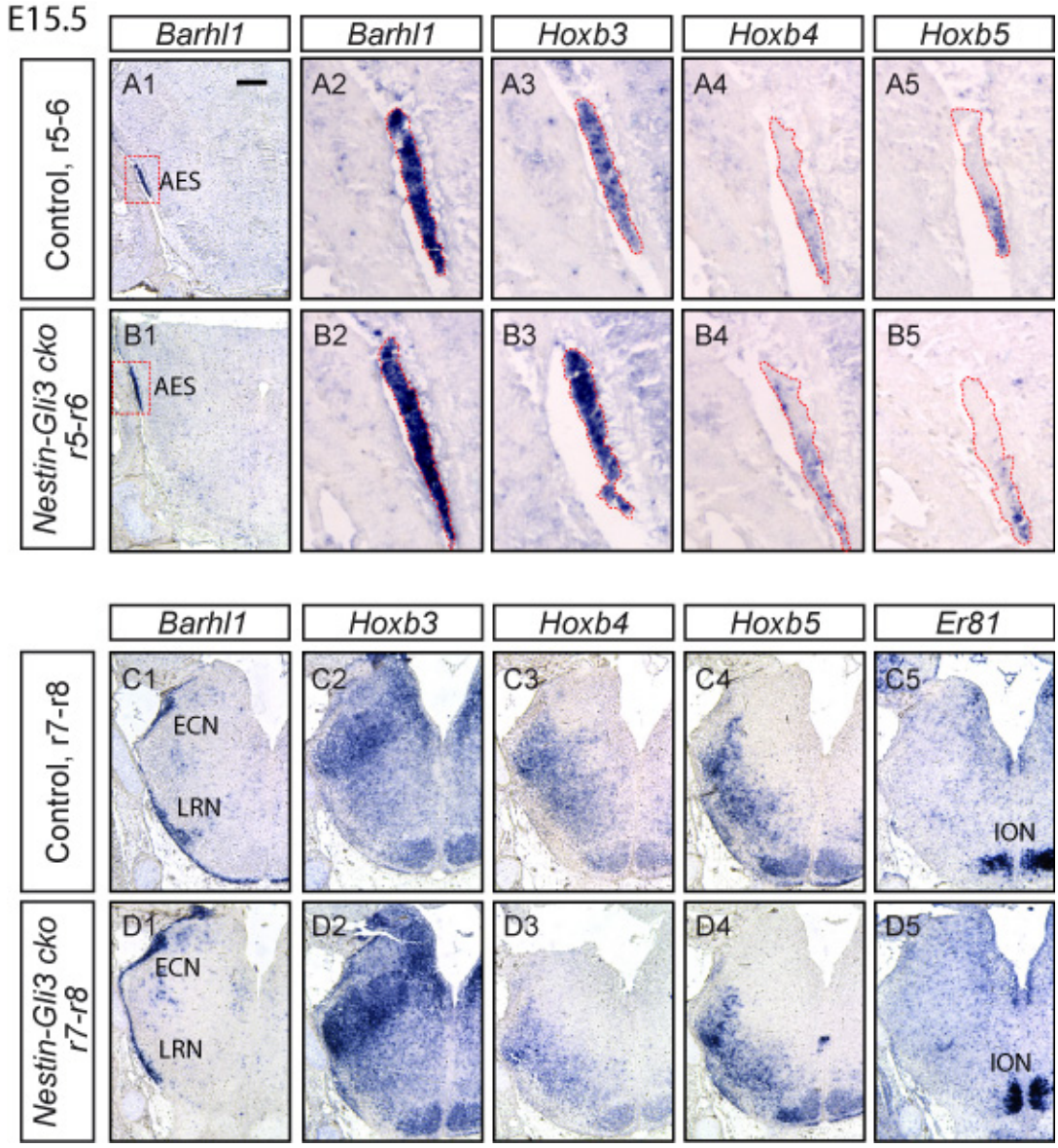

Figure 30. The MFN extramural streams remain unchanged in the *Nes-Gli3 cko*. Coronal sections of E15.5 control and *Nes-Gli3 cko* hindbrains hybridized for *Barhl1*, *Hoxb3, Hoxb4,* and *Hoxb5 in situ* probes. **(A-B)** The AES forms a single compact cluster with a Hox gene expression, which is comparable between controls and *Nes-Gli3 ckos*. **(C-D)** The PES is not delayed and the AES does not invade the ventral regions at r7-r8 in mutants. The LRN, ECN, and ION also show a normal Hox gene expression and morphology. N=4. Scale bars: 200 μm.

4.13. The spinal trigeminal tract is disrupted in *Gli3*$^{xt/xt}$ mutants

Based on the analysis presented so far, GLI3 plays a non-cell-autonomous role in the development of the precerebellar neurons that occurs before E10.5. However, only subtle alterations in the development of the hindbrain were detected (change in the neurotransmitter phenotype in the Pr5 and Sp5ic) and it appears unlikely that this would be the cause for the precerebellar migratory effects observed in *Gli3*$^{xt/xt}$ mutants. An alternative could be that GLI3 influences the development of structures that originate outside the CNS that could interact with the precerebellar neurons during migration. Nichols and Bruce showed that the MFN migrate in close contact with several elements of the peripheral nervous system, including the 5th, 7th, and 8th cranial nerves (5n, 7n, and 8n respectively; Figure 4C; Nichols and Bruce 2006). Moreover, it was recently shown that the AES preferentially travels over a NTN1-rich substrate provided by the basal membrane that does not exist in the cranial nerve roots (Moreno-Bravo et al., 2018; Yung et al., 2018). Thus, the AES cells are not attracted towards the 5n, 7n, and 8n, suggesting that the AES cells could use the cranial nerve roots as points to direct their migration. In the absence of NTN1 or DCC, the AES neurons exit the CNS using the cranial nerve roots (Moreno-Bravo et al., 2018; Yung et al., 2018), suggesting that the cranial sensory tracts could, in principle, work as corridors for precerebellar migration. Johnson (1967) described that one of the earliest phenotypic alterations in the *Gli3*$^{xt/xt}$ mouse is the presence of an excessively large mandibular pharyngeal arch, a structure containing the sensory neurons of the trigeminal ganglion (5Gn). The descending sensory projections of the 5Gn, known as the spinal trigeminal tract (sp5), run along the lateral periphery of the hindbrain at a dorsoventral level that is close to the position of the anteriotly-directed AES (Watson, 2012). The sp5 innervates the Pr5 and Sp5, which seem to be altered in the *Gli3*$^{xt/xt}$ hindbrain, and potential changes in the sp5 could play a role in the alteration of these nuclei in the *Gli3*$^{xt/xt}$ hindbrain. Thus, cranial ganglia and their projections were examined in *Gli3*$^{xt/xt}$ mutants. Immunostaining for ISL1, a regulator of sensory neuron development (Sun et al., 2008), indicated that the 5Gn and its root were enlarged and posteriorly expanded in *Gli3*$^{xt/xt}$ mutants (Figure 31A-D). The number of cells in the 5Gn of *Gli3*$^{xt/xt}$ mutants was significantly increased and the number of apoptotic cells (cleaved caspase-3 positive cells) was significantly decreased as compared to controls (Figure 31E,F,G,H). The size of other cranial ganglia was not obviously altered in *Gli3*$^{xt/xt}$ mutants (e.g. 10Gn; Figure 31M1, N1). DiI labeling of the 5Gn at E14.5 (Figure 32A, B1-I1 and D2-I2) and whole-mount immunostaining of E18.5 brains for peripherin (PRPH) (Figure 32J-M), an intermediate filament protein that is primarily expressed in neurons of the peripheral nervous system (PNS), indicated that the sp5 tract was highly disorganized and less dense in *Gli3*$^{xt/xt}$ mutants. The DiI labeling made the radial collaterals of the sp5 tract innervating the Sp5 visible and indicated possible

disorganization of the neuronal modules or barrelettes in the Sp5 in *Gli3*$^{xt/xt}$ mutants (Figure 32D3-I3). These results suggested that loss of *Gli3* function affects the development of the 5Gn and its central projections, as well as the ultrastructure of the Sp5 nucleus.

4.14. The r7-r8 cell subset in the AES is in close apposition to the spinal trigeminal tract during anterior migration

To examine whether the MFNs in the AES interact with the sp5 tract during their migration, coronal sections of E14.5 controls and *Gli3*$^{xt/xt}$ mutants were immunostained for PRPH to label cranial tracts and for DCC to label MFNs. In controls, the AES was located dorsally to the sp5 (Figure 31O). During its anterior-oriented migration, the AES was positioned just lateral to the sp5 and cells in the ventral two-thirds of the AES appeared to be in close contact with the sp5 (Figure 31K,M). At r3-r4, where the AES reaches the root of the 5n to turn towards the ventral midline, the AES was separated from the sp5 (Figure 31I). In *Gli3*$^{xt/xt}$ mutants, analysis of the PRPH immunostaining confirmed that the sp5 was disorganized and less fasciculated than in controls. DCC immunostaining confirmed that the AES was fragmented into small clusters in *Gli3*$^{xt/xt}$ mutants, as previously shown with *Barhl1 in situ* hybridizations (compare with Figure 16B1-B2). The DCC+ cells migrating ventrally in r7-r8 were not in contact with the sp5, but were in some cases in contact with DCC+ fibers (Figure 31P), while DCC+ cells in r4-r6 were largely detached from the sp5 (Figure 31L,N). These data show that the AES neurons normally migrate in close apposition to the sp5 during their anteriorly-oriented movement and that the loss of *Gli3* results in the defasciculation of sp5 and an apparent detachment of AES neurons from the sp5. Together these results suggest that the sp5 could function as a scaffold during AES anterior migration and that its disorganization might be one factor contributing to the defects in AES migration in *Gli3*$^{xt/xt}$ embryos.

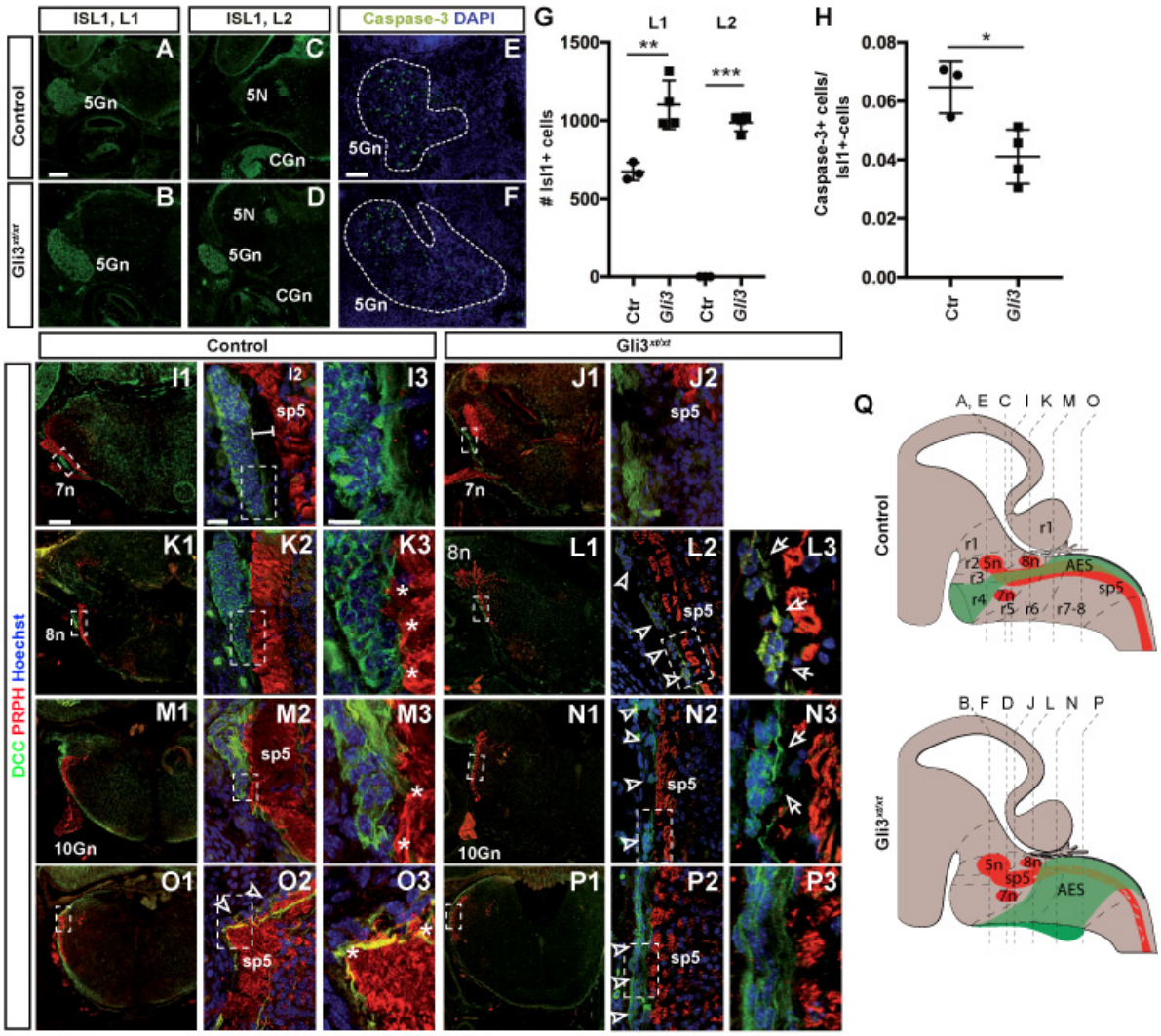

Figure 31. The ventral subset of the AES is in close apposition to the spinal trigeminal tract during anterior migration in controls but not in *Gli3*$^{xt/xt}$ mutants. (A-F) *Gli3* inactivation results in a posterior expansion of the trigeminal ganglia (5Gn) and reduced cell death in 5Gn. E14.5 coronal slides, immunostaining for ISL1 (A-D), and cleaved caspase-3 (E,F). **(G,H)** Quantification of ISL1+ cells (G) and of cleaved caspase-3 positive cells in 5Gn; n=3 controls, n=4 mutants. *p<0.05, **p<0.01, ***p<0.01, two-tailed Student's t-test. Values are represented as mean ± SD. (I1-P3) AES and the spinal trigeminal tract (sp5). E14.5 coronal slides, immunostaining for PRPH and DCC. The PRPH-expressing sp5 extends from r3/r4 to the upper cervical spinal cord. In the control hindbrain, the DCC-positive AES is positioned close to the sp5 before (O, asterisks in O3) and during the anterior phase of migration (K,M) and separates from the sp5 during the final ventral phase of migration in r3/r4 (I). Cells in the ventral AES appear to be in direct contact with the sp5 during their anterior migration (K3,M3, asterisks). In *Gli3*$^{xt/xt}$ mutants, the sp5 is disorganized and increased in size at anterior levels (J) but thinned out and less fasciculated at posterior levels (L,N,P). The AES is fragmented in small clusters (arrowheads in L2,N2,P2) and detached from the sp5 (arrows in L3,N3,P3). At the level of r3/r4, the AES is not visible in the mutants (J2), thus no higher magnification is shown. (I3-P3) Maximum intensity projections of Z-stacks acquired with structured illumination. 3 control and 3 mutant embryos were analyzed. (Q) Summary schematic. 5n, trigeminal nerve; 5N, motor trigeminal nucleus; 7n, facial nerve; 8n; vestibulocochlear nerve; 10Gn, vagus nerve ganglion; CGn, cochlear (spiral) ganglion. Scale bars: 200 µm (A-D; I1-P1), 100 µm (E,F), 25 µm (I2-P2), 12.5 (I3-P3) µm.

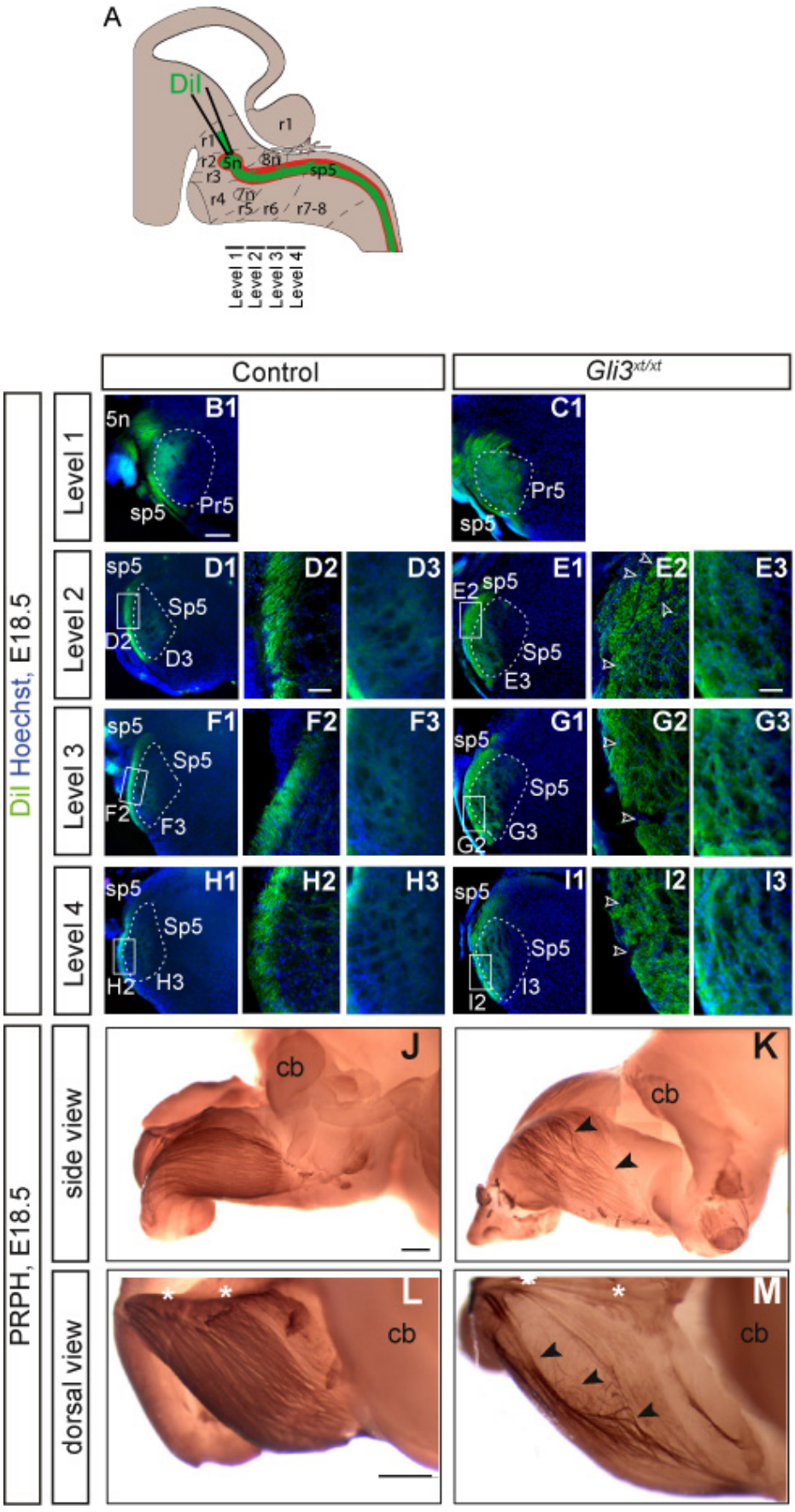

Figure 32. Figure legend continues on the following page.

Figure 32. Disorganization of the spinal trigeminal tract in *Gli3*$^{Xt/Xt}$ mutants. (A-I) Retrograde tracing of central trigeminal projections by injecting DiI into the trigeminal ganglia (5Gn) of E18.5 control and *Gli3*$^{Xt/Xt}$ mutants. (A) DiI diffusion results in labeling of ascending tract axons innervating the principal trigeminal nucleus (Pr5) and of descending projections forming the spinal trigeminal tract (sp5), which innervate the spinal trigeminal nucleus (Sp5). The anteroposterior levels shown in B-I are indicated. (B-I) In the control, the sp5 tract is a compact axonal bundle that sends perpendicular projections into the barrelette neurons of the Pr5 (B) and Sp5 nuclei (D, F, H). In the *Gli3*$^{Xt/Xt}$ mutants the sp5 tract is defasciculated (arrowheads in E´,G´,I´) and the projections into the barrelettes of the Pr5 and Sp5 are disorganized (C, E, G, I). D´ - I´ are maximum intensity projections of Z-stacks acquired with structured illumination; areas are indicated in D-I. Note that the red fluorescent DiI signal was changed to green for better visualization. n=8 controls, n=2 *Gli3*$^{Xt/Xt}$ mutants. (J-M) Whole-mount immunostaining for peripherin (PRPH) to visualize the trigeminal tract shows the disorganization of the sp5 in *Gli3*$^{Xt/Xt}$ mutants. Side view (J,K) and dorsal view (L,M). Asterisks indicate the dorsal midline. Note that the images are composed of several stitched images to have the entire hindbrain in focus. n=4 controls, n=2 mutants. Scale bars: 200 µm (B-M), 50 µm (D´-I´).

5. DISCUSSION

Studies using *Gli3* null and hypomorph mutants have shown that GLI3 plays a role in the development of several dorsal brain structures by directly influencing early developmental processes such as dorsoventral patterning, cell proliferation, and cell survival. In the hindbrain, Johnson (1967) described phenotypic alterations in the *Gli3*$^{xt/xt}$ mouse that included an open neural tube, dorsally misplaced otic vesicles and enlarged anterior rhombomeres (r1-r4). Persson et al. (2002) and Lebel et al. (2007) demonstrated that GLI3 is required for proper patterning of several intermediate and ventral progenitor domains in the hindbrain and spinal cord. These studies supported the role of GLI3 as a suppressor of ventral progenitor fate. Recently, Arellano showed that precerebellar nuclei, which are derived from progenitor neurons in the clRL (Arellano, 2011), are not properly established in *Gli3*$^{xt/xt}$ embryos, indicating a potential role of GLI3 in patterning of the clRL or in regulating the migration of precerebellar neurons.

This thesis investigates GLI3 function in the development of the posterior hindbrain by analyzing *Gli3*$^{xt/xt}$ mutant embryos and mutant mice in which *Gli3* is conditionally inactivated. Based on this analysis, it concludes that in absence of functional GLI3, the precerebellar nuclei originating from progenitors in the clRL are the most severely affected nuclei in the hindbrain. To gain insight into the role of GLI3 in the development of the precerebellar system, the function of GLI3 was dissected during the establishment of the clRL, and during the migration and nuclei formation of precerebellar neurons in these mouse models. The thesis provides evidence for an indirect role of GLI3 in regulating precerebellar migration and proposes that the precerebellar phenotype might be a consequence of altered trigeminal central sensory fibers in the hindbrain.

5.1. Role of GLI3 in hindbrain patterning

GLI3 regulates early patterning events in the spinal cord, cortex, dorsal midbrain, and cerebellum (Blaess et al., 2008; Persson et al., 2002; Theil et al., 1999). Previous studies in the spinal cord and hindbrain, which show similarities in regard to progenitor domains and patterning strategies (Figure 2; Hernandez-Miranda et al., 2017), indicate that GLI3 is required to restrict the expression of intermediate and ventral progenitor domains from expanding dorsally, but dispensable for the induction of the most dorsal progenitors (Persson et al., 2002; Meyer and Roelink, 2003). In the spinal cord, the ventral (V2 V1, V0) and intermediate (dI6; homologous to dB4 in the hindbrain) progenitors expand dorsally at the expense of more dorsal progenitors (i.e. dI4, dI5; homologous to dB1 and dB3 domains in the hindbrain) (Persson et al., 2002). Ventralization in the absence of functional GLI3 occurs also in the forebrain (Theil et al., 1999, Tole et al., 2000). In contrast to these findings, the results in this thesis show that in the hindbrain, the extent of transcription factors defining the

clRL, including *Olig3*, *Atoh1*, *Ascl1,* and NGN1, are comparable between controls and *Gli3*$^{xt/xt}$ mutants. Analysis of the proliferative potential of *Atoh1*+ and *Ngn1*+ progenitors, and the expression of *Wnt1* (an important proliferative regulator), also indicate that loss of *Gli3* does not affect the proliferation of clRL progenitors. The only difference that could be detected when comparing the clRL in controls and *Gli3* mutants was a slight reduction of the *Ptf1a* domain, but only in r8 (Figure 10T). Since the ION and Sp5ic originate from the *Ptf1a* domain in r7-r8 (Yamada et al., 2007, Iskusnylch et al 2016), the reduction of the *Ptf1a* domain in *Gli3*$^{xt/xt}$ mutants might have a direct influence on their development. Nonetheless, it is unlikely to be the cause for the altered distribution of MFNs in *Gli3*$^{xt/xt}$ mutants unless the changes in the Sp5ic alter the organization of the sp5. These possibilities are discussed in the next sections.

5.2. A potential cell-autonomous role of GLI3 in the *Ptf1a* progenitor domain

Based on the results described above and the maintained expression of *Gli3* in the *Ptf1a* domain at E9.5 and E10.5 (Figure 5), GLI3 might have a direct influence in the establishment of the *Ptf1a* progenitor domain and thus, an influence on ION and Sp5ic progenitor specification. Analysis of the ION in *Gli3*$^{xt/xt}$ mutants showed that the anterior ION was reduced in size and that the distribution of the neurons was altered. Hox gene expression analysis to separate the CFNs into subpopulations based on their rhombomeric origin indicated a proportional reduction of r7- and r8-derived neurons in *Gli3*$^{xt/xt}$ mutants, pointing out an overall reduction of the ION. Conditional inactivation of *Gli3* in the CNS at E10.5 (*Nes-Gli3* cko) had no effect on ION morphology or size (Figure 29 and Figure 30), excluding a role for *Gli3* in CFN differentiation or migration after E10.5. The IMS was separated using the expression of *Er81* (present in CFN progenitor cells and a subpopulation of differentiated neurons) and *Brn3.2* (only present in a subpopulation of differentiated CFN). Three subpopulations were identified in controls: a *Brn3.2+/Er81-*, a *Brn3.2+/Er81+,* and a *Brn3.2-/Er81+* subpopulation. Of these, the *Er81*+/*Brn3.2*- subset is absent in *Gli3*$^{xt/xt}$ mutants. Consistent with the general ION size reduction, *Er81* is expressed throughout most of the ION (except for the MAO and DM). Interestingly, the *Er81*+/*Brn3.2*- CFNs are the subpopulation leading the IMS and thus, it is possible that they might be the earliest to exit the ventricular zone. Since CFNs arise only between E9-E11, it is possible that the conditional ablation of *Gli3* in *Nes-Gli3* cko mice would not allow to detect an early cell-autonomous role of GLI3 in these CFN progenitors. Whether the slight reduction of the *Ptf1a* domain is sufficient to explain the phenotype in *Gli3*$^{xt/xt}$ mutants is not clear. Other potential changes in the progenitors could be an increase in cell death, altered cell cycle exit or changes in the fate of generated neurons. To obtain insight into potential alterations in CFN differentiation (as a consequence of changes in CFN progenitors), an analysis of the

neurotransmitters expressed in ION neurons was performed at E14.5. In *Gli3*$^{xt/xt}$ mutants, the *vGlut2*+ neurons composing most of the ION were reduced in number, but this seemed to be proportional to the overall size reduction of the ION. Moreover, GABAergic neurons were found in areas where the ION is normally present in controls. This last observation may point to a change of fate in ION neurons In *Gli3*$^{xt/xt}$ mutants, but it is more likely that these are non-ION GABAergic neurons invading the area normally occupied by the ION in the wild-type hindbrain. Thus, the primary cause for the reduced size of the ION remains to be investigated.

As indicated in section 5.1., the Sp5ic also originates from the *Ptf1a* domain in r7-r8 (Yamada et al., 2007, Iskusnylch et al 2016). The analysis of the *Gli3*$^{xt/xt}$ hindbrain using various markers at E14.5 indicated a strong decrease in *Gad1*-expressing neurons (Figure 26) in the Sp5ic, indicating that the fate of some neurons within this nucleus had changed. DiI anterograde labeling of 5Gn sensory projections in *Gli3*$^{xt/xt}$ mutants shows that the barrelette organization in the Sp5ic is altered (Figure 31). Therefore, the phenotype in the Sp5ic in absence of *Gli3* could be caused by intrinsic changes in the development of its progenitors (as discussed for the ION) or could be due to the disrupted innervation by the sp5 (the descending central projections of the 5Gn). In conclusion, changes in *Ptf1a*-expressing progenitors in *Gli3*$^{xt/xt}$ mutants may contribute to the reduction in CFN neurons and altered cell composition of the Sp5ic, but further experiments assessing cell death, proliferation and cell cycle exit at early developmental stages (E9.5, E10.5) will be necessary to investigate this possibility.

5.3. GLI3 functions non-cell-autonomously in the development of *Atoh1*-derived neuronal populations in the hindbrain

The migration of precerebellar MFNs is severely altered in *Gli3*$^{xt/xt}$ mutants (Figure 6, Figure 7, and Figure 15), while the *Atoh1*-expressing MFN progenitor domain was normal in *Gli3*$^{xt/xt}$ mutants (Figure 5). Moreover, differentiation of MFNs was unaffected, as all *Atoh1*-lineage markers (*Barhl1*, *Barhl2*, and *Lhx2*) and Hox genes were present at the time points analyzed. *Gli3* was only expressed in the *Atoh1* progenitor domain at r6-r8 before E10.5, but the MFNs are generated from this domain between E11.5-E17.5. This dynamic expression pattern of *Gli3* suggested a non-cell autonomous role of GLI3 in MFN development. This was confirmed using conditional inactivation of *Gli3* in *Atoh1-expressing* progenitors (*Atoh1* Gli3 cko) and in the CNS after E10.5 (*Nestin* Gli3 cko) since the phenotype between controls and mutans was comparable.

To study whether non-precerebellar neurons that are generated from the *Atoh1* lineage in the clRL before E10.5 are altered and could potentially influence precerebellar MFN migration, the caudal rhombic lip stream, which gives rise to a small subset of Sp5ic neurons and the

cuneate nucleus (Rose et al., 2009), was analysed in controls, *Gli3*$^{xt/xt}$ mutants, and *Atoh1-Gli3* cko mutants (Figure 14). No changes were found in the migratory stream or in the distribution of the neurons in the Sp5ic or cuneate nucleus (positive for *Lhx2*, *Lhx9*, and/or *Barhl2*; Rose et al., 2009) between controls and *Gli3*$^{xt/xt}$ mutants (Figure 14, Figure 24, Figure 25, and Figure 26).

To examine whether GLI3 influences the development of other *Atoh1*-derived neurons in the hindbrain, the CES and VCN (derived from r2-r5) (Figure 27), as well as the SOC (r4/5) and VLL (derived from r4 and not yet identified sources) (Figure 26, Figure 24, and not shown) were analyzed. For all these nuclei, the cell distribution in controls, *Gli3*$^{xt/xt}$ mutants, and *Atoh1* Gli3 cko mutants was comparable. The only other *Atoh1*-derived neuronal population that has been reported to be altered in *Gli3*$^{xt/xt}$ mutants are the cerebellar granule cells derived from the uRL (r1), which are reduced in number and are abnormally distributed (Blaess et al., 2008). These alterations are non-cell autonomous and due to early patterning events, as no alterations are observed in *Atoh1*- or *Nes-Gli3* cko mutants (Blaess et al., 2008 and data not shown). The early patterning defects are caused by a widened expression domain of *Fgf8* in the isthmic organizer of *Gli3*$^{xt/xt}$ mutants (Blaess et al., 2008). Overall, these data suggest that *Gli3* does not play a cell-autonomous role in the development of *Atoh1*-expressing progenitors in the RL.

5.4. Role of GLI3 in trigeminal ganglia and spinal trigeminal tract development

The 5Gn is a cluster of peripheral neurons and glial cells in the head that arises from an ectodermal thickening, the trigeminal placode, and neural crest cells (NCCs) generated from the most dorsal edge of the anterior hindbrain between E8-E9 (Barlow, 2002; Steventon et al., 2014; Frisdal and Trainor, 2014). The trigeminal placode-derived neurons contribute predominantly to the distal part of the 5Gn, whereas the neural crest-derived neurons to the proximal components and associated glia. Several pieces of evidence indicate that NCCs play an essential role in 5Gn condensation and in the proper establishment of central projections to the hindbrain (Steventon et al., 2014), being the position of a particular cranial nerve directly related to the NCC migratory pathway (Chen et al., 2011; Schwarz et al., 2008, Freter et al., 2013).

The original description of the *Gli3*$^{xt/xt}$ phenotype had already pointed out a cranial sensory ganglia enlargement in the absence of *Gli3* (Johnson et al., 1967). Johnson described that one of the earliest hallmarks of the phenotype was a remarkable enlargement of the maxillary and mandibular divisions of the first pharyngeal arch (Johnson et al., 1967), which are metameric structures colonized by NCCs that generate most cartilages, bones and connective tissue of the craniofacial and neck bones (Fridal and Trainor, 2014). Interestingly, mutations affecting *Gli3* or the GLIA:GLIR ratio are linked to facial malformations, including

upper jaw (Johnson, 1967), calvarial and parietal bone (Tabler et al, 2016), midfacial widening (Chang et al., 2016) and ectopic ossification in the interfrontal suture together with craniosynostosis (Veistinen et al., 2012); alterations that phenocopy the severe craniofacial malformations characteristic of the human Greig cephalopolysyndactyly syndrome, a condition caused by loss of function mutations in the *Gli3* gene (Biesecker, 2008). These observations point to the potential role of GLI3 in regulating NCC proliferation. Indeed, *Gli3* downregulation is linked to NCC over-proliferation (Murdoch and Copp, 2010; Chang et al, 2016) due to expanded *Fgf8* expression (Shao et al., 2015; Tabler et al., 2016), a known survival factor, fate determinant and chemoattractant for NCC (Minoux and Rijli, 2009; Chen et al., 2012). GLI3 is a negative regulator of *Fgf8* (Aoto et al., 2002) and it can also inhibit Wnt signaling (Ulloa et al., 2007), which is reported to be important for NCC survival, differentiation, and cell adhesion in mice (Brault et al, 2001; Hari et al, 2002). In $Gli3^{xt/xt}$ mutants, the expression of *Fgf8* from the isthmic organizer is enhanced and expands caudally (Blaess et al., 2008). FGF8 from the isthmic organizer plays crucial functions in the development of the trigeminal placode and NCCs (Trainor et al., 2002; Canning et al., 2008; Minoux et al., 2008; Chen et al., 2012, Frisdal and Trainor, 2014). In particular, it regulates NCCs populating the first pharyngeal arch (which arise from the posterior midbrainand r1-r3 and populate the 5Gn; Irving and Mason, 2000; Trainor et al., 2002; Tümpel et al., 2009), and cooperates with WNT signaling to induce *Pax3* expression in the trigeminal placode (Canning et al., 2008), which is required for proper 5Gn/5n development (Stark et al., 1997; Dude et al., 2009). In addition, GLI3 may influence NCC development by regulating the activity of genes normally activated by SHH since inactivation of *Smo* in NCCs, a genotype that should lead to an increase in GliR:GliA ratio results in decreased proliferation and increased apoptosis of NCC, and facial truncation (Jeong et al., 2004). Evidence from *Xenopus laevis* indicate that Gli2 (expressed in prospective, premigratory and migratory NCCs) is required for induction, specification and survival (but not proliferation) of NCCs and that it plays a cell-autonomous role in NCC migration and cranial ganglia formation (Cerrizuela et al., 2018). Consistently, conditional inactivation of *Ptch1* in mice, which results in an increase of SHH signaling, generates an abnormal integration of NCCs and placodal cells into cranial ganglia, and strong alterations of the 5n and 7n (Kurosaka et al., 2015). Based on these observations and the fact that *Gli3* is expressed in the 5Gn at E9.5 and E10.5 (Figure 5), GLI3 could play a role in the proper establishment of the 5Gn by influencing the development of NCCs (and potentially the trigeminal placode). Since the 5Gn gives rise to the sp5, and the sp5 seems to be important for MFN migration (discussed below), the non-cell autonomous role of GLI3 in MFN migration could be its influence on 5Gn development.

5.5. Role of GLI3 in regulating migration of precerebellar neurons

5.5.1. IMS

Even though the generation of CFNs appeared to be compromised in *Gli3*$^{xt/xt}$ mutants, the neurons followed the correct intramural migratory route. Moreover, after tangential migration, the CFNs formed a layered structure that partially resembled the subdivisions of the ION in controls. Thus, CFN migration during ION nucleogenesis appeared to be normal in *Gli3*$^{xt/xt}$ mutants. Slit molecules in the floor plate and ROBO1/ROBO2 receptors in the ION seem to play a role in regulating the organization of ION neurons during nucleogenesis (Backer et al., 2007; Di Meglio et al., 2008). *Robo1/Robo2* expression in the ION was comparable between controls and *Gli3*$^{xt/xt}$ mutants at E13.5 and E15.5 (Figure 19 and Figure 22). This is consistent with the normal distribution of CFNs in *Nes-Gli3* cko embryos since a direct role of GLI3 in regulating migration would be expected to result in an abnormal phenotype in this conditional ko mutant. Therefore, the altered ION structure in *Gli3*$^{xt/xt}$ mutants is not due to alterations in migration, but, as discsussed above, is likely the consequence of alterations in CFN progenitors.

5.5.2. AES

The AES is a compact and well-defined migratory stream that maintains an internal order based on the rhombomeric origin of its cells (r6-r8). Based on the expression of *Lhx2*, *Barhl2*, *Brn3.2, Hoxb3*, *Hoxb4*, and *Hoxb5* (this thesis; Di Meglio et al., 2013), three subpopulations can be identified (Figure 16). This thesis demonstrates that in *Gli3*$^{xt/xt}$ mutants, the AES is fragmented into clusters that are distributed all along the AP axis. The cells arising from r7-r8 fail to turn anteriorly and remain in the same rhombomeres where they originate, while the cells arising from r6 maintain, to some degree, their ability to migrate anteriorly. Analysis of the different guidance receptors in *Gli3*$^{xt/xt}$ mutants reveal that DCC (Figure 21B, D, F, and Figure 31I-P) and *Robo3* (Figure 23A5-H5) are present in all AES cell clusters, but that *Cxcr4,* which is expressed throughout the AES in controls, is only present in the r7-r8-derived cells (Figure 22F3, F4, H3, H4). The *Cxcr4* downregulation in r6-derived neurons could be the cause for promiscuous intramural delaminations of AES neurons in anterior rhombomeres in *Gli3*$^{xt/xt}$ mutants (Figure 7F-H) since similar derailments from the marginal stream also occur in *Cxcr4* null mutants (Zhu et al., 2009). Nonetheless, since the r6 population maintains its ability to migrate anteriorly and *Cxcr4* is only down-regulated in this population, it is unlikely that changes in *Cxcr4* expression can by itself explain the AES phenotype in *Gli3* mutants. Overall, these observations indicate that alterations in guidance receptors in MFNs are an unlikely explanation for the inability of most AES neurons to migrate anteriorly in *Gli3*$^{xt/xt}$ mutants. This and the lack of phenotype in *Atoh1-Gli3* cko

embryos is consistent with a non-cell autonomous role of GLI3 in anteriorly-directed MFN migration (Figure 24 and Figure 25). Moreover, since *Nes-Gli3* cko embryos lack a phenotype in MFN migration (Figure 29 and Figure 30), the cause for the altered migration in *Gli3*$^{xt/xt}$ mutants is either a change in early patterning events in the hindbrain or alterations in non-CNS structures that in turn influence AES migration. Indeed, this thesis provides evidence supporting the potential role of a non-CNS derived structure (the sp5) in MFN migration by showing an apparent direct contact between the sp5 and MFNs during rostral AES migration (Figure 31), that the sp5 and AES are altered in *Gli3*$^{xt/xt}$ mutants (Figure 31 and Figure 32), and that the interaction between the sp5 and AES seems to be compromised in *Gli3*$^{xt/xt}$ mutants.

How could the sp5 regulate AES migration? The cell adhesion molecules (CAMs) establish homophilic (e.g. cadherins) or heterophilic (e.g. TAG-1) interactions to bind cells to other cells, or cells to their substrate. These adhesive interactions provide cell polarization and promote neuron gliding along a substrate during migration (Taniguchi et al., 2006; Kawauchi et al., 2006; Luccardini et al., 2013; Rieger et al., 2009). The sp5 is a substrate rich in cadherins (Redies et al., 1992; Shimamura et al., 1992; Redies and Takeichi, 1996; Korematsu et al., 1998; Wolfer et al., 1994), and even though no study has explored if cadherins are expressed in the AES, the literature indicates that *Ncad*, *Cad8*, *Cad11*, *Cad6,* and *Tag-1* are expressed in the PES (Taniguchi et al., 2006; Kawauchi et al., 2006; Yee et al., 1999; Kyriakopoulou et al., 2002), potentially suggesting that expression of cadherins might be a general feature of MFN migration. Cell migration in the AES proceeds in a loose arrangement during ventral migration (phase 1 and phase 3), but in a compact arrangement during their anterior movement (phase 2) (Figure 4C; Geisen et al., 2008). This cell arrangement seems to be necessary for phase 2 to occur since most of the AES neurons fail to migrate anteriorly when the AES keeps the loose arrangement used during ventral migration, as seen in *Cxcr4*$^{-/-}$, *Unc5c*$^{-/-}$, *Robo1*$^{-/-}$, and *Robo2*$^{-/-}$ mutants (Zhu et al., 2009; Kim and Ackerman, 2011; Di Meglio et al., 2008). This thesis indicates that the neurons in the AES never acquire a compact arrangement in *Gli3*$^{xt/xt}$ mutants and that they tend to continue their ventrally-oriented migration instead of turning anteriorly. The neurons in the most ventral part of the AES (r7-r8-derived neurons) seem to be particularly affected since they completely fail to reach axial levels anterior to r6-r7 (Figure 17 and Figure 18). Interestingly, this same ventral subset appears to interact with the sp5 during rostral migration in control embryos. This interaction is lost in *Gli3*$^{xt/xt}$ mutants (Figure 31). These observations might indicate that the interactions of the ventral AES with the sp5 are necessary for the AES to acquire a compact arrangement and to change the ventral migratory behavior of phase 1 and phase 3, to one allowing anterior migration (phase 2).

Overall, these observations point to the potential involvement of the sp5 in AES migration that needs to be clarified by additional experiments. As of yet, the mechanisms that allow the AES to reach the anterior hindbrain are not understood. The interactions with the sp5 could explain this migratory behavior and are worth exploring further. In this respect, it is interesting that other neuronal populations assemble in compact organizations and/or interact with a scaffold/corridor to undergo long tangential migrations within the CNS. Similar to the MFNs migrating in the AES, the facial branchiomotor neurons (FBMNs) composing the 7N undergo a long process of tangential migration, assemble in a compact arrangement while moving perpendicular to the AP axis, and contact an axonal tract: the medial longitudinal fasciculus, a bundle of pioneer longitudinal axons that arise in the midbrain and transverses the whole hindbrain. FBMNs originate in r4 and migrate as a group of cells that follow a leader cell (the first FBMN to migrate) towards r5. Once in r5, the neurons use the medial longitudinal fasciculus as scaffold to reach the base of r6 (Wanner and Prince, 2013; Rebman et al., 2016), where they settle and form the 7N. At the molecular level, FBMNs tangential migration is regulated by the nested expression of Hox genes (HoxPG1, HoxPG2) and other transcription factors (e.g. *Phox2b*, *Nkx6.1*, and *Ebf1*) that coordinate the expression of effectors required for particular phases of migration (Di Meglio and Rijli 2013; Sotelo and Chedotal, 2013). These include several CAMs and guidance receptors, like *Tag1*/*Cxcr4* during initiation, receptor tyrosine kinase *Ret* and *Cxcr4*/*Cxcr7* during transition, *cadherin-8* during transition/ending phase (Garel et al., 2000; Chandrasekhar, 2004; Cubedo et al., 2009). Interactions between FBMNs and the medial longitudinal fasciculus occur via cadherins, and N-cadherin conditional inactivation in FBMNs (mosaic or complete inactivation) slows migration and induces ectopic positioning of several neurons (Rebman et al., 2016). Other examples of neurons using scaffolds during migration are neuroblasts interacting with astrocytic tubes via CAMs to migrate from the cortex to the olfactory bulb (the rostral migratory stream; Lois et al., 1996), and GnRH1-expressing neurons using the cranial nerve zero as scaffold during their migration from the olfactory pit to the hypothalamus (Vilensky 2014; Taroc et al., 2017). Therefore, the use of scaffolds to direct neuronal migrations across long distances might be a normal process in brain development.

5.5.3. PES

The PES expresses *Brn3.2* before midline crossing (Benzing et al., 2011) and *Er81* when the neurons that constitute the ECN separate from those in the LRN (this thesis). The expression of these transcription factors is conserved in *Gli3*$^{xt/xt}$ mutants, but the onset of PES migration is delayed for half a day to up to one day (Figure 15A-J). Moreover, several ECN/LRN neurons colonize ectopic positions at the midline and laterally in the alar plate, and the ECN does not form properly. Similar to the AES, it is unlikely that changes in guidance receptors

known to be involved in PES migration cause the alterations in the PES of *Gli3*$^{xt/xt}$ mutants since their expression is comparable between controls and *Gli3*$^{xt/xt}$ mutants (Figure 21 – Figure 23). Moreover, a cell-autonomous role is unlikely since no visible alterations exist in *Atoh1-Gli3* cko or *Nes-Gli3* cko mutants. Therefore, indirect effects are likely to cause the delayed migration and ectopic positioning of PES neurons in *Gli3*$^{xt/xt}$ mutants. Potential indirect influence on PES migration could be the presence of AES neurons at caudal levels itself since these ectopic cells might work as a physical barrier hampering proper PES cell flow towards the contralateral side. The collision between two groups of cells can cease migration or even revert its course, and thus, generate ectopic populations (Roycroft and Mayor, 2016). This mechanism could potentially explain why several PES neurons remain within the stream or even invade the space between the two hemispheres of the ION. Still, this does not explain why the PES is delayed from the beginning.

As discussed above, the sp5 could be important in guiding the AES anteriorly. The sp5 may also play a role in PES migration since the sp5 appears to reach the caudal hindbrain at ~ E13.5 in the rat (corresponding to ~ E12 in mouse) (Erzurumlu and Jhaveri, 1992; Miyahara, 2003). Moreover, the PES moves on top of the sp5 at the initial and end phase of its migration. As stated in section 5.5.2, the PES expresses several CAMs (Taniguchi et al., 2006; Yee et al., 1999; Kyriakopoulou et al., 2002), and interestingly, inhibiting their expression or activity (e.g. by using a pan-cadherin dominant negative construct, an RNAi-based gene knock-down of *Ncad*, or polyclonal antibodies blocking TAG-1 activity) results in delayed migration and ectopic distribution of PES neurons in a way that resembles the alterations seen in *Gli3*$^{xt/xt}$ mutants (Taniguchi et al., 2006; Kawauchi et al., 2006; Yee et al., 1999; Kyriakopoulou et al., 2002). Alterations in the sp5 could potentially delay PES migration if it is used as a substrate during the initial phase of migration.

5.6. GLI3 as a non-cell autonomous regulator of neuronal migration in other brain areas

Aside from precerebellar neuron migration, GLI3 has only been reported to influence neuronal migration in a few cases. In all of them, GLI3 plays a non-cell autonomous role by influencing the development of a substrate required for migration. Gonadotropin-releasing hormone 1 (GnRH1)-expressing neurons migrate from the olfactory pit into the hypothalamus and it has been proposed that they use the terminal nerve (also known as cranial nerve zero or cranial nerve N) as a migrating scaffold (Vilensky 2014; Taroc et al., 2017). In *Gli3*$^{xt/xt}$ mutants, the terminal nerve is disorganized and the *GnRH1*-expressing neurons fail to migrate properly (Genis, 2018). The mitral cells migrate from the ventricular zone to the intermediate zone in the cortex, where they send axons that provide guidance to the lateral olfactory tract connecting with the piriform cortex. In *Gli3*$^{xt/xt}$ mutants, the mitral cells are

unable to undergo their normal ventral migration and form ectopic clusters. *In vitro* assays suggest that *Gli3* might act cell-autonomously in regulating ventral migration of mitral cells (Tomioka et al., 2000; Kawasaki et al., 2006). However, conditional inactivation of *Gli3* in the cortex does not result in aberrant migration of these cells (Amaniti et al., 2015), indicating that GLI3 plays an indirect role in mitral cell migration. GLI3 also has been reported to play an indirect role in axon guidance. Midline crossing of callosal axons at the cortico-septal boundary is dependent on the presence of glial and neuronal cell populations serving as a guidepost. In the absence of *Gli3*, *Fgf8* and *Slit2* expand at the cortical midline resulting in severe disorganization of guidepost cells and in agenesis of the corpus callosum (Amaniti et al, 2013; Magnani et al, 2014). Finally, corticothalamic axon guidance is dependent on the proper establishment of the subplate and in *Gli3* mutants, a strong diminishment of subplate neurons occurs that generates indirect alterations in the corticothalamic tract (Magnani et al, 2010; Magnani et al., 2013). Taken together, these pieces of evidence show that GLI3 plays a non-cell autonomous role in neural migration and axonal guidance in several brain areas.

These observations are consistent with the non-cell-autonomous role of GLI3 in MFN migration and suggest that this role might be the proper establishment of structures that provide a substrate or environment necessary for normal MFN migration (discussed in section 5.5). Aside from the precerebellar system, the only obvious alterations in the hindbrain of *Gli3*$^{xt/xt}$ mutants occurred in the cerebellum, the Pr5, and Sp5ic. Changes in the cerebellum were explored as a potential non-cell autonomous role of GLI3 in MFN migration since PN/RTN axonal extension and targeting events respond to contact with the synaptic target (Diaz et al., 2002), and since alterations in the cerebellum of *Lurcher* mice (Caddy and Biscoe, 1979), are accompanied by the presence of eMFNs distributed along the AP axis as in *Gli3*$^{xt/xt}$ mutants (Resibois et al., 1997). The results in this thesis indicate that changes in the cerebellum of *Gli3*$^{xt/xt}$ mutants are not related to the alterations in the precerebellar system since conditional inactivation of *Gli3* in the midbrain/r1 region has no influence on MFN/CFN distribution or arrangement (*En1-Gli3cko*; Figure 28). Changes in the Pr5 and Sp5ic also seem unlikely to influence MFN migration at first sight since the AES move on top of the sp5 and do not contact the Sp5 nuclei at any time point (Figure 31). Nonetheless the Sp5 and Pr5 are the target area for the sp5, and this thesis suggests that this tract could work as a scaffold for rostral AES migration (discussed in section 5.5) Thus, alterations in the Pr5 and Sp5 nuclei could contribute to the alterations in the sp5 (or the other way around; discussed in section 5.2). Therefore, additional experiments clarifying this option are needed.

5.7. Consequences of the altered precerebellar migration in *Gli3*$^{xt/xt}$ mutants for the establishment of connections of precerebellar neurons to the cerebellum

Abnormal formation of precerebellar nuclei is likely to impact on the development of projections to the cerebellum. Indeed, retrograde axonal tracing experiments using the lipophilic dye DiI demonstrated that only a small cluster of eMFNs and a few CFNs establish connections with the cerebellum in *Gli3*$^{xt/xt}$ mutants (few labeled cells in the side contralateral to the DiI crystal placed in the cerebellum; Figure 9B and F). In the case of the eMFNs, only those located at the ventral midline of r7-r8 were DiI labeled. How projections of these neurons reach the cerebellum has not been clarified, however, based on other mouse mutants in which AES migration is altered and MFNs settle ectopically (e.g. in mouse mutants with ectopic expression of *Ntn1* in the mantle layer and in dorsal progenitors), it appears that eMFNs, at least the ones that are located anterior to r6, are able to establish connections with the cerebellum (Di Meglio et al., 2013). In the case of the CFNs, alterations in tangential migration, but not in nucleogenesis, seem to alter connections of the ION. In mutants for *Ntn1*, *Dcc,* and *Robo3,* which show aberrant tangential migration (Marcos et al., 2009; Marillat et al., 2004), connections to the cerebellum are decreased (but not abolished). In contrast, cerebellar projections are correctly established in *Robo1/Robo2* and *Slit1/Slit2* mutants, in which CFN tangential migration is normal, but nucleogenesis is altered (Di Meglio et al., 2008; Dominici et al., 2018). This suggests that other alterations in the hindbrain of *Gli3*$^{xt/xt}$ mutants might influence precerebellar connections. The most likely explanation is the severe cerebellar phenotype of *Gli3*$^{xt/xt}$ mutants (see the introduction, Blaess et al. 2008), which is characterized by a reduced size and highly aberrant cerebellar foliation.

6. CONCLUSIONS

This study shows that GLI3 is necessary for the normal development of the precerebellar system and populations within the trigeminal nuclei. GLI3 is not required for proper patterning of the clRL but is important for establishing the ION and for the correct distribution of mossy fiber neurons (MFNs) in the hindbrain. In absence of *Gli3*, a subpopulation of climbing fiber neurons (CFNs) is not generated and the size of the inferior olivary nucleus is reduced. Analysis of mice in which *Gli3* is inactivated after E10.5 indicates that the alterations in the CFNs are either caused by early changes in clRL development that were not detected in our analysis or are non-cell autonomous. In the MFN population, GLI3 is required for the normal onset of PES migration, and for AES neurons (in particular r7-r8 derived neurons) to migrate anteriorly. Inactivation of *Gli3* after E10.5 or specifically in MFN progenitors does not result in an aberrant MFN phenotype, providing evidence for a non-cell autonomous function of GLI3 in MFN migration. In the wild-type, the r7-r8 derived neurons in the AES appear to contact the spinal trigeminal tract (sp5) during their anterior-oriented migration. In absence of GLI3, the sp5 is highly disorganized and the AES neurons seem to detach from the sp5. In summary, this thesis provides evidence for an indirect role of GLI3 in precerebellar neuron development and proposes a potential novel mechanism required for proper MFN migration.

7. OUTLOOK

7.1. Role of GLI3 in the establishment of the progenitor niche and neuronal differentiation

This thesis analyzed the role of GLI3 in patterning of the clRL. In general, no changes were found in the progenitor domains defining the clRL of *Gli3*$^{xt/xt}$ mutants, except for r8, where the extent of the *Ptf1a* domain was reduced (section 4.7.1). CFNs (a type of dA4 neurons) and GABAergic neurons in the Sp5ic (a type of dB1 neurons) derive from the *Ptf1a* domain (see Figure 2), and both are reduced in *Gli3*$^{xt/xt}$ mutants. If the reduced size of the Ptf1a domain in r8 accounts for the loss of both types of neurons or if it only explains part of the phenotype, was not examined since changes in cell death or in cell cycle exit in the progenitors were not analyzed. To understand if changes in cell death/proliferation contribute to the size reduction of the Ptf1a domain in r8 and thus, to the reduction of dA4 and dB1 neurons in the ION and Sp5ic of *Gli3*$^{xt/xt}$ mutants, cleaved caspase-3 or TdT-mediated dUTP-biotin nick end labeling (TUNEL), and BrdU labeling in *Ptf1a*-expressing progenitors should be performed in brain slices of controls and *Gli3*$^{xt/xt}$ mutants at E9.5-E10.5.

Alterations in the ION/Sp5ic could also be generated if the *Ptf1a*-expressing progenitor domain no longer generates dA4 or dB1 neurons, but instead other types of neurons. Interestingly, the Sp5ic is not only composed of *Ptf1a*-derived neurons like those of the dB1 class, but also by dA1 (glutamatergic *Atoh1*-derived neurons; Rose et al., 2009) and dB3 neurons (glutamatergic *Ascl1*-derived neurons; Iskusnykh et al., 2016). In *Ptf1a* null mutants, an excess of the dB3 neurons populate the Sp5c, and the dA4 neurons in the ION and dB1 in the Sp5c are reduced (Iskusnykh et al., 2016). If an increase in dB3 neurons also occurs in the hindbrain of *Gli3*$^{xt/xt}$ mutants was not studied, but *Lbx1,* which defines all neurons of the class B (including dB1 neurons), expands dorsally in the spinal cord of *Gli3*$^{xt/xt}$ mutants (Persson et al., 2002). Therefore, a change of fate could also contribute to the decrease in CFNs and GABAergic neurons of the SP5ic seen in *Gli3*$^{xt/xt}$ mutants. To clarify this, ISH for *Lbx1* should be performed in the hindbrain (at r6-r8) of *Gli3*$^{xt/xt}$ mutants at E9.5-E10.5. Moreover, *Ptf1a*^{Cre}*, R26*$^{flox\text{-}stop\text{-}flox\ EYFP}$*, Gli3*$^{xt/+}$ controls, and *Ptf1a*^{Cre}*, R26*$^{flox\text{-}stop\text{-}flox\ EYFP}$*, Gli3*$^{xt/xt}$ mutants should be generated (Vasyutina et al., 2007; Matei et al., 2005) to analyze a potential change in the contribution of *Ptf1a*-derived neurons to the Sp5ic. Immunostaining for LMX1B (LIM homeobox transcription factor ß; a marker of dB3 neurons) and GFP (*Ptf1a*-derived neurons) should be performed in sections of these mice and each cell type should be quantified in the Sp5ic/ION. If a change in the contribution of both cell types is confirmed, experiments analyzing the neuronal populations composing the ION and Sp5ic in mutants in which *Gli3* is conditionally inactivated in *Ptf1a*-expressing cells (using *Ptf1a*^{Cre} *to* inactivate *Gli3;* Nakhai et al., 2007; Blaess et al., 2008) and in *Lbx1*-expressing cells (using *Lbx1*^{Cre} *to* inactivate *Gli3;* Vasyutina et al., 2007; Blaess et al., 2008) mouse lines should be performed

to validate a potential cell-autonomous role of GLI3 in *Ptf1a*+ and *Lbx1*+ progenitor differentiation.

Finally, as discussed in section 5.2, the alterations in the sp5 tract of *Gli3*$^{xt/xt}$ mutants could also influence the organization of the Sp5ic. To validate this option, the structure of the Sp5ic should be analyzed in mutants with a normal *Ptf1a* domain but with an altered sp5. This could be achieved by specifically affecting NCC generation (e.g. in mice with conditional ablation of *Sox10* in the dorsal hindbrain using *Wnt1*^{Cre}; Mao et al., 2014) and analyzing cell distribution in the Sp5ic using GAD1 and LMX1B immunostaining.

7.2. Role of GLI3 in neural crest and placodal cell development. Potential influence on the development of the 5Gn and sp5

This thesis indicates that alterations in guidance receptor expression in MFN is an unlikely explanation for the abnormal AES and PES migration found in *Gli3*$^{xt/xt}$ mutants (section 4.8, 4.12; discussed in section 5.5), and suggests that instead, changes in the environment (substrates used for MFN migration) might be involved (section 4.14; discussed in sections 5.5). The thesis suggests that the sp5 might be such a substrate based on the close apposition between AES and sp5 during anterior AES migration. Moreover, the thesis shows that GLI3 might influence 5Gn/NCC development based on the expression of *Gli3* in the dorsal hindbrain (before E10.5) and trigeminal placode/5Gn (E9.5 and E10.5) (section 4.1, discussed in section 5.4), and since the size, organization, and rate of cell death in the 5Gn, as well as the fasciculation of the sp5 are altered in *Gli3*$^{xt/xt}$ mutants.

To confirm if GLI3 is required for NCC or trigeminal placode development and if normal sp5 formation is indeed required for AES migration, an analysis of 5Gn/sp5 development and precerebellar migratory streams should be done in a mouse model where *Gli3* is conditionally ablated from NCCs (*Sox10*$^{Cre/+}$, *Gli3*$^{flox/flox}$; Matsuoka et al., 2005; Blaess et al., 2008) or in placode cells (*Tbx3*$^{Cre/+}$, *Gli3*$^{flox/flox}$; Hoogaars et al., 2007; Hodge et al., 2007; Blaess et al., 2008). Since NCCs and placode cells are required for proper 5Gn/5n formation (Steventon et al., 2014), an influence of GLI3 on their development should affect the sp5. If that occurs, and if the sp5 plays a role in AES migration, comparable alterations in 5Gn/sp5 and MFN distribution to those in *Gli3*$^{xt/xt}$ mutants should occur. These experiments are crucial to shed light on a potential cell-autonomous role of GLI3 in 5Gn/sp5 development and its relationship with the non-cell autonomous alterations in the AES of *Gli3*$^{xt/xt}$ mutants. If the results confirm this hypothesis, experiments proposed in section 7.3 should be performed.

7.3. Role of GLI3 in precerebellar neuronal migration: Interactions between the AES and sp5

If conditional inactivation of *Gli3* in NCCs results in an MFN phenotype that is comparable to the MFN alterations observed in *Gli3*$^{xt/xt}$ mutants, the interactions between sp5 and MFNs should be studied in detail. One possible mechanism is that these interactions could be mediated via homophilic cadherin interactions between MFNs and sp5 (discussed in section 5.7). Cadherin expression has been characterized in the PES, but no study has focused on the expression in the AES. Therefore, a first step would be to identify which cadherins are expressed in the AES by performing an expression analysis using mRNA ISH and IHC for different cadherins. The cadherins expressed in the sp5 at the time of the potential interactions between the AES and sp5 should as well be studied. Once identified the cadherins expressed in the AES (see section 7.4) and sp5, the next experiments could be done. Second, it would be important to gain insight into the cell behavior/morphological changes that the AES neurons undergo while migrating in close apposition to the sp5 and during phase 1 and phase 3. To visualize a small group of AES neurons, mosaic labeling of *Atoh1*-derived neurons using tamoxifen-induced recombination could be performed. In this inducible transgenic mouse model, an estrogen receptor ligand-binding domain (ER) is activated at the desired time with a low dose of tamoxifen to induce Cre-mediated recombination in only some *Atoh1*-derived neurons (*Atoh1*^{CreER}). Using *Atoh1*^{CreER}*, R26*$^{flox\text{-}stop\text{-}flox\ EYFP}$*, Gli3*$^{xt/+}$ controls and *Atoh1*^{CreER}*, R26*$^{flox\text{-}stop\text{-}flox\ EYFP}$*, Gli3*$^{xt/xt}$ mutants (Chow et al., 2006; Matei et al., 2005) electroporated in the 5Gn at E13.5 with a tdTomato-labeled construct would allow the visualization of a small group of AES neurons (EYFP+ cells) and sp5 axons (mosaicism of tdTomato+ axons due to electroporation efficiency) Cre-mediated recombination could be induced by administering tamoxifen directly after electroporation. Electroporation into the 5Gn should be possible since this structure is positioned in a superficial and lateral location of the head and the approach has been successfully deployed in chicken (Shiau et al., 2009). Labeling of the sp5 should be verified, but based on other systems with long axonal projections, it would be expected to occur 3 - 5 days after electroporation (Treubert-Zimmerman et al., 2002). The experiment would be a challenge since only 1:8 animals would be *Gli3*$^{xt/xt}$ mutants with induced recombination, and since survival of the embryos would be reduced due to electroporation and tamoxifen treatment. Next, time-lapse imaging using confocal laser scanning microscopy or 2-photon microscopy on E16.5-E18.5 hindbrain slices of these mouse lines could be performed (Watanabe and Murakami, 2009; Shinohara et al., 2013). An approximate of 2 hrs should be possible to image based on the EYFP reporter fluorophore and number of channels. Specific morphological changes/behaviors in AES neurons could be studied in each migratory phase and condition. Clear morphological changes should occur during phase 2 when the neurons

contact the sp5. Potentially, these changes should not occur in *Gli3*$^{xt/xt}$ mutants. To study the potential mechanism of interaction between the AES and sp5, mis- and overexpression of cadherins in the sp5 should be performed using the same electroporation approach described above, but replacing the fluorescent-labeled constructs electroporated in the 5Gn with full length or dominant-negative fluorescent constructs of the cadherins identified in the sp5 (Taniguchi et al., 2006; Kawauchi et al., 2006; Treubert-Zimmerman et al., 2002). Individual and multiple overexpression/inhibition experiments using different cadherin constructs should be tested. Total inhibition could be achieved using a pan-cadherin dominant negative construct (Taniguchi et al., 2006). This strategy should make it clear if cadherins in the sp5 are required for AES migration, which ones are important, and how changes in their concentration influence AES migration.

7.4. Pontine migration as a model of collective migration

This thesis shows that the compact arrangement that the AES acquires during rostral migration in controls is lost in *Gli3*$^{xt/xt}$ mutants, where the stream fragments into small cell-clusters that settle ventrally at ectopic axial levels (section 4.7.4). As discussed in section 5.5.2, this compact arrangement is lost in several mutants that display an MFN distribution which is comparable to the one observed in *Gli3*$^{xt/xt}$ mutants, thus suggesting that this compact arrangement might be required for AES anterior migration. FBMNs also migrate tangentially in a compact arrangement and use an axonal bundle in the process (Wanner and Prince, 2013). FBMNs move using collective migration since the neurons remain interconnected via cadherin interactions and a pioneer neuron (leader cell) directs a group of follower cells (Rebman et al., 2016). The collective assembly of FBMNs is required for normal migration since the conditional inactivation of N-cadherin compromises their cell-cell interactions and FBMN migration (Rebman et al., 2016). If AES migration is also collective is unknown, but it could well be a prerequisite for anterior AES migration to occur. To study this possibility, the time-lapse cell imaging approach already proposed in section 7.3 could be also used to study cell-cell interactions between MFNs in the AES during the different phases of AES migration. In this case, *Gli3*$^{xt/+}$ and *Gli3*$^{xt/xt}$ mice could be electroporated in the clRL at E13.5 with fluorescent constructs and full-length or dominant-negative constructs of the cadherins expressed in the AES (section 7.3; Taniguchi et al., 2006), when all PES neurons are already generated and the AES starts to form. This approach should allow the visualization of a small group of GFP labeled cells and their cell-cell interactions (in those neurons with signal colocalization) in the AES. Studying the interactions between cells in the different phases of AES migration should indicate if the AES moves collectively during the anterior phase of migration a collective type of migration, how the mechanical forces in the AES distribute in the stream, and if a leader/follower cell behavior exists.

8. REFERENCES

Agerman K, Baudet C, Funding B, Willson C, Emfors C. (2000). Attenuation of a caspase-3 dependent cell death in NT4- and p75-deficient embryonic sensory neurons. Mol Cell Neurosci. 16: 258-68

Ahn S and Joyner AL. (2005). *In vivo* analysis of quiescent adult neural stem cells responding to Sonic hedgehog. Nature 437: 894-7

Alvarez-Medina R, Cayuso J, Okubo T, Takada S, Marti E (2008). Wnt canonical pathway restricts graded Shh/Gli patterning activity through the regulation of Gli3 expression. Develompent 135:237-47

Alvarez-Medina R, Le Dreau G, Ros M, Martí E (2009). Hedgehog activation is required upstream of Wnt signalling to control neural progenitor proliferation. Development, 136: 3301-09

Amaniti EM, Hasenpusch-Theil K, Li Z, Magnani D, Kessaris N, Mason JO, Theil T. (2013). Gli3 is required in Emx+ progenitors for the development of the corpus callosum. Dev Biol., 376(2):113-24

Amaniti EM, Kelman A, Mason JO, Theil T. (2015). Cerebral cortex expression of *Gli3* is required for normal development of the lateral olfactory tract. PLoS ONE 10 (10). E0141525

Aoto K, Nishimura T, Eto K, Motoyama J. (2002). Mouse GLI3 regulates Fgf8 expression and apoptosis in the developing neural tube, face, and limb bud. Dev Biol. 251 (2): 320-32

Arellano C. (2011). The role of the zinc finger transription factor Gli3 in the development of the precerebellar system. Diploma thesis. University of Bonn, Bonn.

Backer S, Sakurai T, Grumet M, Sotelo C, Bloch-Gallego E. (2002). Nr-CAM and TAG-1 are expressed in distinct populations of developing precerebellar and cerebellar neurons. Neuroscience, 113:743-8

Backer S, Hidalgo-Sanchez M, Offner N, Portales-Casamar E, Debant A, Fort P, Gauthier-Rouviere C, Bloch-Gallego E. (2007). Trio controls the mature organization of neuronal clusters in the hindbrain. J Neurosci. 27(39): 10323-32

Bai CB, Stephen D, Joyner AL. (2004). All mouse ventral spinal cord patterning by hedgehog is Gli dependent and involves an activator function of Gli3. Dev. Cell 6, 103-15

Barlow LA. (2002). Cranial nerve development: placodal neurons ride the crest. Curr Biol. 12:R171-3

Begbie J, Graham A. (2001). Integration between the epibranchial placodes and the hindbrain. Science. 294(5542):595-8

Benzing K, Flunkert S, Schedl A, Engelkamp D. (2011). A novel approach to selectively target neuronal subpopulations reveals genetic pathways that regulate tangential migration in the vertebrate hindbrain. PloS Genet., 7(6): e1002099.

Bielen H, Houart C. (2014). The Wnt cries many: Wnt regulation of neurogenesis through tissue patterning, proliferation, and asymmetric cell division. Dev Neurobiol., 74(8): 772-80

Biesecker LG. (2008). The Greig cephalopolysyndactyly syndrome. Orphanet J Rare Dis. 3:10

Blaess S, Corrales JD, Joyner AL. (2006). Sonic hedgehog regulates Gli activator and repressor functions with spatial and temporal precision in the mid/hindbrain region. Development, 133(9): 1799-809

Blaess S, Stephen D, Joyner AL. (2008). Gli3 coordinates three-dimensional patterning and growht of the tectum and cerebellum by integrating Shh and Gfg8 signaling. Development, 135 (12): 2093-103

Bloch-Gallego E, Causeret F, Eyan F, Backer S, Hidalgo-Sanchez M. (2005). Development of the precerebellar nuclei: Instructive factors and intracellular mediators in neuronal migration, survival and axon pathfinding. Brain Res Rev., 49: 253-266

Blockus H, Chédotal A. (2016). Slit-Robo signaling. Development, 143: 3037-44

Bonner J, Gribble SL, Veien ES, Nikolaus OB, Weidinger G, Dorsky RI. (2008). Proliferation and patterning are mediated independently in the dorsal spinal cord downstream of canonical Wnt signaling. Dev Biol., 313:398–407.

Borday C, Cabochette P, Parain K, Mazurier N, Janssens S, Tran HT, Sekkali B, Bronchain O, Vleminckx K, Locker M, Perron M. (2012). Antagonistic cross-regulation between Wnt and Hedgehog signalling pathways controls post-embryonic retinal proliferation. Development, 139: 3499-509

Bourrat F, Sotelo C. (1990) Early development of the rat precerebellar system: migratory routes, selective aggregation and neuritic differentiation of the inferior olive and lateral reticular nucleus neurons. An overview. Arch Ital Biol., 128:151–170.

Brault V, Moore R, Kutsch S, Ishibashi M, Rowitch DH, McMahon AP, Sommer L, Boussadia O, Kremler R. (2001). Inactivation of the beta-catenin gene by Wnt1-Cre-mediated deletion results in dramatic brain malformation and failure of craniofacial development. Development 128: 1253 - 64.

Briscoe J, Thérond PP. (2013). The mechanisms of Hedgehog signalling and ist roles in development and disease. Nat Rev Mol Cell Biol., 14(7):416-29

Bruce LL, Mc Haffie JG, Stein BE. (1987). The organization of trigeminotectal and trigeminothalamic neurons in rodents: a double-labeling study with fluorescent dyes. J Comp Neurol., 262: 315–330.

Bulfone A, Menguzzalo E, Broccoli V, Marchitiello A, Gattuso C, Mariani M, Consalez GG, Martinez S, Ballabio A, Banfi S. (2000). Barhl1, a gene belonging to a new subfamily of mammalian homeobox genes, is expressed in migrating neurons of the CNS. Hum Mol Genet. 9: 1443-52

Caddy, KW, and Biscoe TJ. (1979). Structural and quantitative studies on the normal C3H and Lurcher mutant mouse. Philos. Trans. R. Soc. Lond. B Biol. Sci., 287: 167–201

Canning CA, Lee L, Luo S, Graham A, Jones CM. (2008). Neural tube derived Wnt signals cooperate with FGF signaling in the formation and differentiation of the trigeminal placodes. Neural Dev., 3:35

Causeret F, Danne F, Ezan F, Sotelo C, Bloch-Gallego E. (2002). Slit antagonizes netrin-1 attractive effects during the migration of inferior olivary neurons. Dev Biol., 246:429-40

Cerrizuela S, Vega-Lopez GA, Palacio MB, Tribulo C, Aybar MJ. (2018). Gli2 is required for the induction and migration of Xenopus laevis neural crest. Mech Dev., 154: 219-39

Chandrasekhar A. (2004). Turning heads: development of vertebrate branchiomotor neurons. Dev. Dyn., 229: 143-161.

Chang CF, Chang YT, Grethel M, Brugmann SA. (2016). Craniofacial ciliopathies reveal specific requirements for GLI proteins during development of the facial midline. PLOS Genet. 12(11): e1006351. Doi:10.1371/journal.pgen.1006351

Chellapa R, Li S, Pauley S, Jahan I, Jin K, Xiang M. (2008). Barhl1 regulatory sequences required for cell-specific gene expression and autoregulation in the inner ear and central nervous system. Mol Cell Biol., 28(6): 1905-14

Chen Y, Takano-Maruyama M, Gaufo GO. (2011). Plasticity of neural crest-placode interaction in the developing visceral nervous system. Dev Dyn., 240(8): 1880-8

Chen Y, Moon AM, Gaufo GO. (2012). Influence of mesodermal Fgf8 on the differentiation of neural crest-derived postganglionic neurons. Dev Biol., 361(1): 125-36

Chesnutt C, Burrus LW, Brown AM, Niswander L. (2004). Coordinate regulation of neural tube patterning and proliferation by TGFbeta and WNT activity. Dev Biol., 274(2): 334-47

Chizhikov VV, Millen KJ. (2004). Mechanisms of roof plate formation in the vertebrate CNS. Nat Rev Neurosci., 5(10):802-12

Chizhikov VV, Lindgren AG, Mishima Y, Roberts RW, Aldinger KA, Miesegaes GR, Currie DS, Monuki ES, Millen KJ. (2010). Lmx1a regulates fates and location of cells originating from the cerebellar rhombic lip and telencephalic cortical hem. Proc Natl Acad Sci USA. 107(23): 10725-30

Chow LM, Tian Y, Weber T, Corbett M, Zuo J, Baker SJ. (2006). Inducible Cre recombinase activity in mouse cerebellar granule cell precursors and inner ear hair cells. Dev Dyn., 235(11): 2991-8

Ciani L, Salinas PC. (2005). Wnts in the vertebrate nervous system: from patterning to neuronal connectivity. Nat Rev Neurosci 6(5): 351-62

Copp AJ. (1994). Genetic models of mammalian neural tube defects. Ciba Found Symp. 181: 118-43

Cordero D, Marcucio R, Hu D, Gaffield W, Tapadia M, Helms JA. (2004) Temporal perturbations in sonic hedgehog signaling elicit the spectrum of holoprosencephaly phenotypes. J Clin Invest., 114: 485–494.

Cubedo N, Cerdan E, Sapede D, Rossel M (2009). CXCR4 and CXCR7 cooperate during tangential migration of facial motoneurons. Mol Cell Neurosci., 40(4): 474-84

Denaxa M, Kyriakopoulou K, Theodorakis K, Trichas G, Vidaki M, Takeda Y, Watanabe K, Karagogeos D. (2005). The adhesion molecule TAG-1 is required for proper migration of the superficial migratory stream in the medulla but not of cortical interneurons. Dev Biol. 288(1): 87-99

Diaz E, Ge Y, Yang YH, Loh KC, Serafini TA, Okazaki Y, Hayashizaki Y, Speed TP, Ngai J, Scheiffele P. (2002). Molecular anaylsis of gene expression in the pontocerebellar projection system. Neuron, 36:417-34

Di Bonito M, Narita Y, Avallone B, Sequino L, Mancuso M, Andolfi G, Franzè AM, Puelles L, Rijli FM, Studer M. (2013a). Assembly of the auditory circuitry by a hox genetic network in the mouse brainstem. PLoS Genet. 9(2): e1003249

Di Bonito M, Glover JC, Studer M (2013b). Hox genes and region-specific sensorimotor circuit formation in the hindbrain and spinal cord. Dev Dyn., 242(12):1348-68

Di Meglio T, Nguyen-Ba-Charvet KT, Tessier-Lavigne M, Sotelo C, Chédotal A. (2008). Molecular mechanisms controlling midline crossing by precerebellar neurons. J Neurosci., 28:6285-94

Di Meglio T, Kratochwil CF, Vilain N, Loche A, Vitobello A, Yonehara K, Hrycaj SM, Roska B, Peters AH, Eichmann A, Wellik D, Ducret S, Rijli FM. (2013). Ezh2 orchestrates topographic migration and connectivity of mouse precerebellar neurons. Science., 339(6116): 204-7

Di Meglio T and Rijli FM (2013). Transcriptional regulation of tangential neuronal migration in the vertebrate hindbrain. In: Rubenstein J and Rakic P editors. Cellular migration and formation of neuronal connections. p. 377–404. ISBN: 978-0-12-397266-8

Ding Q. (2009). The role of BARHL2 in the neurogenesis of mouse retina and spinal cord. PhD thesis. University of Rochester, Rochester, New York.

Ding Q, Joshi PS, Xie ZH, Xiang M, Gan L. (2012). Barhl2 transcription factor regulates the ipsilateral/contralateral subtype divergence in postmitotic dI1 neurons of the developing spinal cord. Proc Natl Acad Sci USA., 209(5): 1566-71

Domanitskaya E, Wacker A, Mauti O, Baeriswyl T, Esteve P, Bovolenta P, Stoeckli ET . (2010). Sonic hedgehog guides post-crossing commissural axons both directly and indirectly by regulating Wnt activity. J Neurosci., 30(33): 11167-76

Dominici C, Moreno-Bravo JA, Puiggros SR, Rappeneau Q, Rama N, Vieugue P, Bernet A, Mehlen P, Chédotal A. (2017). Floor-plate-derived netrin-1 is dispensable for commissural axon guidance. Nature, 545(7654): 350-54

Dominici C, Rappeneau Q, Zelina P, Fouquet S, Chédotal A., (2018). Non-cell autonomous control of precerebellar neuron migration by Slit and Robo proteins. Development, 145(2) pii: dev150375.

Dude CM, Kuan CY, Bradshaw JR, Greene ND, Relaix F, Stark MR, Baker CV. (2009). Activation of Pax3 target genes is necessary but not sufficient for neurogenesis in the ophthalmic trigeminal placode. Dev Biol. 326: 314–326.

Engelkamp D, Rashbass P, Seawright A, van Heyningen V. (1999). Role of Pax6 in development of the cerebellar system. Development, 126(16): 3585-96

Erzurumlu RS and Jhaveri S (1992). Trigeminal ganglion cell processes are spatially ordered prior to the differentiation of the vibrissa pad. J Neurosci., 12(10): 3946-55

Farago AF, Awatramani RB, Dymecki SM. (2006). Assembly of the brain cochlear nuclear complex is revealed by intersectional and substractive genetic fate maps. Neuron 50(2):205-18

Falli V, Bachy I, Rétaux S. (2002). Expression of the LIM-homeodomain gene Lmx1a (dreher) during development of the mouse nervous system. Mech Dev. 118 (1-2): 225-8

Fredette BJ, Adams JC, Mugnaini E. (1992). GABAergic neurons in the mammalian inferior olive and ventral medulla detected by glutamate decarboxylase immunocytochemistry. Jcomp Neurol. 321(4): 501-14

Freter S, Fleenor SJ, Freter R, Liu KJ, Begbie J. (2013). Cranial neural crest cells form corridors prefiguring sensory neuroblast migration. Development 140:3595–600

Friedrichs M, Larralde O, Skutella T, Theil T. (2008). Lamination of the cerebral cortex is disturbed in Gli3 mutant mice. Dev Biol., 318**,** 203-14.

Frisdal A, Trainor PA. (2014). Development and evolution of the pharyngeal apparatus. Wiley Interdiscip Rev Dev Biol., 3(6):403-18

Garcia AD, PetrovaR, Eng L, Joyner AL. (2010). Sonic hedgehog regulates discrete populations of astrocytes in the adult mouse forebrain. J Neurosci., 30: 13597-608

Garel, S., Garcia-Dominguez, M. and Charnay, P. (2000). Control of the migratory pathway of facial branchiomotor neurones. Development, 127: 5297- 5307.

Geisen MJ, Di Meglio T, Pasqualett M, Ducret S, Brunet JF, Chedotal A, Rijli FM. (2008). Hox paralog group 2 genes control the migration of mouse pontine neurons through slit-robo signaling. PloS Biol. 2008 10;6(6)

Genis EA. (2017). Effects of an Impaired Sonic Hedgehog Signaling Pathway and a Nonfunctional Gli3 Protein on GnRH-1 Neuronal Migration in Gli3 xt/xt mutants. Honors thesis, University of Albany. 1–21

Glasgow SM, Henke RM, Macdonald RJ, Wright CV, Johnson JE. (2005). Ptf1a determines GABAergic over glutamatergic neuronal cell fate in the spinal cord dorsal horn. Development, 132:5461-9

Goetz SC, Anderson KV. (2010). The primary cilium: a signalling centre during vertebrate development. Nat Rev Genet., 11(5):331-44

Goffinet AM. (1984). Events governing organization of postmigratory neurons: studies on brain development in normal and reeler mice. Brain Res., 319(3): 291-96

Goffinet AM. (1992). The reeler gene: a clue to brain and development and evolution. Int J Dev Biol., 36(1): 101-7

Goulding MD, Chelapakis G, Deutsch U, Erselus JR, Gruss P. (1991). Pax-3, a novel murin DNA binding protein expressed during early neurogenesis. EMBO J. 10(5): 1135-47

Gray PA. (2013). Transcription factors define the neuroanatomical organization of the medullary reticular formation. Fron Neuroanat. 14;7:7

Greene NDE, Copp AJ (2014). Neural tube defects. Annu Rev Neurosci., 37: 221-42

Grove EA, Tole S, Limon J, Yip L, Ragsdale CW. (1998). The hem of the embryonic cerebral cortex is defined by the expression of multiple Wnt genes and is compromised in Gli3-deficient mice. Development, 125(12): p. 2315-25.

Guthrie S. (2007). Patterning and axon guidance of cranial motor neurons. Nat Rev Neurosci 8 (11):859-71

Haddad-Tovolli R, Heide M, Zhou X, Blaess S, Alvarez-Bolado G. (2012). Mouse thalamic differentiation: Gli-dependent pattern and Gli-independent pattern. Front Neurosci 6:27

Hari L, Brault V, Kléber M, Lee HY, Ille F, Leimeroth R, Paratore C, Sueter U, Kernier R, Sommer L. (2002). Lineage-specific requirements of beta- catenin in neural crest development. J Cell Biol., 159: 867 - 880

Hashimoto M, Ito R, Kitamura N, Namba K, Hisano Y. (2012). Epha4 controls the midline crossing and contralateral axonal projecitons of inferior olive neurons. J Comp Neurol., 520(8): 1702-20

Hernandez-Miranda LR, Müller T, Birchmeier C. (2017). The dorsal spinal cord and hindbrain: From developmental mechanisms to functional circuits. Dev Biol., 432(1): 34-42

Hägglund AC, Dahl L, Carlsson L. (2011). Lhx2 is required for patterning and expansion of a distinct progenitor cell population committed to eye development. PLoS One. 6(8):e23387

Hui CC, Angers S. (2011). Gli proteins in development and disease. Annu Rev Cell Dev Biol., 27: 513-37

Ille F, Atanasoski S, Falk S, Ittner LM, Märki D, Büchmann-Moller S, Wurdak H, Suter U, Taketo MM, Sommer L. (2007). Wnt/BMP signal integration regulates the balance between proliferation and differentiation of neuroepithelial cells in the dorsal spinal cord. Dev Biol., 304(1): 394-408

Irving C, Mason I. (2000). Signalling by FGF8 from the isthmus patterns anterior hindbrain and establishes the anterior limit of Hox gene expression. Develoment, 127(1)-177-86

Iskusnykh IY, Steshina EY, Chizhikov VV. (2016). Loss of Ptf1a leads to a widespread cell-fate misspecification in the brainstem, affecting the development of somatosensory and viscerosensory nuclei. J Neurosci., 36(9): 2691-710

Jeong J, Mao J, Tenzen T, Kottmann AH, McMahon AP. (2004). Hedgehog signaling in the neural crest cells regulates the patterning and growth of facial primordia. Genes Dev., 18: 937-951.

Johnson DR. (1967). Extra-toes: a new mutant gene causing multiple abnormalities in the mouse. J Embryol Exp Morphol., 17: 543-81

Joksimovic M, Jeannotte L, Tuggle CK. (2005). Dynamic expression of murine HOXA5 protein in the central nervous system. Gene Expression patterns., 5: 792-800

Kawasaki T, Ito K, Hirata T. (2006). Netrin 1 regulates ventral tangential migration of guidepost neurons in the lateral olfactory tract. Development, 133: 845-853

Kawauchi D, Taniguchi H, Watanabe H, Saito T, Murakami. (2006). Direct visualization of nucleogenesis by precerebellar neurons: involvement of ventricle-directed, radial fibre-associated migration. Development, 133 (6): 1113-23

Kawauchi D, Saito T (2008). Transcriptional cascade from Math1 to Mbh1 and Mbh2 is required for cerebellar granule cell differentiation. Dev Biol 322(2):345-54

Kawauchi D, Muroyama Y, Sato T, Saito T. (2010). Expression of major guidance receptors is differentially regulated in spinal commissural neurons transfated by mammalian *Barh* genes. Dev Biol., 344(2): 1026-34

Kiecker C, Lumsden A. (2005). Compartments and their boundaries in vertebrate brain development. Nat Rev Neurosci., 6(7): 553-64

Kiecker C, Lumsden A. (2012). The role of organizers in patterning the nervous system. Annu Rev Neurosci., 35: 347-67

Kim EJ, Battiste J, Nakagawa Y, Johnson JE. (2008). Ascl1 (Mash1) lineage cells contribute to discrete cell populations in CNS architecture. Mol Cel Neurosci., 38: 595-606

Kim D, Ackerman SL. (2011). The UNC5C netrin receptor regulates dorsal guidance of mouse hindbrain axons. J Neurosci., 31(6): 2167-79

Kimmel RA, Turnbull DH, Blanquet V, Wurst W, Loomis CA, Joyner AL. (2000). Two lineage boundaries coordinate vertebrate apical ectodermal ridge formation. *Genes Dev.* 14:1377-*89.*

Klisch TJ, Yi Y, Flora A, Wang L, Li W, Zoghbi HY. (2011). In vivo Atoh1 targetome reveals how a proneural transcription factor regulates cerebellar development. Proc Natl Acad Sci USA, 108(8): 3288-93

Kmita M, Duboule D. (2003). Organizing axes in time and space; 25 years of colinear tinkering. Science, 18: 331-333

Korematsu K, Nishi T, Okamura A, Goto S, Morioka M, Hamada J, Ushio Y. (1998). Cadherin-8 protein expression in gray matter structures and nerve fibers of the neonatal and adult mouse brain. Neuroscience, 87(1): 303-15

Kratochwil CF, Maheshwari U, Rijli FM. (2017). The long journy of pontine nuclei neurons: from rhombic lip to cortico-ponto-cerebellar circuit. Front Neural Circuits., 11:33

Kurosaka H, Trainor PA, Leroux-Berger M, Iulianella A. (2015). Cranial nerve development requires co-ordinated Shh and canonical Wnt signaling. PLoS One, 10(3):e0120821

Kuschel, S., Ruther, U. & Theil, T (2003). A disrupted balance between Bmp/Wnt and Fgf signaling underlies the ventralization of the Gli3 mutant telencephalon. Developmental biology, 260**,** 484-495

Kyriakopoulou K, de Diego I, Wassef M, Karagogeos D. (2002). A combination of chain and neurophilic migration involving the adhesion molecules TAG-1 in the caudal medulla. Development, 129(2):287-96

Lai K, Kaspar BK, Gage FH, Schaffer DV. (2003). Sonic hedgehog regulates adult neural progenitor proliferation in vitro and in vivo. Nature Neurosci., 6: 21-7

Lai HC, Klisch TJ, Roberts R, Zoghbi HY, Johnson JE. (2011). *In vivo* neuronal subtype-specific targets of Atoh1 (Math1) in dorsal spinal cord. J Neurosci., 31(30)10859-71

Landsberg RL., Awatramani RB., Hunter NL, Farago AF., DiPietrantonio HJ, Rodriguez CI., Dymecki SM. (2005). Hindbrain rhombic lip is comprised of discrete progenitor cell populations allocated by Pax6. Neuron, 48: 933-47

Laumonnerie C, Tong YG, Alstermark H, Wilson SI. (2015). Commissural axonal corridors instruct neuronal migration in the mouse spinal cord. Nat Commun., 6: 6028

Lee RT, Zhao Z, Ingham PW (2016). Hedgehog signalling. Development 143(3)367-72

Lebel M, Mo R, Shimamura K, Hui CC (2007). Gli2 and Gli3 play distinct roles in the dorsoventral patterning of the mouse hindbrain. Dev Biol., 302: 345-55.

Lendahl U, Zimmerman LB, McKay RD. (1990). CNS stem cells express a new class of intermediate filament protein. Cell 60: 585–595.

Liem KF Jr, Jessell TM, Briscoe J (2000). Regulation of the neural patterning activity of sonic hedgehog by secreted BMP inhibitors expressed by notochord and somites. Development 127(22):4855-66

Litingtung Y and Chiang C. (2000) Specification of ventral neuron types is mediated by an antagonistic interaction between Shh and Gli3. Nat Neurosci 3:979-85

Lei Q, Jeong Y, Misra K, Li S, Zelman AK, Epstein DJ, Matise MP. (2006). Wnt signaling inhibitors regulate the transcriptional response to morphogenetic Shh-Gli signaling in the neural tube. Dev Cell., 11(3):325-37

Li S, Qiu F, Xu A, Price SM, Xiang M. (2004). Barhl1 regulates migration and survival of cerebellar granule cells by controlling expression of the neurotrophin-3 gene. J. Neurosci., 24: 3104-14

Liem KF Jr. He M, Ocbina PJ, Anderson KV. (2009). Mouse Kif7/Costal2 is a cilia-associated protein that regulates Sonic hedgehog signaling. Proc Natl Acad Sci USA. 106:13377-82

Liu A, Niswander LA. (2005). Bone morphogenetic protein signalling and vertebrate nervous system development. Nat Rev Neurosci., 6(12):945-54

Liu F, Massague´ J, Ruiz i Altaba A. (1998) Carboxy-terminally truncated Gli3 proteins associate with Smads. Nat Genet., 20: 325-326.

Liu Z, Li H, Hu X, Yu L, Liu H, Han R, Colella R, Mower GD, Chen Y, Qiu M. (2008). Control of precerebellar neuron development by Olig3 bHLH transcription factor, J Neurosci, 28 10124-33.

Lois C, García-Verdugo JM, Alvarez-Buylla A. (1996). Chain migration of neuronal precursors. Science 271(5251):978-81

Louvi A, Sisodia SS, Grove EA. (2004). Presinilin1 in migration and morphogenesis in the central nervous system. Development 131(13): 3093-105

Luccardini C, Hennekinne L, Viou L, Yanagida M, Murakami F, Kessaris N, Ma X, Adelstein RS, Mege RM, Metin C. (2013). N-cadherin sustains motility and polarity of future cortical interneurons during tangential migration. J Neurosci., 33(46):18159-60

Magnani D, Hasenpusch-Theil K, Jacobs EC, Campagnoni AT, Price DJ, Theil T. (2010). The Gli3 hypomorphic mutation Pdn causes selective impairment in the growth, patterning, and axon guidance capability of the lateral ganglionic eminence. J Neurosci., 30: 13883-94

Magnani D, Hasenpusch-Theil K, Theil T. (2013). Gli3 controls subplate formation and growth of cortical axons. Cereb Cortex, 23(11): 2542-51

Magnani D, Hasenpusch-Theil K, Benadiba C, Yu T, Basson MA, Price DJ, Lebrand C, Theil T. (2014). Gli3 Controls Corpus Callosum Formation by Positioning Midline Guideposts During Telencephalic Patterning. Cereb Cortex, 24(1):186-98

Marcelle C, Stark MR, Bronner-Fraser M. (1997). Coordinate actions of BMPs, Wnts, Shh and noggin mediate patterning of the dorsal somite. Development 124(20):3955-63

Marcos S, Backer S, Causeret F, Tessier-Lavigne M, Bloch-Gallego. (2009). Differential roles of Netrin-1 and its receptor DCC in inferior olivary neuron migration. Mol Cell Neurosci., 41: 429-39

Marshall H, Morrison A., Studer M, Popperl H, Krumlauf R. (1996). Retinoids and Hox genes. FASEB J., 10: 969-78

Matsuoka T, Ahlberg PE, Kessaris N, Iannarelli P, Dennehy U, Richardson WD, McMahon AP, Koentges G (2005). Neural crest origins of the neck and shoulder. Nature, 436(7049):347-55

Maynard TM, Jain MD, Balmer CW, Lamantia AS (2002). High-resolution mapping of the Gli3 mutation extra-toes reveals a 51.5-kb deletion. Mamm Genome, 13:58-61

Megason SG, McMahon AP. (2002). A mitogen gradient of dorsal midline Wnts or- ganizes growth in the CNS. Development, 129:2087–98.

Meyer NP, Roelink H (2003). The amino-terminal region of Gli3 antagonizes the Shh response and acts in dorsoventral fate specification in the developing spinal cord. Dev Biol 257(2):343-55

Minoux M, Antonarakis G, Kmita M, Dubole D, Rijli FM. (2009). Rostral and caudal pharyngeal arches share a common neural crest ground pattern. Development, 136:637-645

Minoux M, Rijli FM. (2010). Molecular mechanisms of cranial neural crest cell migration and patterning in craniofacial development. Development, 137(16):2605-21

Miyahara M, Shirasaki R, Tashiro Y, Muguruma K, Heizmann CW, Murakami F. (2003). Pathfinding and growth termination of primary trigeminal sensory afferents in the embryonic rat hindbrain. J Comp Neurol, 460(4): 503-13

Mo R, Freer AM, Zinyk DL, Crackower MA, Michaud J, Heng HH, Chik KW, Shi XM, Tsui LC, Cheng SH, Joyner AL, Hui C. (1997). Specific and redundant functions of Gli2 and Gli3 zinc finger genes in skeletal patterning and development. Development, 124: 113-123.

Mo, Z., Li, S., Yang, X. and Xiang, M. (2004). Role of the Barhl2 homeobox gene in the specification of glycinergic amacrine cells. Development, 131:1607-18.

Moreno-Bravo JA, Roig Puiggros S, Blockus H, Dominici C, Zelina P, Mehlen P, Chédotal A. (2018). Commissural neurons transgress the CNS/PNS boundary in absence of ventricular zone-derived netrin 1. Development, 145(2). Pii: dev159400

Müller T, Anlag K, Wildner H, Britsch S, Treier M, Birchmeier C. (2005). The bHLH factor Olig3 coordinates the specification of dorsal neurons in the spinal cord. Genes Dev., 19: 733-743

Murdoch JN, Copp AJ. (2010). The relationship between sonic hedgehog signaling, cilia, and neural tube defects. Birth defects Res A Clin Mol Teratol 88(8):633-52

Muroyama Y, Fujihara M, Ikeya M, Kondoh H, Takada S. (2002). Wnt signaling plays an essential role in neuronal specificaiton of the dorsal spinal cord. Genes Dev., 16(5):548-53

Nakhai H, Sel S, Favor J, Mendoza-Torres L, Paulsen F, Duncker GI, Schmid RM. (2007). Ptf1a is essential for the differentiation of GABAergic and glycinergic amacrine cells and horizontal cells in the mouse retina. Development, 134(6):1151-60

Nguyen V, Chokas AL, Stecca B, Ruiz i Altaba A. (2005). Cooperative requirement oft he Gli proteins in neurogenesis. Development, 132(14): 3267-79

Nichols DH. (1986). Formation and distribution of neural crest mesenchyme to the first pharyngeal arch region of the mouse embryo. Am J Anat 176: 221-31

Nichols DH and Bruce LL. (2006). Migratory routes of fate cells transcribing the Wnt-1 gene in the murine hindbrain. Dev Dyn., 235(2): 285 -300

Niehrs C. (2012). The complex word of WNT receptor signalling. Nat Rev Mol Cell Biol 13(12): 761-79

Nielsen CM and Dymecki SM. (2010). Sonic hedgehog is required for vascular outgrowth in the hindbrain choroid plexus. Dev Biol. 340: 430-7

Nothwang HG, Ebbers L, Schlüter T, Willaredt MA. (2015). The emerging framework of mammalian auditory hindbrain development. Cell tissue Res. 361: 33 - 48

Ng J and Curran T. (2011). The Hedgehog´s tale: developing strategies for targeting cancer. Nature Rev Cancer, 11: 493-501

Okada T, Keino-Masu K, Masu M. (2007). Migration and nucleogenesis of mouse precerebellar neurons visualized by *in utero* electroporation of a green fluorescent protein gene. Neurosci Res., 57(1) 40-9

Ono K, Kawamura K. (1990). Mode of neuronal migration of the pontine stream in fetal mice. Anat Embryol (Berl), 182(1): 11-9

Oury F Murakami Y, Renaud JS, Pasqualetti M, Charnay P, Ren SY, Rijli FM. (2006). Hoxa2 and rhombomere-dependent development of the mouse facial somatosensory map. Science, 313 (5792) 1408-13

Park HL, Bai C, Platt KA, Matise MP, Beeghly A, Hui CC, Nakashima M, Joyner AL. (2000). Mouse Gli1 mutants are viable but have defects in SHH signaling in combination with a Gli2 mutation. Development, 127, 1593-1605.

Patten I, Placzek M. (2002). Opponent activities of Shh and BMP signaling during floor plate induction in vivo. Curr. Biol., 12: 47–52.

Paxinos G., Halliday G., Watson C, Koutcherov Y, Wang HQ (2007) . Atlas of the developing mouse brain at E17.5, P0 and P6. Elsevier academic press, San Diego.

Paxinos G et al, (2012). Chapter 8 - Organization of brainstem nuclei. In: Mai JK and Paxinos G editors. The human nervous system. p. 260–327. ISBN: 978-0-12-374236-0

Pazour GJ, Witman GB. (2003). The vertebrate primary cilium is a sensory organelle. Curr Opin Cell Biol., 15(1): 105-10

Persson M, Stamataki D, te Welscher P, Andersson E, Böse J, Rüthner U, Ericson J, Briscoe J. (2002). Dorsal-ventral patterning of the spinal cord requires Gli3 transcriptional repressor activity. Genes Dev, 16(22): 2865-78.

Rahimi-Balaei M, Afsharinezhad P, Bailey K, Buchok M, Yaganeh B, Maryban H. (2015). Embryonic stages in cerebellar afferent development. Cerebellum Ataxias, 2:7

Rallu M, Machold R, Gaiano N, Corbin JG, McMahon AP, Fishell G. (2002). Dorsoventral patterning is established in the telencephalon of mutants lacking both Gli3 and Hedgehog signaling. Development,

Ray RS, Dymecki SM. (2009). Rautenlippe Redux-toward an unified view of the precerebellar rhombic lip. Curr Opin Neurobiol., 21: 741-747

Rebman JK, Kirchoff KE, Walsh GS. (2016). Cadherin-2 is required cell autonomously for collective cell migration of facial brachiomotor neurons. PLoS One, 11(10):e0164433

Redies C, Inuzuka H, Takeichi M. (1992). Restricted expression of N- and R-cadherin on neuritis of the developing chicken CNS. J Neurosci., 12(9): 3525-34

Redies C and Takeichi. (1996). Cadherins in the developing central nervous system. An adhesive code for segmental and functional subdivisions. Dev Biol., 180: 413-23

Reeber SL, White JJ, Geroge-Jones NA, Sillitoe RV. (2013). Architecture and development of olivocerebellar circuit topography. Front Neural Circuits. 6:115. doi: 10.3389/fncir.2012.00115

Reig G, Cabrejos ME, Concha ML. (2007). Functions of BarH transcription factors during embryonic development. Dev Biol. 302: 367-75

Resibois A, Cuvelier L, Goffinet AM. (1997). Abnormalities in the cerebellum and brainstem in homozygous Lurcher mice. Neurosci., 80:175-90

Richard JTW. (2001). The rhombic lip and early cerebellar development. Curr Opin Neurobiol., 11: 82-88

Rieger S, Senghaas N, Walch A, Köster RW. (2009). Cadherin-2 controls directional chain migration of cerebellar granule neurons. PLoS Biol., 7(11):e1000240. Doi: 10.1371/journal.pbio.1000240

Robbins DJ, Fei DL, Riobo NA. (2012). The hedgehog signal transduction network. Sci Signal 5(246):re6

Rohatgi R, Milenkovic L, Scott MP. (2007). Patched1 regulates hedgehog signaling at the primary cilium. Science, 317(5836):372-6

Rose MF, Ahmad KA, Thaller C, Zoghbi HY. (2009). Excitatory neurons of the proprioceptive, interoceptive, and arousal hindbrain networks share a developmental requirement for Math1. Proc Natl Acad Sci USA. 106 (52):22462-7

Roycroft A, Mayor R. (2016). Molecular basis of contact inhibition of locomotion. Cell Mol Life Sci. 73(6): 1119-30

Saba R, Nakatsuji N, Saito T (2003). Mammalian BarH1 confers commissural neuron identity on dorsal cells in the spinal cord. J Neurosci., 23: 1987-91

Saba R, Johnson JE, Saito T. (2005). Crommissural neuron identity is specified by a homeodomain protein, Mbh1, that is directly downstream of Math1. Development, 132:2147-55

Schambra U and Connelly B. (2008). Prenatal mouse brain atlas. Springer. ISBN: 978-0-387-47089-4

Schimmang T, Lemaistre M, Vortkamp A, Ruther U. (1992). Expression of the zinc finger gene Gli3 is affected in the morphogenetic mouse mutant extra-toes (Xt). Development, 116:799-804

Schlosser G. (2006). Induction and specification of cranial placodes. Dev Biol 294(2):303-51

Schwarz Q, Vieira JM, Howard B, Eickholt BJ, Ruhrberg C. (2008). Neuropilin 1 and 2 control cranial gangliogenesis and axon guidance through neural crest cells. Development, 135:1605– 1630

Shao M, Liu C, Song Y, Ye W et al., (2015). Fgf8 signalling sustains progenitor status and multipotency of cranial neural crest-derived mesenchymal cells in vivo and in vitro. J Mol Cell Biol 7(5): 441-54

Shiau CE, Bronner-Fraser M. (2009). N-cadherin acts in concert with Slit1-Robo2 signaling in regulating aggregation of placode-derived cranial sensory neurons. Development 136(24):4155-64

Shimamura K, Takahashi T, Takeichi M. (1992). E-cadherin expression in a particular subet of sensory neurons. Dev Biol., 152(2):242-54

Shinohara M, Zhu Y, Murakami F. (2013). Four-dimensional analysis of nucleogenesis of the pontine nucleus in the hindbrain. J Comp Neurol., 521 (14): 3340-57

Sieber MA, Storm R, Martinez-de-la-Torre M, Müller T, Wende H, Reuter K, Vasyutina E, Birchmeier C. (2007). Lbx1 acts as a selector gene in the fate determination of somatosensory and viscerosensory relay neurons in the hindbrain. J Neurosci., 27:4902-9

Sillitoe RV, YuHong F, Watson C. (2012). Chapter 11 – Cerebellum. In Watson C, Paxinos G, Puelles L editors. The mouse nervous system. P 360 – 397. ISBN: 978-0-12-369497-3

Sotelo, C. (2004). Cellular and genetic regulation of the development of the cerebellar system. Prog. Neurobiol., 72: 295-339.

Sotelo C and Chedotal A. (2013). Hindbrain tangential migration. In: Rubenstein J and Rakic P editors. Cellular migration and formation of neuronal connections. p. 345–62. ISBN: 978-0-12-397266-8

Stark MR, Sechrist J, Bronner-Fraser M, Marcelle C. (1997). Neural tube-ectoderm interactions are required for trigeminal placode formation. Development, 124: 4287-95.

Steventon B, Mayor R, Streit A. (2014). Neural crest and placode interaction during the development of the cranial sensory system. Dev Biol, 389(1):28-38

Storm R, Cholewa-Waclaw J, Reuter K, Bröhl D, Sieber M, Treier M, Müller T, Birchmeier C. (2009). The bHLH transcription factor Olig3 marks the dorsal neuroepithelium of the hindbrain and is essential for the development of brainstem nuclei. Development, 136(2): 295-305

Suzuki SC, Inoue T, Kimura Y, Tanaka T, Takeichi M. (1997). Neuronal circuits are subdivided by differential expression of type-II classic cadherins in postnatal mouse brains. Mol Cell Neurosci., 9:433 - 47.

Tabler JM, Rice CP, Liu KJ, Wallingford JB. (2016). A novel ciliopathic skull defect arising from excess neural crest. Dev. Biol., 417 (1):4-10

Takahashi M, Osumi N (2008). Expression study of cadherin7 and cadherin20 in the embryonic and adult rat central nervous system. BMC Dev Biol., 8:87.

Taniguchi, H., Tamada, A., Kennedy, T. E. and Murakami, F. (2002). Crossing the ventral midline causes neurons to change their response to floor plate and alar plate attractive cues during transmedian migration. Dev. Biol. 249: 321-332.

Taniguchi H, Kawauchi D, Nishida K, Murakami F. (2006). Classic cadherins regulate tangential migration of precerebellar neurons in the caudal hindbrain. Development, 133 (10): 1923-31

Taroc EZM, Prasad A, Lin JM, Froni PE. (2017). The terminal nerve plays a prominent role in GnRH-1 neuronal migration independent from proper olfactory and vomeronasal connections to the olfactory bulbs. Biol Open., 6(10):1552-1568

Tassir F, Goffinet AM. (2003). Reelin and brain development. Nat Rev Neurosci., 4:496-505

Theil D, Fatzer R, Schiller I, Caplazi P, Zurbriggen A, Vandevelde M. (1998). Neuropathological and aetiological studies of sporadic non-suppurative meningoencephalomyelitis of cattle. Vet Rec. 143(9): 244-9

Theil, T, Alvarez-Bolado G, Walter A, Rüther U. (1999). Gli3 is required for Emx gene expression during dorsal telencephalon development. Development, 1999. 126(16): 3561-71

Theil T. (2005). Gli3 is required for the specification and differentiation of preplate neurons. Dev Biol, 286**:** 559-71.

Thien H, Rüther U. (1999). The mouse mutation Pdn (Polydactyly Nagoya) is caused by the integration of a retrotransposoin into the Gli3 gene. Mamm Genome, 10:205-9

Tole S, Ragsdale CW. Grove EA. (2000). Dorsoventral patterning of the telencephalon is disrupted in the mouse mutant extra-toes(J). Dev Biol., 217**:** 254-65.

Tomioka N, Osumi N, Sato Y, Inoue T, Nakamur S, Fujisawa H, Hirata T. (2000). Neocortical origin and tangential migration of guidepost neurons in the lateral olfactory tract. J Neurosci., 20: 5802-12

Trainor PA, Ariza-McNaughton L, Krumlauf R. (2002). Role of the isthmus and FGFs in resolving the paradox of neural crest plasticity and prepatterning. Science, 295:1288-91

Treubert-Zimmerman U, Heyers D, Redies C. (2002). Targeting axons to specific fiber tracts in vivo by altering cadherin expression. J Neurosci., 22(17): 7617-26

Tronche F, Kellendonk C, Kretz O, Gass P, Anlag K, Orban PC, Bock R, Klein R, and Schütz G. (1999). Disruption of the glucocorticoid receptor gene in the nervous system results in reduced anxiety. Nat Genet., *23*, 99-103.

Tümpel S., Wiedemann LM, Krumlauf R. (2009) Hox genes and segmentation of the vertebrate hindbrain. Curr Top Dev Biol. 88: 103-137

Ueta E, Nanba E, Naruse I. (2002). Integration of a transposon into the Gli3 gene in the Pdn mouse. Congenit Anom (Kyoto), 42: 318-22

Ulloa F, Itasaki N, Briscoe J. (2007). Inhibitory Gli3 activity negatively regulates Wnt/beta-catenin signaling. Curr Biol., 17(6): 545-50

Ulloa F, Martí E. (2010). Wnt won the war: antagonistic role of Wnt over Shh controls dorso-ventral patterning of the vertebrate neural tube. Dev Dyn., 239(1): 69-76

Van Amerongen R, Mikels A Nusse R. (2008). Alternative wnt signaling is initiated by distinct receptors. Sci Signal., 1(35):re9

Varadarajan SG, Kong JH, Phan KD, Kao TJ, Panaitof SC, Cardin J, Eltzschig H, Kania A, Novitch BG, Butler SJ. (2017). Netrin1 produced by neural progenitors, not floor plate cells, is required for axon guidance in the spinal cord. Neuron 94(4):790-99

Vasyutina E, Lenhard DC, Wende H, Erdmann B, Epstein JA, Birchmeier C. (2007). RBP-J (Rbpsuh) is essential to maintain muscle progenitor cells and to generate satellite cells. Proc Natl Acad Sci USA. 104(11): 4443-8

Veistinen L, Takatalo M, Tanimoto Y, Kesper DA, Vortkamp A, Rice DP. (2012). Loss-of-function of Gli3 in mice causes abnormal frontal bone morphology and premature synostosis of the interfrontal suture. Front Physiol., 3: 121.

Vilensky JA. (2014). The neglected cranial nerve: nervus terminalis (cranial nerve N). Clin Anat., 27(1): 46-53

Vilz TO, Moepps B, Engele J, Molly S, Littman DR, Schilling K. (2005). The SDF-1/CXCR4 pathway and the development of the cerebellar system Eur J Neurosci., 22: 1831-39

Vortkamp A, Franz T, Gessler M, Grzeschick KH. (1992). Deletion of GLI3 supports the homolog oft he human Greig cephalopolysyndactyly syndrom (GCPS) and the mouse mutant extra toes (Xt). Mamm Geneome, 3(8): 461-3

Watson C. (2012). Chapter 12 – Hindbrain. In Watson C, Paxinos G, Puelles L editors. The mouse nervous system. P 398 – 423. ISBN: 978-0-12-369497-3

Wang B, Fallon JF, Beachy PA. (2000). Hedgehog-regulated processing of Gli3 produces an anterior/posterior repressor gradient in the developing vertebrate limb. Cell 100(4): 423-34

Wang VY et al. Rose MF, Zoghbi HY. (2005). Math1 expression redefines the rhombic lip derivatives and reveals novel lineages within the brainstem and cerebellum. Neuron 48: 31-43

Wang W, Mullikin-Kilpatrick D, Crandall JE, Gronostajski RM, Litwack ED, Kilpatrick DL (2007). Nuclear factor I coordinates multiple phases of cerebellar granule cell development via regulation of cell adhesion molecules. J Neurosci., 27:6115-27

Wang W, Crandall JE, Litwack ED, Gronostajski RM, Kilpatrick DL (2010). Targets of the nuclear factor I regulon involved in early and late development of postmitotic cerebellar granule neurons. J Neurosci Res., 88: 258-65

Wang H, Ge G, Uchida Y, Luu B, Ahn S. (2011). Gli3 is required for maintenance and fate specification of cortical progenitors. J Neurosci 31(17): 6440-8

Wang H, Kane AW K, Lee C, Ahn S. (2014). Gli3 repressor controls cell fates and cell adhesion for proper establishment of neurogenic niche. Cell Rep 8(4):1093-104

Wanner SJ, Prince VE. (2013). Axon tracts guide zebrafish facial branchiomotor neuron migration through the hindbrain. Development, 140(4):906-15

Watanabe Y, Duprez D, Monsoro-Burq AH, Vincent C, Le Douarin NM. (1998). Two domains in vertebral development: antagonistic regulation by SHH and BMP4 proteins. Development, 125(14): 2631-9.

Watanabe H, Murakami F. (2009). Real time analysis of pontine neurons during initial stages of nucleogenesis. Neurosci Res., 64(1): 20-9

Wingate RJ, Lumsden A (1996). Persistence of rhombomeric organisation in the postsegmental hindbrain. Development 122:2143-52

Wolfer DP, Henehan-Beatty A, Stoeckli ET, Sonderegger P, Lipp HP. (1994). Distribution of TAG-1/axonin-1 in fibre tracts and migratory streams of the developing mouse nervous system. J Comp Neurol., 345:1-32

Wilson SI, Shafer B, Lee KJ, Dodd J. (2008) A molecular program for contralateral trajectory: Rig-1 control by LIM homeodomain transcription factors. Neuron, 59:413–424.

Xiang M, Gan L, Zhou L, Klein WH, Nathans J. (1996). Targeted deletion of the mouse POU domain gene Brn-3a causes selective loss of neurons in the brainstem and trigeminal ganglion, uncoordinated limb movement, and impaired suckling. Proc Natl Acad Sci USA, 93(21): 11950-5.

Yamada M, Terao M, Terashima T, Fujiyama T, Kawaguchi Y, Nabeshima Y, Hoshino M. (2007). Origin of climbing fiber neurons and their developmental dependence on Ptf1a. J Neurosci 27(41):10924-34

Yamada M, Seto Y, Taya S, Owa T, Inoue YU, Inoue T, Kawauchi Y, Nabeshima Y, Hoshino M. (2014). Specification of spatial identities of cerebellar neuron progenitors by ptf1a and atoh1 for proper production of GABAergic and glutamatergic neurons. J Neurosci 34(14):4786-800

Yamaguchi M, Saito H, Suzuki M, Mori K. (2000). Visualization of neurogenesis in the central nervous system using nestin promoter-GFP transgenic mice. Neuroreport 11: 1991-1996.

Yamauchi K, Yamazaki M, Abe M, Sakimura K, Lickert H, Kawasaki T, Murakami F, Hirata T. (2017). Netrin-1 derived from the ventricular zone, but not the floor plate, directs hindbrain commissural axons to the ventral midline. Sci Rep., 7(1): 11992

Yung AR, Druckenbrod NR, Cloutier JF, Wu Z, Tessier-Lavigne M, Goodrich LV (2018). Netrin-1 confines rhombic lip-derived neurons to the CNS. Cell Rep., 22(7): 1666-80

Yu W, McDonnell K, Taketo MM, Bai CB. (2008). Wnt signaling determines ventral spinal cord cell fates in a time - dependent manner. Development, 135: 3687–3696.

Yee KT, Simon HH, Tessier-Lavigne M, O´Leary DM. (1999). Extension of long leading processes and neuronal migration in the mammalian brain directed by the chemoattractant netrin-1. Neuron, 24(3): 607-22

Zechner D, Fujita Y, Hulsken J, Muller T, Walther I, Taketo MM, Crenshaw EB 3rd, Birchmeier W, Birchmeier C. (2003). Beta-Catenin signals regulate cell growth and the balance between progenitor cell expansion and differentiation in the nervous system. Dev Biol., 258(2): 406-18

Zechner D, Müller T, Wende H, Walther I, Taket MM, Crenshaw EB 3rd, Treier M, Birchmeier W, Birchmeier C (2007). Bmp and Wnt/beta-catenin signals control expression of the transcription factor Olig3 and the specification of spinal cord neurons. Dev Biol., 303:181-90

Zhang YE. (2009). Non-Smad pathways in TGF-ß signaling. Cell Res., 19(1): 128-39

Zhu Y, Matsumoto T, Mikami S, Nagasawa T, Murakami F. (2009). SDF1/CXCR4 signalling regulates two distinct processes of precerebellar neuronal migration and its depletion leads to abnormal pontine nuclei formation. Development, 136(11):1919-28

Zhu Y and Murakami F. (2012). Chemokine CXCL12 and its receptors in the developing central nervous system: emerging themes and future perspectives. Dev Neurobiol., 72(10)1349-62

9. ACKNOWLEDGEMENTS

I would like to express my deep appreciation to Prof. Dr. Sandra Blaess for her support; from the time I applied for funding to work in her group, and until finishing my Ph.D. I deeply appreciate her will to act as my first supervisor and all the effort she put to review this thesis. Her valuable comments and critics, as well as her patience and good attitude, were key to complete this thesis.

I also would like to thank Prof. Dr. Oliver Brüstle for providing a nice working environment in the Institute, for the nice talks and orientation, and for his willingness to lend an ear when needed.

I am grateful to the people directly involved in evaluating this thesis: Prof. Dr. Walter Witke who agreed to be my second supervisor, and also Prof. Dr. Stephan Baader and Prof. Dr. Ulrich Kubitscheck, who accepted to be part of my thesis committee. In particular, I want to thank Prof. Dr. Stephan Baader for giving me orientation and support in difficult times.

I gratefully acknowledge the German Academic Exchange Service (DAAD) for financing my studies and for being a world-class institution who sees for his scholarship holders.

I take advantage of the opportunity to thank current and former members of the Institute of Reconstructive Neurobiology for lending a helping hand whenever needed. In particular, I would like to thank the friendly people, who in addition, contributed to keeping a smile while working: Bärbel Wagner, Alexandra Rabe, Andy Till, Daniel Poppe, Steffi Kalisch, Ksenia Vinnikova, Katharina Günther, Melanie Bloschies, Julia Fischer, Jasmin Jatho-Gröger, Leon Bischoff, Karen Laupman, Frederike Klaus, Lea Flitsch, Anke Leinhaas, Barbara Steinfarz, and Monika Veltel.

I also thank all my colleagues in the Blaess Group for the time together during these last years.

I wish to express my appreciation to the people who became friends while living in Germany. Their contribution was not academic, but it was essential to finish this thesis. Many thanks, Shohreh Karimian, Johannes Ziemer, Stephan Giepner, Sarah Kuhnert, Christian Wolf, Dennis Große-Plankermann, Mina Attahie, Sofia Markou, Jürgen Meisenbach, Sylvia Vollmar, Hendrik Wiethoff, Nadja Spennemann, and Adrián López Fernández.

Finally, I want to thank my family for their unconditional support and encouragement throughout my life. In particular to my mother and grandma, whose example helped me to keep going and maintain a steady mind and heart.